Forward and back-propagation of compressional waves in horizontal transverse isotropy (HTI) media

Propagacja fal podłużnych „w przód" i „wstecz" w ośrodkach o horyzontalnej izotropii poprzecznej (HTI)

Andrzej Kostecki, Krzysztof Żuławiński

Forward and back-propagation of compressional waves in horizontal transverse isotropy (HTI) media

Propagacja fal podłużnych „w przód" i „wstecz" w ośrodkach o horyzontalnej izotropii poprzecznej (HTI)

Instytut Nafty i Gazu – Państwowy Instytut Badawczy

2016

Redaktor naukowy: prof. nzw. dr hab. Piotr Such
Recenzent: prof. dr hab. inż. Ryszard Ślusarczyk

DOI: 10.18668/PN2016.212

Wydawca:
Instytut Nafty i Gazu – Państwowy Instytut Badawczy
ul. Lubicz 25A
31-503 Kraków

Redaktor wydania: Agnieszka J. Kozak
Korekta językowa: Brian Scott
Skład i łamanie, DTP, projekt okładki: Paweł Noszkiewicz

Druk i oprawa:
Drukarnia K&K reklama i poligrafia
ul. Zakopiańska 9, 30-418 Kraków

Nakład: 70 egz.

Copyright © 2016 INiG – PIB Kraków, ul. Lubicz 25A, Poland

ISSN 2353-2718, ISBN 978-83-65649-17-1

Wszelkie prawa zastrzeżone. Żadna część niniejszej publikacji nie może być, bez uprzedniej pisemnej zgody wydawcy, gromadzona w systemach zbierania informacji, transmitowana lub reprodukowana, włączając w to fotokopie, fotografie, zapis magnetyczny lub inny.
Prenumeratę i wysyłkę prac naukowo-badawczych oraz materiałów informacyjnych prowadzi redakcja.

Spis treści

Abstract 8

Streszczenie 10

Introduction 12

Chapter 1. Equations of wave motion in HTI(Ψ) in the function of azimuthal angle Ψ 17

Introduction – dispersion equation – pseudo-acoustic equations 17

Basic equation 17

Chapter 2. Pseudo-acoustic wave equations 29

The stability 34

Signal testing 36

Results of azimuthal modeling 42

Chapter 3. Seismic migration in anisotropic media of type HTI(Ψ) in the function of azimuthal angle Ψ 106

Introduction 106

Basic equation for depth extrapolation of wavefields 107

Pre-stack migration 108
Zero-offset migration 110
Depth extrapolation operators 111
Modeling and migration of zero-offset time sections 112

Conclusions 189

References 191
Table of figures 196
Appendix A_1 207
Appendix A_2 210
Appendix A_3 215
Appendix A_4 217

Abstract

The present monograph, describing in detail compressional wave propagation in horizontal transverse isotropy (HTI) media as a function of azimuthal angle Ψ (angle between the two vertical planes: isotropy plane and plane of measurement), comprises the comprehensive study of wave spreading in anisotropic environment. The paper contains both the account of algorithmic relations of seismic modeling and migration and the abundant set of correctness verifying computer simulations as well.

The starting point for theoretical considerations is basic relation between stress and strain according to Hooke's law and the elastic wave equation, which lay down the full system of elastic equations. The dispersion equation derived from it in wavenumber domain, allows to get its eigenvalues – temporal frequency and vertical wavenumber. Temporal frequency was used to build our one-way wave equation for forward-propagation modeling, while the vertical wavenumber provides the main element of wave propagator for depth extrapolation, i.e. for seismic migration. As the solution of third degree equation, we show the exact version and two approximate versions. Those approximate solutions may be successfully applied in practice as shown by numerous examples of propagation simulation (errors do not exceed 1.6%). The approximate version of the depth extrapolator was also validated for zero-offset migration. We verified these algorithms in the range of ε [–0.3; 0.3], δ [–0.2; 0.2] parameter variability, i.e. typical properties for rock anisotropy in oil exploration. The zero-offset migration algorithm, proposed in this monograph, is the adapted version of MG(F-K) migration in wavenumber and frequency domain, developed by the authors for compressional and converted wave seismic migration as well as applied in VTI (Vertical Transverse Isotropy) and TTI (Tilted Transverse Isotropy) media.

The accuracy and high quality of wave propagation has been verified in plentiful zero-offset modeling and relevant seismic migration experiments for the two models,

for the multilayer anticline and for the fault zone. The wavefield images, obtained by the one-way equation in wavenumber domain, are deprived of the noise, including inherent for the wave equations in space domain "diamond shape" noise and multiple waves interferences.

Streszczenie

Niniejsza monografia, traktująca o propagacji fal podłużnych w ośrodku o poprzecznie poziomej izotropii HTI (*Horizontal Transverse Isotropy*) jako funkcji azymutalnego kąta Ψ (pomiędzy pionowymi płaszczyznami: izotropii oraz pomiarową), stanowi obszerne studium właściwości rozprzestrzeniania się fal w ośrodku anizotropowym. Praca zawiera zarówno opis relacji algorytmicznych procesów modelowania i migracji, jak i bogaty zestaw przykładów dokumentujących poprawność symulacji komputerowych.

Punktem wyjściowym w rozważaniach teoretycznych jest podstawowy związek pomiędzy naprężeniem a odkształceniem według prawa Hooke'a oraz równanie ruchu falowego, które formułują pełny system równań sprężystych. Wyprowadzone stąd równanie dyspersyjne w dziedzinie liczb falowych pozwala uzyskać wartość własną – częstotliwość czasową oraz pionową liczbę falową. Częstość czasowa posłużyła do sformułowania oryginalnego równania falowego jednostronnego, będącego podstawowym narzędziem modelowania „w przód", natomiast pionowa liczba falowa stanowi główny element propagatora falowego w procesie ekstrapolacji głębokościowej – migracji. W zakresie modelowania zaprezentowano ścisłą wersję rozwiązania równania trzeciego stopnia oraz dwie wersje aproksymacyjne, które – jak wykazały liczne przykłady symulacji propagacji – z powodzeniem mogą być również stosowane w praktyce (błędy ok. 1,6%). Także w zakresie migracji zero-offset stwierdzono przydatność aproksymacyjnej wersji ekstrapolatora. Weryfikację tych algorytmów przeprowadzono w zakresie zmienności parametrów: ε [−0,3; 0,3], δ [−0,2; 0,2], a więc w obszarze stanowiącym podstawowy przedmiot poszukiwań naftowych. Algorytm migracji zero-offset zaproponowany w niniejszej monografii jest zaadaptowaną wersją MG(F-K) migracji w dziedzinie liczb falowych i częstotliwości, opracowaną przez autorów dla izotropowej wersji dla fal podłużnych i przemiennych oraz dla anizotropowych ośrodków typu VTI (*Vertical Transverse Isotropy*) i TTI (*Tilted Transverse Isotropy*).

Szeroki zakres modelowań sekcji czasowych zero-offset i odpowiadających im obrazów odwzorowań migracyjnych, wykonanych dla modelu wielowarstwowej antykliny i strefy uskokowej, potwierdziły wysoką dokładność i jakość propagacji falowej pozbawionej efektów zakłócających typu *diamond shape*, będących immanentną cechą równań falowych we współrzędnych przestrzennych oraz fal wielokrotnych w konsekwencji stosowania jednostronnego równania we współrzędnych liczb falowych.

Introduction

The problem of taking into consideration the anisotropy of compressional wave velocity in seismic prospection was ignored for a long time, because of mathematical difficulties in quantitative description of the physical phenomena and deficiency in effective measurements and methodical estimation of anisotropy parameters.

Intensified theoretical and experimental investigations have followed spectacular defeats in matching the reflectors from seismic sequence analysis to drilling data in North Sea [5]. The detailed analyses have shown that the reason for deeper position of Jurassic sand – the main object of geophysical researches – was the overestimation of stack velocity. The result was created by anisotropy of compressional wave velocities of overlaying cretaceous shale series with substantial thickness. This caused an increase of the average quadratic velocity V_{NMO}. Likewise, Kendall, Grey and Miao [23] noted that the floor of salt diaper was moved about 400 m by the application of velocity charged with anisotropy influence (Mohogany field in Gulf of Mexico).

Now, many comparative examples of deep structures imaging for isotropy and anisotropy versions of wavefields exist, which indicates substantial influence of anisotropy parameters on structures imaging accuracy, even for small parameters of anisotropy. Although this paper is devoted to the application of compressional waves in oil prospection, we should underline the role of shear wave S splitting phenomena into modes with different polarizations SV and SH [12]. Analysis of this phenomenon is applied for crack orientation evaluation and reservoir parameters estimation.

The practical considerations and theoretical substantiations have determined acceptance of transverse isotropy (TI) models. In the case of thin horizontal layering, the shale – sands periodic scheme, we have the model of VTI type (Vertical Transverse Isotropy) with vertical symmetry axis, perpendicular to the isotropy plane, mathematically justified by G. M. Postma [42]. In the case, where the axis of symmetry and the vertical axis form a θ angle, this is

a monoclinal medium described by the tilted transverse isotropy (TTI) model. In the special case, where the angle $\theta = 90°$, we have horizontal transverse isotropy (HTI). A way for the calculation of wavefield characteristics as the function of azimuthal angle Ψ (angle between horizontal axis of acquisition X and the projection of vertical isotropy plane on xy-plane) is one of the two aims of this research project. Generally, the forward modeling of wavefields in anisotropic media should be executed by the solution of the full system of the elastic wave equations, determined by Hooke's law and equations of motion. Various methods are used: finite element, finite difference, spectral and pseudo-spectral, etc. [8, 55, 37, 52, 26, 64, 58, 14]. The ray tracing method, despite its limitations, can also be used to analyze wavefield characteristics [11] and successfully applied to modeling in laterally inhomogeneous media. Anyway, the numerical solution of the full system of the elastic wave equations in 3D media is a very time and resource consuming computational operation. As result, we have the components of field displacement, which respect the motion of compressional and shear waves. The interpretation of wave phenomena in this case is a complicated task and taking in consideration insufficient knowledge of anisotropy parameters in 3D media, this way of modeling is rarely used. For these reasons, the growing tendency to simplify the theory and to limit oneself to pseudo-acoustic equations has emerged. The basic assumption for this method is that the velocity of the shear wave $V_{SV} = 0$. This assumption results from Alkhalifah's [1, 2] numerical experiments, showing that the influence of the shear S wave on the velocity of the compressional wave P, is insignificant.

In seismic, the azimuthal dependence of measurement characteristics is directly connected with the type of anisotropy media. Transverse isotropy (TI) model with horizontal symmetry axis demonstrates such properties. That means that the compressional wave velocity differs in perpendicular and parallel direction to the isotropy plane. Grechka V. and Tsvankin I. [21] have derived the following relation for velocity V_{NMO} as the function of Ψ angle between the direction of the measurement line and the projection of the isotropy plane on the horizontal xy-plane:

$$\frac{1}{V_{NMO}^2(\Psi)} = W_{11}\cos^2\Psi + 2W_{12}\sin\Psi\cos\Psi + W_{22}\sin^2\Psi$$

where $W_{ij} = \tau_0\left(\frac{\partial p_i}{\partial x_j}\right)$ and $p_i = \frac{\partial \tau}{\partial x_i}$ for $(i = 1, 2)$ are the horizontal components of the slowness vector (the elements of W matrix) and τ_0 means one-way travel time from the zero-offset point.

From the above relation follows, that the dependence of velocity $V_{NMO}(\Psi)$ on the azimuthal angle Ψ has an elliptical character. This creates a practical prerequisite to determinate shale cracks orientation by seismic methods. The elliptical character of dependence $V_{NMO}(\Psi)$ velocity occurs also in more complicated orthorhombic media, e.g. in the combination of HTI and VTI models. Tsvankin I. and Grechka V. [53] determined the following dependence for orientation crack Φ_S:

$$\Phi_S = \tan^{-1}\left\{\frac{W_{22} - W_{11} + \left[\left(W_{22} - W_{11}\right)^2 + 4{W_{12}}^2\right]^{\frac{1}{2}}}{2W_{12}}\right\}$$

based on eigenvalue decomposition of symmetrical matrix W. The intensity of cracks is determined by the ratio of maximum to minimum eigenvalues of this matrix.

Recently one can notice substantial progress in the accuracy gain of traveltimes calculations in TTI media [40] and in the application of full azimuthal schema of common offset migration [56]. The well-known Taner and Koehler's [50] formula was adapted to anisotropy media by taking into consideration dip angles, azimuthal angles, inclination angle of crack plane.

A numerical experiment done by X. Sun and S. Sun [49] has shown that the application of the formula with fourth term taken into account, improves extraction effect in common image gather (CIG) not only in the surface domain of offset, but also when the angle of incident and azimuthal angle are defined in the subsurface domain of angles – migration LAD (Local Angle Domain) [25, 43].

Pseudo-acoustic wave equations in space-time domain derived by T. Alkhalifah [1, 2] are fundamental for compressional wave implementation in VTI media. Zhang et al. [60] adapting phase-velocity in VTI media to TTI (Tilted Transverse Isotropy) media obtained a differential equation of fourth order, which is in accordance with Alkhalifah's relation for VTI case. They demonstrated an interesting experiment through the comparison of the vertical component Z from a full wave equation with acoustic solution for a compressional wave. They found that results are kinematically similar but dynamically they differ considerably.

Alkhalifah's relations were subjected to many transformations in VTI media [62, 15, 16] and in TTI media [60, 63, 61, 18].

Starting with the phase velocities for P-wave and shear SV-wave Zhan et al. [59] developed decoupled equations for modeling and reverse time migration (RTM). The general feature of those solutions is the application of velocity approximation in Daley and Hron's [13] terms in space coordinates.

The authors of this paper [32] presented another concept of zero–offset time section modeling, based on the determination of time–frequency eigenvalue of the dispersion equation obtained from a full elastic equation for TTI media. In specific cases in 2D version we obtained the solution for VTI model and for HTI model when azimuthal angle $\Psi = 90°$. The modeling procedure is performed in space domain and in wavenumber–frequency domain. In heterogeneous medium, we use a pseudo-spectral method. This requires application of Fourier transform ($x \rightarrow k_x$) and its inverse ($k_x \rightarrow x$).

We obtain time zero–offset section based on the solution of one–way wave equation, which defines unequivocally the direction of compressional wave propagation. In general, the wavefield for arbitrary offset requires the solution of second order equation vs. time. The authors of this work proposed after all, the one-way equation of propagation wave in space domain and wavenumber – frequency domain, to simulate the wavefield for arbitrary offset. The advantage of this proposition is the elimination of multiples. This approach requires additional reformulating of the calculations procedure. This task will be the subject of works in the nearest future for the use of HTI(Ψ) model simulation for different azimuthal angles Ψ. The same velocity model for layered anticline as in the TTI model (for $\Psi = 90°$) [32], will be used for wave effects comparison for different anisotropy models.

The second aim of this research project was working out seismic depth migration in azimuthal anisotropy media. Back wavefield propagation, i.e. migration, can be produced in time–space or dual domain: wave numbers (K) – frequency (F) and time–space. In time–space domain, migration is made with Kirchhoff's theory and requires many multipathings [11, 48, 47]. In this category, special position in view of its effectiveness, takes up migration in reverse time [6, 39, 16, 18, 57].

In this process, we use forward modeling and record waves in reverse time taking into consideration the condition of imaging depth target.

Besides the mentioned Kirchhoff's method and reverse time migration there exist also algorithms of "phase shift plus interpolation" type, i.e. migration in wavenumbers and frequency domain [24, 45]. For those methods, the basic difficulties are the determination of the relation between the vertical and horizontal wavenumbers and anisotropy parameters.

Uzcategui [54] adapted an algorithm of finite difference to the extrapolation using a lateral convolution variant whereas Ristow and Rühl [44] worked out the algorithm based on finite difference with an approximate formula of velocity for "weak" anisotropy. Han and Wu [22] on the basis of Christoffel's equation reached a relation for a vertical wavenumber suitable in GSP (Generalized Screen Propagator). The propagator has the form of a one--way solution of wave equation and requires correction of the wavefield by the implicit finite difference method, which is very time-consuming. MG(F-K) (Generalized Migration in Wavenumber–Frequency) belongs to the group of one-way solution algorithms in the wavenumber–frequency domain, projected initially for compressional waves in pre-stack [27, 28] and zero-offset version [28] and then adapted to converted waves P-S [29].

Results of using MG(F-K) migration in TTI anisotropic media (Tilted Transverse Isotropy) were presented in the monograph [32] on examples of layered anticline and vertical fault (VTI) and in the paper [31].

In anisotropy media of HTI(Ψ) type the authors of this project proposed the application of MG(F-K) migration in the wavenumber – frequency domain, tested on synthetic models of VTI and TTI type models, inter alia on strong heterogeneous Marmousi dataset. In general, the downward extrapolation operator in TI media (Transverse Isotropy) is obtained from the dispersion equations derived from the full system elastic equations. In the case of the azimuthal operator, it requires to define the elasticity tensor for HTI in the function of azimuthal angle Ψ.

The correctness of azimuthal migration programs was tested on synthetic models of layering anticline and vertical thrust checked-out formerly for VTI and TTI migration algorithms.

Chapter 1. Equations of wave motion in HTI(Ψ) in the function of azimuthal angle Ψ

Introduction – dispersion equation – pseudo-acoustic equations

In this chapter we derive the full system of elastic equations from Hooke's law and the equation of motion in case of 3D – HTI(Ψ) media in the function of azimuthal angle Ψ. Building on this equation system we define the dispersion equation, allowing to derive eigenvalue – temporal frequency, on which we create a pseudo-acoustic equation of wave propagation.

Basic equation

Starting point under consideration is Hooke's law, which we use in the frame of symmetrical theory of elasticity. From it results, that each component of stress tensor T_{ij} is a linear function of strain E_{lk}

$$\begin{aligned} T_{ij} &= C_{ijkl}E_{kl} = C_{ijkl} \cdot E_{lk} \\ E_{lk} &= 1/2\left(U_{l,k} + U_{k,l}\right) \end{aligned} \tag{1.1}$$

where $C_{ijkl} = C$ is a four rank tensor of elastic modulus and $U_{l,k} = \frac{\partial U_l}{\partial k}$ is a partial derivative

l – component of displacement U in respect to k-th coordinate. Stress tensor $T_{ij} = T_{ji}$ is symmetrical which reduces from 9 to 6, the number of independent equations. Stiffness tensor C is given by symmetrical 6 × 6 matrix:

$$C = \begin{bmatrix} C_{11} & C_{12} & C_{13} & 0 & 0 & 0 \\ C_{12} & C_{11} & C_{13} & 0 & 0 & 0 \\ C_{13} & C_{13} & C_{33} & 0 & 0 & 0 \\ 0 & 0 & 0 & C_{44} & 0 & 0 \\ 0 & 0 & 0 & 0 & C_{44} & 0 \\ 0 & 0 & 0 & 0 & 0 & C_{66} \end{bmatrix} \tag{1.2}$$

Stiffness tensor C consists of five independent modulus of elasticity: C_{11}, C_{33}, C_{13}, C_{44}, C_{66} and $C_{12} = C_{11} - 2\,C_{66}$.

The four of them can be determined directly by velocities:

$$\begin{aligned} V_{P\|} &= \left(\frac{C_{11}}{\rho}\right)^{1/2} \\ V_{P\perp} &= \left(\frac{C_{33}}{\rho}\right)^{1/2} \\ V_{SH} &= \left(\frac{C_{66}}{\rho}\right)^{1/2} \\ V_{SV} &= \left(\frac{C_{44}}{\rho}\right)^{1/2} \end{aligned} \tag{1.3}$$

where $V_{P\|}$ and $V_{P\perp}$ are compressional velocities in parallel and perpendicular directions to the symmetry plane (plane of lamination); V_{SH} is a velocity of shear wave propagating in the isotropy plane with polarization also in this plane, then V_{SV} is a velocity of a shear wave S propagating in a plane perpendicular to the isotropy plane and polarized in this plane, ρ is density of media.

For isotropic media we have relations:

$$\begin{aligned} C_{11} &= C_{33} = \lambda + 2\mu \\ C_{12} &= C_{13} = \lambda \\ C_{44} &= C_{66} = \mu \\ C_{13} &= C_{33} - 2C_{44} \end{aligned} \tag{1.4}$$

where λ and μ are Lamé parameters.

The ratio of compressional wave velocity to a shear wave velocity is given by a strains rate – transverse to longitudinal i.e. Poisson ratio σ:

$$\frac{V_P}{V_S} = \sqrt{\frac{\lambda + 2\mu}{\mu}} = \sqrt{\frac{2(1-\sigma)}{1-2\sigma}} > \sqrt{2} \tag{1.5}$$

Describing anisotropy models we use Thomsen's parameters:

$$\varepsilon = \frac{C_{11} - C_{33}}{2C_{33}} \tag{1.6}$$

$$\delta = \frac{(C_{13} + C_{44})^2 - (C_{33} - C_{44})^2}{2C_{33}(C_{33} - C_{44})} \tag{1.7}$$

$$\gamma = \frac{C_{66} - C_{44}}{2C_{44}} \tag{1.8}$$

The relation presented above concerns the range of "weak anisotropy", which exist in most bulk elastic media [51]. Determination of the parameter δ requires measurements of phase velocity for angle $\theta = 0°, 45°, 90°$ and δ may be defined as:

$$\delta = 4\left[V_{P(\pi/4)}/-V_{P(0)} - 1\right] - \left[V_{P(\pi/2)}/V_{P(0)} - 1\right] \tag{1.9}$$

Parameter δ has essential meaning for imaging VTI media.

Normal-moveout velocity V_{NMO} obtained from velocity analyses will be:

$$V_{NMO} = V_{P(0)}\sqrt{1+2\delta} \tag{1.10}$$

where $V_{P(0)}$ is the velocity of a compressional wave in the vertical direction, i.e. perpendicular to the plane of lamination in the VTI media.

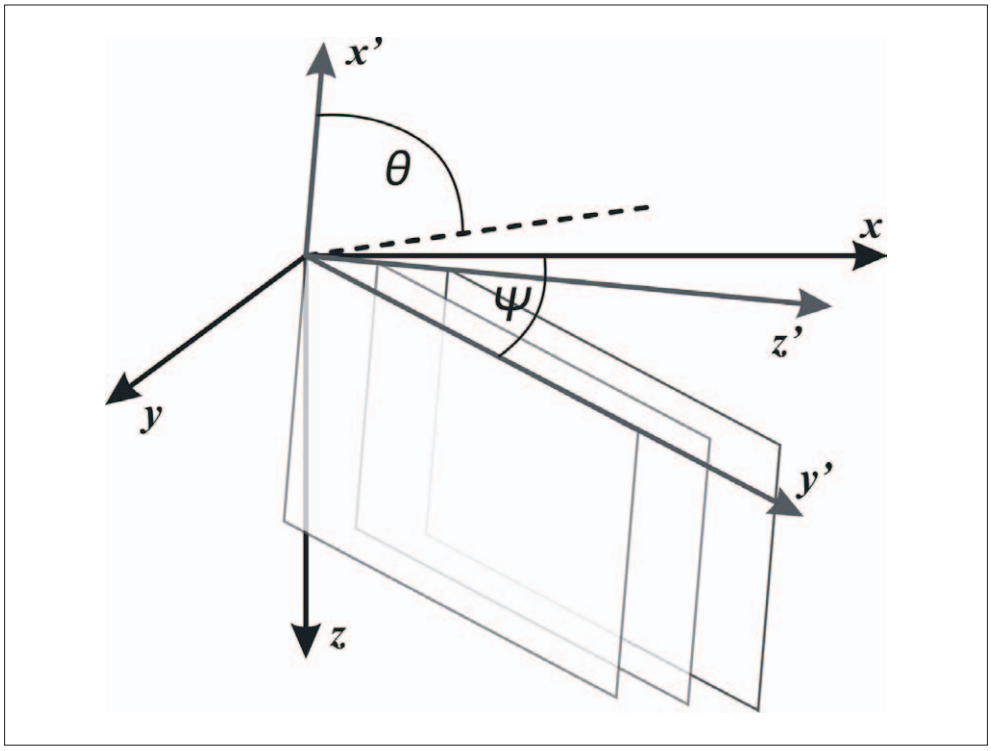

Fig. 1.1. Right-handed coordinate measurement system *x*, *y*, *z* and *x'*, *y'*, *z'* system tied with inclined, inter bedding layering simulating tilted media TTI (Titled Transverse Isotropy)

In considerations about algorithms of modeling, we often use relations:

$$\begin{aligned} C_{13} &= \rho\left(1+2\delta\right)^{1/2} V_{P\perp}^2 \\ C_{11} &= \rho V_{P\perp}^2 (1+2\varepsilon) \\ C_{11}+C_{33} &= 2\rho V_{P\perp}^2 (1+\varepsilon) \end{aligned} \tag{1.11}$$

where $V_{P\perp}$ is the velocity in a perpendicular direction to the lamination of thinly – layered media. Generally the stiffness tensor C (relation 1.2) describes the characteristic of anisotropy TI model (Transverse Isotropy). When symmetry axis perpendicular to the isotropy plane (the lamination of thinly – layered media) is directed vertically, we have model VTI (Vertical Transverse Isotropy). In general terms, the stiffness matrix depends on the orientation of anisotropy model in space.

The orientation of the TI medium in respect to the observation system x, y, z is defined by two angles: the dip angle θ and the angle Ψ between the strike of the isotropy plane and the measurement line. In order to fix the principles of propagation waves in the observation system x, y, z one should to perform the rotation of the matrix from x', y', z' system (such as for VTI model) to x, y, z system. Then using Bond's relation [4, 7, 64] one can obtain the relationship of elasticity modulus D in the observation system x, y, z expressed through the known matrix C – tensor in system x', y', z' rotated by angle Ψ vs. z-axis and dipping at θ angle (vs. horizontal plane):

$$D^{\theta,\Psi} = R \cdot C \cdot R^T \tag{1.12}$$

where the matrix R is as follows:

$$R = \begin{bmatrix} l_1^2 & m_1^2 & n_1^2 & 2m_1n_1 & 2n_1l_1 & 2l_1m_1 \\ l_2^2 & m_2^2 & n_2^2 & 2m_2n_2 & 2n_2l_2 & 2l_2m_2 \\ l_3^2 & m_3^2 & n_3^2 & 2m_3n_3 & 2n_3l_3 & 2l_3m_3 \\ l_2l_3 & m_2m_3 & n_2n_3 & m_2n_3+m_3n_2 & n_2l_3+n_3l_2 & l_2m_3+l_3m_2 \\ l_3l_1 & m_3m_1 & n_3n_1 & m_3n_1+m_1n_3 & n_3l_1+n_1l_3 & l_3m_1+l_1m_3 \\ l_1l_2 & m_1m_2 & n_1n_2 & m_1n_2+m_2n_1 & n_1l_2+n_2l_1 & l_1m_2+l_2m_1 \end{bmatrix} \tag{1.13}$$

and where:

$$\begin{aligned} l_1 &= \cos\theta \sin\Psi, & m_1 &= \cos\Psi, & n_1 &= \sin\theta \sin\Psi \\ l_2 &= -\cos\theta \cos\Psi, & m_2 &= \sin\Psi, & n_2 &= -\sin\theta \cos\Psi \\ l_3 &= -\sin\theta, & m_3 &= 0, & n_3 &= \cos\theta \end{aligned} \tag{1.14}$$

and the matrix R^T is a transposition of the R matrix. The C matrix is determined by relation (1.2). The components of $D^{\theta,\Psi}$ tensor are shown in appendix A_1.

In case of HTI medium, i.e. when the angle $\theta = 90°$, components of tensor $D^{\theta=90°,\Psi}$ are as follows:

$$\begin{aligned} d_{11} &= C_{11}\cos^4\Psi + C_{33}\sin^4\Psi + 2C_{13}\sin^2\Psi\cos^2\Psi + C_{44}\sin^2(2\Psi) \\ d_{12} &= d_{21} = (C_{11} + C_{33})\sin^2\Psi\cos^2\Psi + C_{13}(\sin^4\Psi + \cos^4\Psi) - C_{44}\sin^2(2\Psi) \\ d_{13} &= d_{31} = C_{12}\cos^2\Psi + C_{13}\sin^2\Psi \\ d_{14} &= d_{41} = 0 \\ d_{15} &= d_{51} = 0 \\ d_{16} &= d_{61} = \frac{1}{2}(C_{11} - C_{13})\sin(2\Psi)\cos^2\Psi + \frac{1}{2}(C_{13} - C_{33})\sin(2\Psi)\sin^2\Psi - \\ &\quad -C_{44}\sin(2\Psi)\cos(2\Psi) \end{aligned} \tag{1.15}$$

$$\begin{aligned} d_{22} &= C_{11}\sin^4\Psi + C_{33}\cos^4\Psi + 2C_{13}\sin^2\Psi\cos^2\Psi + C_{44}\sin^2(2\Psi) \\ d_{23} &= d_{32} = C_{12}\sin^2\Psi + C_{13}\cos^2\Psi \\ d_{24} &= d_{42} = 0 \\ d_{25} &= d_{52} = 0 \\ d_{26} &= d_{62} = \frac{1}{2}(C_{11} - C_{13})\sin(2\Psi)\sin^2\Psi + \frac{1}{2}(C_{13} - C_{33})\sin(2\Psi)\cos^2\Psi + \\ &\quad +C_{44}\sin(2\Psi)\cos(2\Psi) \\ d_{33} &= C_{11} \\ d_{34} &= d_{43} = 0 \\ d_{35} &= d_{53} = 0 \\ d_{36} &= d_{63} = \frac{1}{2}(C_{12} - C_{13})\sin(2\Psi) \end{aligned}$$

$$
\begin{aligned}
d_{44} &= C_{44}\cos^2\Psi + C_{66}\sin^2\Psi \\
d_{45} &= d_{54} = \left(C_{66} - C_{44}\right)\sin\Psi\cos\Psi \\
d_{46} &= d_{64} = 0 \\
d_{55} &= C_{44}\sin^2\Psi + C_{66}\cos^2\Psi \\
d_{56} &= d_{65} = 0 \\
d_{66} &= \frac{1}{4}\left(C_{11} - 2C_{13} + C_{33}\right)\sin^2\left(2\Psi\right) + C_{44}\cos^2\left(2\Psi\right)
\end{aligned}
\qquad \text{(1.15, cont.)}
$$

The relationship between stress tensor T_{ij} and strain E_{lk} and the derivatives of displacement U_{lk} in 3D case is given by:

$$
\begin{bmatrix} T_{11} \\ T_{22} \\ T_{33} \\ T_{23} \\ T_{13} \\ T_{12} \end{bmatrix} =
\begin{bmatrix}
d_{11} & d_{12} & d_{13} & 0 & 0 & d_{16} \\
d_{21} & d_{22} & d_{23} & 0 & 0 & d_{26} \\
d_{31} & d_{32} & d_{33} & 0 & 0 & d_{36} \\
0 & 0 & 0 & d_{44} & d_{45} & 0 \\
0 & 0 & 0 & d_{54} & d_{55} & 0 \\
d_{61} & d_{62} & d_{63} & 0 & 0 & d_{66}
\end{bmatrix}
\begin{bmatrix}
E_{xx} = U_{x,x} \\
E_{yy} = U_{y,y} \\
E_{zz} = U_{z,z} \\
2E_{yz} = U_{y,z} + U_{z,y} \\
2E_{xz} = U_{x,z} + U_{z,x} \\
2E_{xy} = U_{x,y} + U_{y,x}
\end{bmatrix}
\qquad (1.16)
$$

The basic equations describing wave propagation are equations of motion

$$
T_{ij,j} = \rho\frac{\partial^2 U_i}{\partial t^2} \qquad (1.17)
$$

where the subscript "*ij,j*" indicates the partial derivative of the tensor with respect to the *j*-th coordinate, *t* is time.

For the component of displacement we obtain:

$$
\begin{aligned}
T_{11,1} + T_{12,2} + T_{13,3} &= \rho\frac{\partial^2 U_1}{\partial t^2} \\
T_{21,1} + T_{22,2} + T_{23,3} &= \rho\frac{\partial^2 U_2}{\partial t^2} \\
T_{31,1} + T_{32,2} + T_{33,3} &= \rho\frac{\partial^2 U_3}{\partial t^2}
\end{aligned}
\qquad (1.18)
$$

where derivatives of stress $T_{ij,j}$ are as follows:

$$
\begin{aligned}
T_{11,1} &= d_{11}U_{x,xx} + d_{12}U_{y,yx} + d_{13}U_{z,zx} + d_{16}\left(U_{y,xx} + U_{x,yx}\right)\\
T_{12,2} &= d_{16}U_{x,xy} + d_{26}U_{y,yy} + d_{36}U_{z,zy} + d_{66}\left(U_{y,xy} + U_{x,yy}\right)\\
T_{13,3} &= d_{54}\left(U_{y,zz} + U_{z,yz}\right) + d_{55}\left(U_{x,zz} + U_{z,xz}\right)\\
T_{21,1} &= d_{61}U_{x,xx} + d_{26}U_{y,yx} + d_{63}U_{z,zx} + d_{66}\left(U_{y,xx} + U_{x,yx}\right)\\
T_{22,2} &= d_{21}U_{x,xy} + d_{22}U_{y,yy} + d_{23}U_{z,zy} + d_{26}\left(U_{y,xy} + U_{x,yy}\right)\\
T_{23,3} &= d_{44}\left(U_{y,zz} + U_{z,yz}\right) + d_{45}\left(U_{x,zz} + U_{z,xz}\right)\\
T_{31,1} &= d_{54}\left(U_{y,zx} + U_{z,yx}\right) + d_{55}\left(U_{x,zx} + U_{z,xx}\right)\\
T_{32,2} &= d_{44}\left(U_{y,zy} + U_{z,yy}\right) + d_{45}\left(U_{x,zy} + U_{z,xy}\right)\\
T_{33,3} &= d_{13}U_{x,xz} + d_{23}U_{y,yz} + d_{33}U_{z,zz} + d_{36}\left(U_{y,xz} + U_{x,yz}\right)
\end{aligned}
\tag{1.19}
$$

Equation systems (1.18) and (1.19) constitute the full equation system of elasticity describing the waves propagation in HTI(Ψ) medium.

Using Fourier transform ($x\rightarrow k_x$, $y\rightarrow k_y$, $z\rightarrow k_z$, $t\rightarrow\omega_a$) to (1.18–1.19) equations we obtain matrix equation normalized for ρ (density) components of displacement vector U expressed in wavenumber domain (k_x, k_y, k_z) and temporal frequency ω_a:

$$
\begin{bmatrix} a_{11} & a_{12} & a_{13} \\ a_{21} & a_{22} & a_{23} \\ a_{31} & a_{32} & a_{33} \end{bmatrix} \begin{bmatrix} U_x \\ U_y \\ U_z \end{bmatrix} = 0 \tag{1.20}
$$

where

$$
\begin{aligned}
a_{11} &= d_{11}k_x^2 + d_{66}k_y^2 + d_{55}k_z^2 + 2d_{16}k_xk_y - \omega_a{}^2\\
a_{12} &= a_{21} = d_{16}k_x^2 + d_{26}k_y^2 + d_{54}k_z^2 + \left(d_{12} + d_{66}\right)k_yk_x\\
a_{13} &= a_{31} = \left(d_{55} + d_{13}\right)k_xk_z + \left(d_{45} + d_{36}\right)k_yk_z\\
a_{22} &= d_{66}k_x^2 + d_{22}k_y^2 + d_{44}k_z^2 + 2d_{26}k_xk_y - \omega_a{}^2\\
a_{23} &= a_{32} = \left(d_{63} + d_{45}\right)k_xk_z + \left(d_{23} + d_{44}\right)k_yk_z\\
a_{33} &= d_{55}k_x^2 + d_{44}k_y^2 + d_{33}k_z^2 + 2d_{45}k_xk_y - \omega_a{}^2
\end{aligned}
\tag{1.21}
$$

The solution of the equation (1.20) requires fulfillment of the condition:

$$\det A = \det\begin{bmatrix} a_{11} & a_{12} & a_{13} \\ a_{21} & a_{22} & a_{23} \\ a_{31} & a_{32} & a_{33} \end{bmatrix} = 0 \tag{1.22}$$

where det means determinant of the matrix A (see appendix A_2).

This determinant is as follows:

$$\det A = H\left(k_x, k_y, k_z, \theta = 90°, \Psi\right) - \omega^6 + \omega^4 B - \omega^2 C = 0 \tag{1.23}$$

or in the equivalent form

$$y^3 - y^2 B + yC - H = 0 \tag{1.24}$$

where $\omega_a^2 = y$,

$$B = \begin{array}{l} k_x^2\left(d_{11} + d_{55} + d_{66}\right) + k_y^2\left(d_{22} + d_{44} + d_{66}\right) + \\ + k_z^2\left(d_{33} + d_{44} + d_{55}\right) + 2k_x k_y\left(d_{16} + d_{26} + d_{45}\right) \end{array} \tag{1.24a}$$

$$C = \begin{cases} \left(d_{11}k_x^2 + d_{66}k_y^2 + d_{55}k_z^2 + 2d_{16}k_x k_y\right)\left[\begin{array}{l} k_x^2\left(d_{55} + d_{66}\right) + k_y^2\left(d_{22} + d_{44}\right) + \\ + k_z^2\left(d_{33} + d_{44}\right) + 2k_x k_y\left(d_{26} + d_{45}\right) \end{array}\right] + \\ + k_x^4 d_{55}d_{66} + k_y^4 d_{22}d_{44} + k_z^4 d_{33}d_{44} + k_x^2 k_y^2\left(d_{66}d_{44} + d_{22}d_{55} + 4d_{26}d_{45}\right) + \\ + k_x^2 k_z^2\left[d_{33}d_{66} + d_{44}d_{55} - \left(d_{63} + d_{45}\right)^2\right] + k_y^2 k_z^2\left[d_{22}d_{33} + d_{44}^2 - \left(d_{23} + d_{44}\right)^2\right] + \\ + 2k_x^3 k_y\left(d_{45}d_{66} + d_{26}d_{55}\right) + 2k_y^3 k_x\left(d_{45}d_{22} + d_{26}d_{44}\right) + \\ + 2k_z^2 k_x k_y\left[d_{55}d_{44} + d_{26}d_{33} - \left(d_{63} + d_{45}\right)\left(d_{23} + d_{44}\right)\right] - \\ - \left[d_{16}k_x^2 + d_{26}k_y^2 + d_{54}k_z^2 + \left(d_{12} + d_{66}\right)k_x k_y\right]^2 - \left[\left(d_{55} + d_{13}\right)k_x k_z + \left(d_{45} + d_{36}\right)k_y k_z\right]^2 \end{cases} \tag{1.24b}$$

$$
\begin{aligned}
H(k_x,k_y,k_z,\theta=90°,\Psi) = {} & k_x^6 a_1^6 + k_y^6 a_2^6 + k_z^6 a_3^6 + k_x^5 k_y a_{1,2}^{5,1} + k_y^5 k_x a_{2,1}^{5,1} + k_x^4 k_y^2 a_{1,2}^{4,2} + \\
& + k_y^4 k_x^2 a_{2,1}^{4,2} + k_z^4 k_x^2 a_{3,1}^{4,2} + k_z^4 k_y^2 a_{3,2}^{4,2} + k_x^4 k_z^2 a_{1,3}^{4,2} + k_y^4 k_z^2 a_{2,3}^{4,2} + \\
& + k_x^3 k_z^2 k_y a_{1,3,2}^{3,2,1} + k_y^3 k_z^2 k_x a_{2,3,1}^{3,2,1} + k_x^3 k_y^2 k_z a_{1,2,3}^{3,2,1} + k_y^3 k_x^2 k_z a_{2,1,3}^{3,2,1} + \\
& + k_z^3 k_x^2 k_y a_{3,1,2}^{3,2,1} + k_z^3 k_y^2 k_x a_{3,2,1}^{3,2,1} + k_z^4 k_x k_y a_{3,1,2}^{4,1,1} + k_x^2 k_y^2 k_z^2 a_{1,2,3}^{2,2,2} + \\
& + k_x^4 k_y k_z a_{1,2,3}^{4,1,1} + k_y^4 k_x k_z a_{2,1,3}^{4,1,1} + k_x^3 k_y^3 a_{1,2}^{3,3} + k_y^3 k_z^3 a_{2,3}^{3,3}
\end{aligned}
\tag{1.24c}
$$

The coefficients $a_{i,j,k}^{m,n,l}$ are shown in appendix A_3.

For 2D case, i.e. when $k_y = 0$ and for the acoustic model of propagation, where $C_{44} = C_{66} = 0$, we obtain the following relations:

$$
\begin{aligned}
& H(k_x,k_y=0,k_z,\theta=90°,\Psi) = k_x^4 k_z^2 \left[d_{11}(d_{33}d_{66} - d_{63}^2) - d_{16}^2 d_{33} + d_{13} d_{16} d_{66} - d_{13}^2 d_{66} \right] \\
& B = k_x^2 (d_{11} + d_{66}) + k_z^2 d_{33} \\
& C = k_x^2 k_z^2 (d_{11}d_{33} + d_{66}d_{33} - d_{63}^2 - d_{13}^2) + k_x^4 (d_{11}d_{66} - d_{16}^2)
\end{aligned}
\tag{1.25}
$$

Let's present relation (1.25) in a convenient to analyze form in dependence with Thomsen's parameters ε and δ:

$$
\begin{aligned}
& H = k_x^4 k_z^2 V_P^6 \sin^2(2\Psi) \cdot h \\
& B = k_x^2 V_P^2 \cdot b_1 + k_z^2 V_P^2 \cdot b_2 \\
& C = k_x^2 k_z^2 V_P^4 \cdot c_1 + k_x^4 V_P^4 \sin^2(2\Psi) \cdot c_2
\end{aligned}
\tag{1.26}
$$

where:

$$
\left.
\begin{aligned}
h &= \frac{1}{4}\left\{
\begin{aligned}
&\left[(1+2\varepsilon)\cos^4\Psi+\sin^4\Psi+\frac{1}{2}(1+\delta)\sin^2(2\Psi)\right]\left[2(1+2\varepsilon)(\varepsilon-\delta)-(2\varepsilon-\delta)^2\right]- \\
&-(1+2\varepsilon)[(2\varepsilon-\delta)\cos^2\Psi+\delta\sin^2\Psi]^2+ \\
&+\sin(2\Psi)[(1+2\varepsilon)\cos^2\Psi+(1+\delta)\sin^2\Psi](\varepsilon-\delta)(2\varepsilon-\delta)- \\
&-2[(1+2\varepsilon)\cos^2\Psi+(1+\delta)\sin^2\Psi]^2(\varepsilon-\delta)
\end{aligned}
\right\} \\
b_1 &= (1+2\varepsilon)\cos^4\Psi+\sin^4\Psi+\frac{1}{2}(1+\delta)\sin^2(2\Psi)+\frac{1}{2}\sin^2(2\Psi)(\varepsilon-\delta) \\
b_2 &= 1+2\varepsilon \\
c_1 &= \sin^4\Psi\cdot 2(\varepsilon-\delta)+\frac{1}{2}\sin^2(2\Psi)\left[(\varepsilon-\delta)(1+2\varepsilon)-\frac{1}{2}(2\varepsilon-\delta)^2\right] \\
c_2 &= \frac{1}{2}\left\{
\begin{aligned}
&\left[(1+2\varepsilon)\cos^4\Psi+\sin^4\Psi+\frac{1}{2}(1+\delta)\sin^2(2\Psi)\right](\varepsilon-\delta)- \\
&-\frac{1}{2}\left[(2\varepsilon-\delta)\cos^2\Psi+\delta\sin^2\Psi\right]^2
\end{aligned}
\right\}
\end{aligned}
\right\} \qquad (1.27)
$$

The analysis of coefficients h, b_1, b_2, c_1, c_2 for Thomsen's parameter's in range of ε (+0.4; –0.3) and δ in interval (+0.3; –0.2) shows the dominating meaning (the Table 1) of b_1 and b_2 coefficients and low values of the h parameter for ε and δ in interval (0.3; –0.2) and that in practice encases the full range of Thomsen's parameters variability in sedimentary rocks which are mean objects of oil recovery.

Taking in equations (1.25–1.26) that $h \approx 0$ we obtain a biquadratic equation

$$
\omega_a^4-\omega_a^2\left[k_x^2\left(d_{11}+d_{66}\right)+k_z^2 d_{33}\right]+k_x^2k_z^2\left[d_{11}d_{33}+d_{66}d_{33}-d_{63}^2-d_{13}^2\right]+k_x^4\left[d_{11}d_{66}-d_{16}^2\right]=0 \qquad (1.28)
$$

If in equation (1.28) we eliminate the d_{66}, d_{63}, d_{16} components, we can obtain the following relation:

$$
\omega_a^4-\omega_a^2\left(d_{11}k_x^2+d_{33}k_z^2\right)+k_x^2k_z^2\left[d_{11}d_{33}-d_{13}^2\right]=0 \qquad (1.29)
$$

Dispersion relations determined by the equation of third order (1.23) and the bi-quadratic equations (1.28) and (1.29) will be the object of testing so as to determine the range of their application.

Tab. 1. The comparison of coefficients in relation 1.27 in dependence of Thomsen's parameters

ε; δ	h	b_1	b_2	c_1	c_2
0.4; 0.3	–0.135	1.40	1.80	0.077	0.027
0.4; 0.2	–0.135	1.40	1.80	0.19	0.09
0.3; 0.2	–0.07	1.30	1.60	0.09	0.04
0.3; 0.1	–0.067	1.30	1.60	0.97	0.097
0.2; 0.1	–0.028	1.20	1.40	0.097	0.047
0.5; 0.1	–0.015	1.15	1.30	0.047	0.022
0.2; –0.15	–0.007	1.20	1.40	0.268	0.169
0.2; –0.2	0.0	1.20	1.40	0.390	0.190
–0.2; 0.1	0.0	0.8	0.6	–0.302	–0.29
–0.3; 0.2	0.023	0.75	0.4	–0.51	–0.26
0.3; –0.2	–0.024	1.09	1.6	0.49	0.24

Chapter 2. Pseudo-acoustic wave equations

In this chapter pseudo-acoustic equations will be derived, i.e. generalized wave equations for transverse isotropy models (TI) in wavenumbers and eigenvalue frequency domain.

The solution of the biquadratic dispersion relation (1.28) has the form

$$\omega_{HTI} = V_p \cdot k_{HTI} = \frac{1}{\sqrt{2}} \left\{ F_{HTI(\Psi)} + \left[F^2_{HTI(\Psi)} - 4G_{HTI(\Psi)} \right]^{1/2} \right\}^{1/2} \tag{2.1}$$

where

$$F_{HTI(\Psi)} = V_P^2 \left\{ \begin{matrix} [(1+2\varepsilon)\cos^4\Psi + \sin^4\Psi + \tfrac{1}{2}(1+\delta)\sin^2(2\Psi) + \\ + \tfrac{1}{2}\sin^2(2\Psi)(\varepsilon-\delta)]k_x^2 + (1+2\varepsilon)k_z^2 \end{matrix} \right\} \tag{2.1a}$$

$$\begin{aligned} G_{HTI(\Psi)} = {} & V_P^4 k_x^2 k_z^2 \left\{ \begin{matrix} \sin^4\Psi + \tfrac{1}{2}\sin^2(2\Psi)[(\varepsilon-\delta)(1+2\varepsilon) - \\ - \varepsilon\left(1+2\delta\right)^{\frac{1}{F}} - \tfrac{1}{2}(2\varepsilon-\delta)^2] \end{matrix} \right\} + \\ & + \tfrac{1}{4}k_x^4 V_P^4 \left\{ \begin{matrix} \sin^2(2\Psi)[(1+2\varepsilon)\cos^4\Psi + \sin^4\Psi + \tfrac{1}{2}(1+\delta)\sin^2(2\Psi)](\varepsilon-\delta) - \\ - \tfrac{1}{2}\sin^2(2\Psi)[(2\varepsilon-\delta)\cos^2\Psi + \delta\sin^2\Psi]^2 \end{matrix} \right\} \end{aligned} \tag{2.1b}$$

In TTI (Titled Transverse Isotropy) medium temporal frequency – the eigenvalue of dispersion relation is given as follows [32]:

$$\omega_{TTI} = V_p \cdot k_{TTI} = \frac{1}{\sqrt{2}} \left\{ F_{TTI}(\pm) + \left[F_{TTI}^2(\pm) - 4G_{TTI}(\pm) \right]^{1/2} \right\}^{1/2} \tag{2.2}$$

where

$$F_{TTI}(\pm) = (d_{11} + d_{55})k_x^2 + (\pm)2k_x \cdot k_z(d_{15} + d_{35}) + (d_{33} + d_{55})k_z^2 \tag{2.2a}$$

$$\begin{aligned} G_{TTI}(\pm) = {} & (d_{11}d_{55} + d_{15}^2)k_x^4 + (\pm)2k_x^3k_z(d_{35}d_{11} - d_{15}d_{31}) + \\ & + [d_{11}d_{33} + 2(d_{15}d_{35} - d_{13}d_{55}) - d_{13}^2]k_x^2k_z^2 + \\ & + (\pm)2k_xk_z^3(d_{15}d_{33} - d_{35}d_{13}) + (d_{55}d_{33} - d_{53}^2)k_z^4 \end{aligned} \tag{2.2b}$$

In relation (2.2a–2.2b) the sign (+) refers to positive direction of measurements in x-axis for "down dip" while sign (–) refers to "up dip" direction, d_{ij} means the components of stiffness tensor $D^{\theta,\Psi=90^\circ}$ for dip angle θ and the azimuthal angle $\Psi = 90°$.

In a special case for VTI model ($\theta = 0°$) and HTI model ($\theta = 90°$, $\Psi = 90°$) we have (for $V_S = 0$):

$$F_{VTI} = V_P^2 \left(qk_x^2 + k_z^2 \right) \tag{2.3a}$$

$$G_{VTI} = V_P^4 \eta_a k_x^2 k_z^2 \tag{2.3b}$$

$$F_{TTI(\theta=90^\circ)} = V_P(k_x^2 + qk_z^2) \tag{2.3c}$$

$$G_{TTI(\theta=90^\circ)} = V_P^4 \eta_a k_x^2 k_z^2 \tag{2.3d}$$

where: $\eta_a = 2(\varepsilon - \delta)$ and ε, δ are Thomsen's parameters, while V_P is compressional velocity in a direction perpendicular to the isotropy plane.

In general, the equation (2.2) was obtained in a 2D case of wave propagation as a result of the matrix equation solution:

$$\begin{bmatrix} a_{11} & a_{12} \\ a_{21} & a_{22} \end{bmatrix} \begin{bmatrix} U_x \\ U_z \end{bmatrix} = 0 \tag{2.4}$$

where the elements of symmetrical matrix $[a_{ik}]$ are a function of the wavenumbers k_x, k_z, Thomsen's parameters and the angles: dip θ and azimuthal Ψ, while U_x and U_z are components of the displacements vector.

The equation (2.4) means, that the U_y component occurs in neither the first nor second line of matrix constructed as a product of the stiffness tensor and strain tensor according to Hooke's law and the solution comes down to the determination of the quadratic matrix 2×2 determinant. The precondition for determination of the two–dimensional wavefield $\frac{\partial U_y}{\partial y} = 0$ does not eliminate component U_y. If the component U_y occurs in each line of the matrix then it produces the necessity of third order determinant computation:

$$\begin{bmatrix} a_{11} & a_{12} & a_{13} \\ a_{21} & a_{22} & a_{23} \\ a_{31} & a_{32} & a_{33} \end{bmatrix} \begin{bmatrix} U_x \\ U_y \\ U_z \end{bmatrix} = 0 \tag{2.5}$$

In this case the eigenvalue of the matrix equation (2.5) i.e. temporal frequency ω_a is expressed by a polynomial equation of sixth order. This stems directly from the presence of temporal frequency raised to second power ω_a^2 in a_{11}, a_{22}, a_{33} elements of the matrix in relation (2.5). The equation can be written in a form called the Cardano equation:

$$x^3 + xf_1 + f_2 = 0 \tag{2.6}$$

which has the following solution:

$$x = \sqrt[3]{-\frac{f_2}{2} - \sqrt{\frac{f_2^2}{4} + \frac{f_1^3}{27}}} + \sqrt[3]{-\frac{f_2}{2} + \sqrt{\frac{f_2^2}{4} + \frac{f_1^2}{27}}} \tag{2.7}$$

where

$$f_1 = C - \tfrac{1}{3}B^2;\ f_2 = \tfrac{1}{3}BC - \tfrac{2}{27}B^3 - H(k_x, k_y, k_z)$$

and sought temporal frequency ω_a is given by relation

$$\omega_a^2 = x + \tfrac{1}{3}B \tag{2.8}$$

where B, C, H are determined by relations (1.24).

Bearing in mind that each component d_{ij} of stiffness tensor consists of velocity V_p^2 in a perpendicular direction to the isotropy plane and taking into consideration the structures of relations: (1.24), (2.1–2.2), and (2.6–2.7) one can note that relation

$$\frac{\omega_a^2}{V_{\mathrm{p}}^2} = k_a^2\left(k_x, k_y, k_z, \theta, \Psi, \varepsilon, \delta\right) \tag{2.9}$$

stands for two and three (equation 2.5) dimensions. In equation (2.9) k_a^2 is the function of wave vector's components, angles: θ and Ψ, Thomsen's parameters (ε and δ).

In isotropic medium function (2.9) is a wave vector i.e.:

$$k_a{}^2 = k^2 = k_x^2 + k_y^2 + k_z^2 \tag{2.10}$$

By multiplying two sides of the equation (2.9) by scalar wavefield $P(k_x, k_y, k_z, \omega_a)$ and performing Fourier transform $F(\omega_a \rightarrow t)$ we obtain:

$$\frac{1}{V_p^2}\frac{\partial^2 P\left(k_x,k_y,k_z,t\right)}{\partial t^2} = -k_a^2 P\left(k_x,k_y,k_z,t\right) \tag{2.11}$$

i.e. second order equation in wavenumber domain called pseudo-acoustic, that describes the motion of compressional waves in transverse isotropy (TI) medium when velocity of shear waves $V_{SV} = 0$.

From relation (2.11) we obtain:

$$\frac{\partial P\left(k_x,k_y,k_z,t\right)}{\partial t} = \pm iV_p k_a P\left(k_x,k_y,k_z,t\right) \tag{2.12}$$

where $i = \sqrt{-1}$, i.e. one-side wave equation; sign (±), before temporal frequency ω_a determines direction of waves propagation. In x, y, z Cartesian coordinates system with positive z-axis directed "down", sign (+), indicates wave propagating to the level of waves recording, i.e. $z = 0$.

The solution of equation (2.11) may be written as follows:

$$P(x,y,z,t) = \sum_{kx}\sum_{ky}\sum_{kz} P\left(k_x,k_y,k_z,t=0\right)\exp\left[i(k_x x + k_y y + k_z z \pm \omega_a t)\right] \tag{2.13}$$

In heterogeneous anisotropic medium, equation (2.12) takes a pseudospectral form and then we have:

$$\frac{\partial P(x,y,z,t)}{\partial t} = \pm iV_p\left(x,y,z\right) F^{-1}\left\{ k_a F\left[P(x,y,z,t)\right]\right\} \tag{2.14}$$

where $F(x\rightarrow k_x, y\rightarrow k_y, z\rightarrow k_z)$ and $F^{-1}(k_x\rightarrow x, k_y\rightarrow y, k_z\rightarrow z)$ are Fourier transform operators from (x, y, z) domain to (k_x, k_y, k_z) and vice versa.

Initial condition for one-way equation (2.14) is the relation (2.13) for $t = 0$, i.e. $P(x, y, z, t = 0)$. Such proceeding eliminates necessity of the source function use, i.e. eliminates the inhomogeneous equation.

Numerical solution of equation (2.14) can be obtained by the application of truncated Taylor series (third – order scheme):

$$P(x,y,z,t)=\sum_{l=0}^{3}\frac{\partial^l P(x,y,z,0)}{\partial t^l}\frac{\Delta t^l}{l!} \tag{2.15}$$

J. Gazdag [20] proved stability of the scheme (2.15) in isotropic case.

The second and third derivatives are determined by:

$$\frac{\partial^2 P(x,y,z,t)}{\partial t^2}=-\mathrm{V}_\mathrm{p}^2(x,y,z)\,F^{-1}\left\{k_a^2 F\left[P(x,y,z,t)\right]\right\} \tag{2.16}$$

$$\frac{\partial^3 P(x,y,z,t)}{\partial t^3}=-i\mathrm{V}_\mathrm{p}^3(x,y,z)\,F^{-1}\left\{k_a^3 F\left[P(x,y,z,t)\right]\right\} \tag{2.17}$$

The relations (2.13) and (2.14–2.17) define the process of waves propagation in a determined direction for the anisotropic medium.

The stability

Stability evaluation of modeling will be done with reference to relation (1.29) taking into consideration the convergence of modeling tests from relation (1.23), (1.28) and (1.29).

Taking equation (1.29) in the form

$$\omega_a^4 - \omega_a^2 F + G = 0 \tag{2.18}$$

we obtain relation

$$\omega_a = \frac{1}{\sqrt{2}}\sqrt{F + \sqrt{F^2 - 4G}} \tag{2.19}$$

where

$$\begin{aligned} F &= d_{11}k_x^2 + d_{33}k_z^2 \\ G &= \left(d_{11}d_{33} - d_{13}^2\right)k_x^2 k_z^2 \end{aligned} \tag{2.20}$$

In order to obtain a real solution of the equation (2.18) the following conditions should be fulfilled:

$$F > 0 \tag{2.21}$$

and

$$F^2 - 4G > 0 \tag{2.22}$$

We consider only the case $\eta_a > 0$, because as it results from work of Grechka et al. [21], the case for $\eta_a < 0$ is treated as unphysical.

In general, the following conditions should be fulfilled:

$$\begin{aligned} q &> 0 \\ 1 + 2\delta &> 0 \end{aligned} \tag{2.23a}$$

and

$$\left\{q\left[q\cos^4\Psi+\sin^4\Psi+2\left(1+2\delta\right)^{1/2}\sin^2\Psi\cos^2\Psi\right]-2\eta_a\sin^4\Psi\right\}>0 \tag{2.23b}$$

It should be noted, that the case for $\Psi = 90°$ accords with the relation presented in the work [32]. The stability of the numerical solution method employing the time differencing scheme, is satisfied as for the "isotropy" case [20] i.e.:

$$\omega_a\Delta t \le 2 \tag{2.24}$$

where Δt is time increment. In practice step $\Delta t = 0.5$ ms seems to be a reasonable compromise between the stability and the accuracy of the method.

Signal testing

We performed a few numerical experiments to check correctness of the modeling process in isotropy and anisotropy media.

We used one-way equation (2.14) and Taylor's series (2.15) in anisotropic media HTI(Ψ) with parameters: $\varepsilon = 0.3$; $\delta = 0.1$ and velocity $V_P = 2000$ m/s in a perpendicular direction to the symmetry plane (plane of isotropy). An excited signal was placed at point ($x = 0$ m; $z = 0$ m).

We used 3 versions of signal: Ricker's 60 Hz signal and two signals presented in Fig. 2.1, i.e. the zero-phase signal and a signal of the "spike" type. In Fig. 2.2 is shown the snapshot of Ricker's signal at the moment $t = 0.2$ s in isotropy media i.e. for the azimuthal angle $\Psi = 0°$.

We can note a noise that follows the spherical wavefront and the phase of the signal. The snapshot in Fig. 2.3 presents the propagation of the zero–phase signal in isotropy media ($\Psi = 0°$). In comparison with the propagation of Ricker's signal we can observe

greater resolution, but undoubtedly the best image in sense of resolution we obtain using "spike" signal (Fig. 2.4).

Here, the one-way wavefields propagation was computed with relation (1.29) i.e. bi-quadratic equation was used. The steps of computation are: $\Delta t = \Delta t = 4m$, $\Delta t = 0{,}5ms$. The change of the azimuthal angle to 30° (parameters: $\varepsilon = 0.3$; $\delta = 0.1$) leads to an ellipsoidal shape of the wavefront (Fig. 2.5).

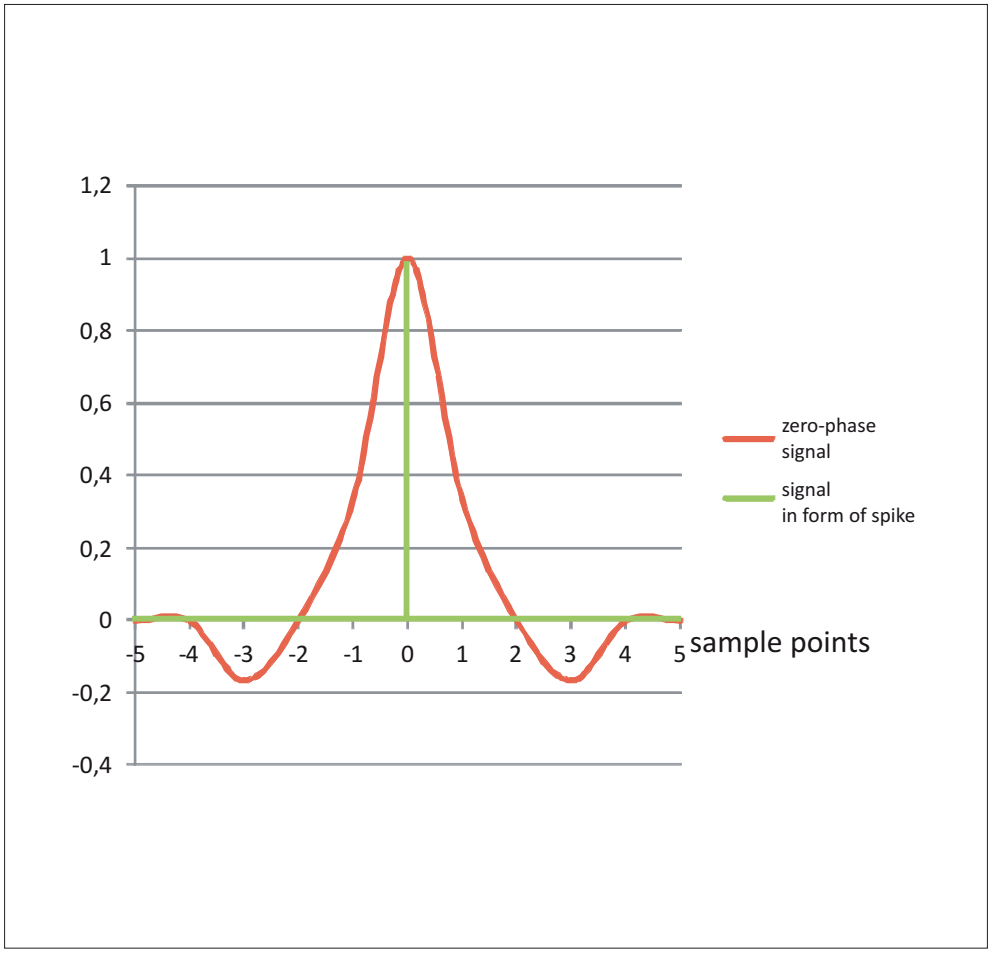

Fig. 2.1. The forms of signal used in testing experiment

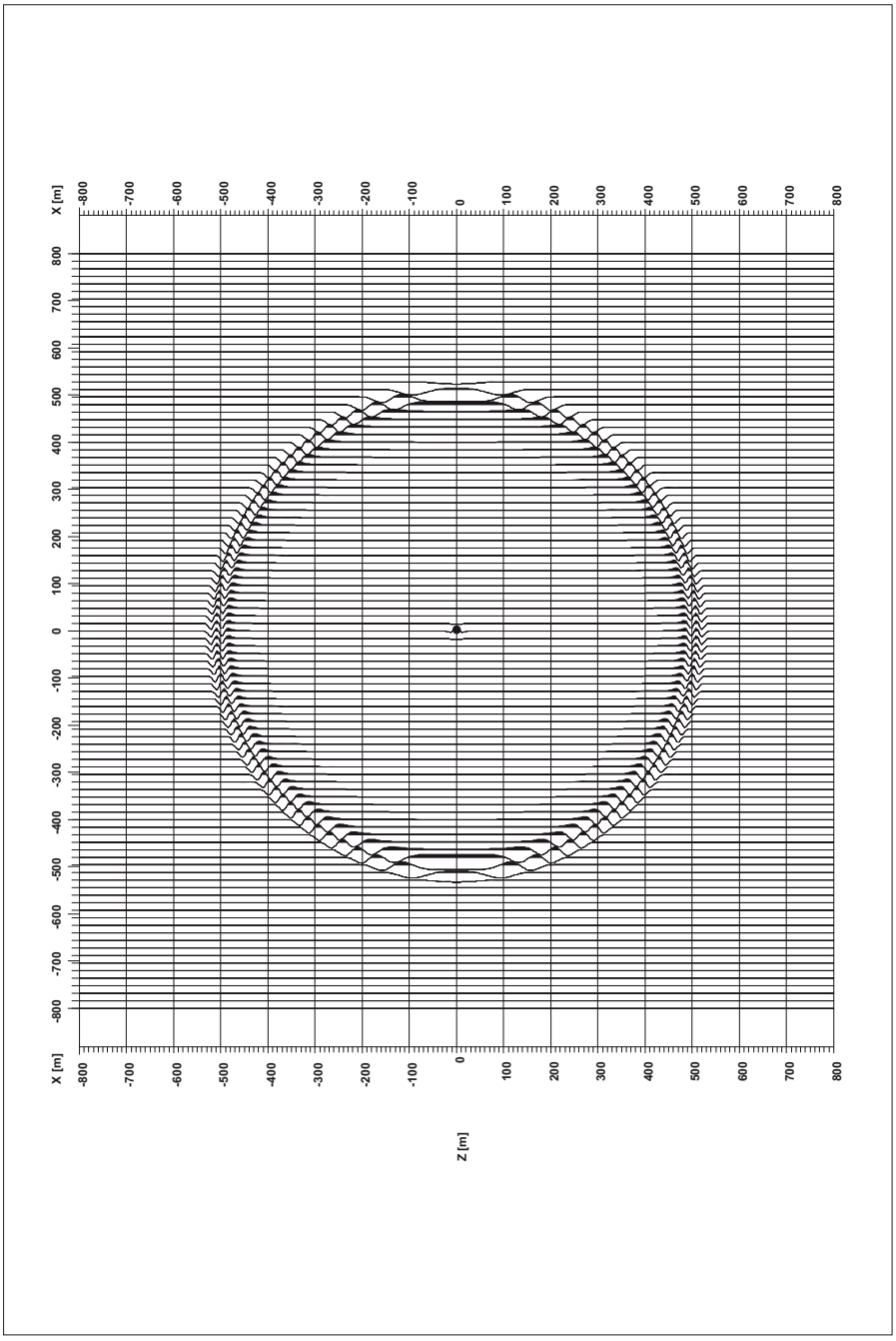

Fig. 2.2. Snapshot of signal Ricker's 60 Hz propagation from relation (1.29) in moment time $t = 0.2$ s; anisotropy parameter's: $\varepsilon = 0.3$; $\delta = 0.1$; azimuthal angle $\Psi=0°$; steps of computations: $\Delta x = \Delta z = 4$ m, $\Delta t = 0.5$ ms

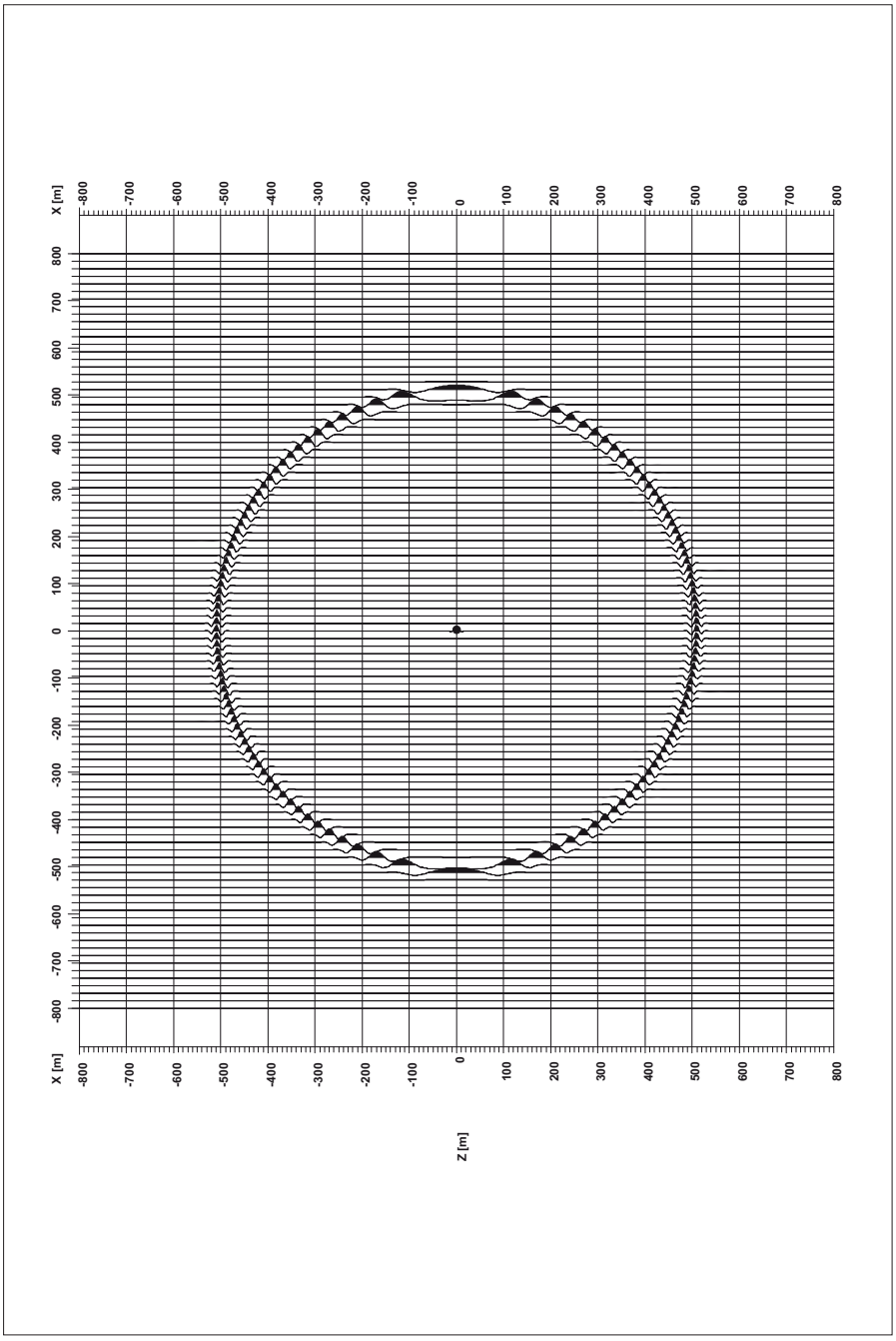

Fig. 2.3. Snapshot of zero-phase signal propagation from relation (1.29) in moment time $t = 0.2$ s; anisotropy parameter's: $\varepsilon = 0.3$; $\delta = 0.1$; azimuthal angle $\Psi = 0°$; steps of computations: $\Delta x = \Delta z = 4$ m, $\Delta t = 0.5$ ms

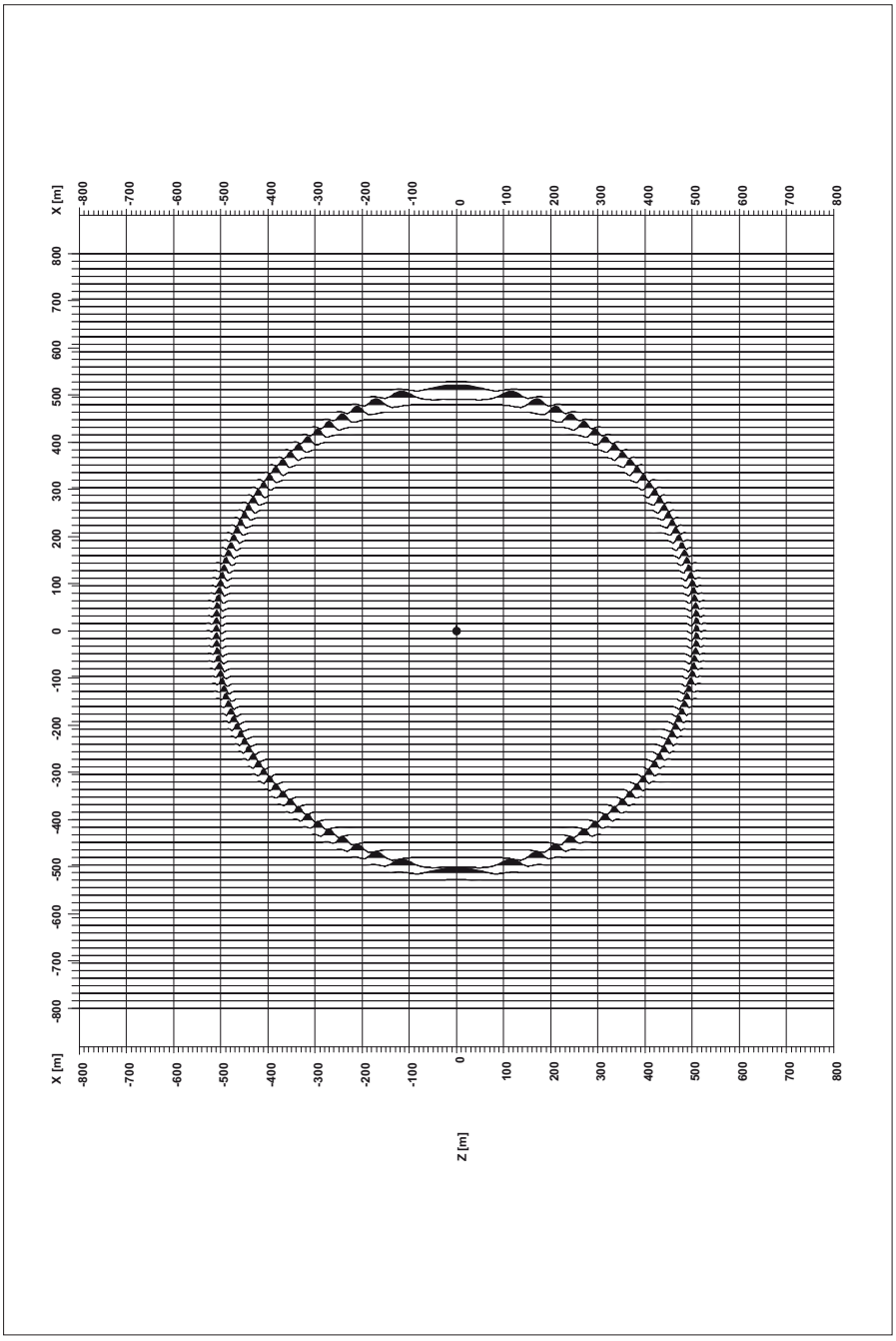

Fig. 2.4. Snapshot of spike signal propagation from relation (1.29) in moment time $t = 0.2$ s; anisotropy parameter's: $\varepsilon = 0.3$; $\delta = 0.1$; azimuthal angle $\Psi = 0°$; steps of computations: $\Delta x = \Delta z = 4$ m, $\Delta t = 0.5$ ms

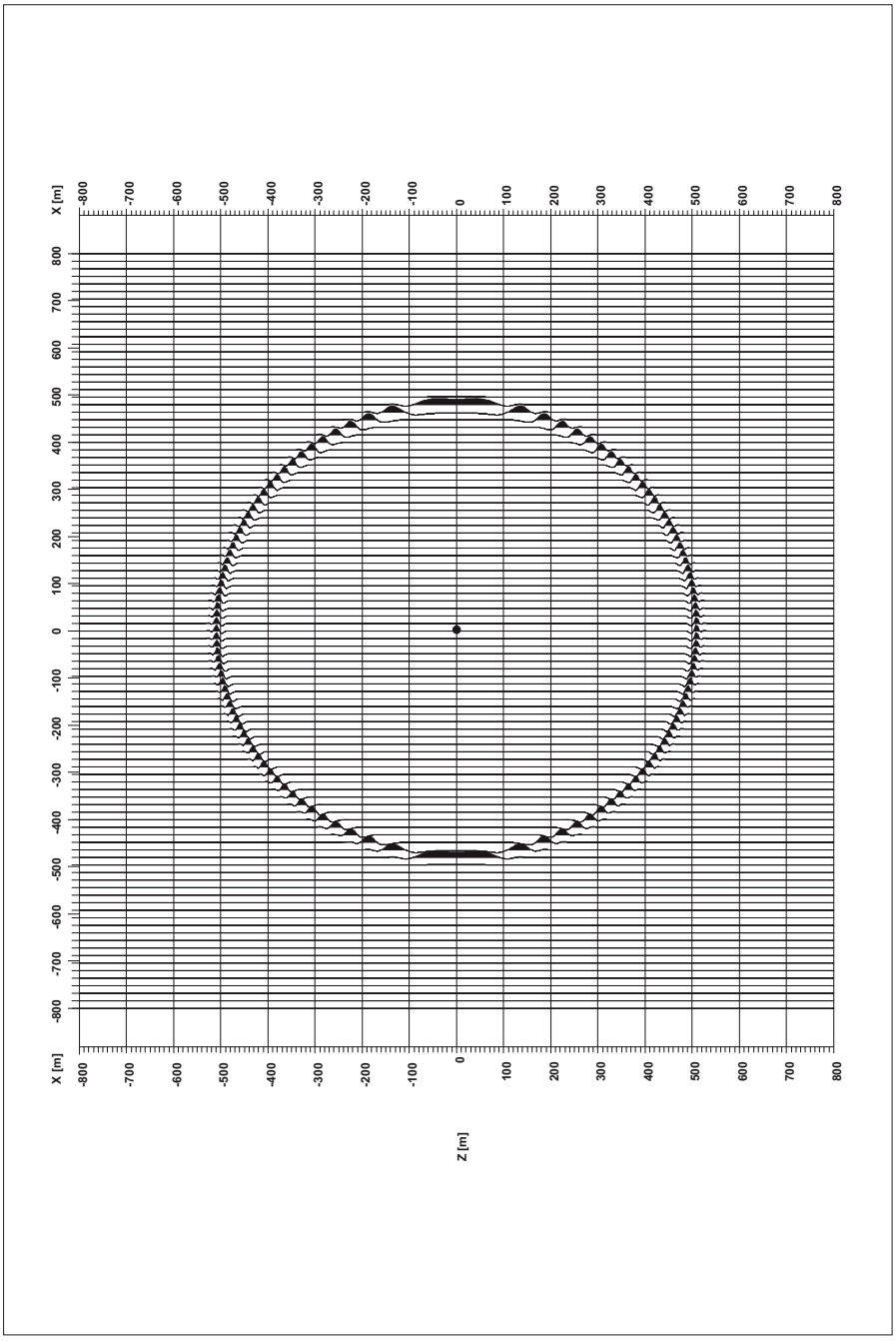

Fig. 2.5. Snapshot of spike signal propagation from relation (1.29) in moment time $t = 0.2$ s; anisotropy parameter's: $\varepsilon = 0.3$; $\delta = 0.2$; azimuthal angle $\Psi = 30°$; steps of computations: $\Delta x = \Delta z = 4$ m, $\Delta t = 0.5$ ms

Results of azimuthal modeling

We have done a wide range of modeling in order to check the correctness and usefulness of the two temporal frequency ω_a approximations as a function of parameters ε, δ (Thomsen's parameters) and azimuthal angle Ψ.

The approximations defined by relations (1.29) and (1.28) were compared with the exact solution of the dispersion equation expressed in the form of algebraic of the sixth degree (1.23) or in a version of third degree Cardano equation.

According to modeling results of different signals (Fig. 2.1–2.5) we did a series of experiments using "spike" shape signal for good resolution of images. The main object of modeling was the experiment of signals propagation in anisotropic media for the ε and δ parameters range from the table (Tab. 1), which justifies application of the approximate solutions, namely biquadratic equations. Some results for media with parameters: $\varepsilon = 0.3$; $\delta = \pm 0.1$ and $\varepsilon = 0.35$; $\delta = \pm 0.1$ are presented here.

A series of experiments for various versions was done: the approximation according to the equation (1.29) [Fig. 2.6–Fig. 2.11], for $\varepsilon = 0.3$; $\delta = -0.1$ and [Fig. 2.24–2.29], for $\varepsilon = 0.35$; $\delta = -0.1$ and [Fig. 2.30–2.34], for $\varepsilon = 0.35$; $\delta = 0.1$; the approximation for equation (1.28) [Fig. 2.12–2.17], for $\varepsilon = 0.3$; $\delta = -0.1$ and [Fig. 2.35–2.40], for $\varepsilon = 0.35$; $\delta = 0.1$ and [Fig. 2.41–Fig. 2.46], for $\varepsilon = 0.35$; $\delta = -0.1$ and for the exact equation (1.23) [Fig. 2.18–2.23], for $\varepsilon = 0.3$; $\delta = -0.1$ and [Fig. 2.47–Fig. 2.52], for $\varepsilon = 0.35$; $\delta = 0.1$ and [Fig. 2.53–Fig. 2.58], for $\varepsilon = 0.35$; $\delta = -0.1$ of wave propagation in media with velocity $V_P = 2000$ m/s of compressional wave for azimuthal angle $\Psi = 90°$. Snapshots of waves propagation from source point ($x = 0$, $z = 0$) were shown at time moments $t = 0.2$ s and $t = 0.4$ s.

In general, the investigation of waves propagation has shown correctness and high accuracy with the exact solution (1.23). Visually the estimation of wave propagation showed the convergence of the longitudes of propagation ways, accordingly to assumptions, whereas numerically, the comparison indicates error about 0.2% for time $t = 0.4$ s for two models i.e. for $\varepsilon = 0.3$ and $\varepsilon = 0.35$.

The difference between propagation according to the exact solution (1.23) and approximations (1.28) and (1.29) is insignificant for $\varepsilon = 0.3$; $\delta = 0.1$ [Fig. 2.59–2.62] and increases to 1.6% [Fig. 2.63–2.65] for $\varepsilon = 0.35$; $\delta = \pm 0.1$. Taking into consideration that the measurements of ways propagation were made along x-axes, one may conclude that the parameter ε is crucial for such estimations. Achieved results are consistent with data coefficients from Tab. 1, where parameter $\varepsilon = 0.4$ limits the use of approximate solution. Snapshots of signal propagation in "spike" form are high quality images without random noise. Images, independently of approximation, are free from noise of "diamond shape"

type, characteristic of the wave propagation described by pseudo-acoustic equations in space coordinates [9].

Computations were made using one–way wave equation, therefore in these experiments two algorithmic versions – propagation "up" and "down" were joined together in final image. Discontinuities of signals visible in some images, are caused by presentation of every forth-trace in figures. This causes loss of the signal coincidence, in places of flatness of wavefront. These occurrences have accidental character.

Fig. 2.66 presents a composition of waves propagation images in media with parameters: $\varepsilon = 0.3$; $\delta = 0.1$ for angles $\Psi = 0°, 15°, 30°, 45°, 60°, 75°, 90°$ in xz-plane. Here we can observe a decrease of velocity with an increase of azimuthal angle on x-axis. For angle $\Psi = 90°$ velocity achieves minimal value, i.e. assuming $V_P = 2000$ m/s in a perpendicular direction to the symmetry plane. Velocity of propagation in direction along z-axis is $V = V_P(1 + 2\varepsilon)^{1/2} = 2529$ m/s (Fig. 2.67). From that we can easily note that velocity as a function of azimuthal angle has an ellipsoidal character and can be written as:

$$V(\Psi) = V_P(1 + 2\varepsilon \cos^2\Psi)^{1/2} \tag{2.25}$$

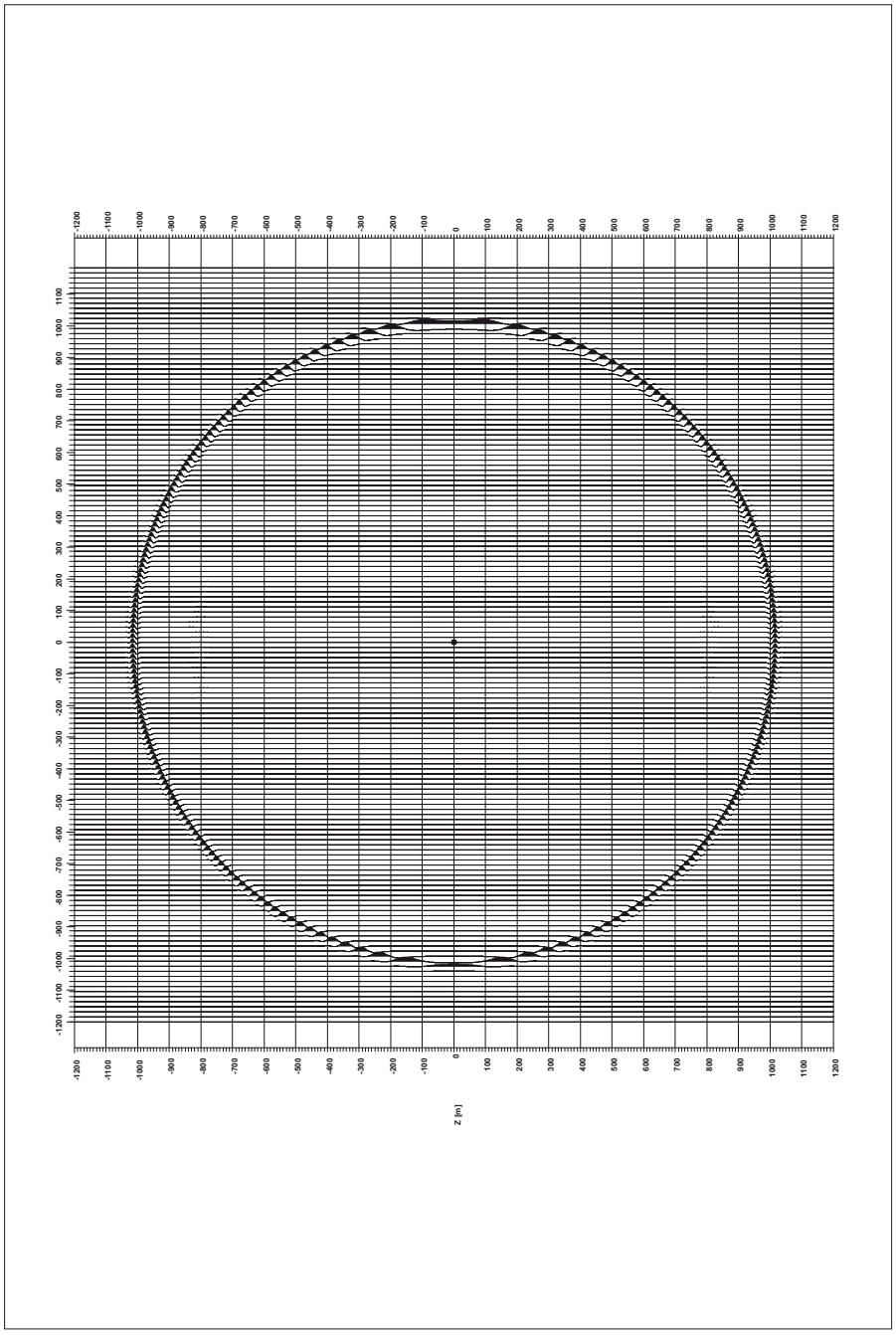

Fig. 2.6. Snapshot of spike wave propagation from algorithm (1.29) for parameters: $\varepsilon = 0.3$; $\delta = -0.1$ azimuthal angle $\Psi = 0°$; in moment time $t = 0.4$ s; steps of computation: $\Delta x = \Delta z = 4$ m, $\Delta t = 0.5$ ms

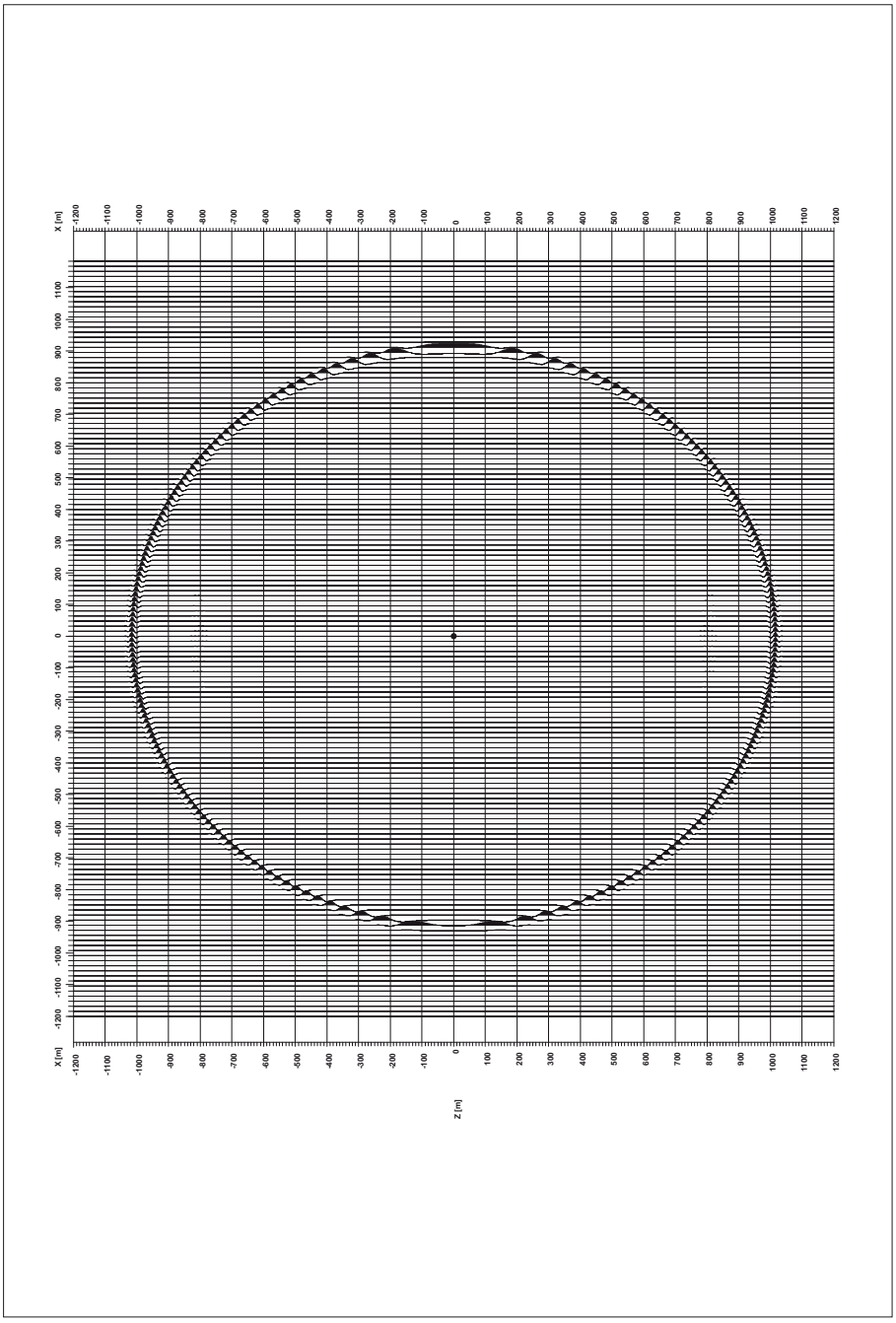

Fig. 2.7. Snapshot of spike wave propagation from algorithm (1.29) for parameters: $\varepsilon = 0.3$; $\delta = -0.1$ azimuthal angle $\Psi = 30°$; in moment time $t = 0.4$ s; steps of computation: $\Delta x = \Delta z = 4$ m, $\Delta t = 0.5$ ms

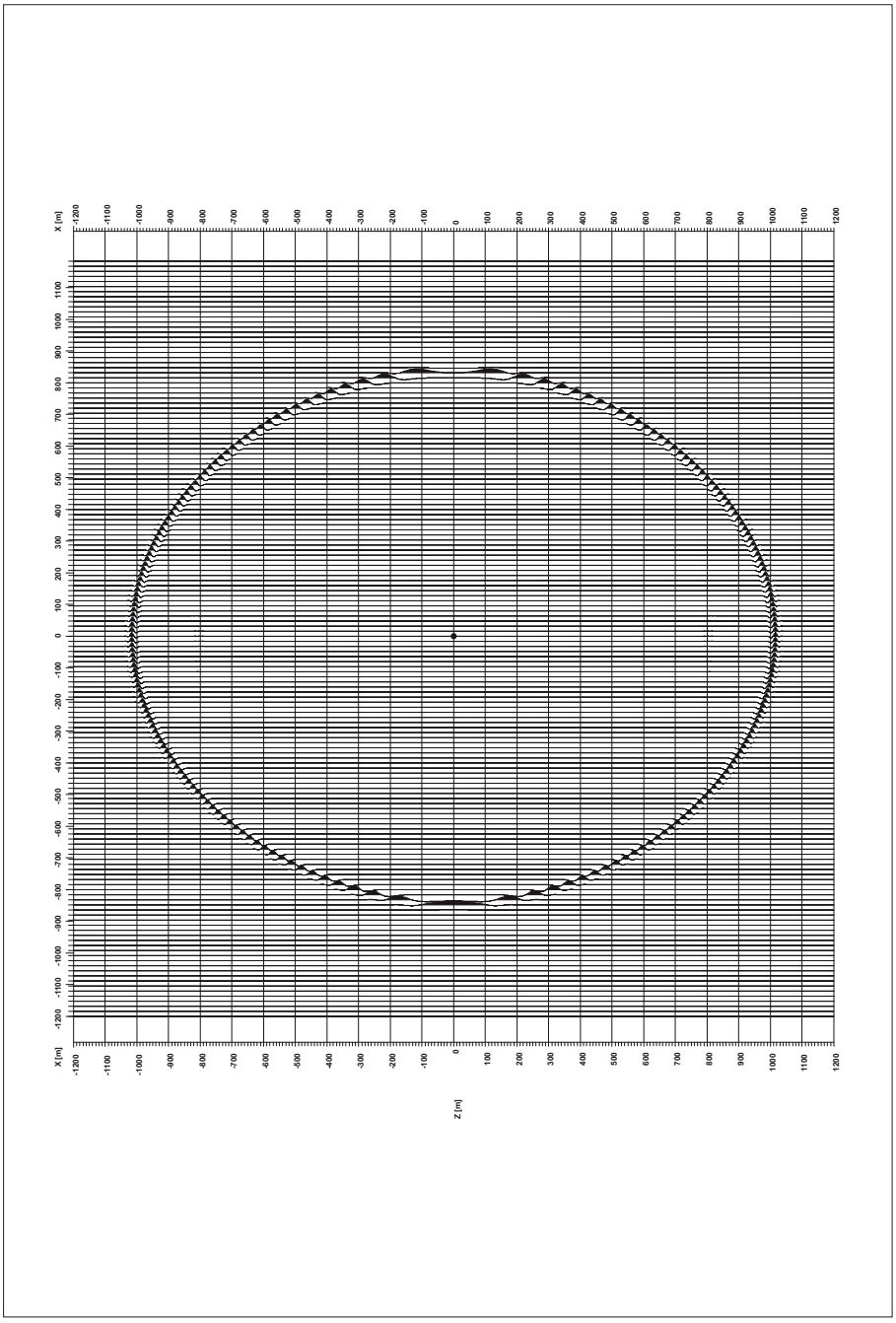

Fig. 2.8. Snapshot of spike wave propagation from algorithm (1.29) for parameters: $\varepsilon = 0.3$; $\delta = -0.1$ azimuthal angle $\Psi = 45°$; in moment time $t = 0.4$ s; steps of computation: $\Delta x = \Delta z = 4$ m, $\Delta t = 0.5$ ms

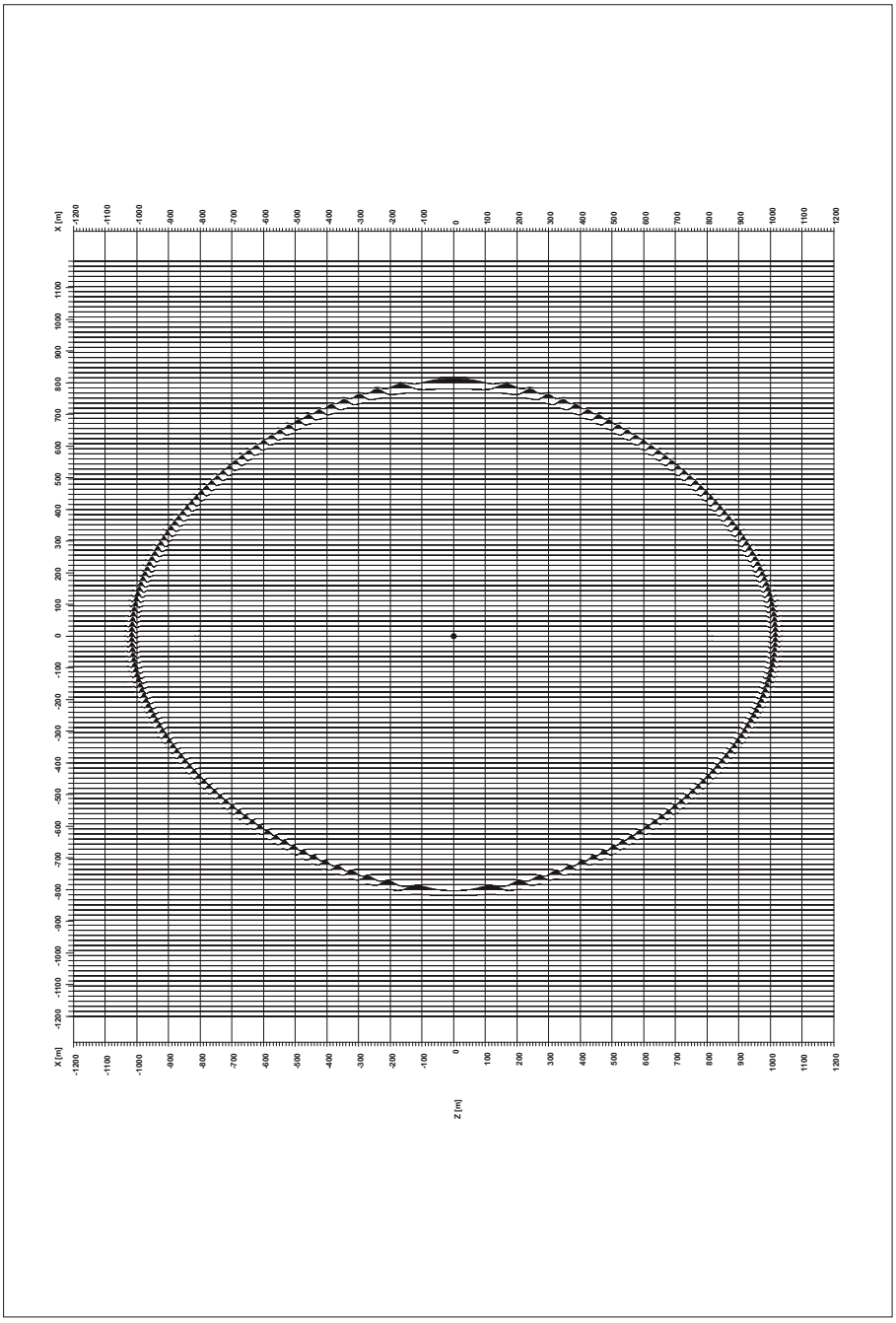

Fig. 2.9. Snapshot of spike wave propagation from algorithm (1.29) for parameters: $\varepsilon = 0.3$; $\delta = -0.1$ azimuthal angle $\Psi = 60°$; in moment time $t = 0.4$ s; steps of computation: $\Delta x = \Delta z = 4$ m, $\Delta t = 0.5$ ms

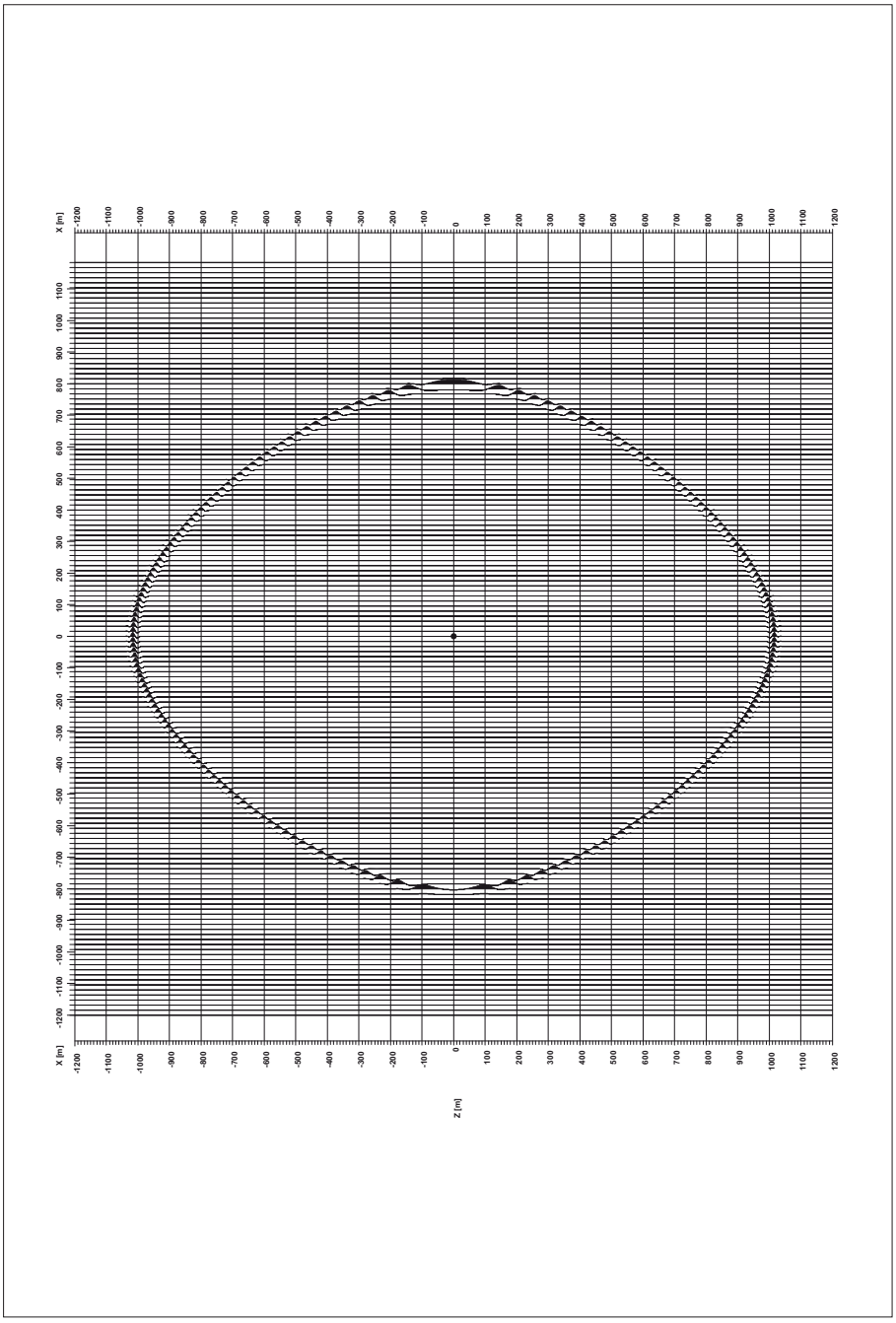

Fig. 2.10. Snapshot of spike wave propagation from algorithm (1.29) for parameters: $\varepsilon = 0.3$; $\delta = -0.1$ azimuthal angle $\Psi = 90°$; in moment time $t = 0.4$ s; steps of computation: $\Delta x = \Delta z = 4$ m, $\Delta t = 0.5$ ms

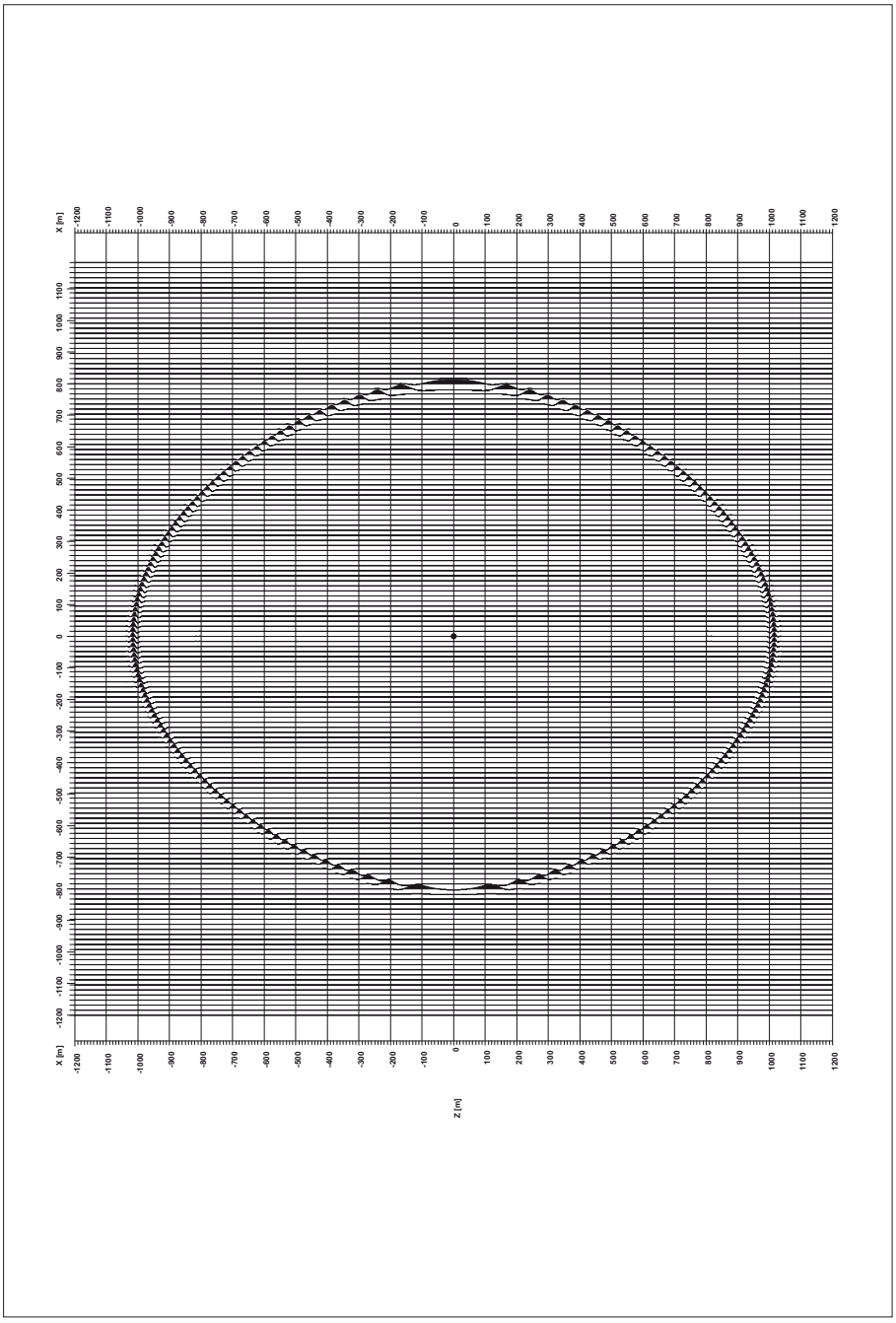

Fig. 2.11. Snapshot of spike wave propagation from algorithm (1.29) for parameters: $\varepsilon = 0.3$; $\delta = -0.1$ azimuthal angle $\Psi = 120°$; in moment time $t = 0.4$ s; steps of computation: $\Delta x = \Delta z = 4$ m, $\Delta t = 0.5$ ms

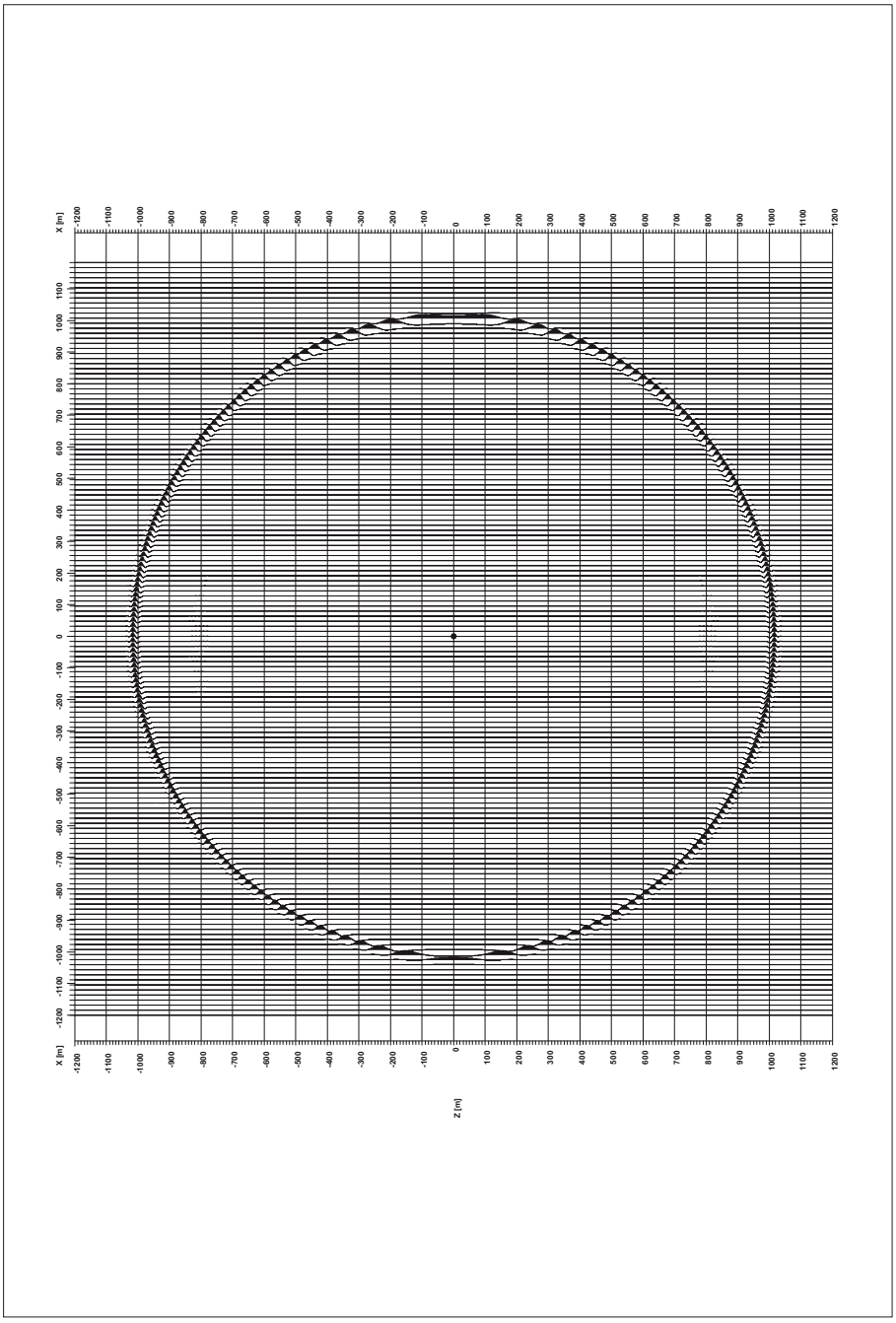

Fig. 2.12. Snapshot of spike wave propagation from algorithm (1.28) for parameters: $\varepsilon = 0.3$; $\delta = -0.1$ azimuthal angle $\Psi = 0°$; in moment time $t = 0.4$ s; steps of computation: $\Delta x = \Delta z = 4$ m, $\Delta t = 0.5$ ms

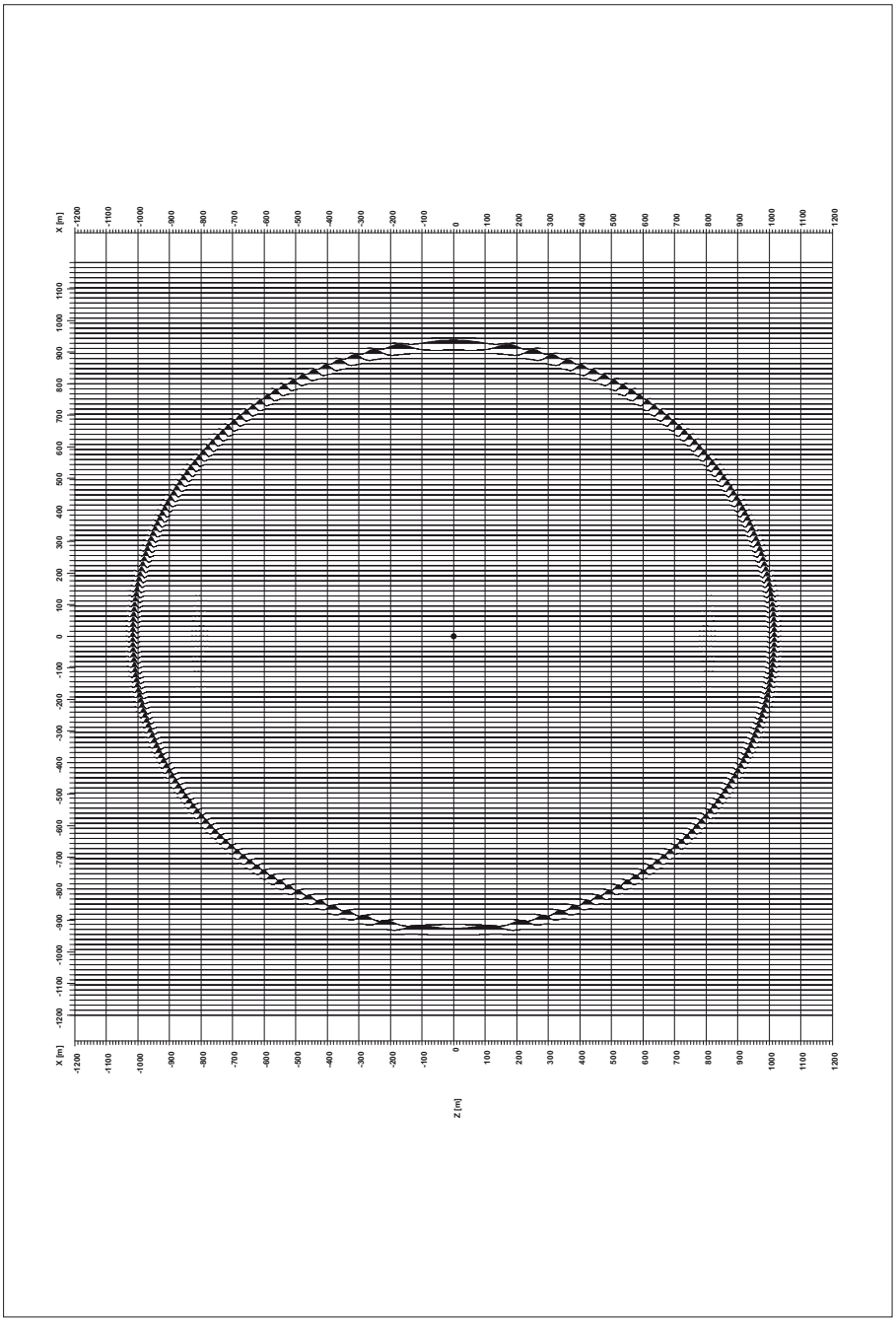

Fig. 2.13. Snapshot of spike wave propagation from algorithm (1.28) for parameters: $\varepsilon = 0.3$; $\delta = -0.1$ azimuthal angle $\Psi = 30°$; in moment time $t = 0.4$ s; steps of computation: $\Delta x = \Delta z = 4$ m, $\Delta t = 0.5$ ms

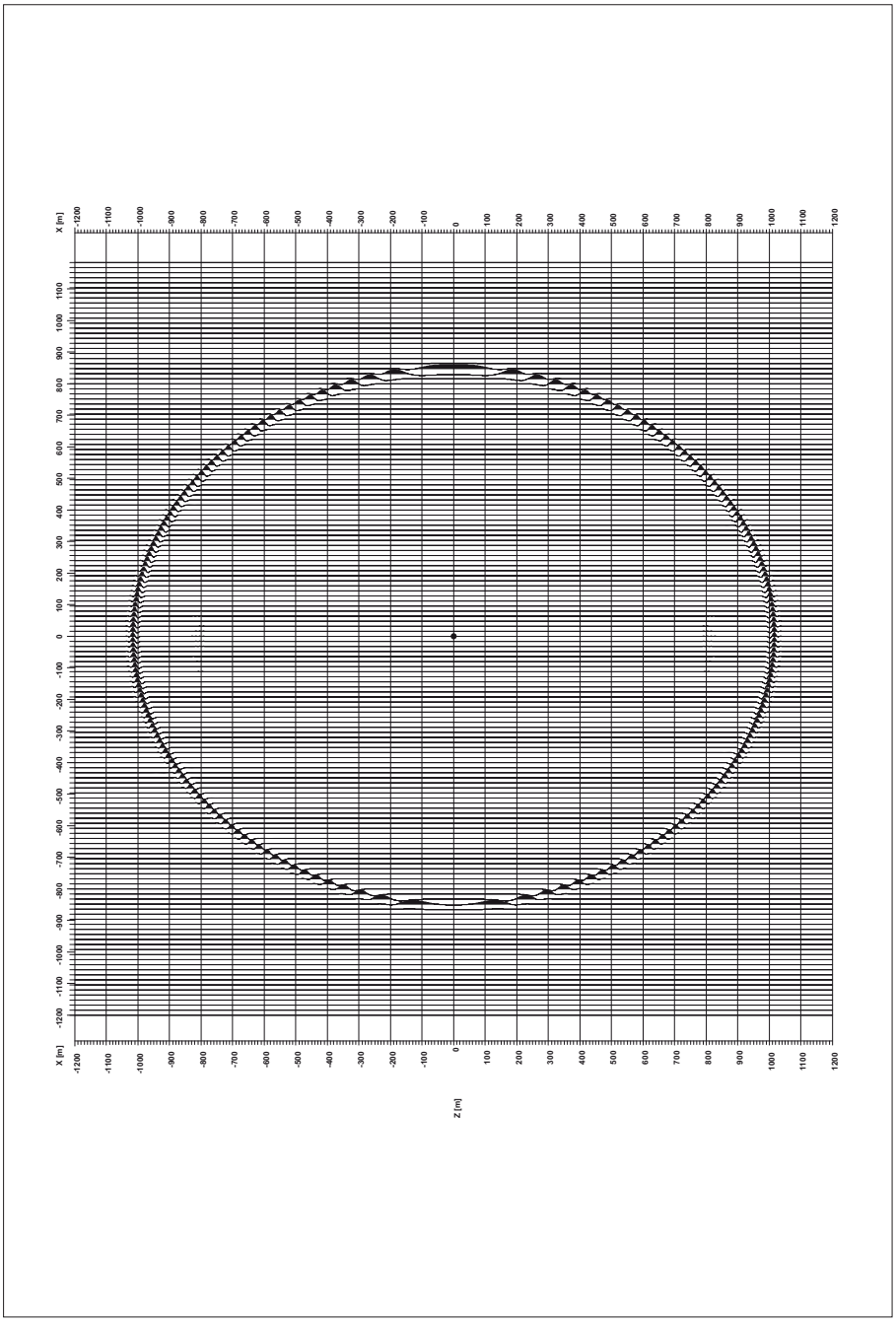

Fig. 2.14. Snapshot of spike wave propagation from algorithm (1.28) for parameters: $\varepsilon = 0.3$; $\delta = -0.1$ azimuthal angle $\Psi = 45°$; in moment time $t = 0.4$ s; steps of computation: $\Delta x = \Delta z = 4$ m, $\Delta t = 0.5$ ms

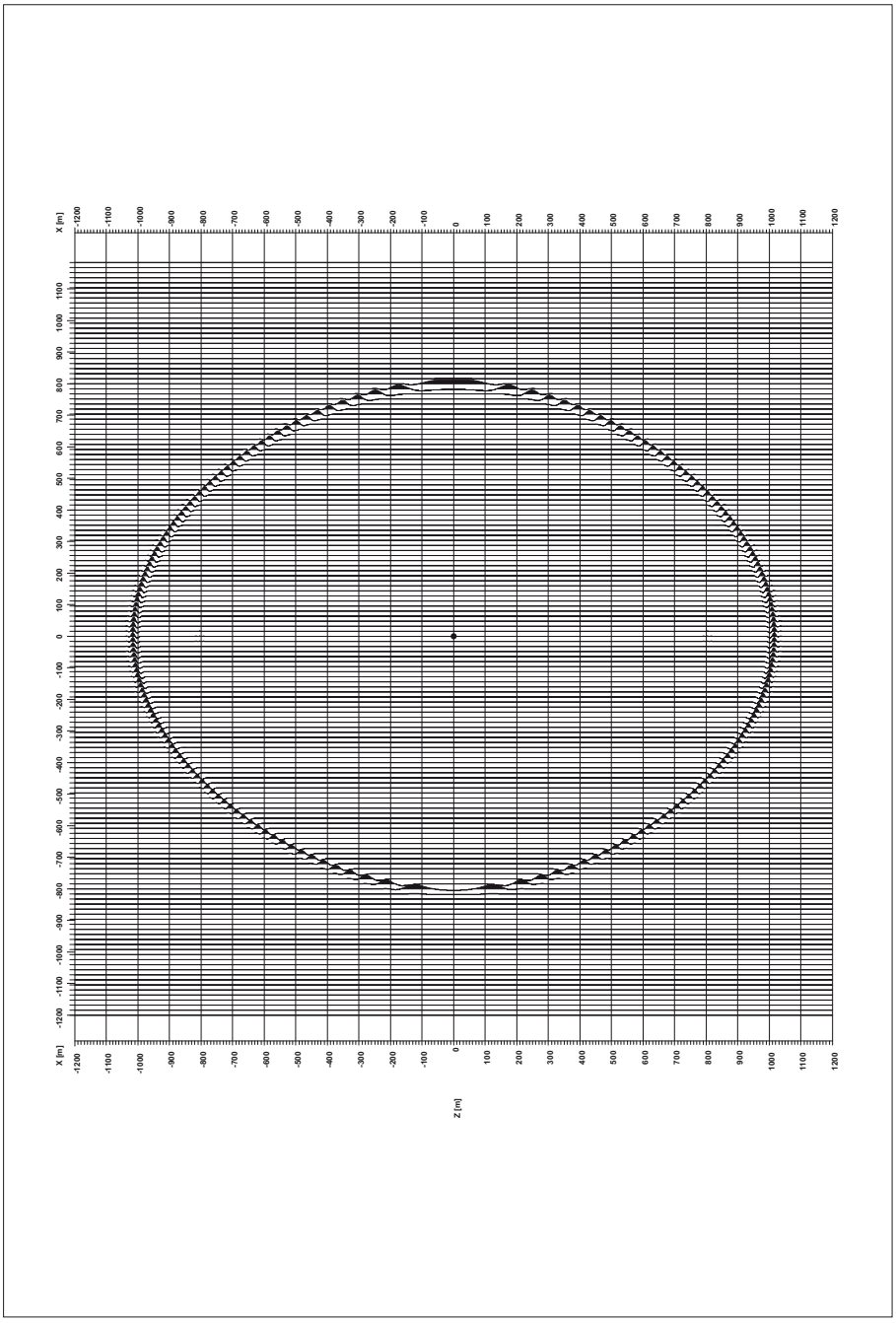

Fig. 2.15. Snapshot of spike wave propagation from algorithm (1.28) for parameters: $\varepsilon = 0.3$; $\delta = -0.1$ azimuthal angle $\Psi = 60°$; in moment time $t = 0.4$ s; steps of computation: $\Delta x = \Delta z = 4$ m, $\Delta t = 0.5$ ms

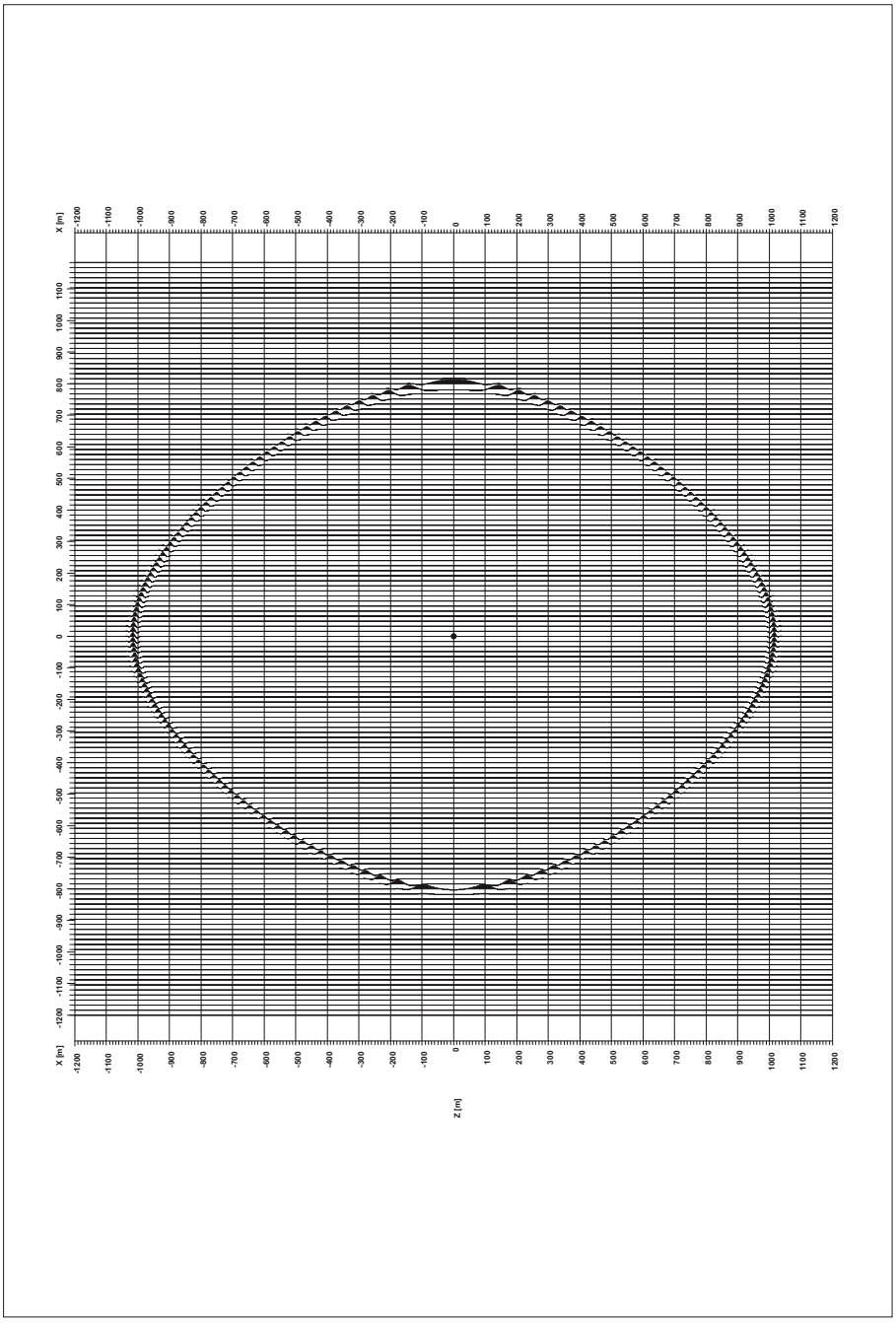

Fig. 2.16. Snapshot of spike wave propagation from algorithm (1.28) for parameters: $\varepsilon = 0.3$; $\delta = -0.1$ azimuthal angle $\Psi = 90°$; in moment time $t = 0.4$ s; steps of computation: $\Delta x = \Delta z = 4$ m, $\Delta t = 0.5$ ms

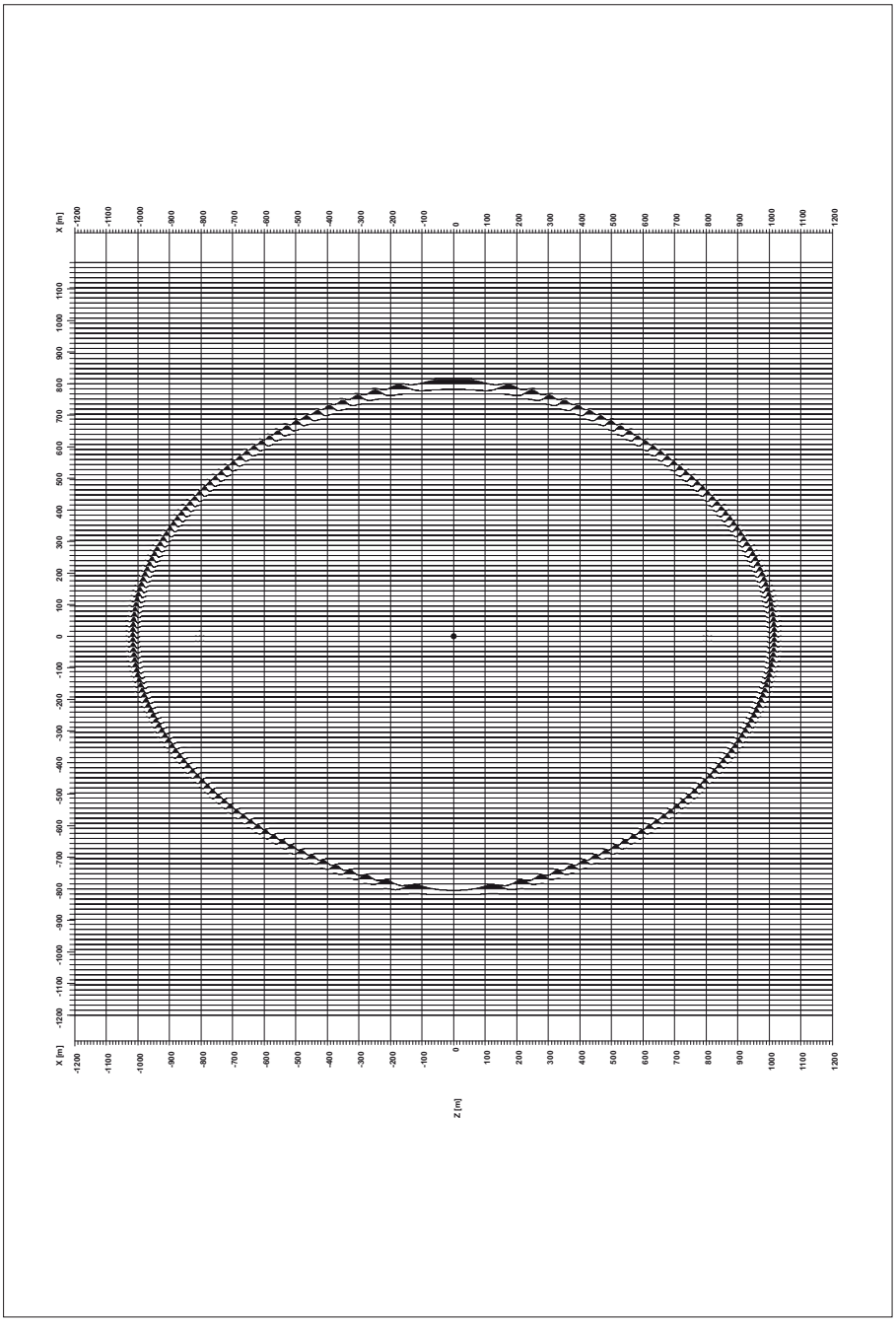

Fig. 2.17. Snapshot of spike wave propagation from algorithm (1.28) for parameters: $\varepsilon = 0.3$; $\delta = -0.1$ azimuthal angle $\Psi = 120°$; in moment time $t = 0.4$ s; steps of computation: $\Delta x = \Delta z = 4$ m, $\Delta t = 0.5$ ms

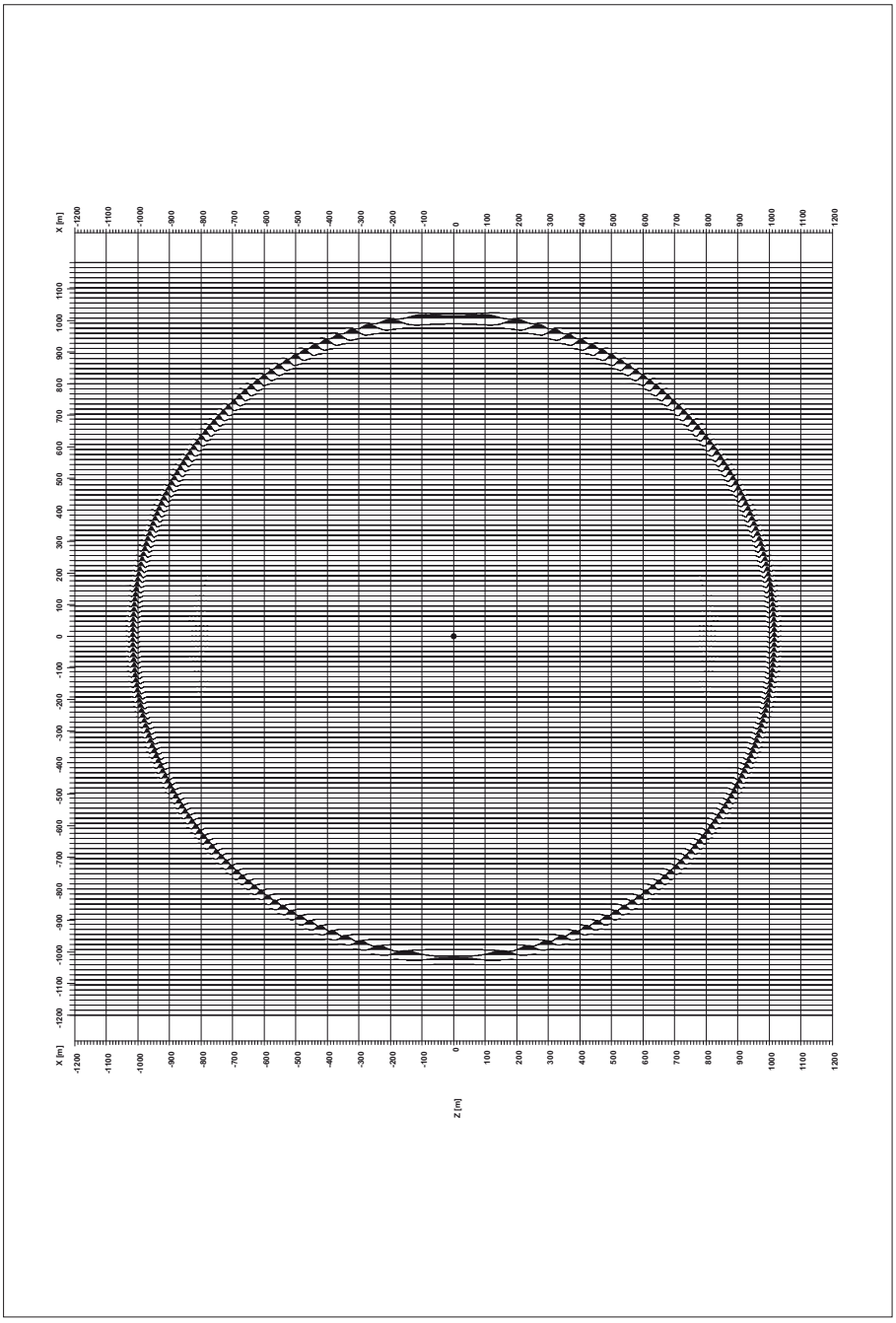

Fig. 2.18. Snapshot of spike wave propagation from algorithm (1.23) for parameters: $\varepsilon = 0.3$; $\delta = -0.1$ azimuthal angle $\Psi = 0°$; in moment time $t = 0.4$ s; steps of computation: $\Delta x = \Delta z = 4$ m, $\Delta t = 0.5$ ms

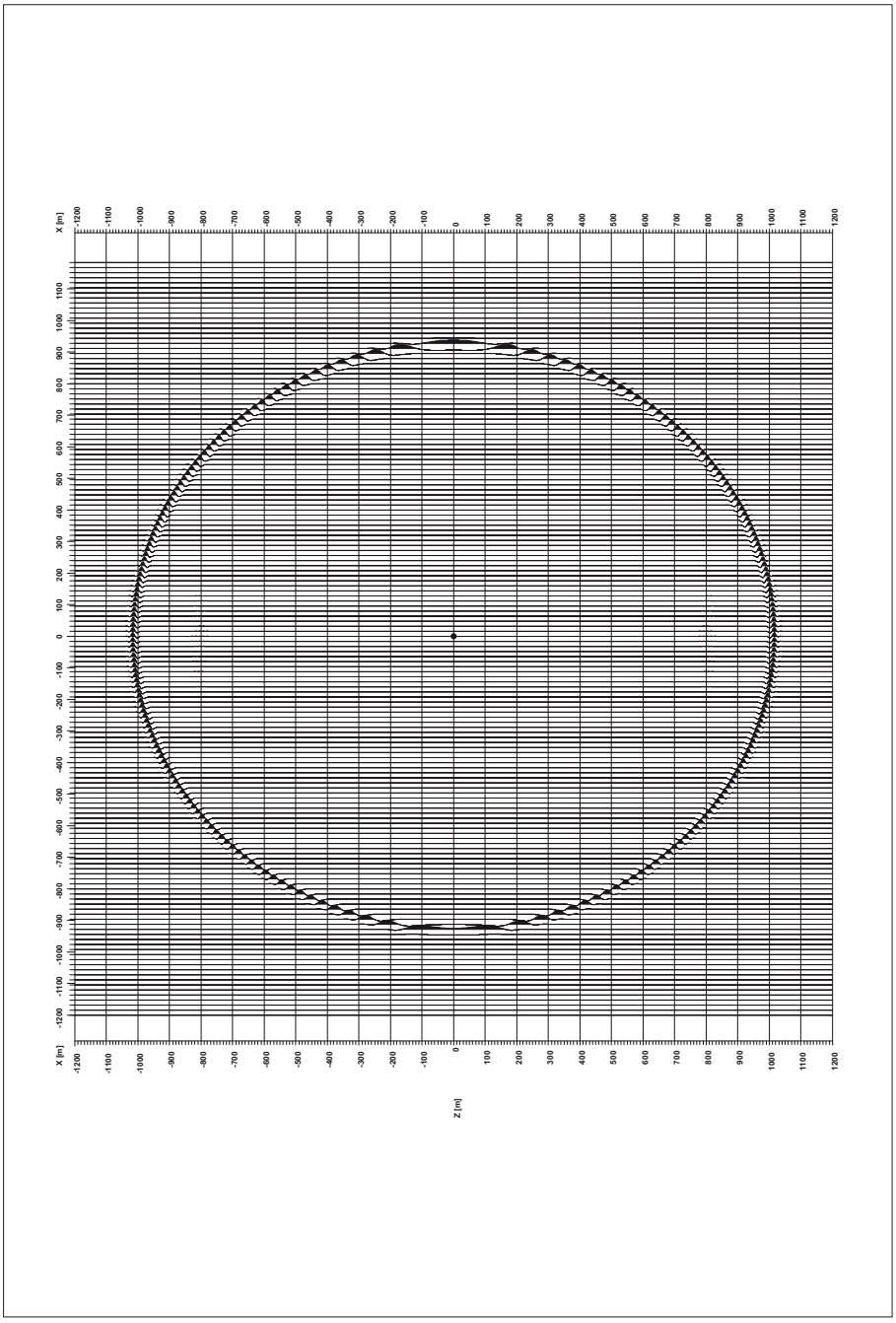

Fig. 2.19. Snapshot of spike wave propagation from algorithm (1.23) for parameters: $\varepsilon = 0.3$; $\delta = -0.1$ azimuthal angle $\Psi = 30°$; in moment time $t = 0.4$ s; steps of computation: $\Delta x = \Delta z = 4$ m, $\Delta t = 0.5$ ms

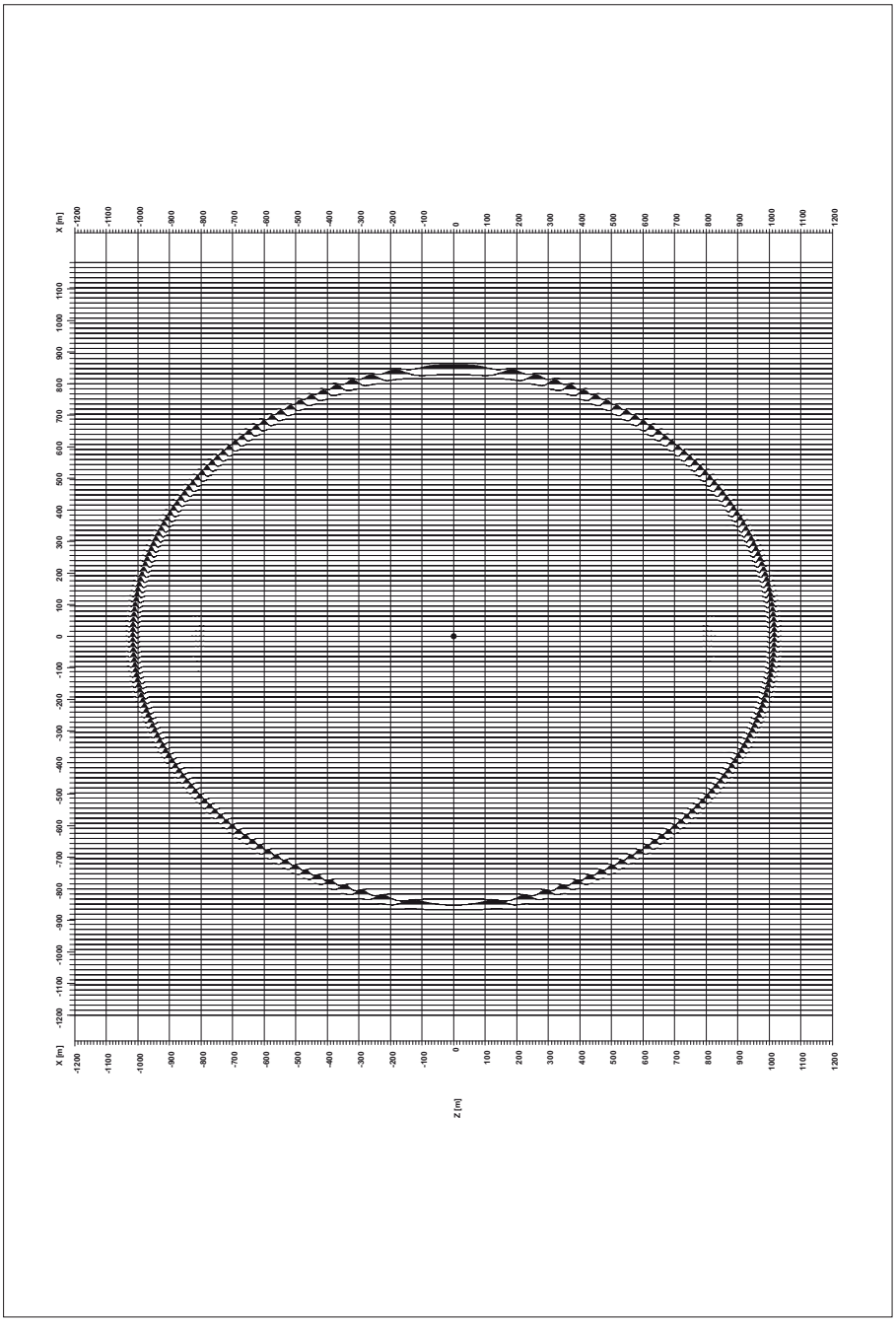

Fig. 2.20. Snapshot of spike wave propagation from algorithm (1.23) for parameters: $\varepsilon = 0.3$; $\delta = -0.1$ azimuthal angle $\Psi = 45°$; in moment time $t = 0.4$ s; steps of computation: $\Delta x = \Delta z = 4$ m, $\Delta t = 0.5$ ms

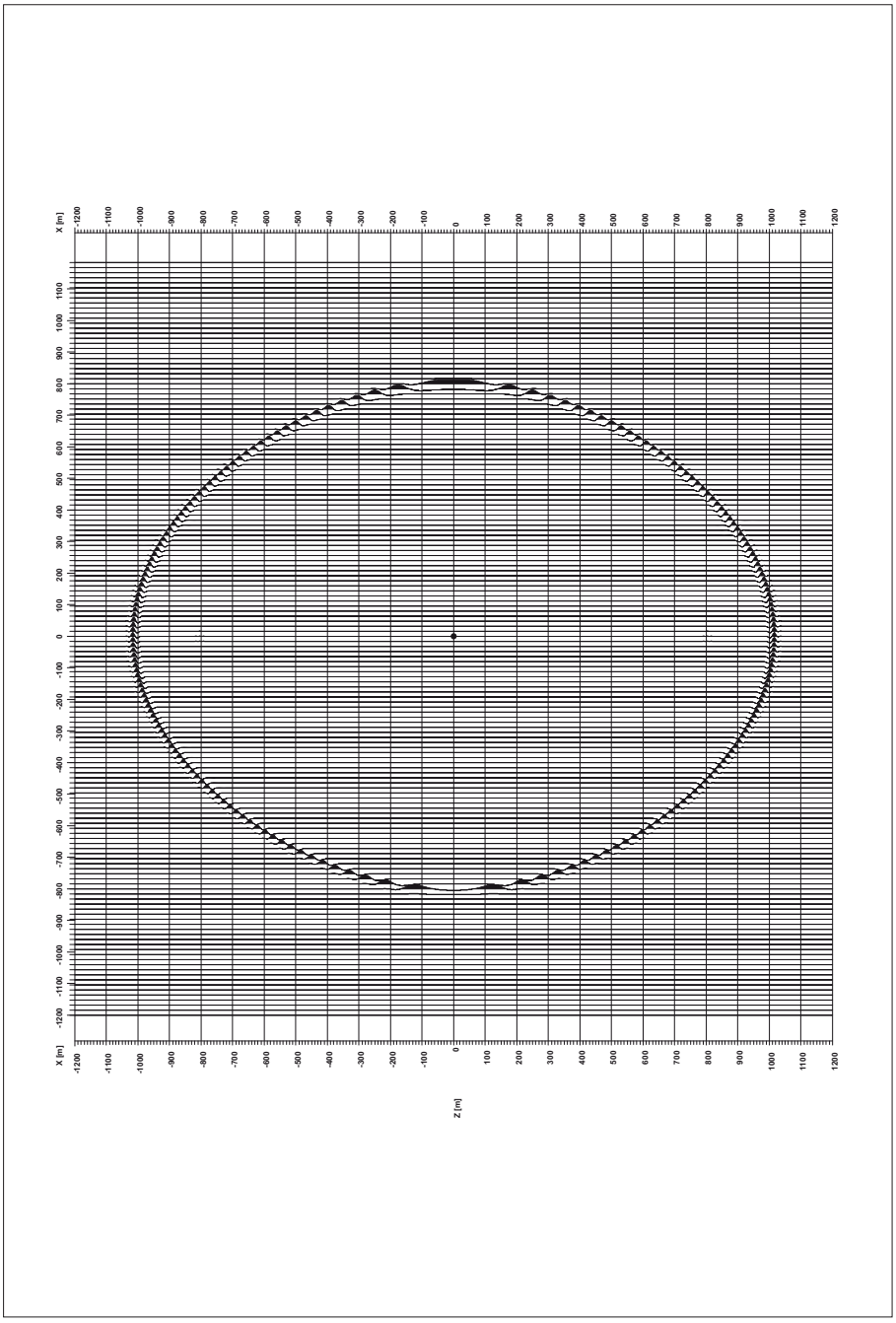

Fig. 2.21. Snapshot of spike wave propagation from algorithm (1.23) for parameters: $\varepsilon = 0.3$; $\delta = -0.1$ azimuthal angle $\Psi = 60°$; in moment time $t = 0.4$ s; steps of computation: $\Delta x = \Delta z = 4$ m, $\Delta t = 0.5$ ms

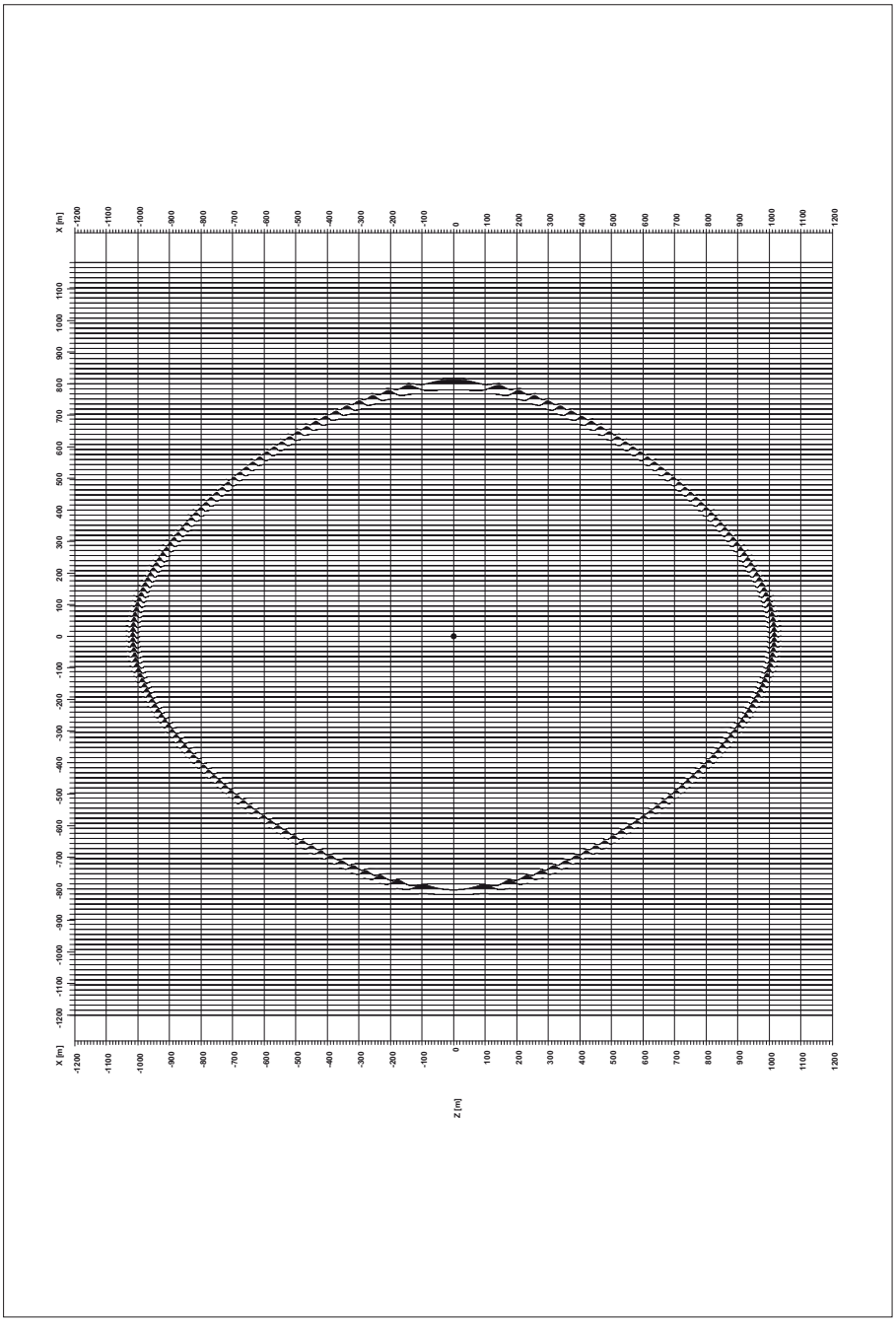

Fig. 2.22. Snapshot of spike wave propagation from algorithm (1.23) for parameters: $\varepsilon = 0.3$; $\delta = -0.1$ azimuthal angle $\Psi = 90°$; in moment time $t = 0.4$ s; steps of computation: $\Delta x = \Delta z = 4$ m, $\Delta t = 0.5$ ms

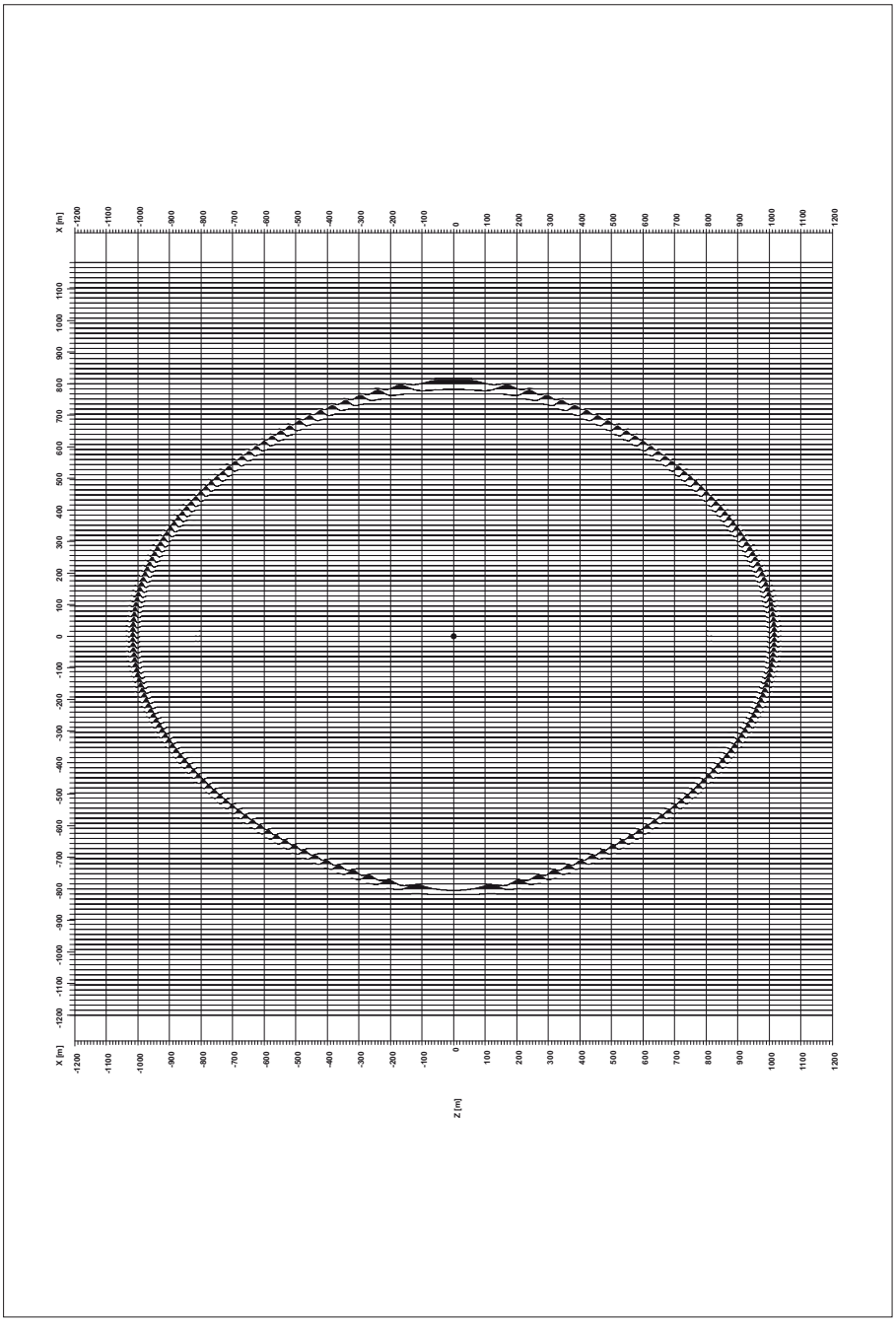

Fig. 2.23. Snapshot of spike wave propagation from algorithm (1.23) for parameters: $\varepsilon = 0.3$; $\delta = -0.1$ azimuthal angle $\Psi = 120°$; in moment time $t = 0.4$ s; steps of computation: $\Delta x = \Delta z = 4$ m, $\Delta t = 0.5$ ms

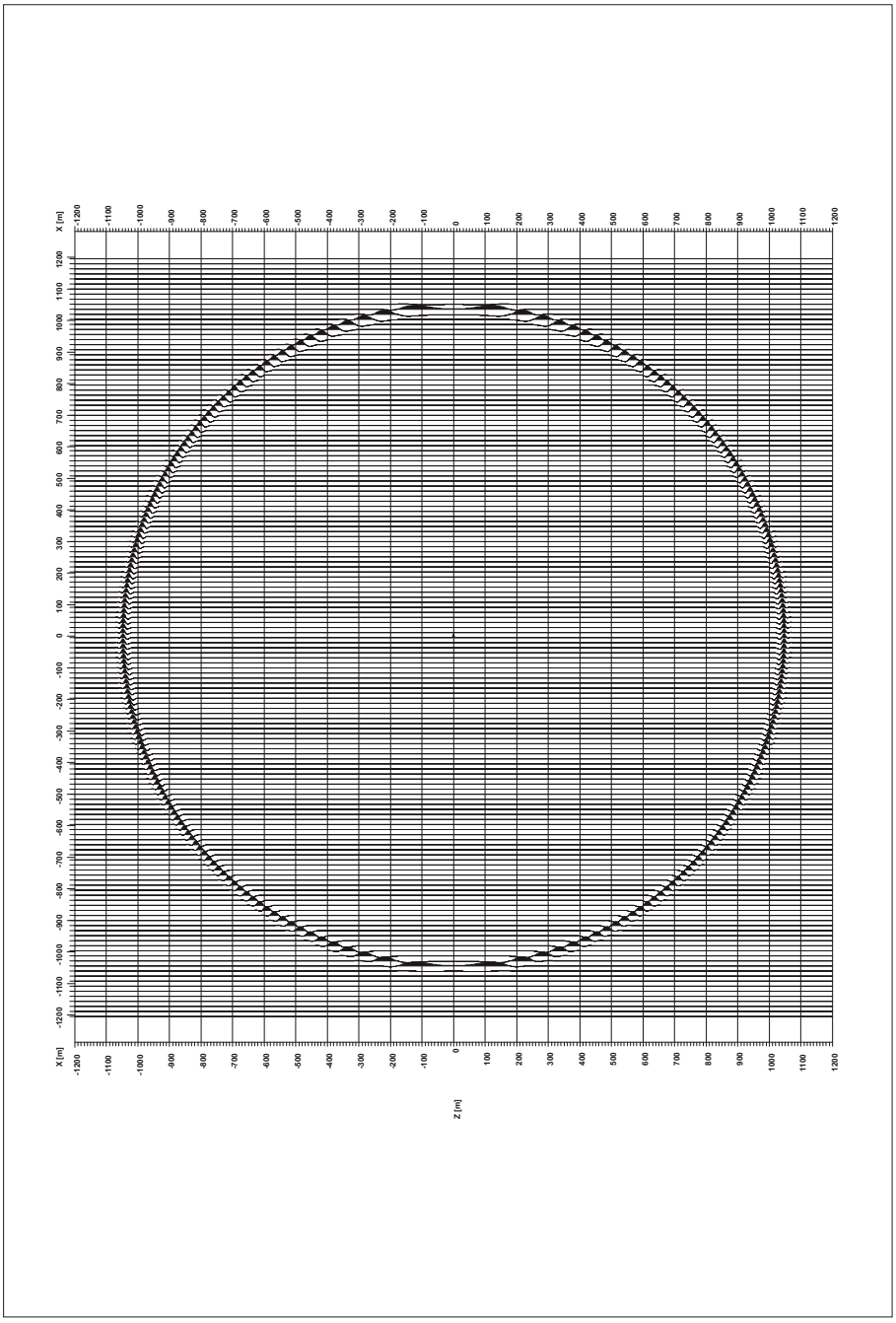

Fig. 2.24. Snapshot of spike wave propagation from algorithm (1.29) for parameters: $\varepsilon = 0.35$; $\delta = -0.1$ azimuthal angle $\Psi = 0°$; in moment time $t = 0.4$ s; steps of computation: $\Delta x = \Delta z = 4$ m, $\Delta t = 0.5$ ms

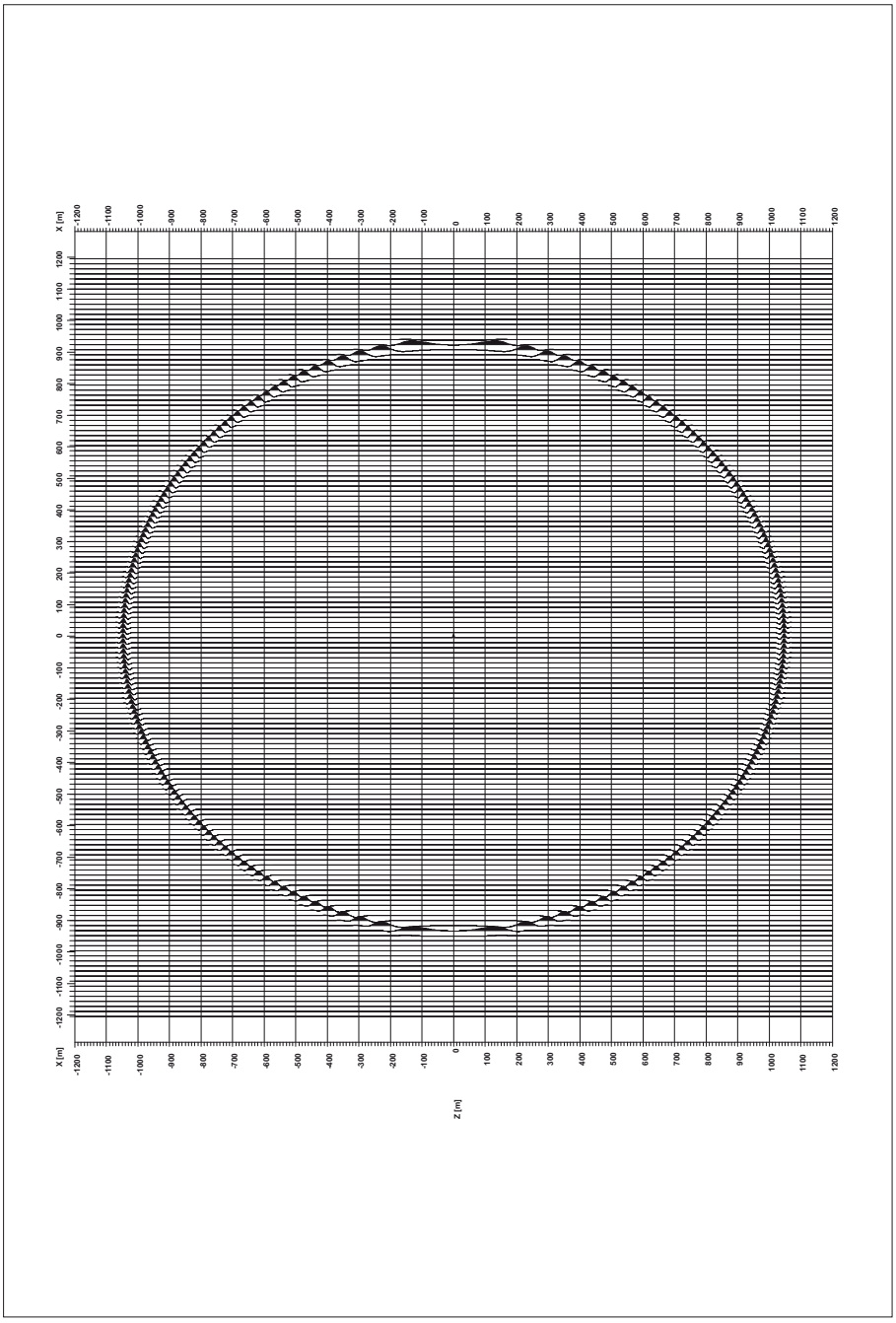

Fig. 2.25. Snapshot of spike wave propagation from algorithm (1.29) for parameters: $\varepsilon = 0.35$; $\delta = -0.1$ azimuthal angle $\Psi = 30°$; in moment time $t = 0.4$ s; steps of computation: $\Delta x = \Delta z = 4$ m, $\Delta t = 0.5$ ms

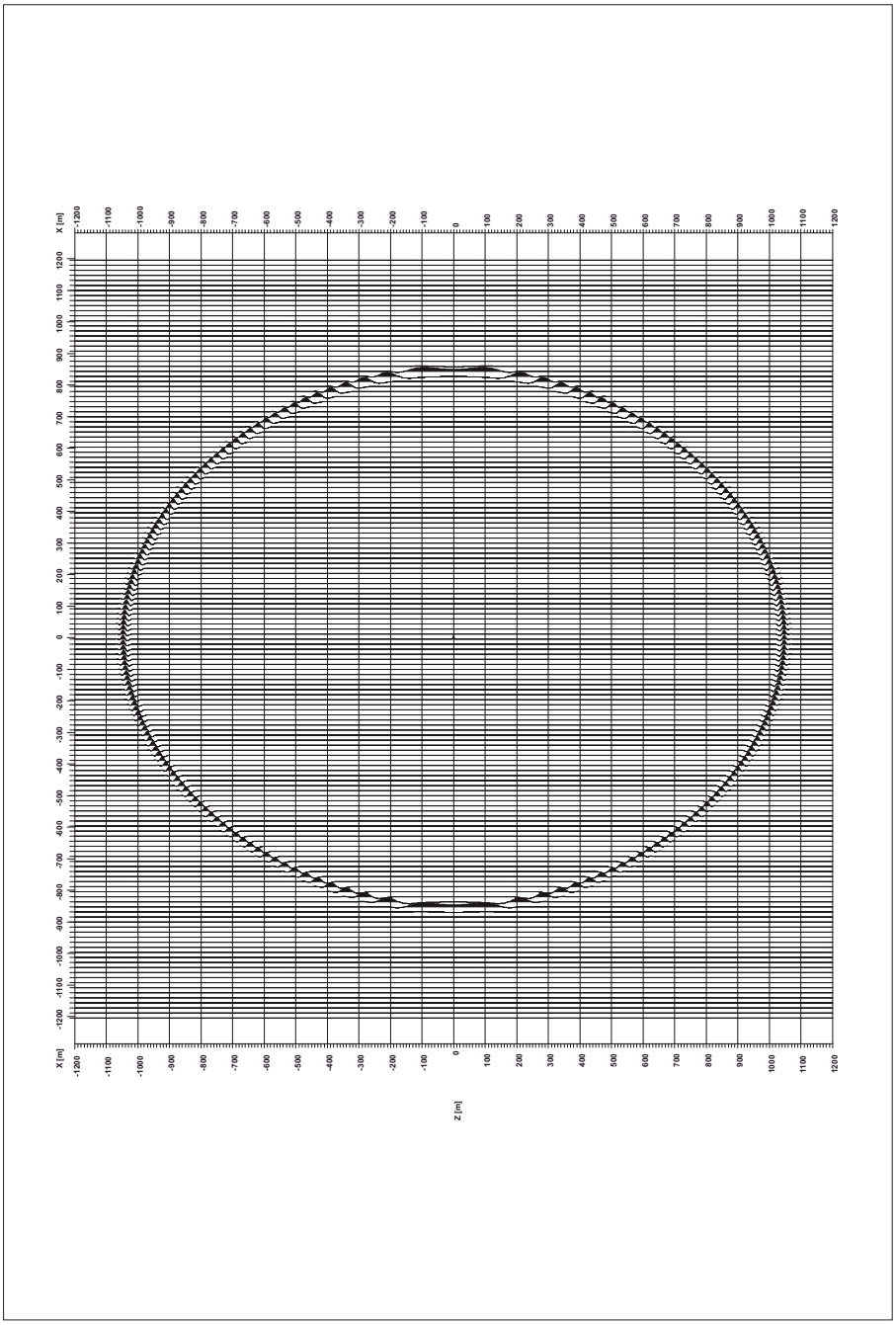

Fig. 2.26. Snapshot of spike wave propagation from algorithm (1.29) for parameters: $\varepsilon = 0.35$; $\delta = -0.1$ azimuthal angle $\Psi = 45°$; in moment time $t = 0.4$ s; steps of computation: $\Delta x = \Delta z = 4$ m, $\Delta t = 0.5$ ms

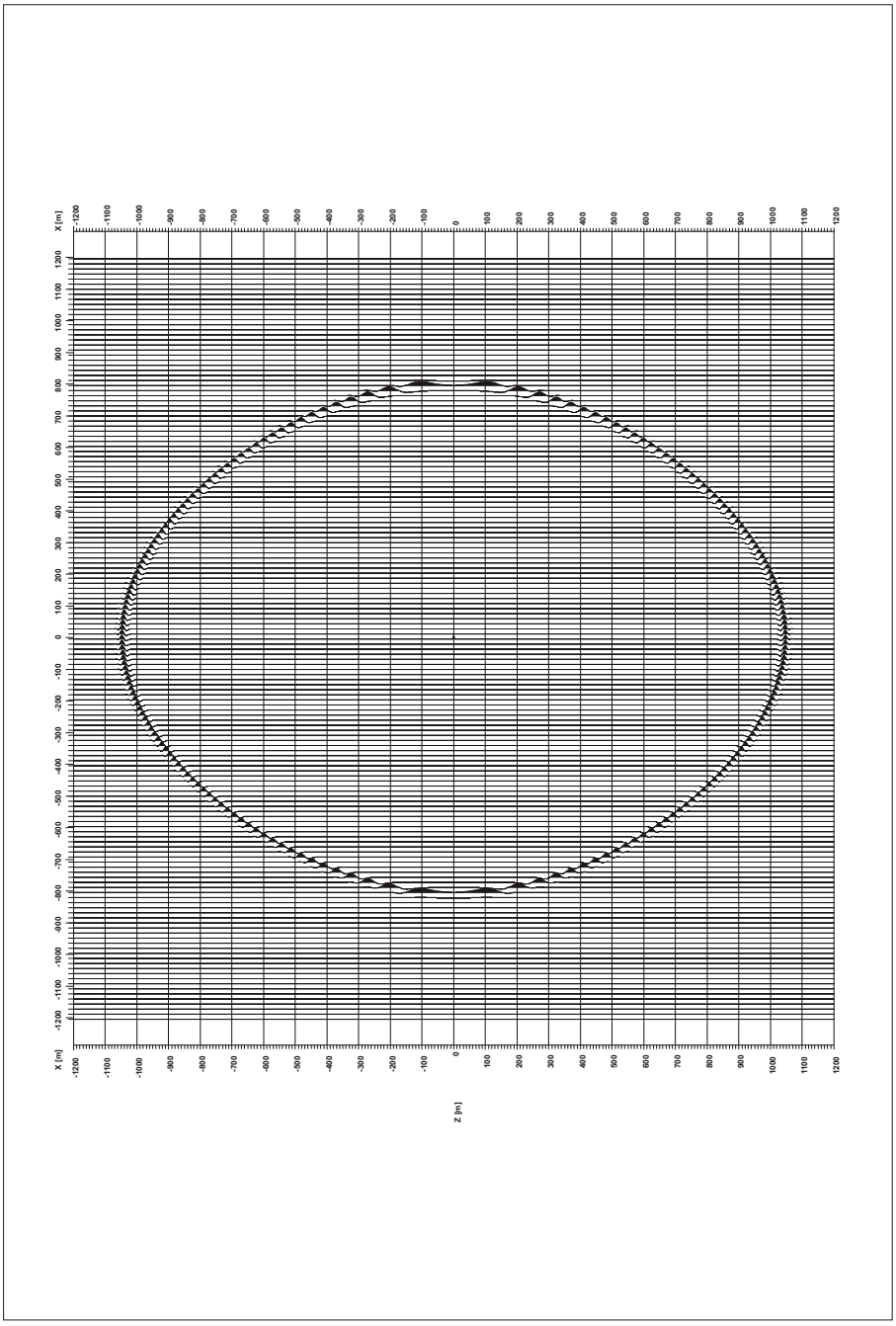

Fig. 2.27. Snapshot of spike wave propagation from algorithm (1.29) for parameters: $\varepsilon = 0.35$; $\delta = -0.1$ azimuthal angle $\Psi = 60°$; in moment time $t = 0.4$ s; steps of computation: $\Delta x = \Delta z = 4$ m, $\Delta t = 0.5$ ms

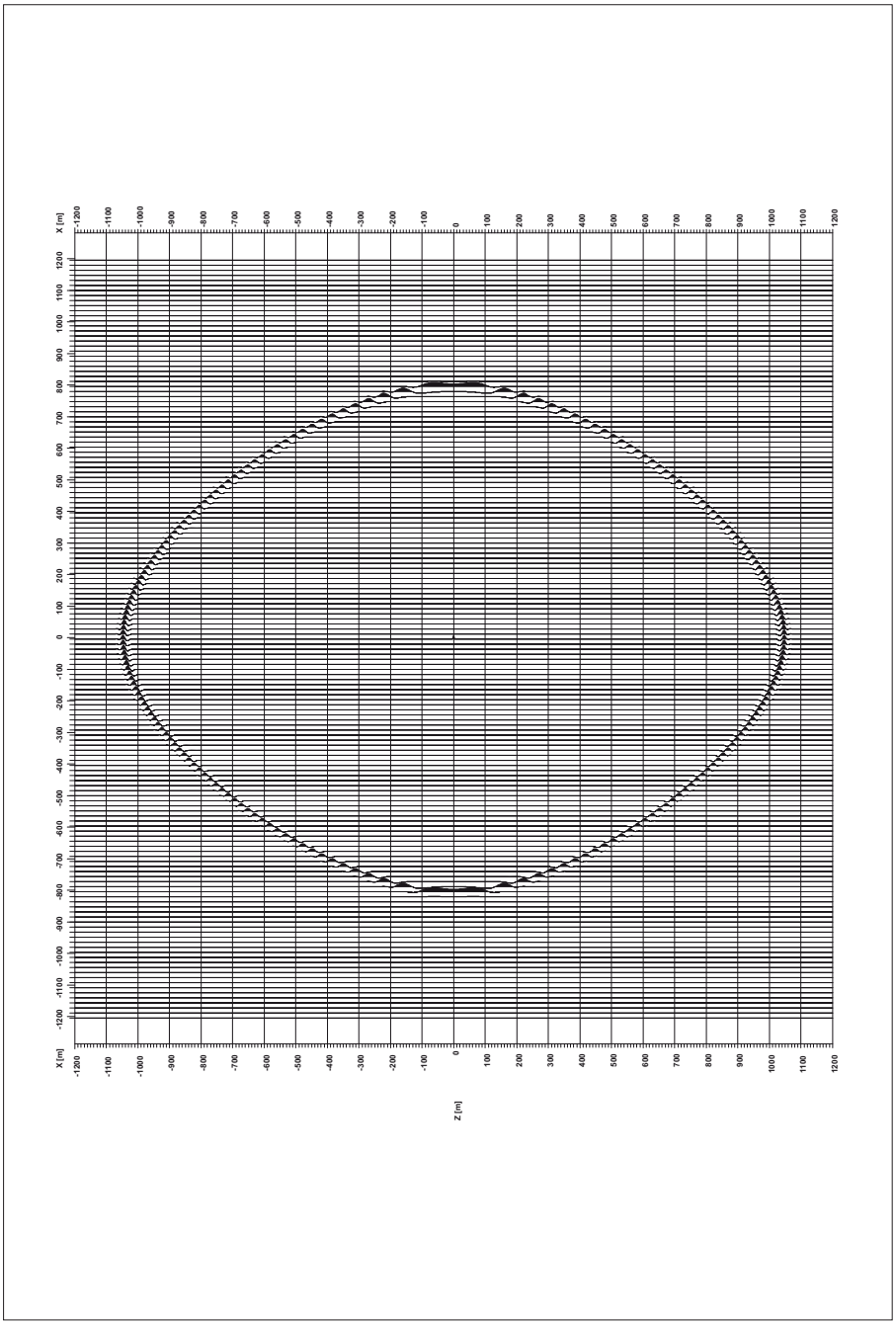

Fig. 2.28. Snapshot of spike wave propagation from algorithm (1.29) for parameters: $\varepsilon = 0.35$; $\delta = -0.1$ azimuthal angle $\Psi = 90°$; in moment time $t = 0.4$ s; steps of computation: $\Delta x = \Delta z = 4$ m, $\Delta t = 0.5$ ms

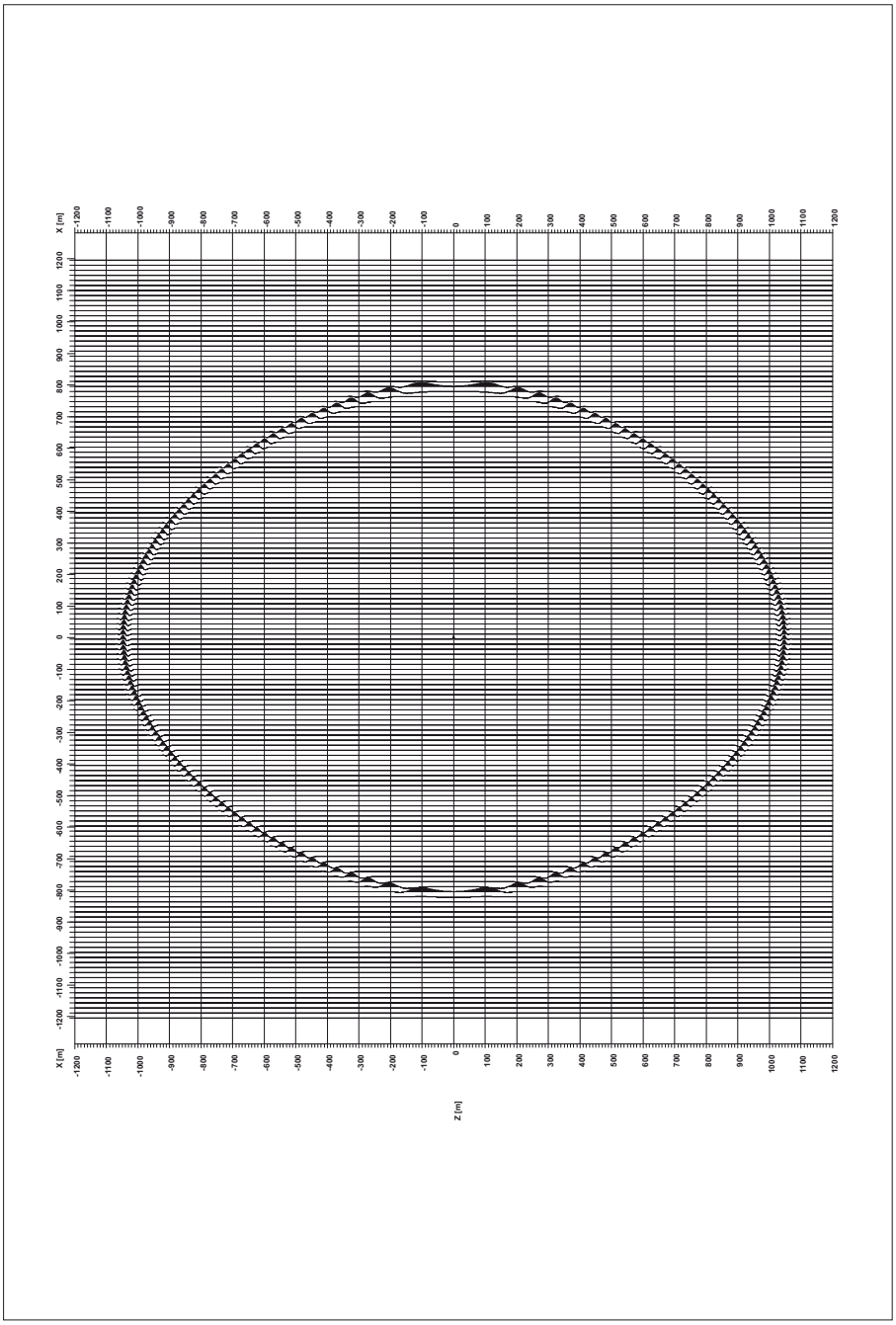

Fig. 2.29. Snapshot of spike wave propagation from algorithm (1.29) for parameters: $\varepsilon = 0.35$; $\delta = -0.1$ azimuthal angle $\Psi = 120°$; in moment time $t = 0.4$ s; steps of computation: $\Delta x = \Delta z = 4$ m, $\Delta t = 0.5$ ms

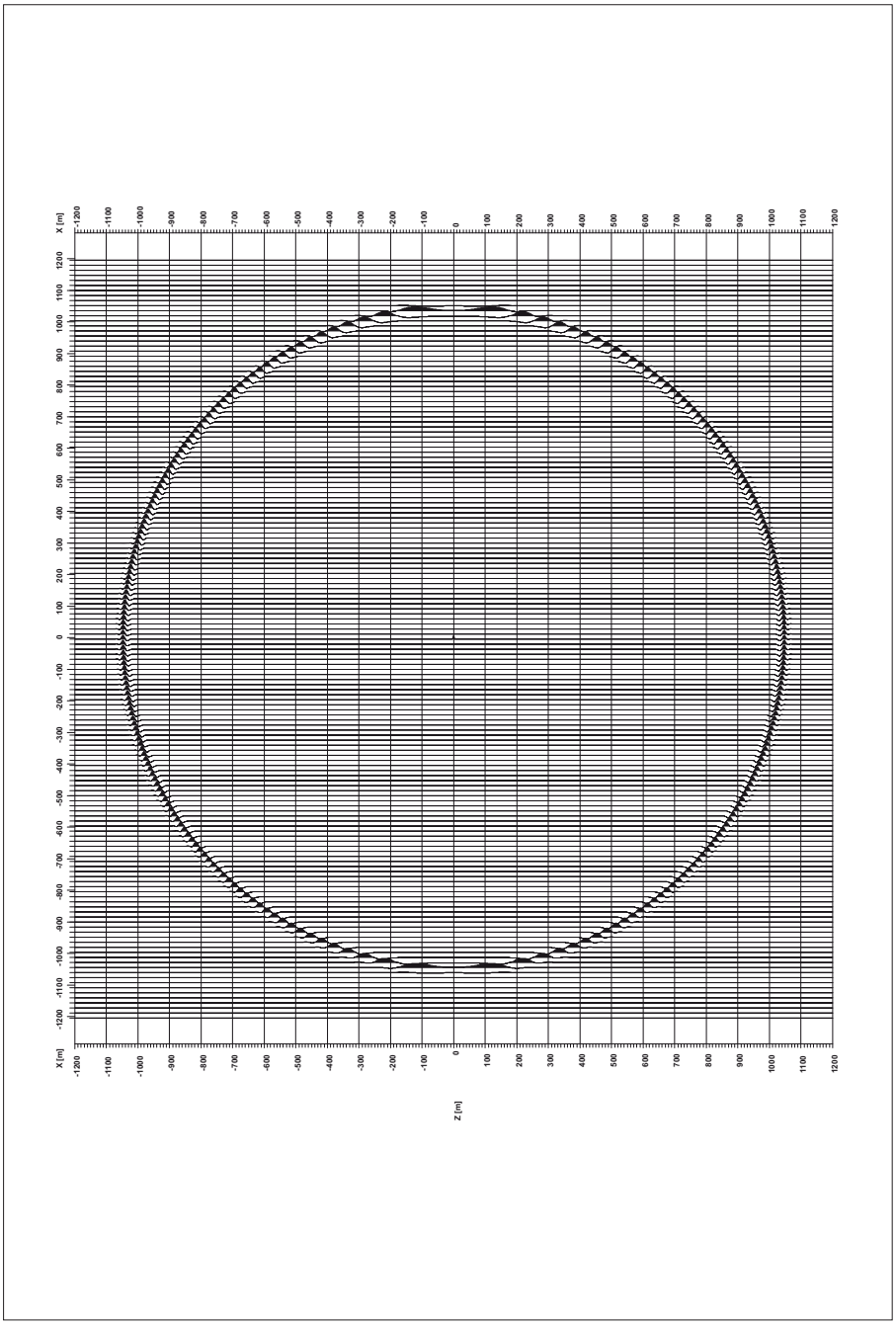

Fig. 2.30. Snapshot of spike wave propagation from algorithm (1.29) for parameters: $\varepsilon = 0.35$; $\delta = 0.1$ azimuthal angle $\Psi = 0°$; in moment time $t = 0.4$ s; steps of computation: $\Delta x = \Delta z = 4$ m, $\Delta t = 0.5$ ms

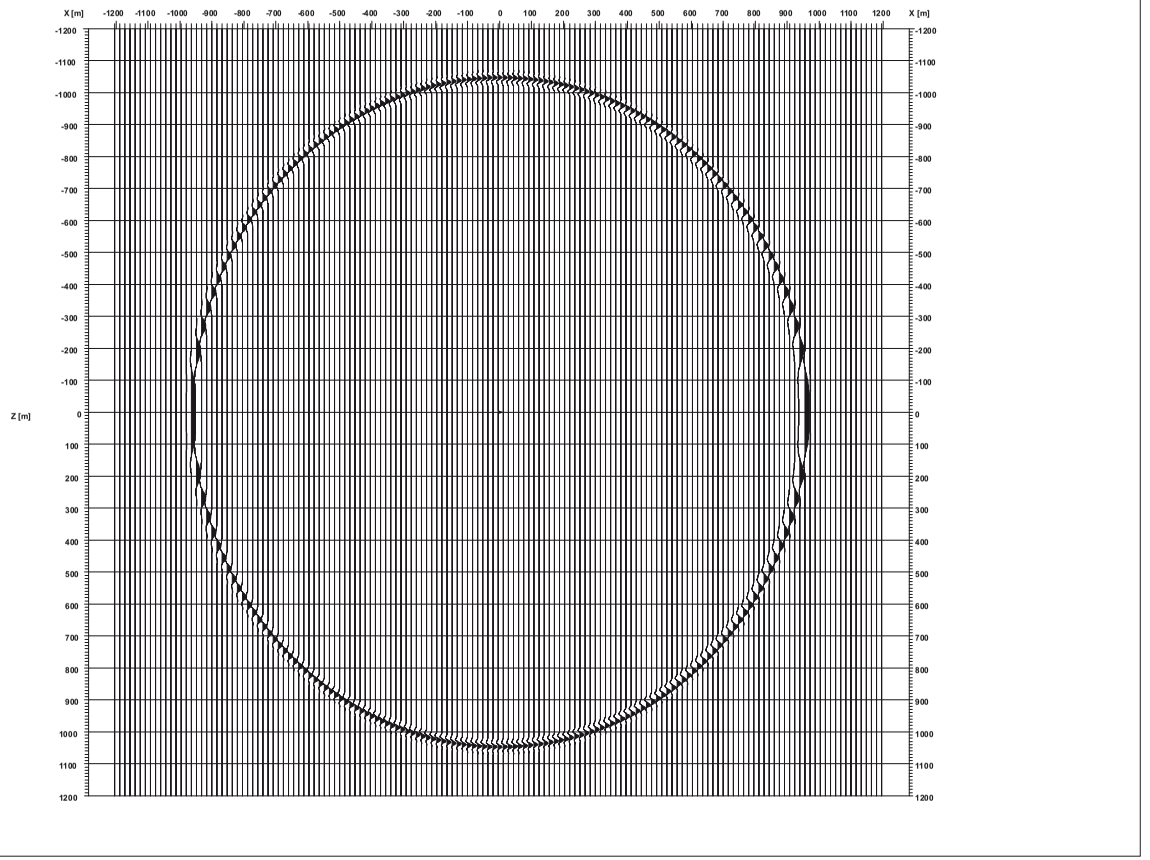

Fig. 2.31. Snapshot of spike wave propagation from algorithm (1.29) for parameters: $\varepsilon = 0.35$; $\delta = 0.1$ azimuthal angle $\Psi = 30°$; in moment time $t = 0.4$ s; steps of computation: $\Delta x = \Delta z = 4$ m, $\Delta t = 0.5$ ms

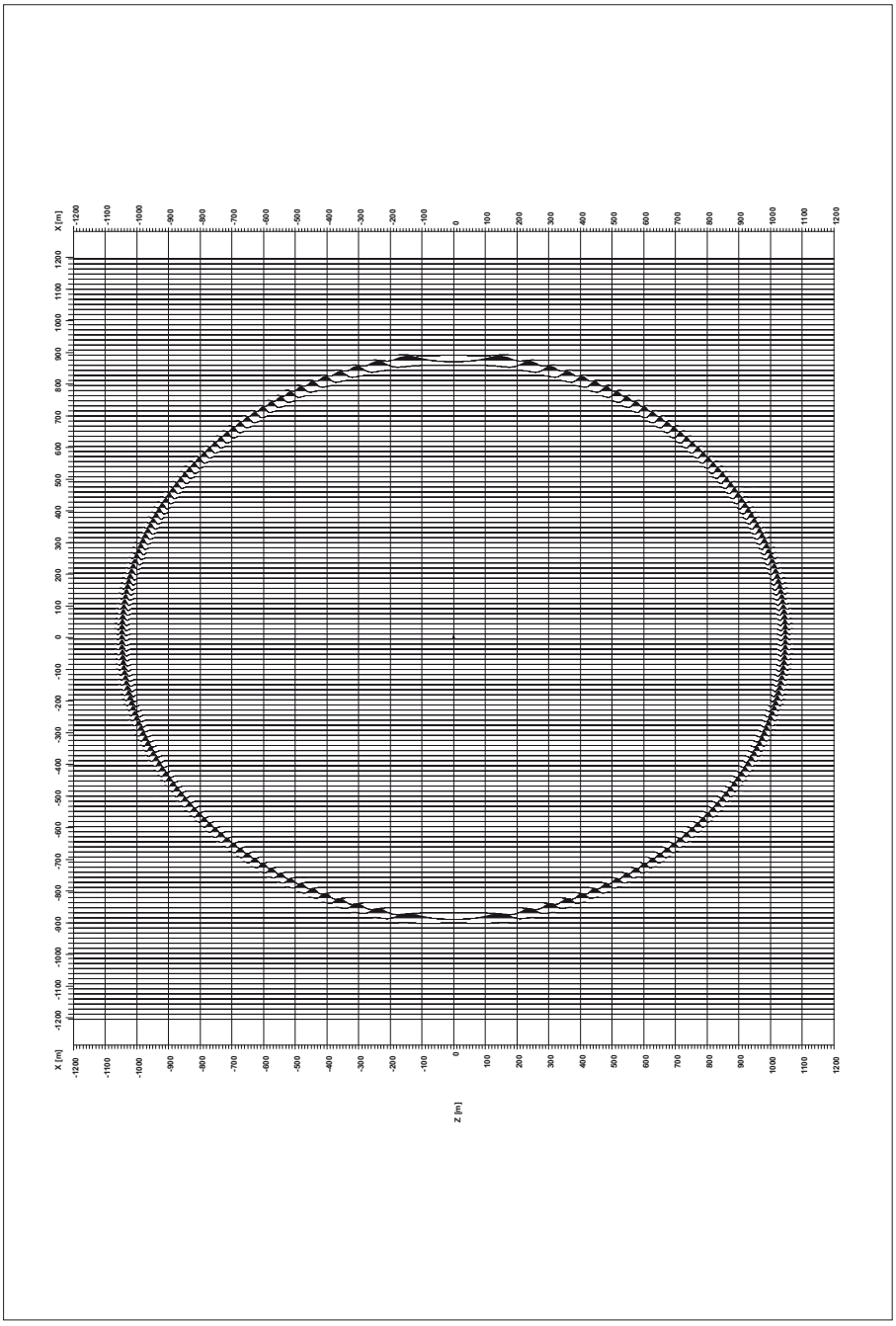

Fig. 2.32. Snapshot of spike wave propagation from algorithm (1.29) for parameters: $\varepsilon = 0.35$; $\delta = 0.1$ azimuthal angle $\Psi = 45°$; in moment time $t = 0.4$ s; steps of computation: $\Delta x = \Delta z = 4$ m, $\Delta t = 0.5$ ms

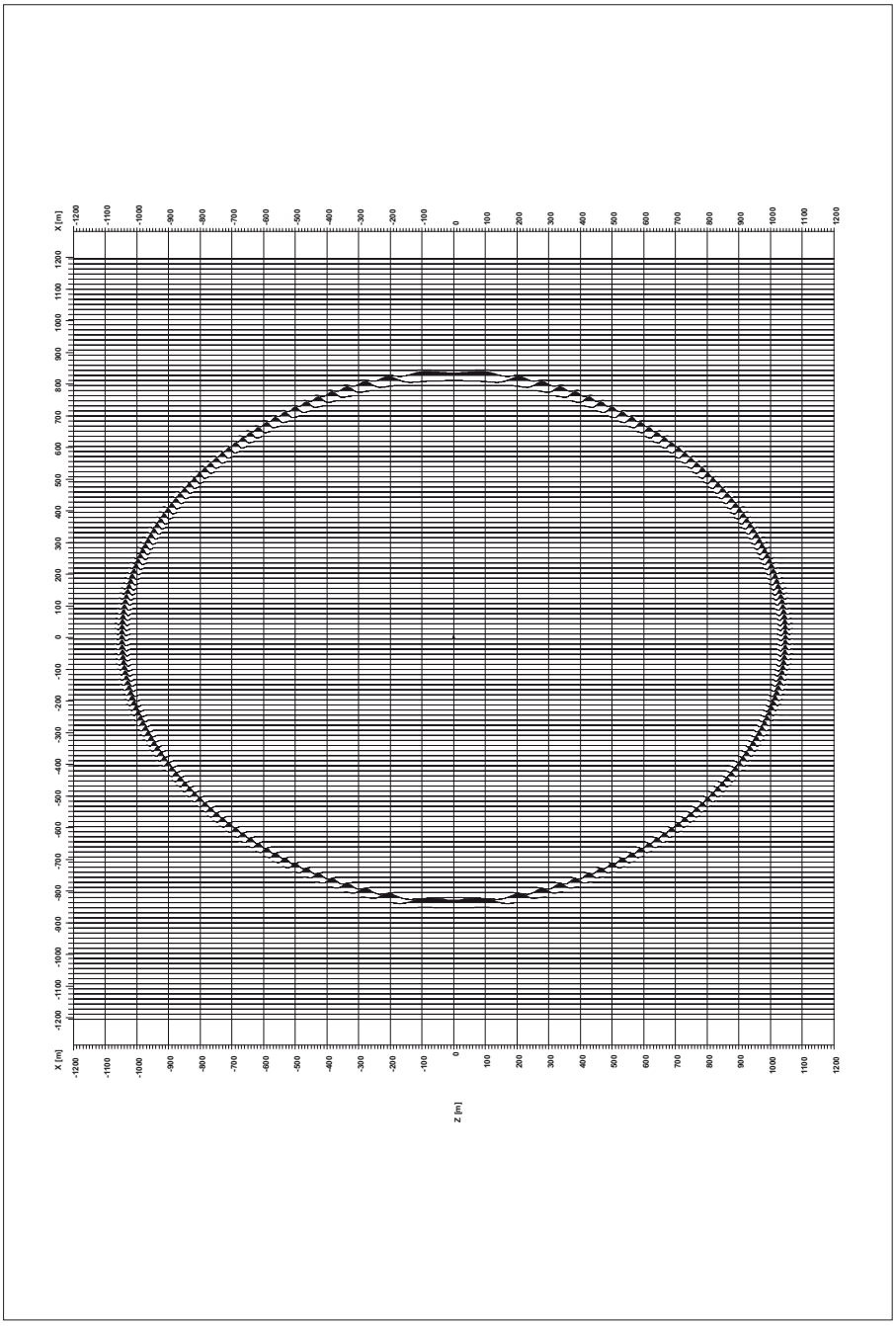

Fig. 2.33. Snapshot of spike wave propagation from algorithm (1.29) for parameters: $\varepsilon = 0.35$; $\delta = 0.1$ azimuthal angle $\Psi = 60°$; in moment time $t = 0.4$ s; steps of computation: $\Delta x = \Delta z = 4$ m, $\Delta t = 0.5$ ms

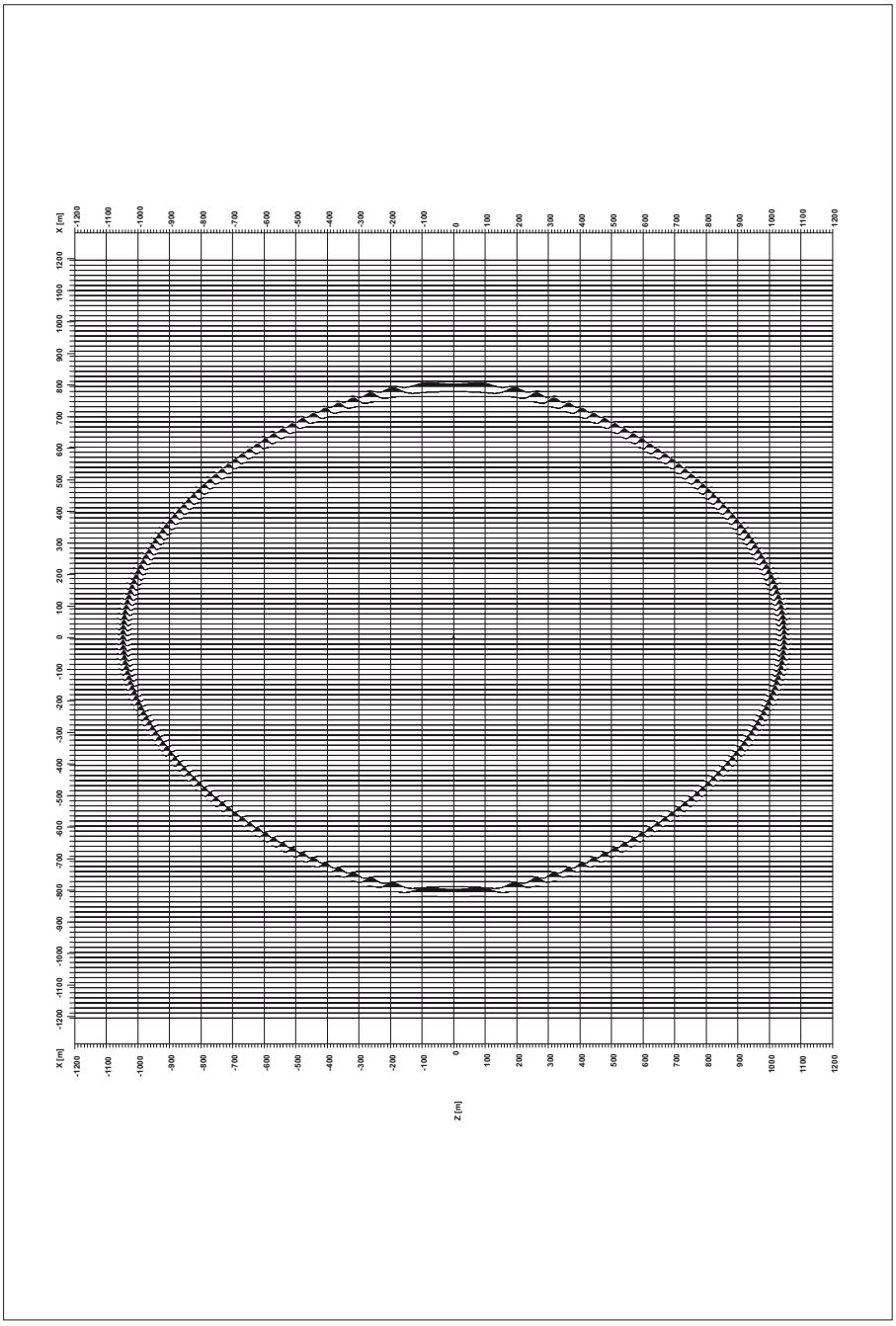

Fig. 2.34. Snapshot of spike wave propagation from algorithm (1.29) for parameters: $\varepsilon = 0.35$; $\delta = 0.1$ azimuthal angle $\Psi = 90°$; in moment time $t = 0.4$ s; steps of computation: $\Delta x = \Delta z = 4$ m, $\Delta t = 0.5$ ms

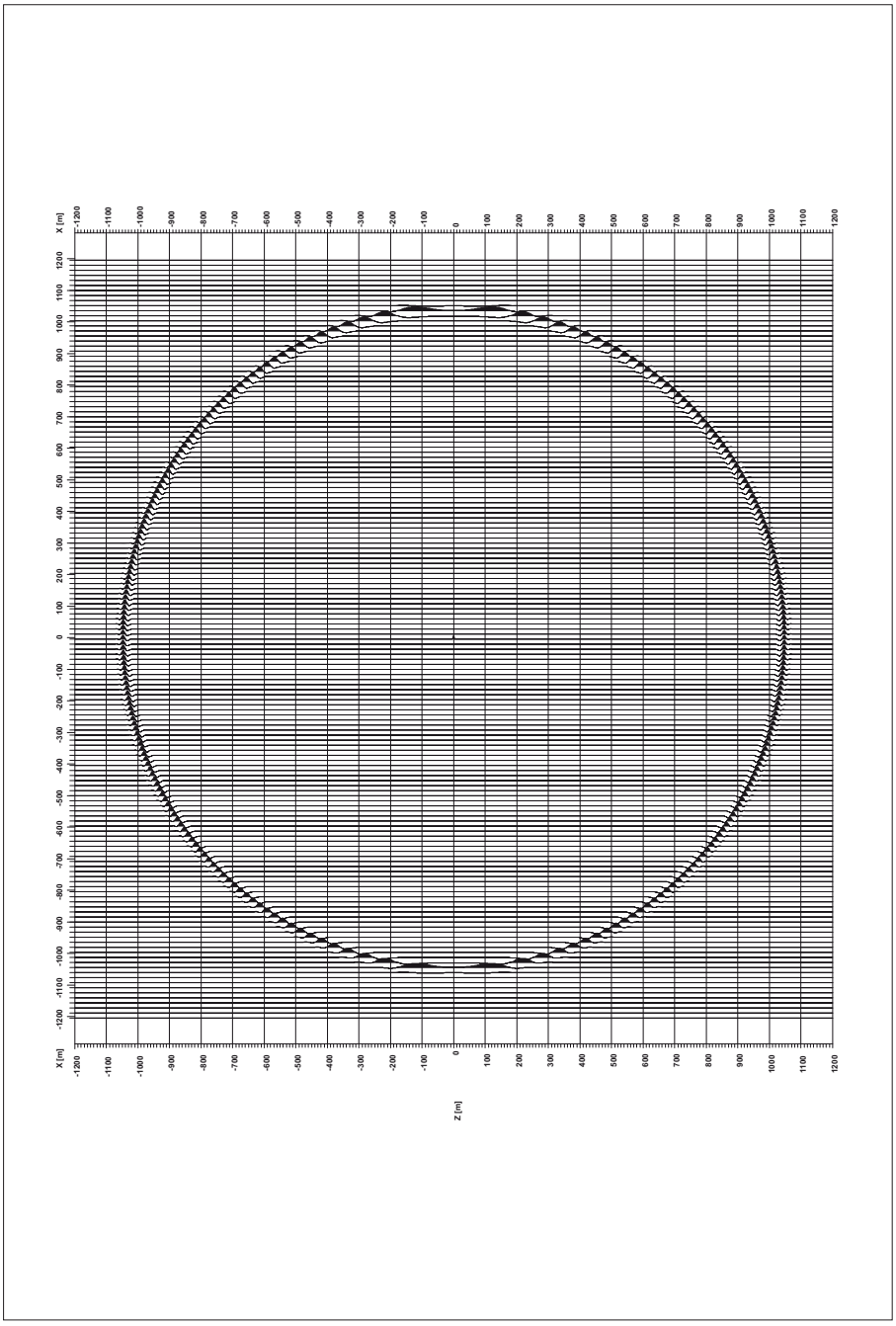

Fig. 2.35. Snapshot of spike wave propagation from algorithm (1.28) for parameters: $\varepsilon = 0.35$; $\delta = 0.1$ azimuthal angle $\Psi = 0°$; in moment time $t = 0.4$ s; steps of computation: $\Delta x = \Delta z = 4$ m, $\Delta t = 0.5$ ms

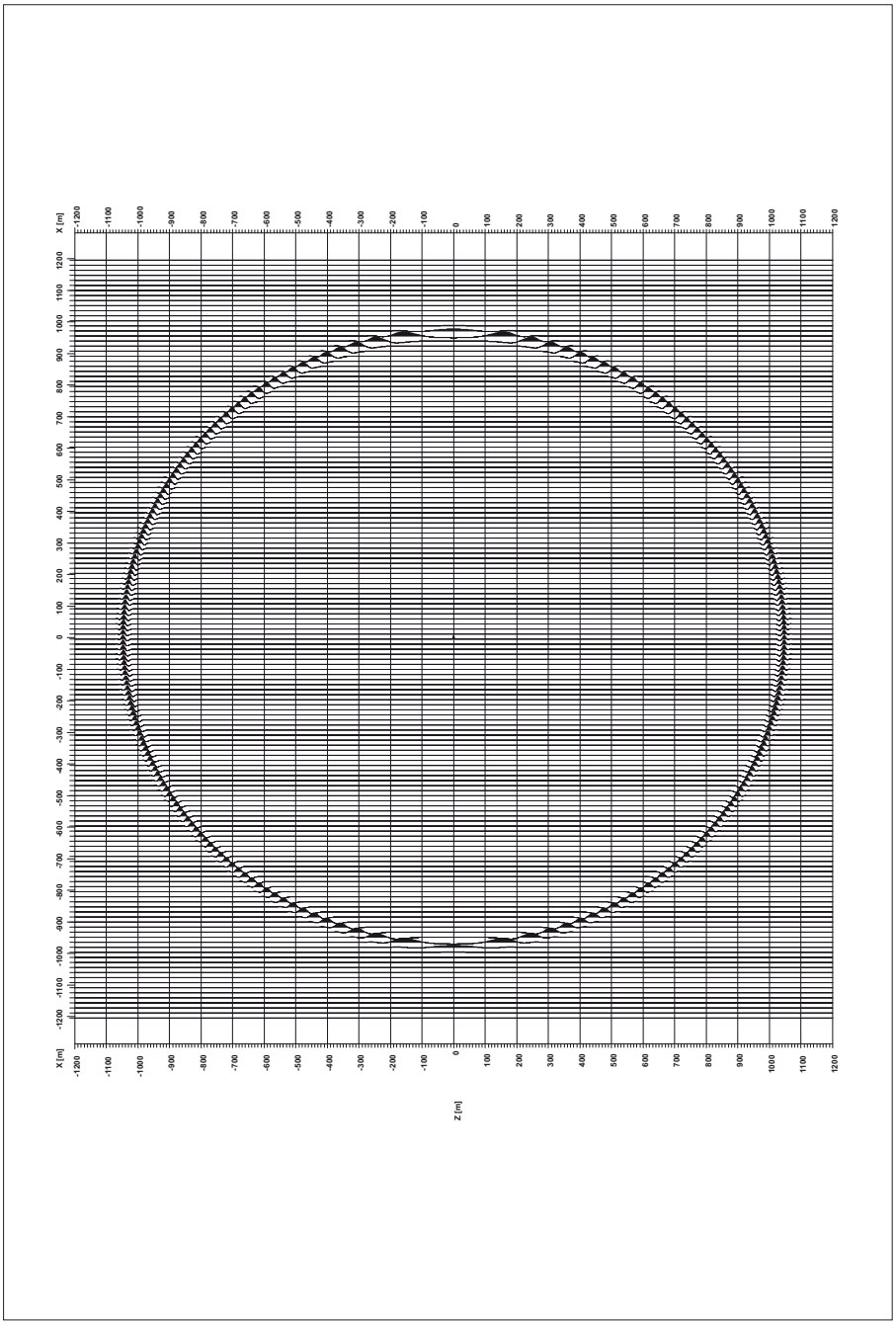

Fig. 2.36. Snapshot of spike wave propagation from algorithm (1.28) for parameters: $\varepsilon = 0.35$; $\delta = 0.1$ azimuthal angle $\Psi = 30°$; in moment time $t = 0.4$ s; steps of computation: $\Delta x = \Delta z = 4$ m, $\Delta t = 0.5$ ms

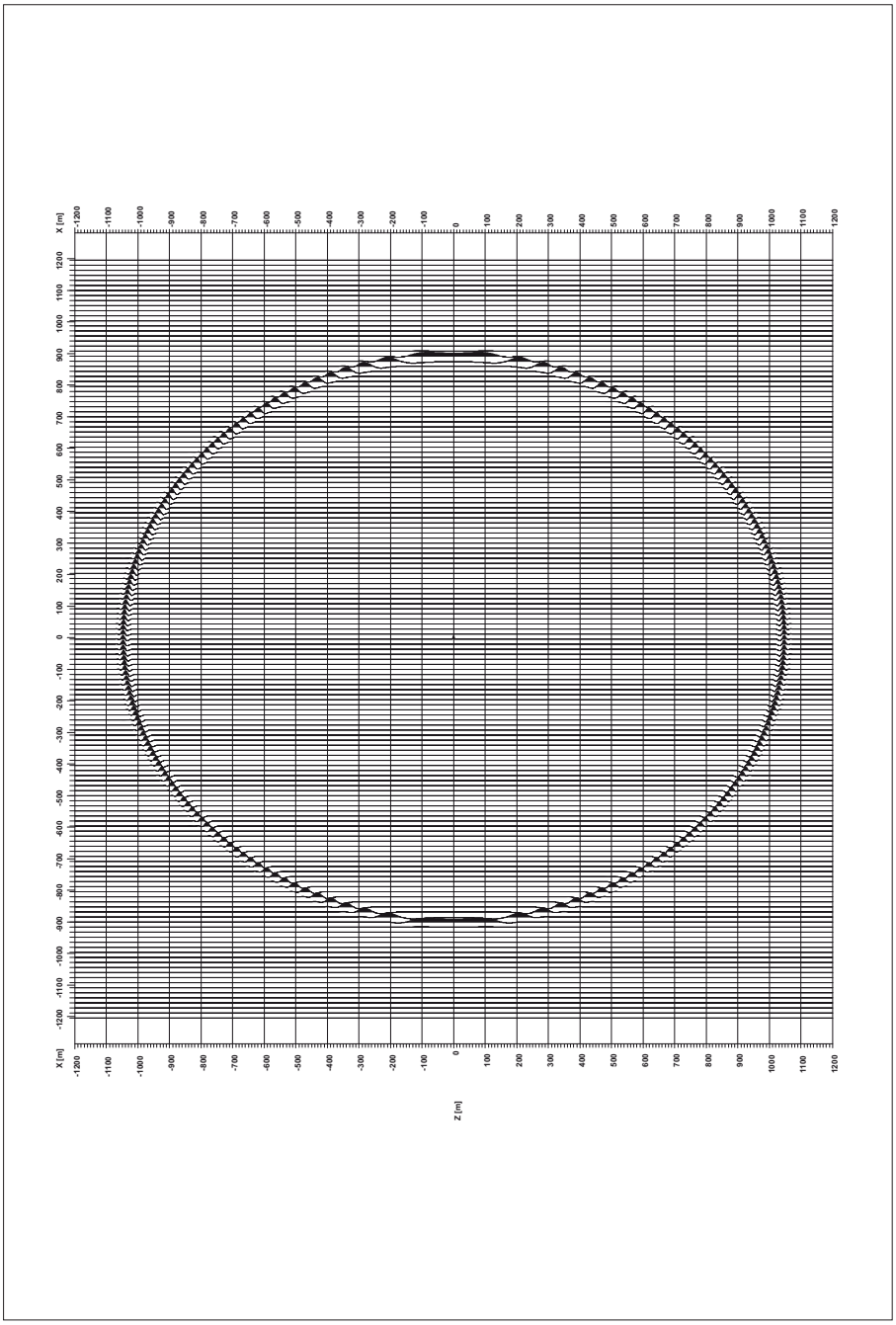

Fig. 2.37. Snapshot of spike wave propagation from algorithm (1.28) for parameters: $\varepsilon = 0.35$; $\delta = 0.1$ azimuthal angle $\Psi = 45°$; in moment time $t = 0.4$ s; steps of computation: $\Delta x = \Delta z = 4$ m, $\Delta t = 0.5$ ms

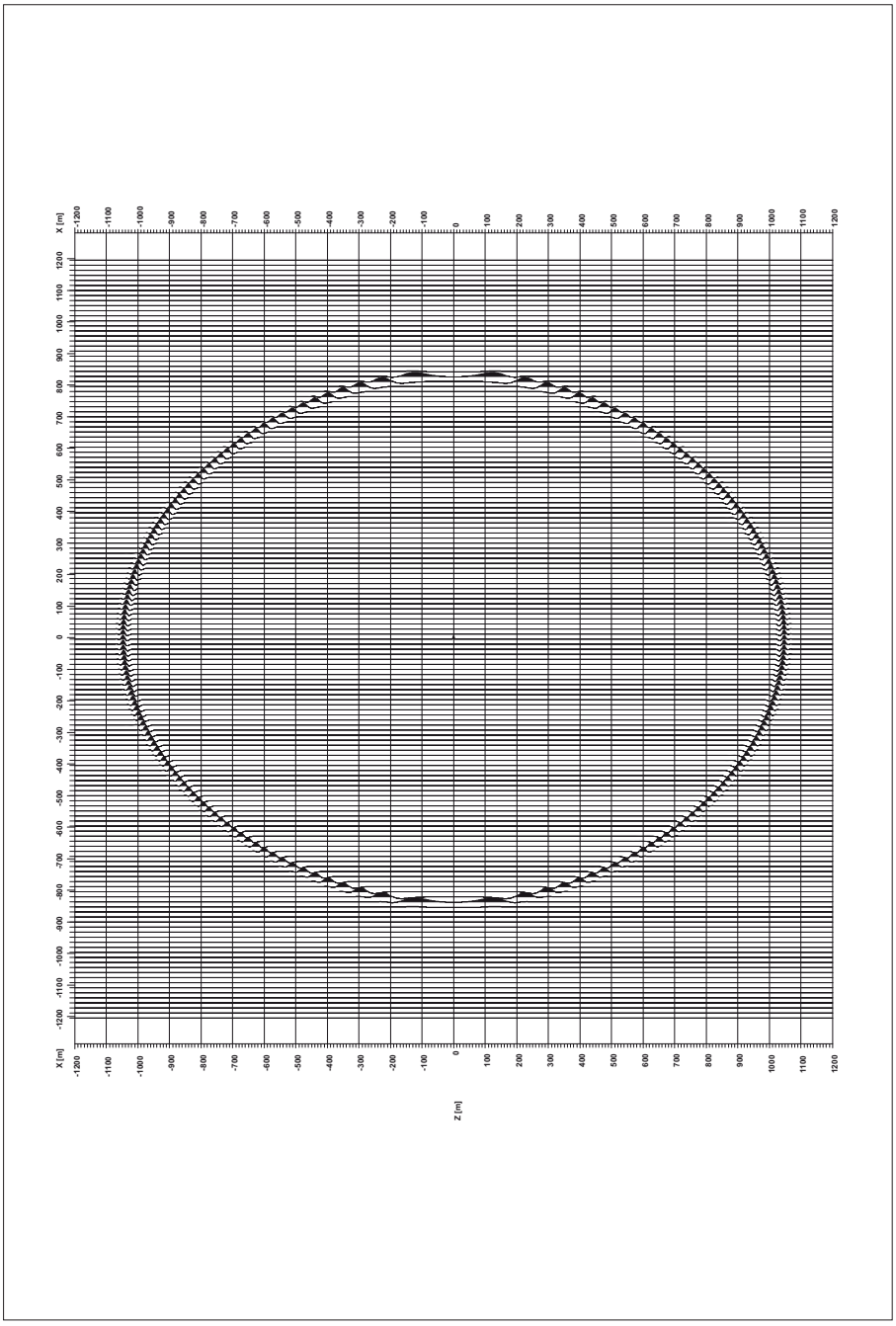

Fig. 2.38. Snapshot of spike wave propagation from algorithm (1.28) for parameters: $\varepsilon = 0.35$; $\delta = 0.1$ azimuthal angle $\Psi = 60°$; in moment time $t = 0.4$ s; steps of computation: $\Delta x = \Delta z = 4$ m, $\Delta t = 0.5$ ms

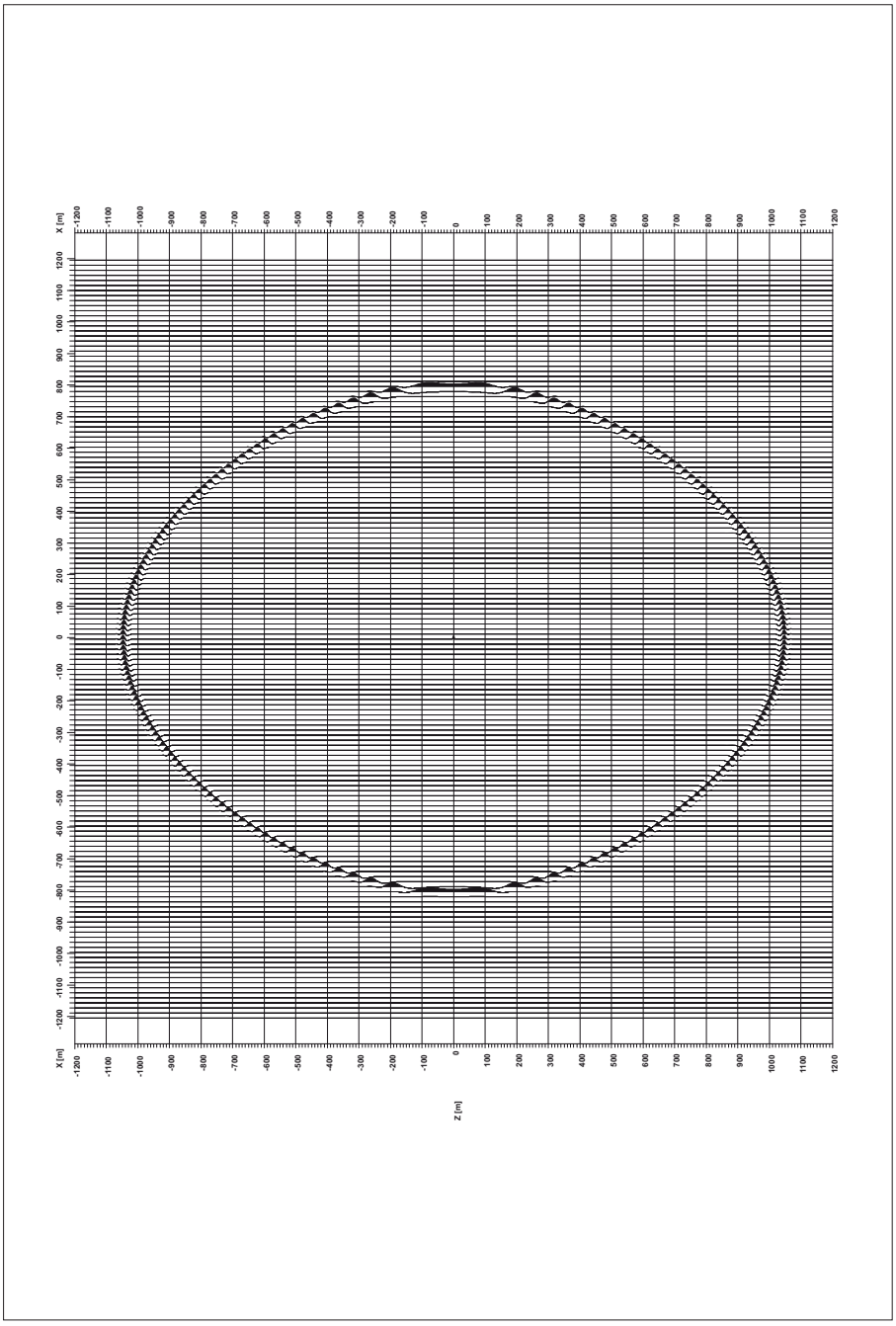

Fig. 2.39. Snapshot of spike wave propagation from algorithm (1.28) for parameters: $\varepsilon = 0.35$; $\delta = 0.1$ azimuthal angle $\Psi = 90°$; in moment time $t = 0.4$ s; steps of computation: $\Delta x = \Delta z = 4$ m, $\Delta t = 0.5$ ms

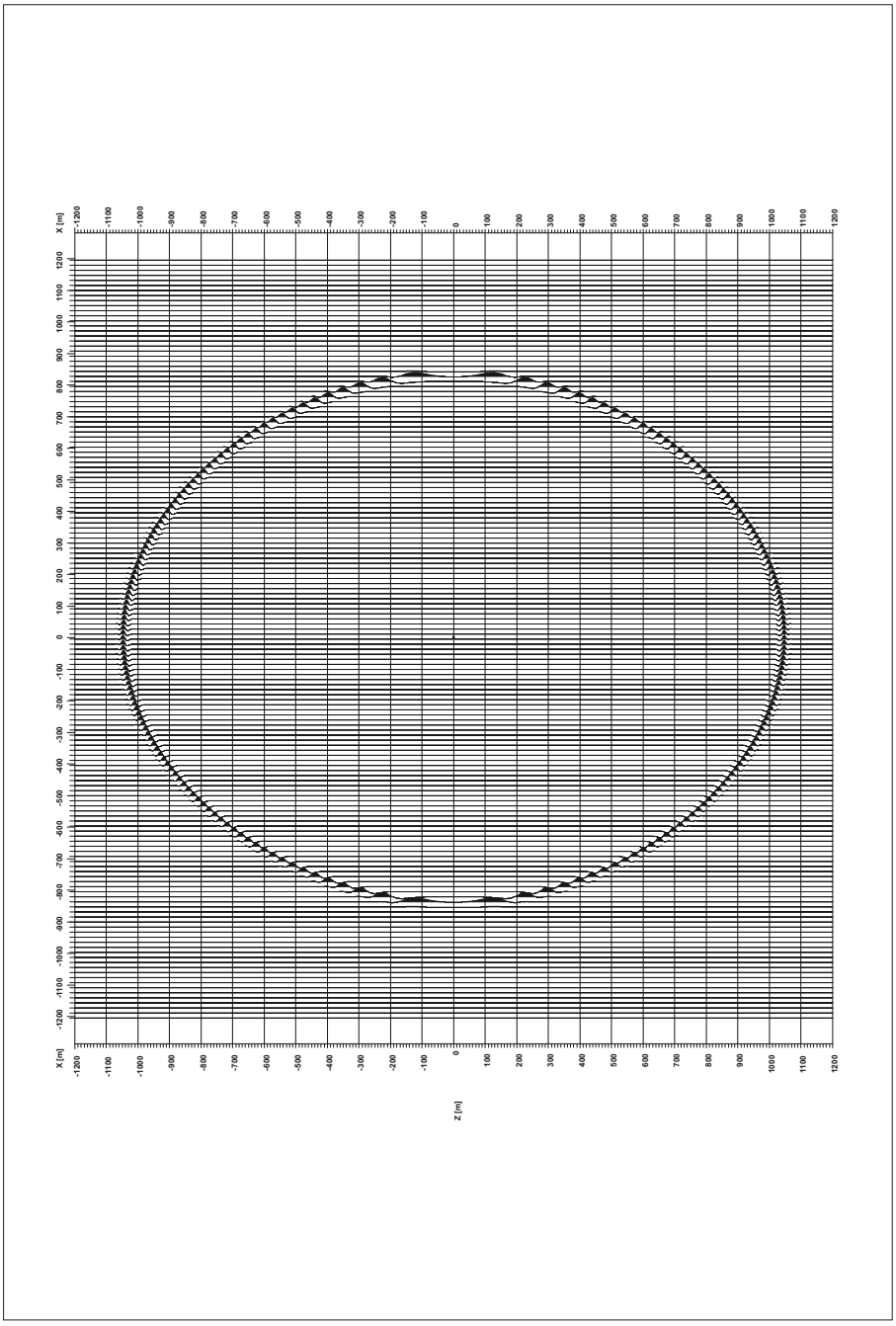

Fig. 2.40. Snapshot of spike wave propagation from algorithm (1.28) for parameters: $\varepsilon = 0.35$; $\delta = 0.1$ azimuthal angle $\Psi = 120°$; in moment time $t = 0.4$ s; steps of computation: $\Delta x = \Delta z = 4$ m, $\Delta t = 0.5$ ms

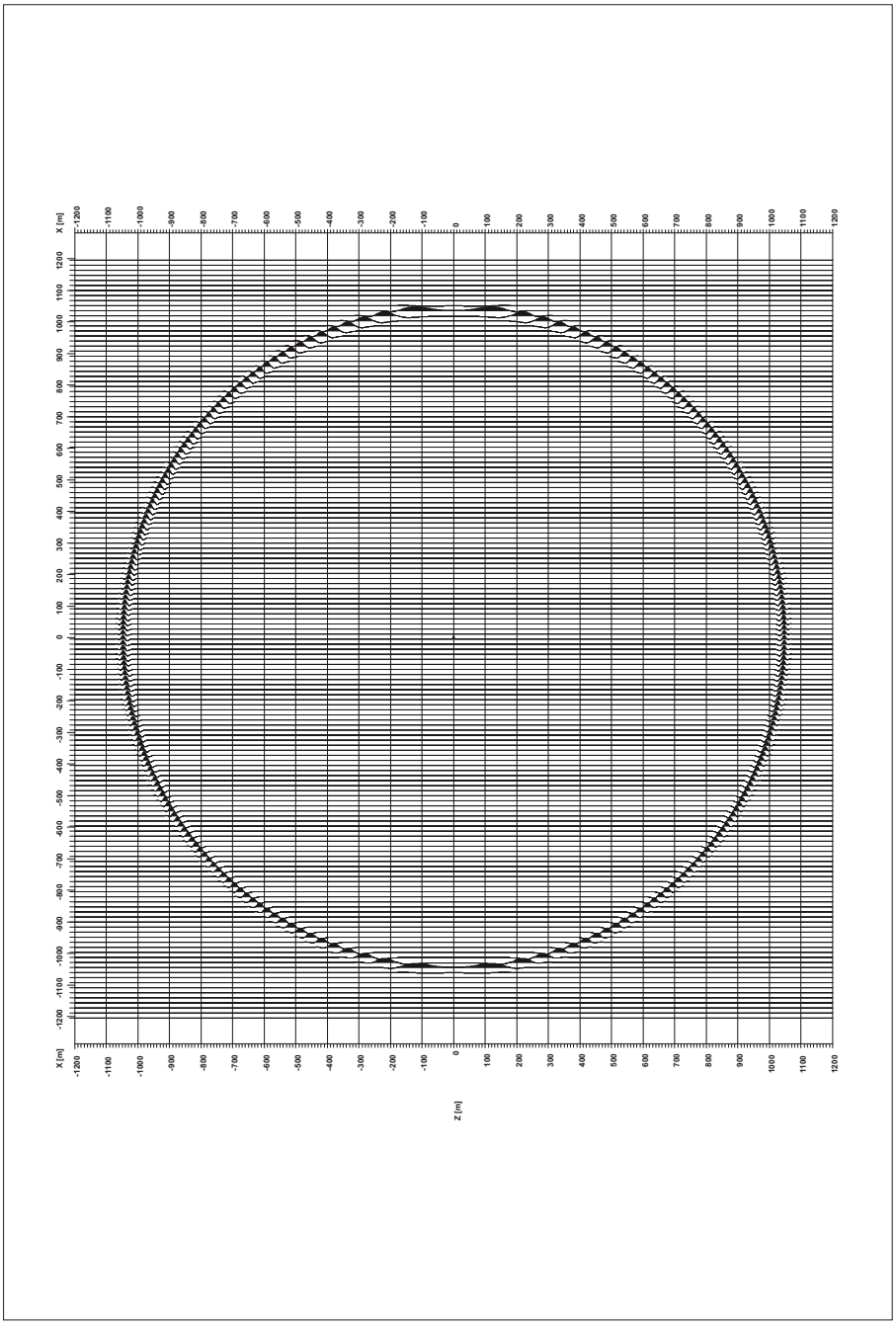

Fig. 2.41. Snapshot of spike wave propagation from algorithm (1.28) for parameters: $\varepsilon = 0.35$; $\delta = -0.1$ azimuthal angle $\Psi = 0°$; in moment time $t = 0.4$ s; steps of computation: $\Delta x = \Delta z = 4$ m, $\Delta t = 0.5$ ms

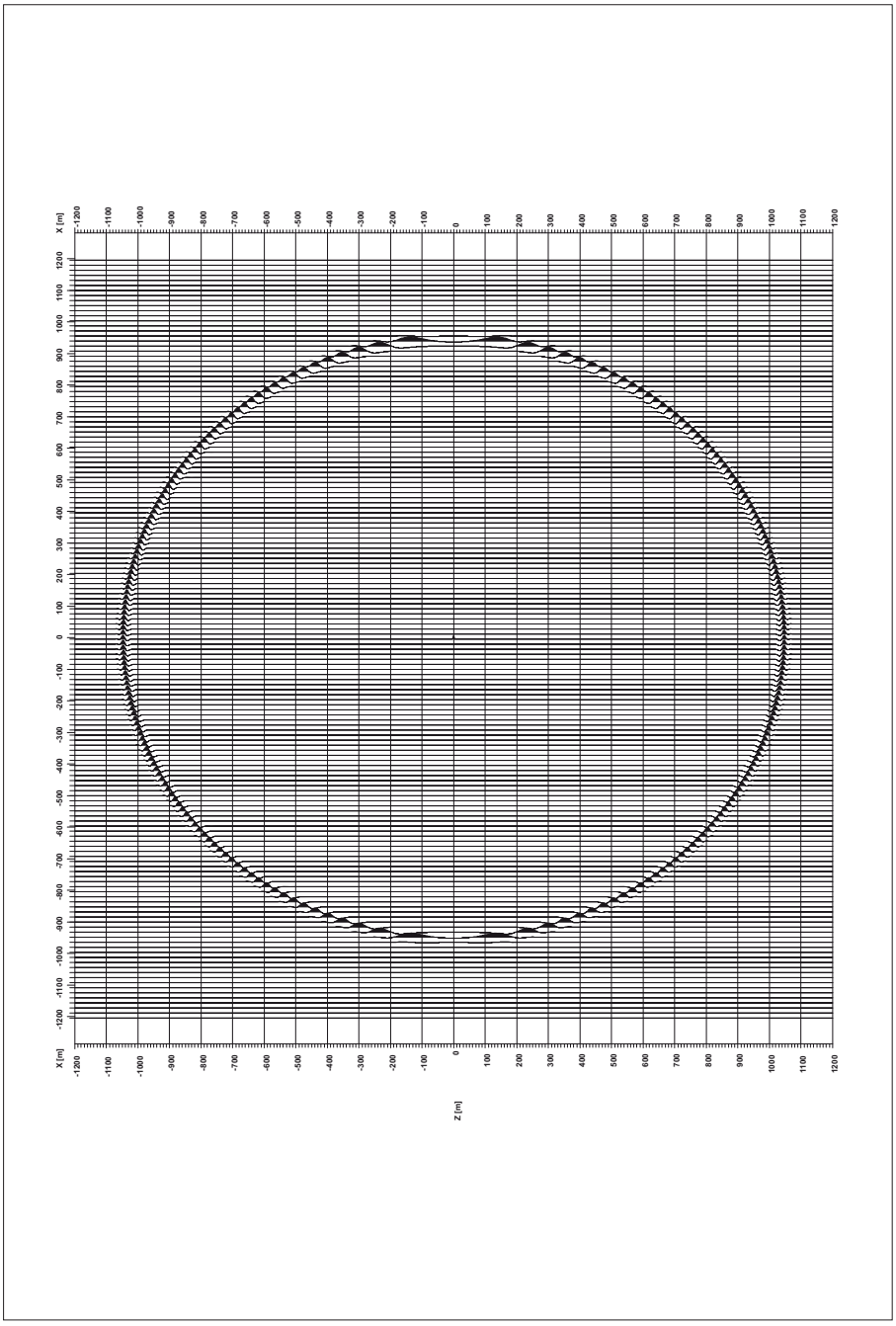

Fig. 2.42. Snapshot of spike wave propagation from algorithm (1.28) for parameters: $\varepsilon = 0.35$; $\delta = -0.1$ azimuthal angle $\Psi = 30°$; in moment time $t = 0.4$ s; steps of computation: $\Delta x = \Delta z = 4$ m, $\Delta t = 0.5$ ms

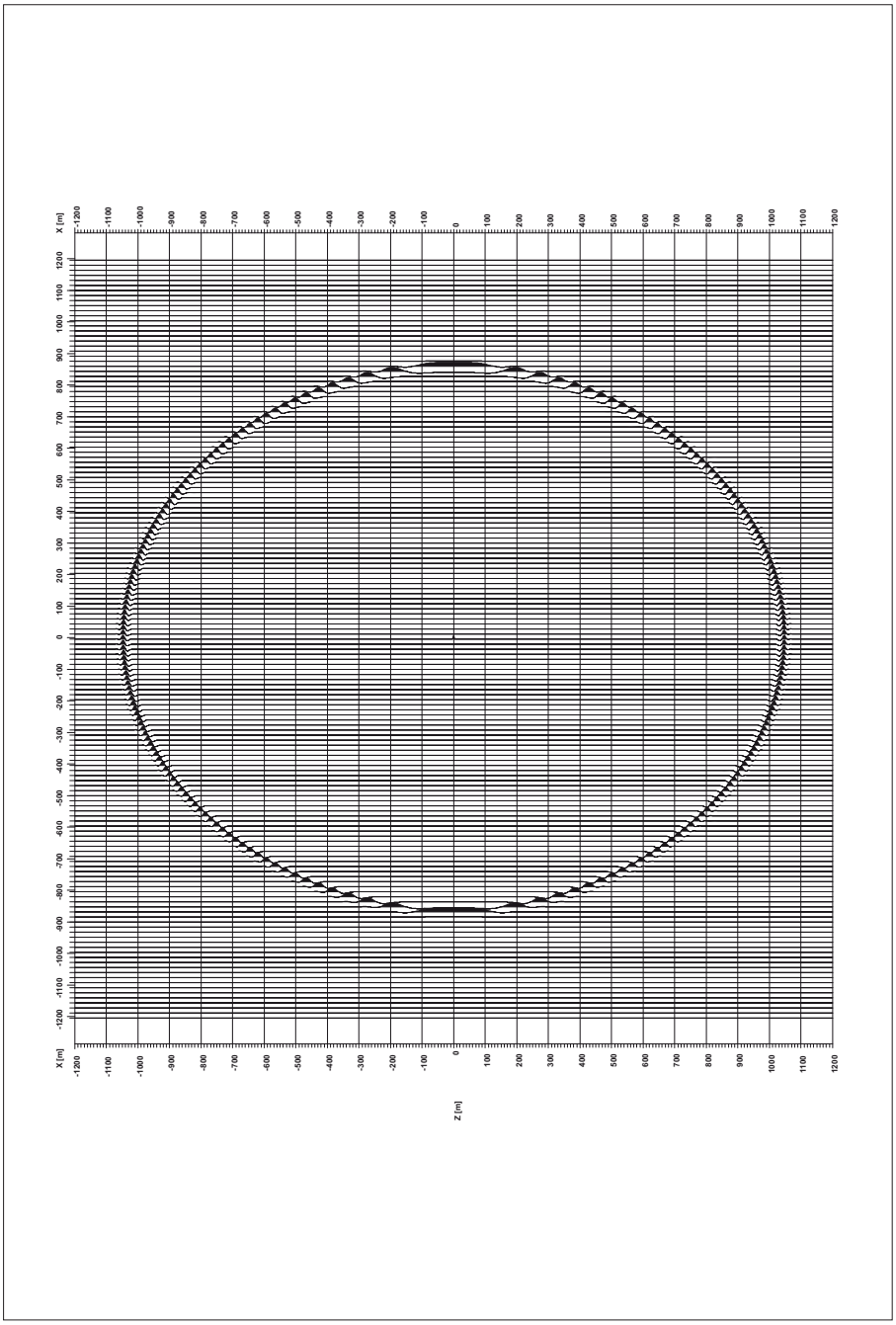

Fig. 2.43. Snapshot of spike wave propagation from algorithm (1.28) for parameters: $\varepsilon = 0.35$; $\delta = -0.1$ azimuthal angle $\Psi = 45°$; in moment time $t = 0.4$ s; steps of computation: $\Delta x = \Delta z = 4$ m, $\Delta t = 0.5$ ms

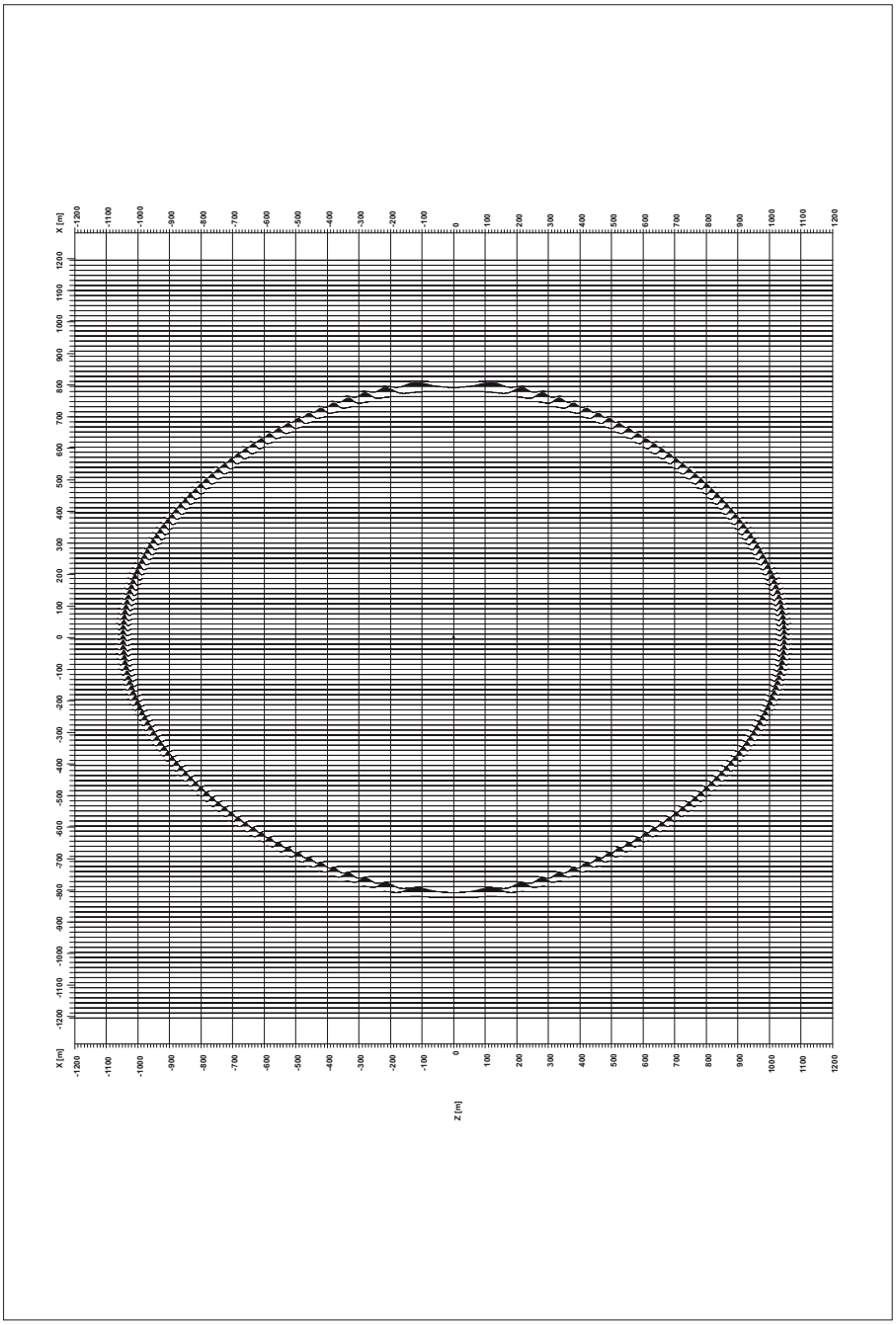

Fig. 2.44. Snapshot of spike wave propagation from algorithm (1.28) for parameters: $\varepsilon = 0.35$; $\delta = -0.1$ azimuthal angle $\Psi = 60°$; in moment time $t = 0.4$ s; steps of computation: $\Delta x = \Delta z = 4$ m, $\Delta t = 0.5$ ms

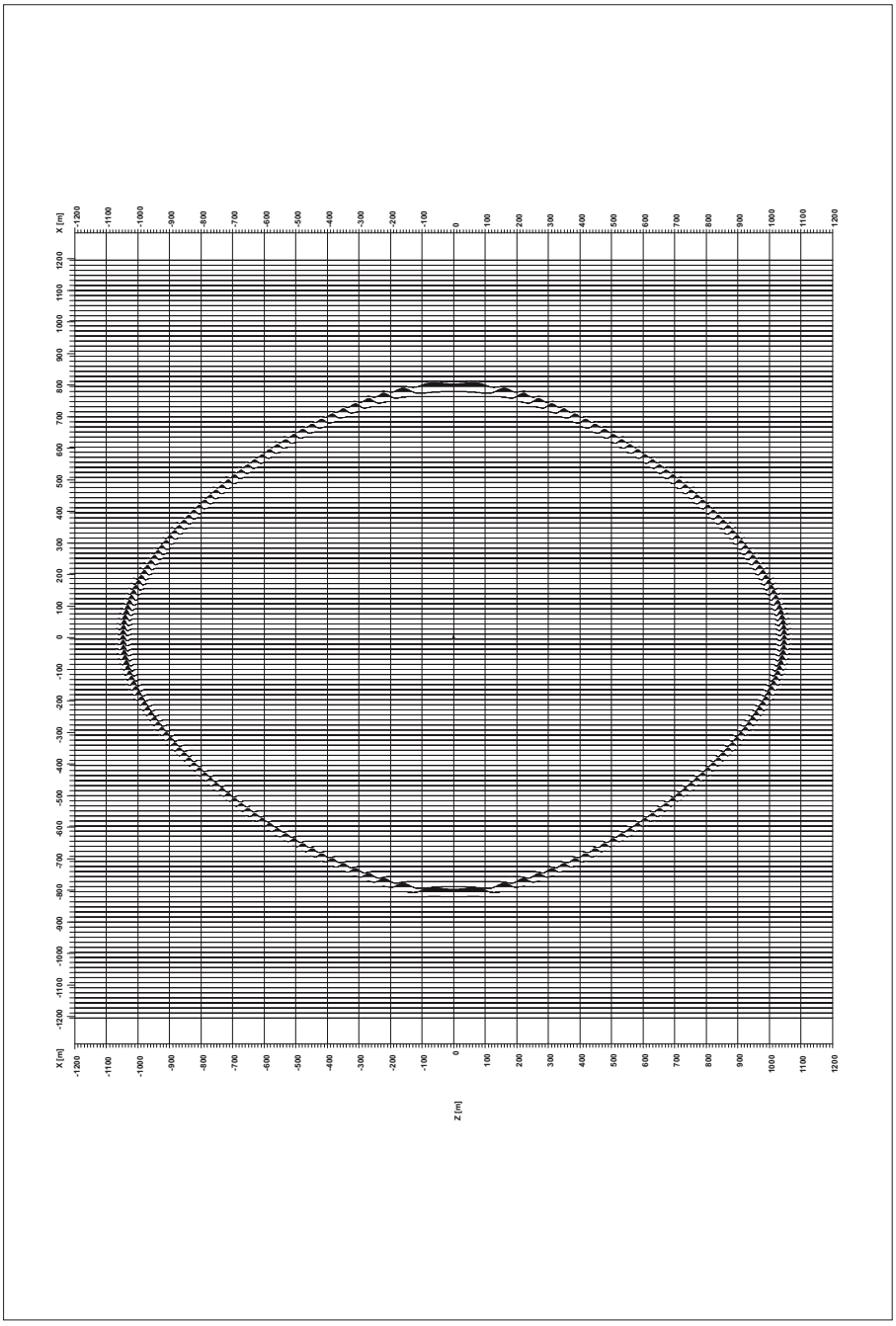

Fig. 2.45. Snapshot of spike wave propagation from algorithm (1.28) for parameters: $\varepsilon = 0.35$; $\delta = -0.1$ azimuthal angle $\Psi = 90°$; in moment time $t = 0.4$ s; steps of computation: $\Delta x = \Delta z = 4$ m, $\Delta t = 0.5$ ms

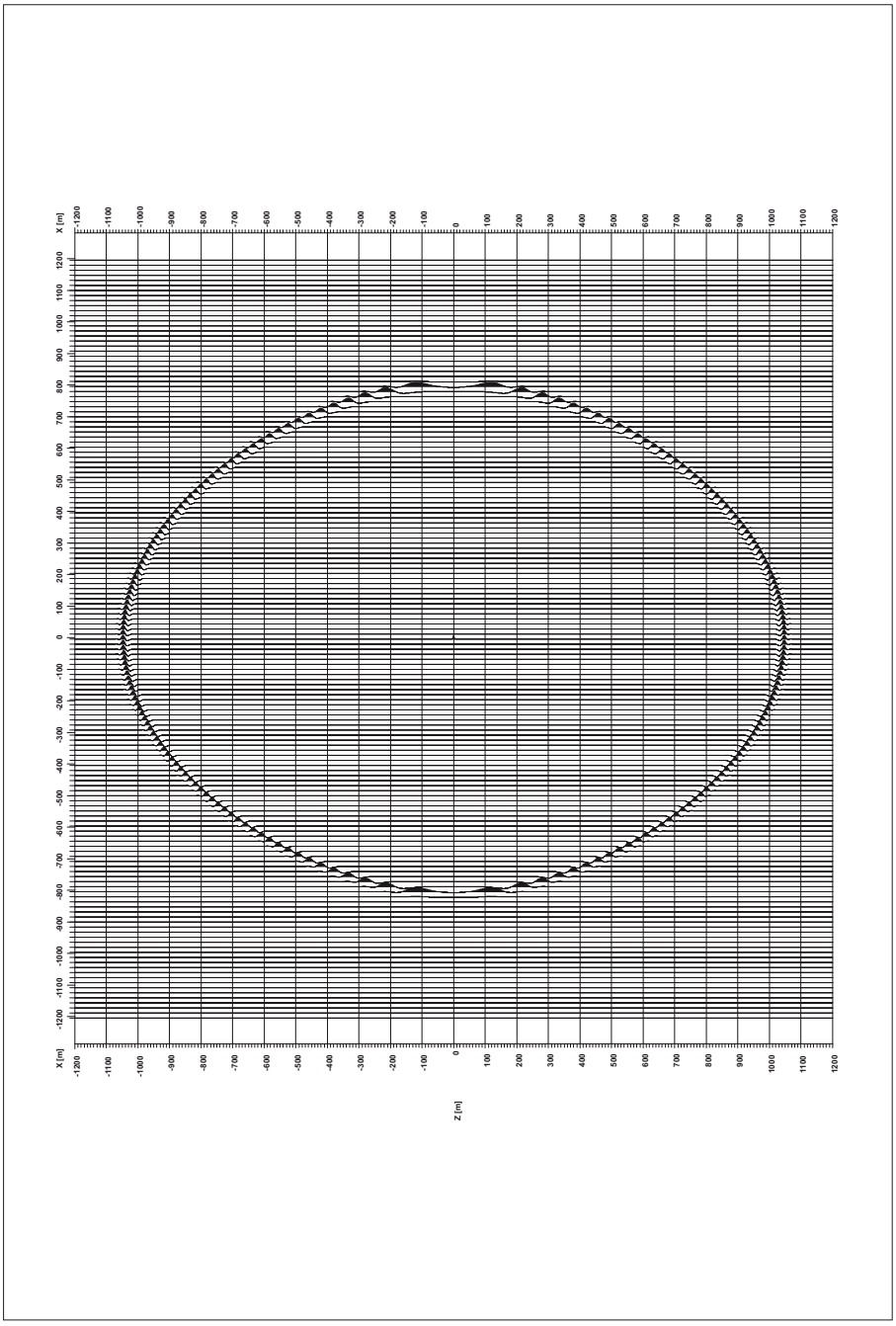

Fig. 2.46. Snapshot of spike wave propagation from algorithm (1.28) for parameters: $\varepsilon = 0.35$; $\delta = -0.1$ azimuthal angle $\Psi = 120°$; in moment time $t = 0.4$ s; steps of computation: $\Delta x = \Delta z = 4$ m, $\Delta t = 0.5$ ms

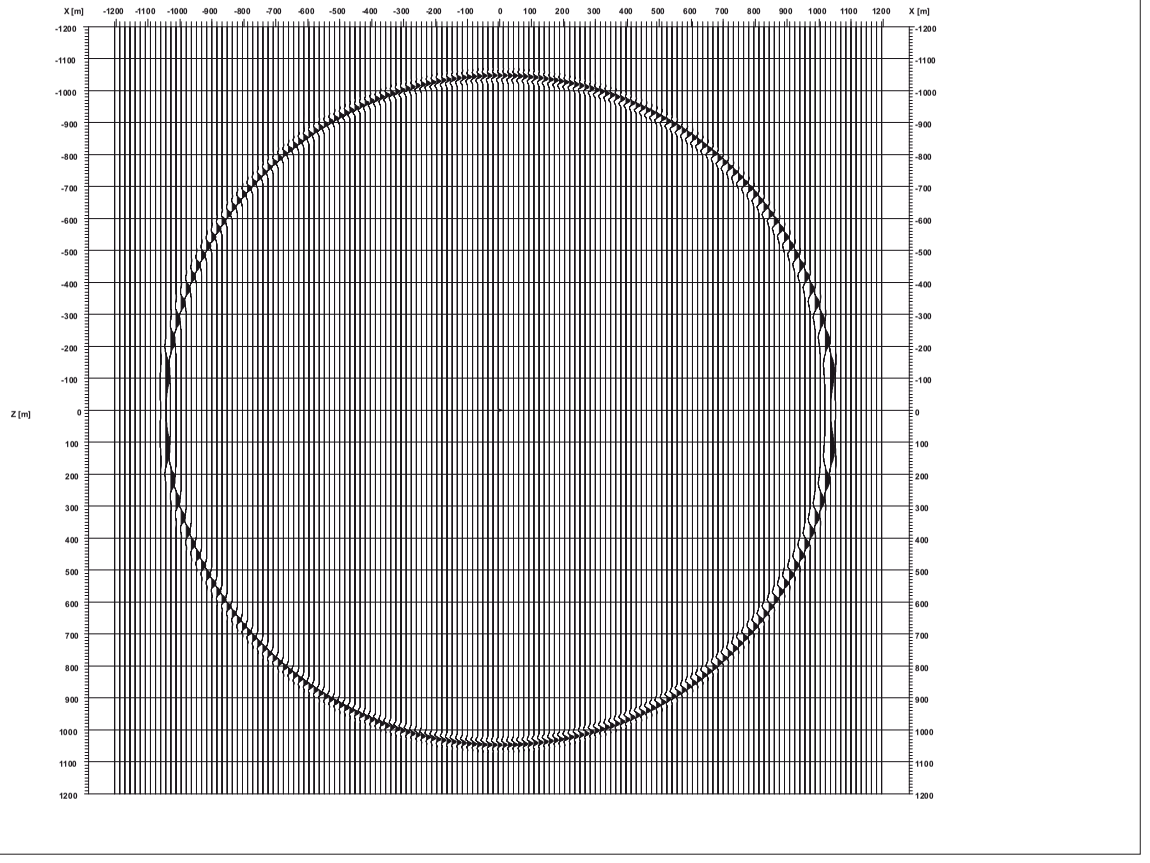

Fig. 2.47. Snapshot of spike wave propagation from algorithm (1.23) for parameters: $\varepsilon = 0.35$; $\delta = 0.1$ azimuthal angle $\Psi = 0°$; in moment time $t = 0.4$ s; steps of computation: $\Delta x = \Delta z = 4$ m, $\Delta t = 0.5$ ms

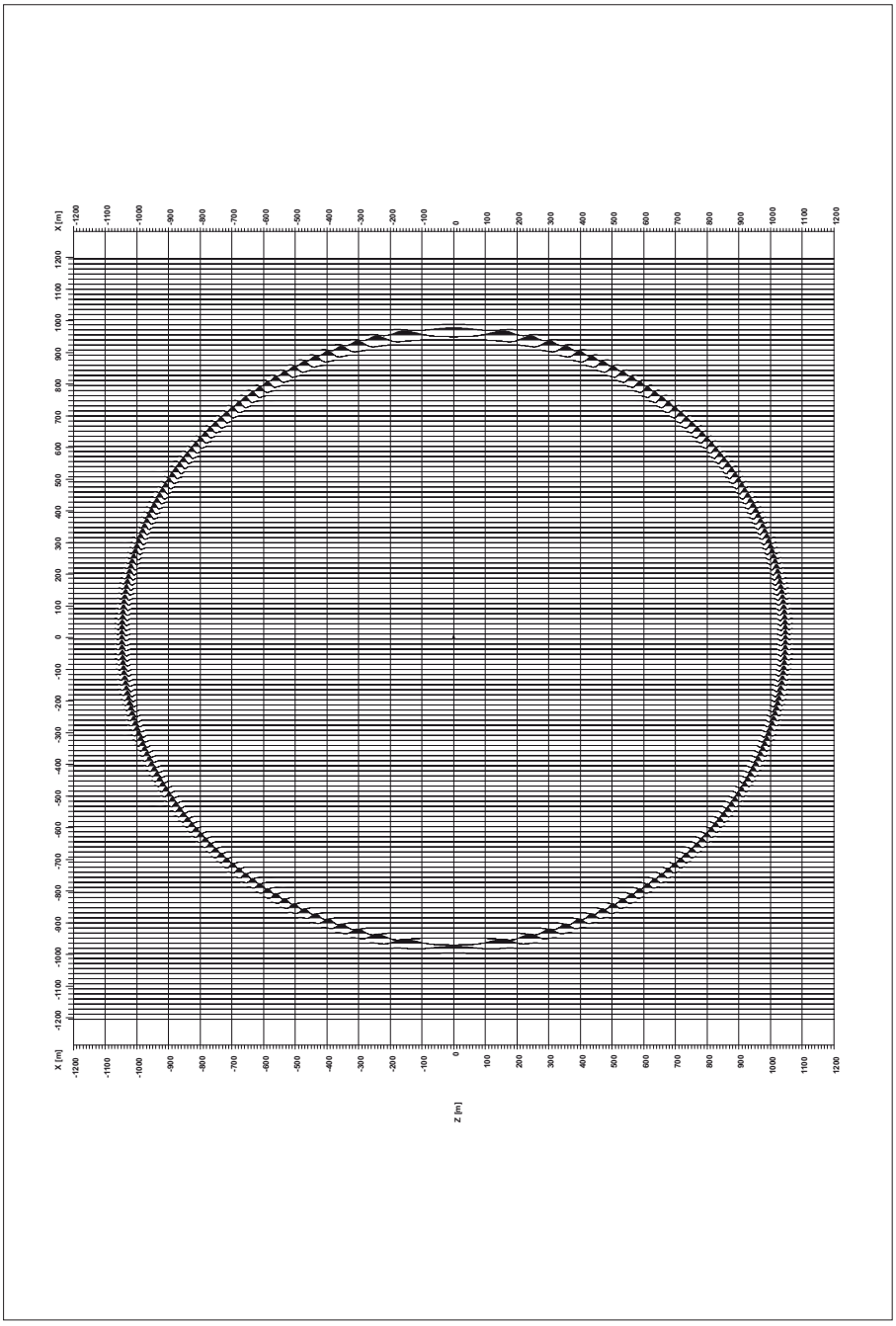

Fig. 2.48. Snapshot of spike wave propagation from algorithm (1.23) for parameters: $\varepsilon = 0.35$; $\delta = 0.1$ azimuthal angle $\Psi = 30°$; in moment time $t = 0.4$ s; steps of computation: $\Delta x = \Delta z = 4$ m, $\Delta t = 0.5$ ms

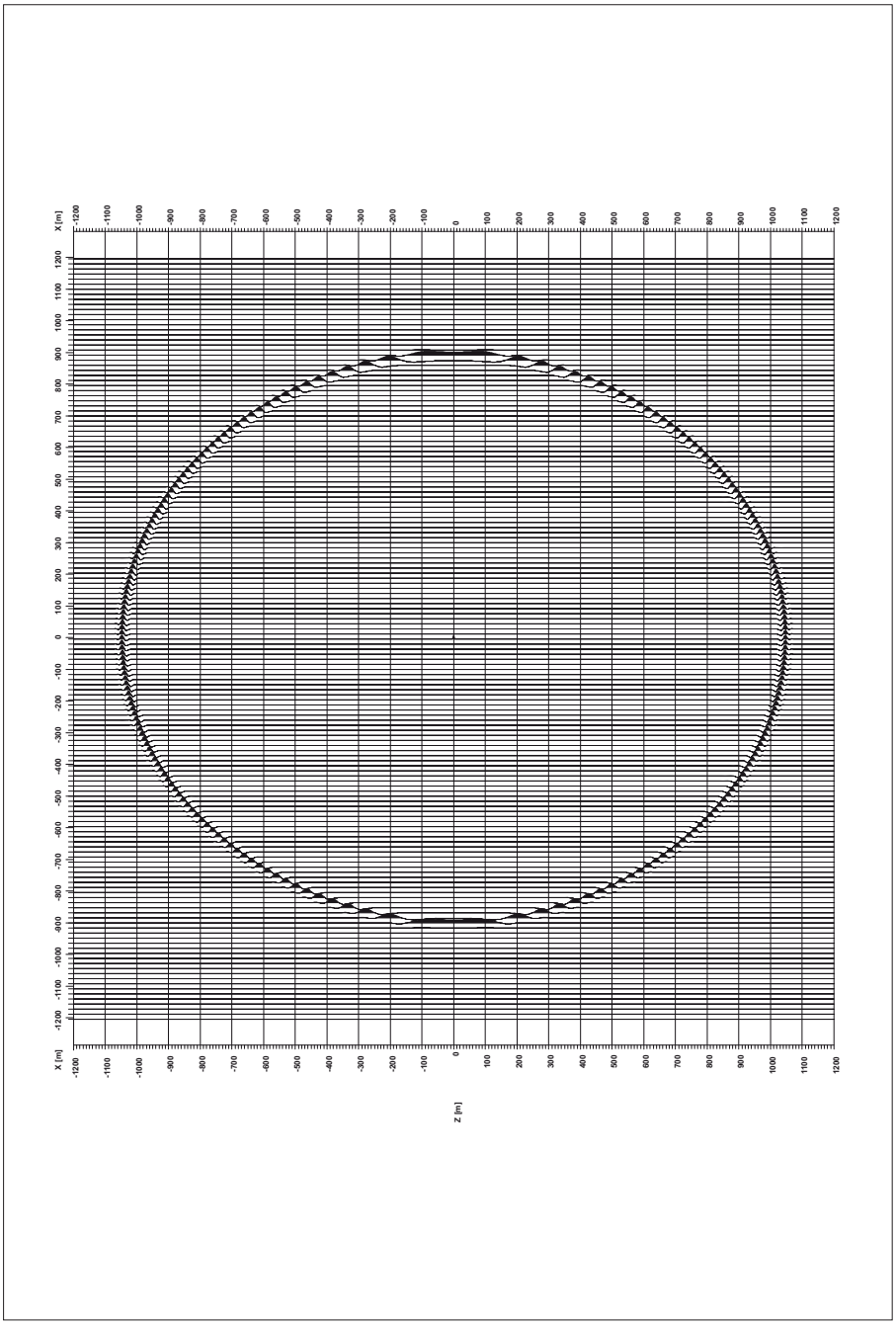

Fig. 2.49. Snapshot of spike wave propagation from algorithm (1.23) for parameters: $\varepsilon = 0.35$; $\delta = 0.1$ azimuthal angle $\Psi = 45°$; in moment time $t = 0.4$ s; steps of computation: $\Delta x = \Delta z = 4$ m, $\Delta t = 0.5$ ms

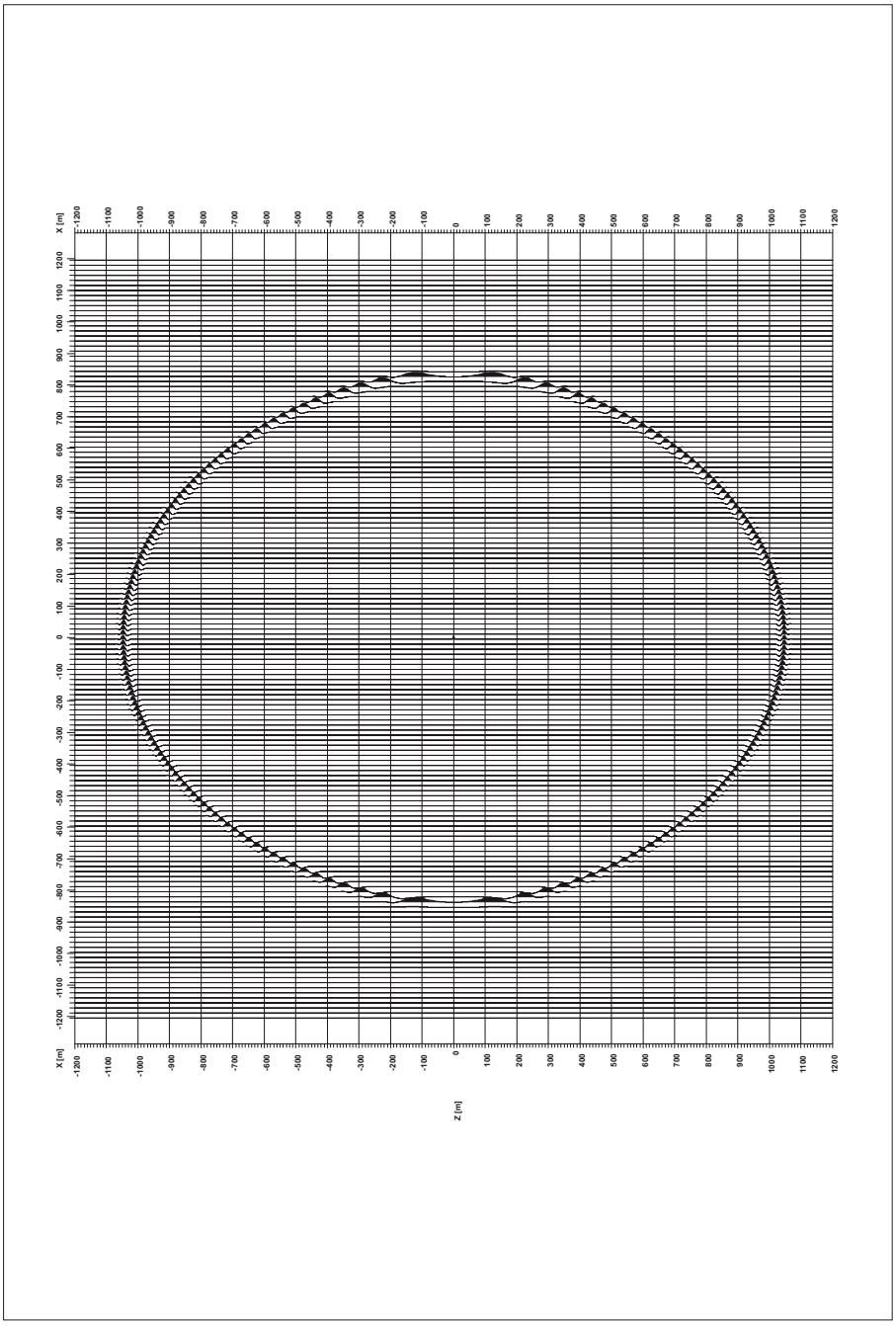

Fig. 2.50. Snapshot of spike wave propagation from algorithm (1.23) for parameters: $\varepsilon = 0.35$; $\delta = 0.1$ azimuthal angle $\Psi = 60°$; in moment time $t = 0.4$ s; steps of computation: $\Delta x = \Delta z = 4$ m, $\Delta t = 0.5$ ms

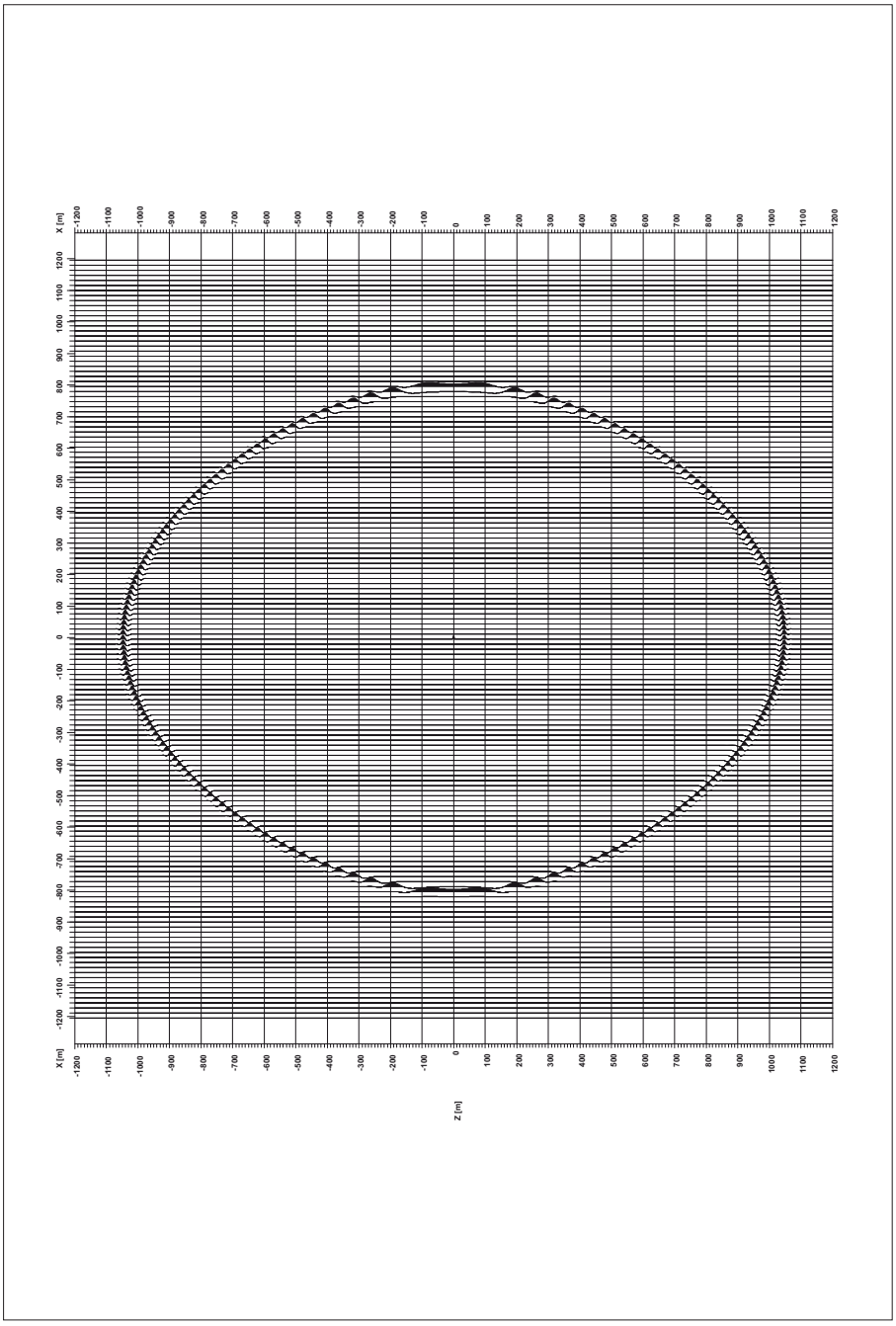

Fig. 2.51. Snapshot of spike wave propagation from algorithm (1.23) for parameters: $\varepsilon = 0.35$; $\delta = 0.1$ azimuthal angle $\Psi = 90°$; in moment time $t = 0.4$ s; steps of computation: $\Delta x = \Delta z = 4$ m, $\Delta t = 0.5$ ms

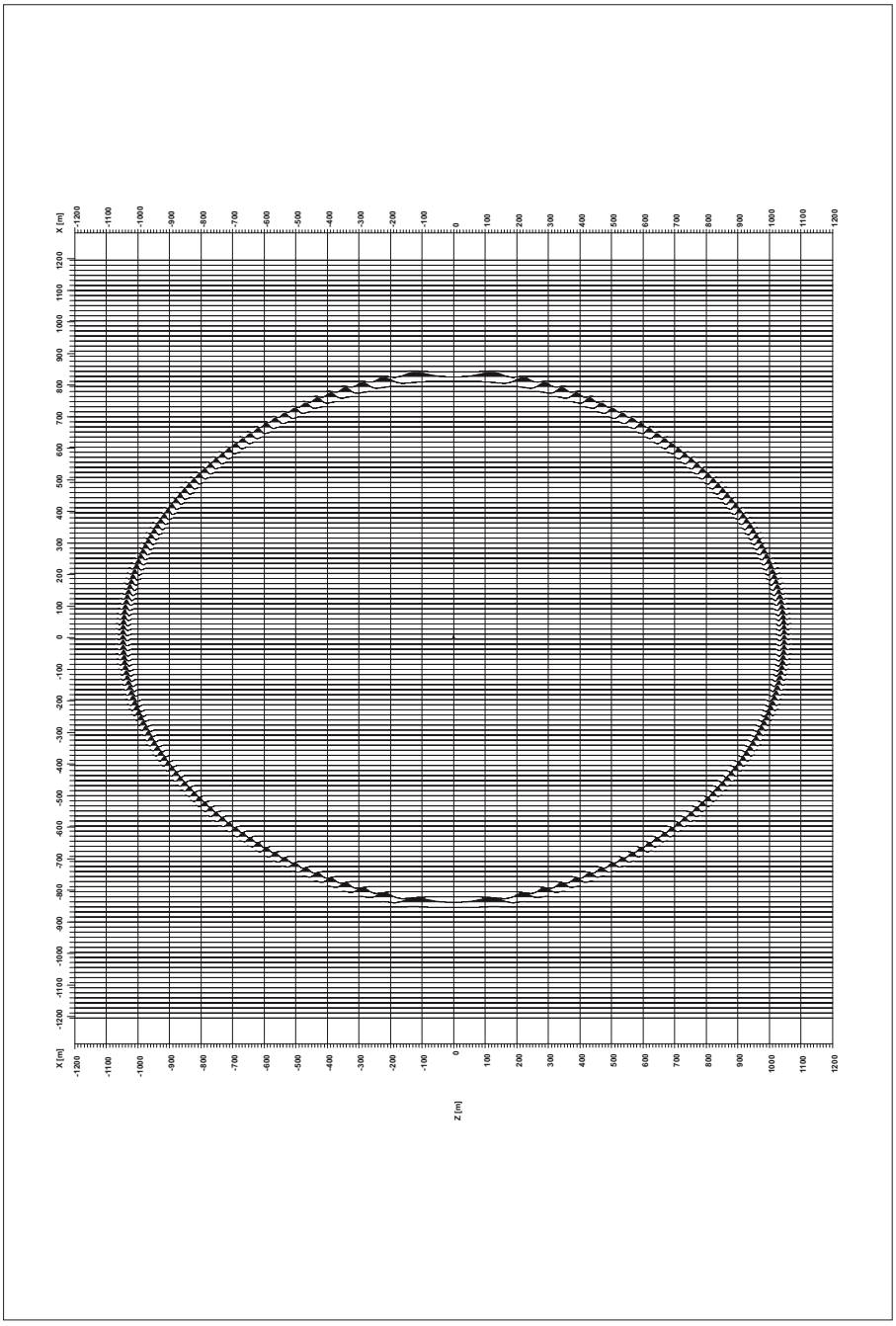

Fig. 2.52. Snapshot of spike wave propagation from algorithm (1.23) for parameters: $\varepsilon = 0.35$; $\delta = 0.1$ azimuthal angle $\Psi = 120°$; in moment time $t = 0.4$ s; steps of computation: $\Delta x = \Delta z = 4$ m, $\Delta t = 0.5$ ms

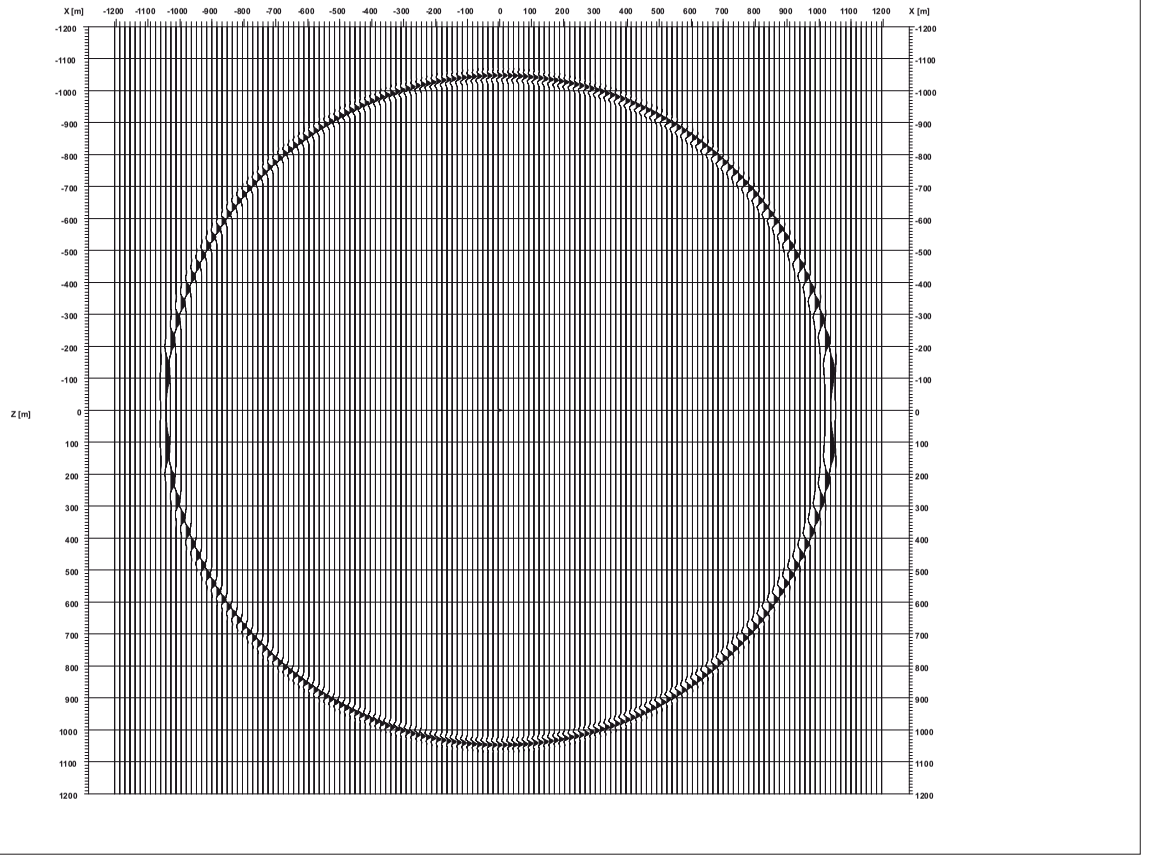

Fig. 2.53. Snapshot of spike wave propagation from algorithm (1.23) for parameters: $\varepsilon = 0.35$; $\delta = -0.1$ azimuthal angle $\Psi = 0°$; in moment time $t = 0.4$ s; steps of computation: $\Delta x = \Delta z = 4$ m, $\Delta t = 0.5$ ms

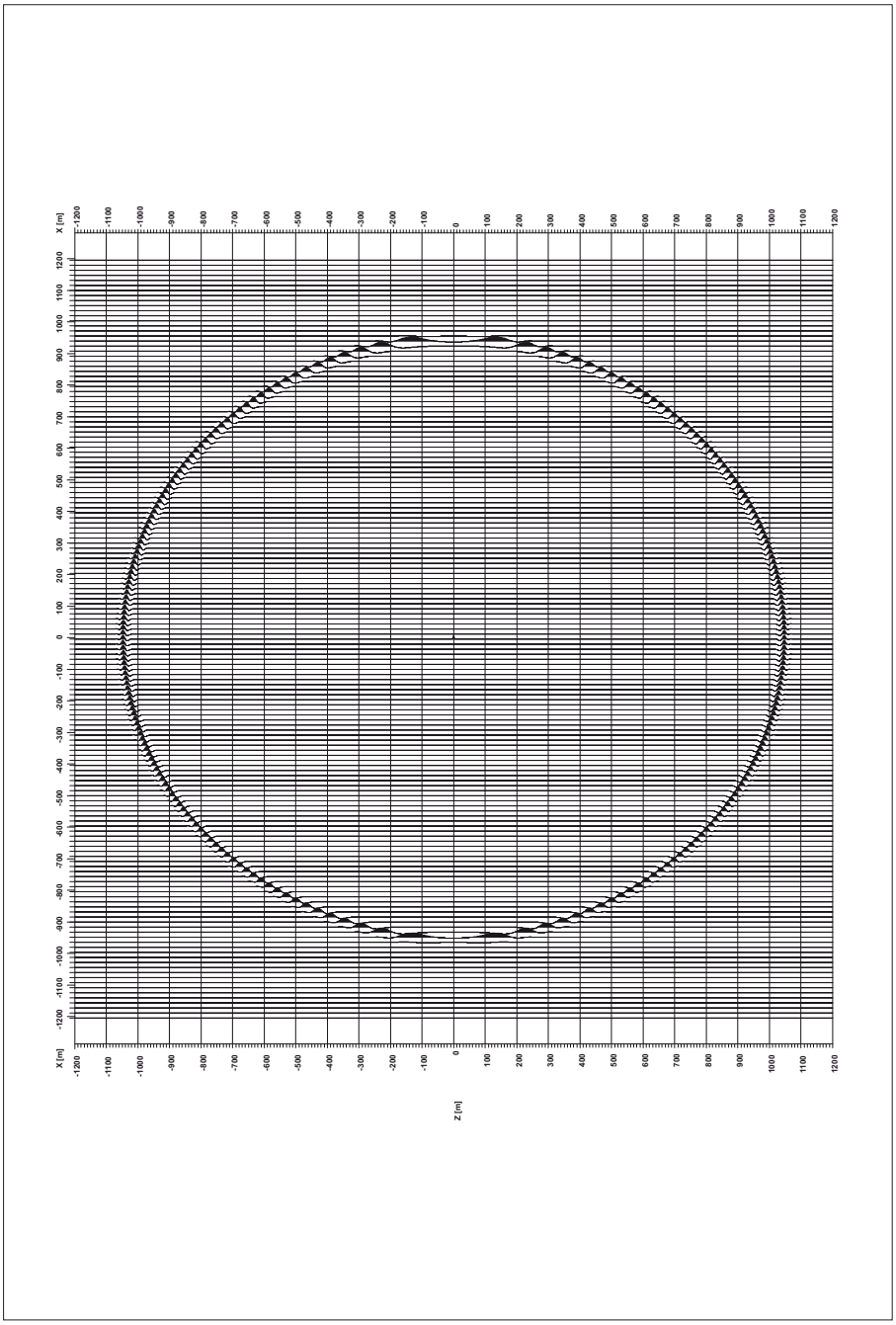

Fig. 2.54. Snapshot of spike wave propagation from algorithm (1.23) for parameters: $\varepsilon = 0.35$; $\delta = -0.1$ azimuthal angle $\Psi = 30°$; in moment time $t = 0.4$ s; steps of computation: $\Delta x = \Delta z = 4$ m, $\Delta t = 0.5$ ms

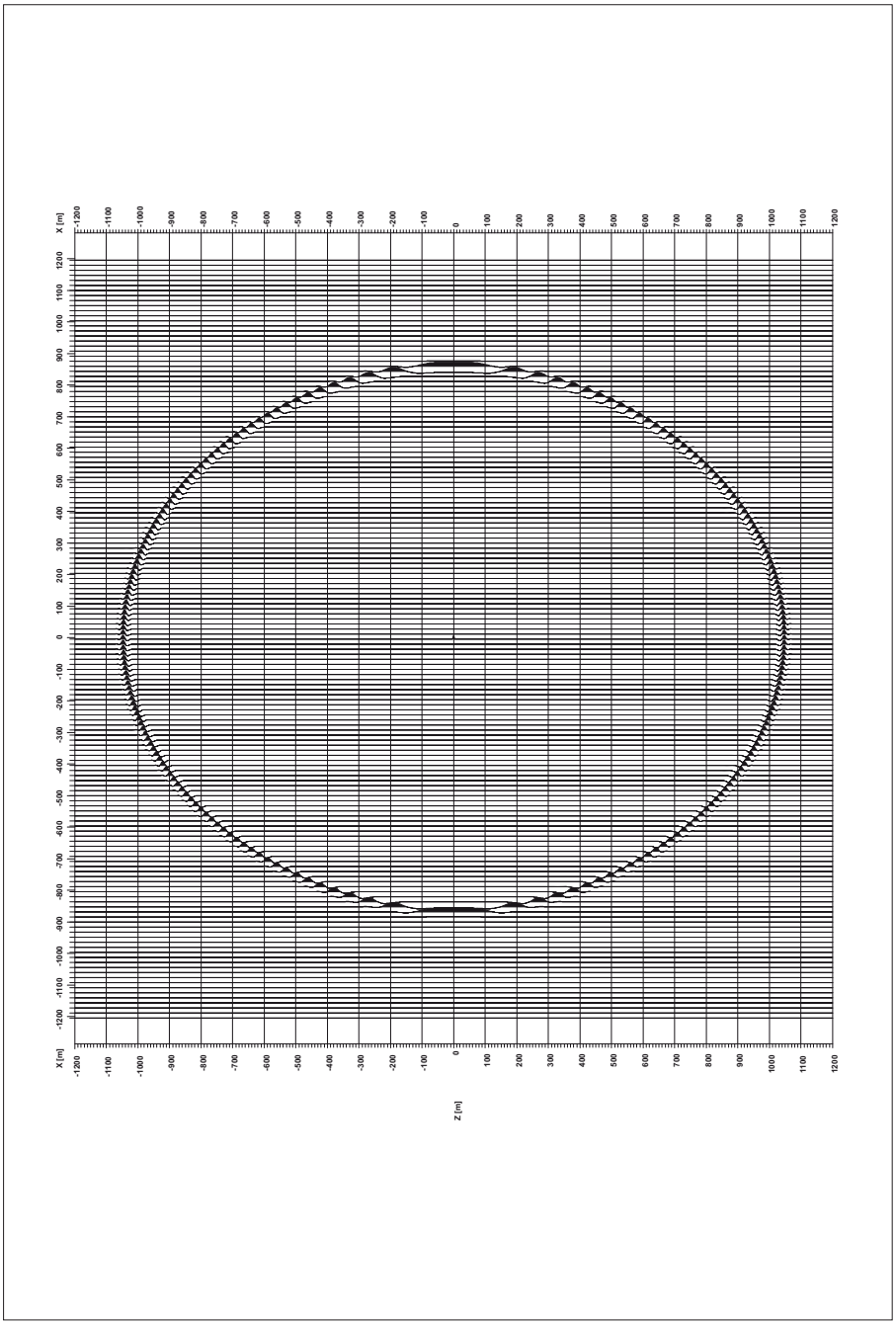

Fig. 2.55. Snapshot of spike wave propagation from algorithm (1.23) for parameters: $\varepsilon = 0.35$; $\delta = -0.1$ azimuthal angle $\Psi = 45°$; in moment time $t = 0.4$ s; steps of computation: $\Delta x = \Delta z = 4$ m, $\Delta t = 0.5$ ms

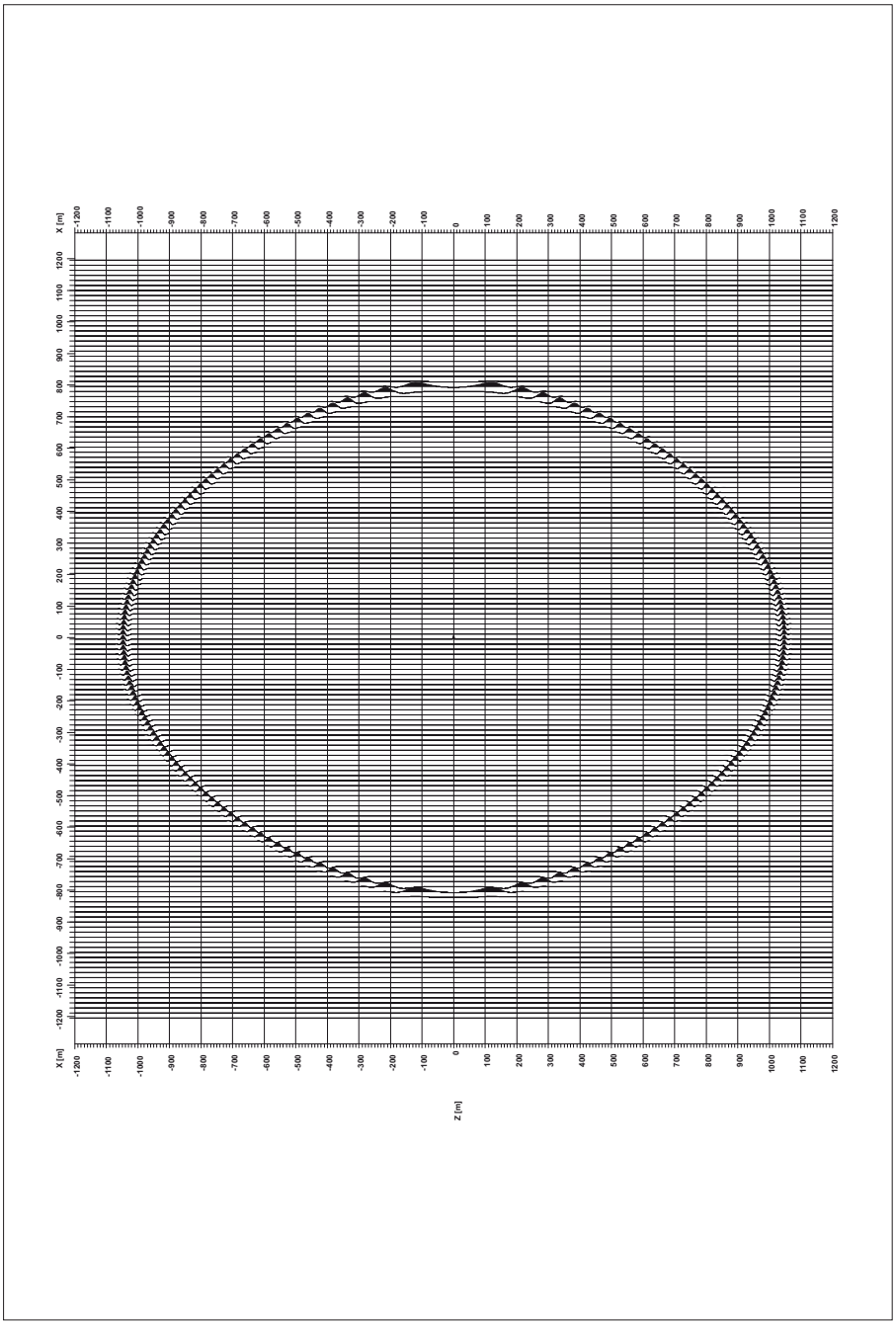

Fig. 2.56. Snapshot of spike wave propagation from algorithm (1.23) for parameters: $\varepsilon = 0.35$; $\delta = -0.1$ azimuthal angle $\Psi = 60°$; in moment time $t = 0.4$ s; steps of computation: $\Delta x = \Delta z = 4$ m, $\Delta t = 0.5$ ms

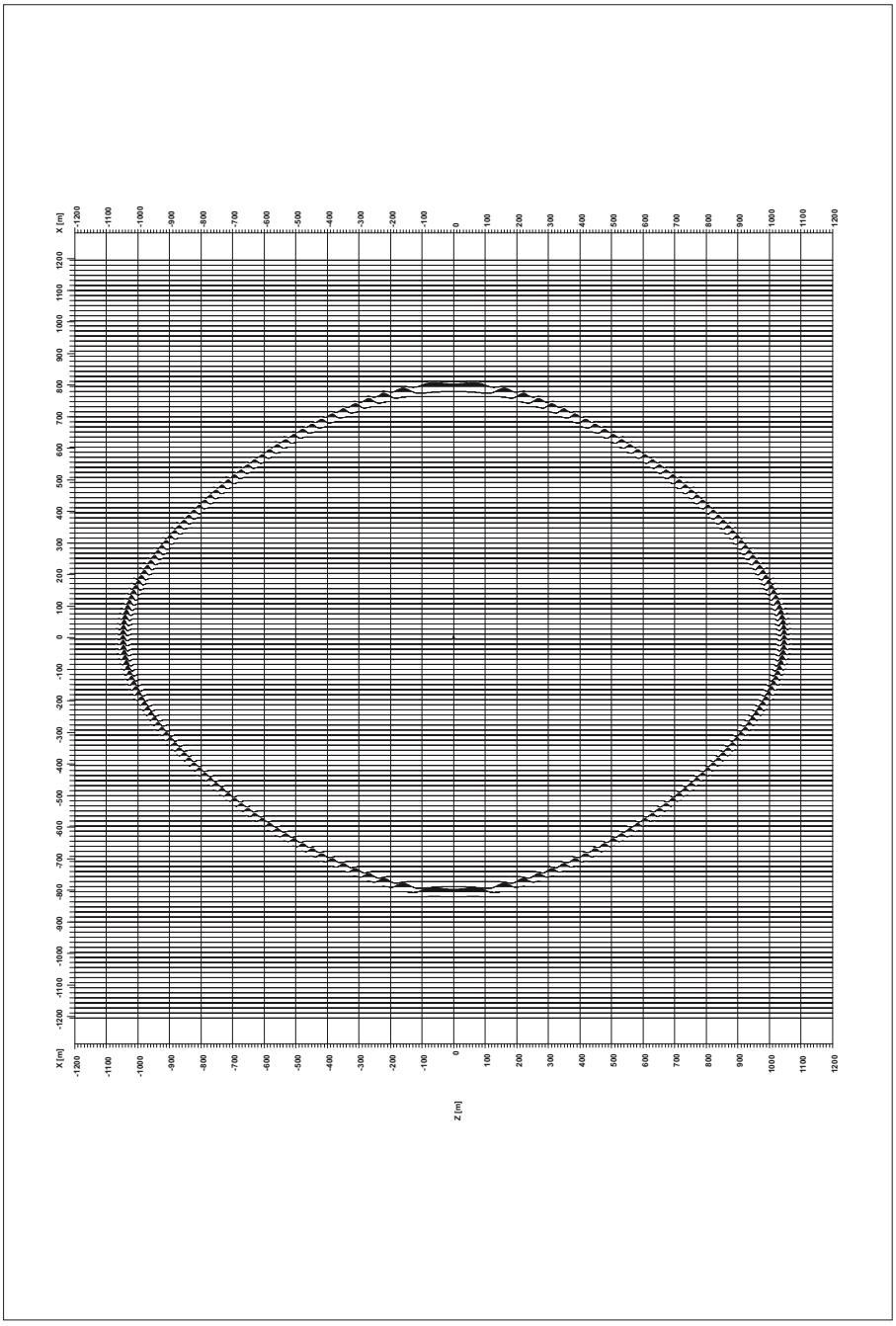

Fig. 2.57. Snapshot of spike wave propagation from algorithm (1.23) for parameters: $\varepsilon = 0.35$; $\delta = -0.1$ azimuthal angle $\Psi = 90°$; in moment time $t = 0.4$ s; steps of computation: $\Delta x = \Delta z = 4$ m, $\Delta t = 0.5$ ms

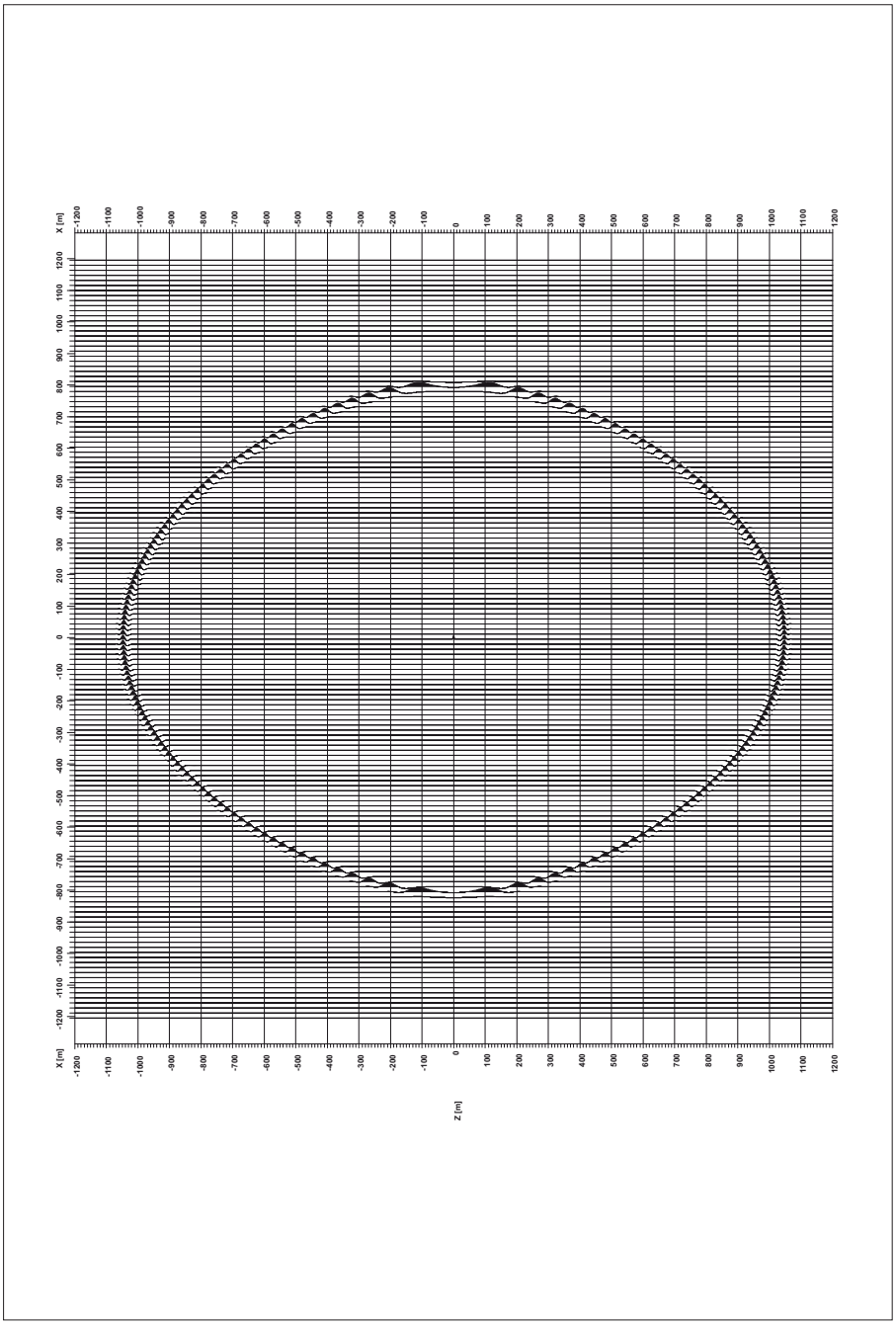

Fig. 2.58. Snapshot of spike wave propagation from algorithm (1.23) for parameters: $\varepsilon = 0.35$; $\delta = -0.1$ azimuthal angle $\Psi = 120°$; in moment time $t = 0.4$ s; steps of computation: $\Delta x = \Delta z = 4$ m, $\Delta t = 0.5$ ms

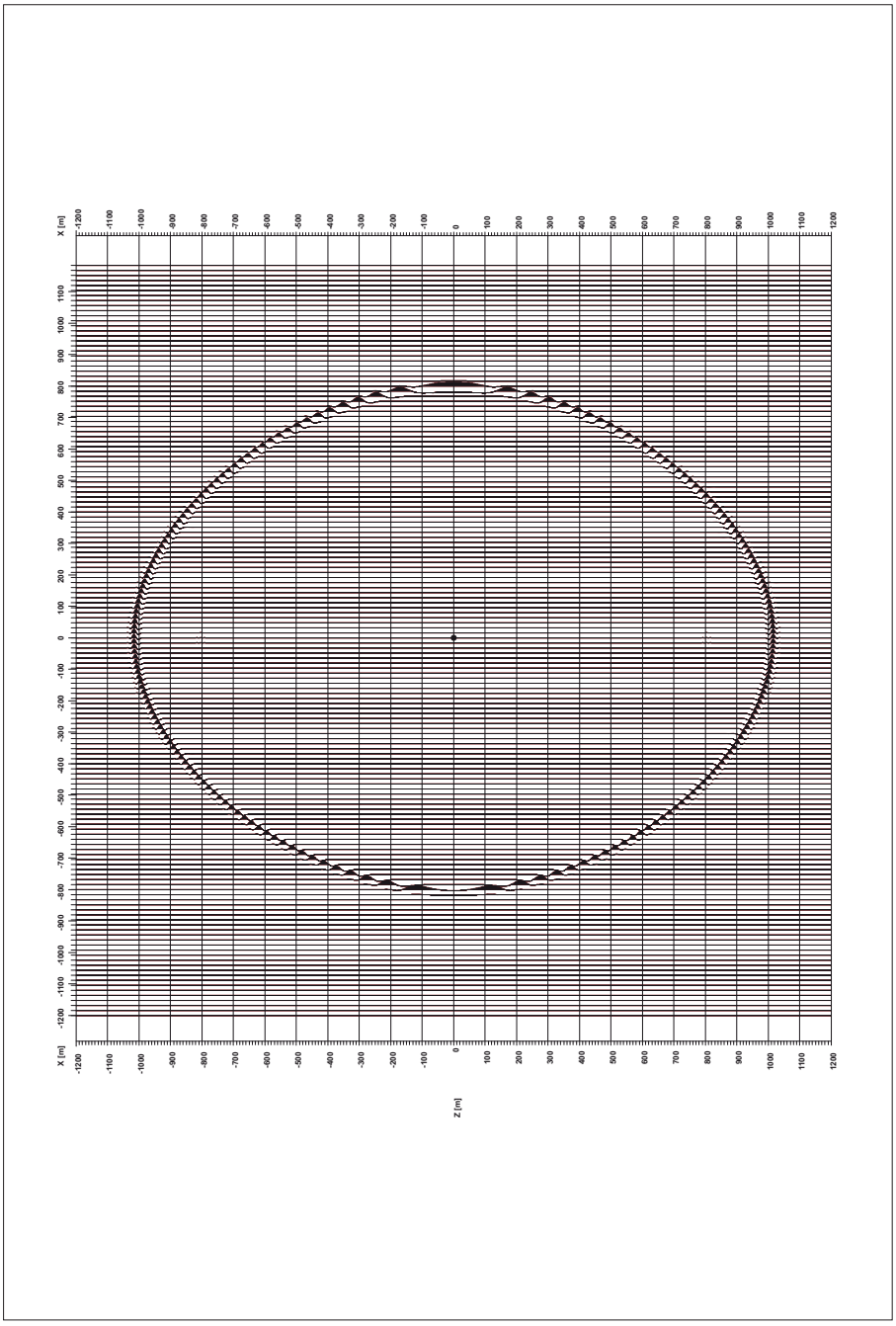

Fig. 2.59. Comparison of (1.29) and (1.28) for $\Psi = 90°$; anisotropy parameters: $\varepsilon = 0.3$; $\delta = 0.1$; in moment time $t = 0.4$ s. Version (1.29) in red color full covered by image of version (1.28). Steps of computations: $\Delta x = \Delta z = 4$ m, $\Delta t = 0.5$ ms

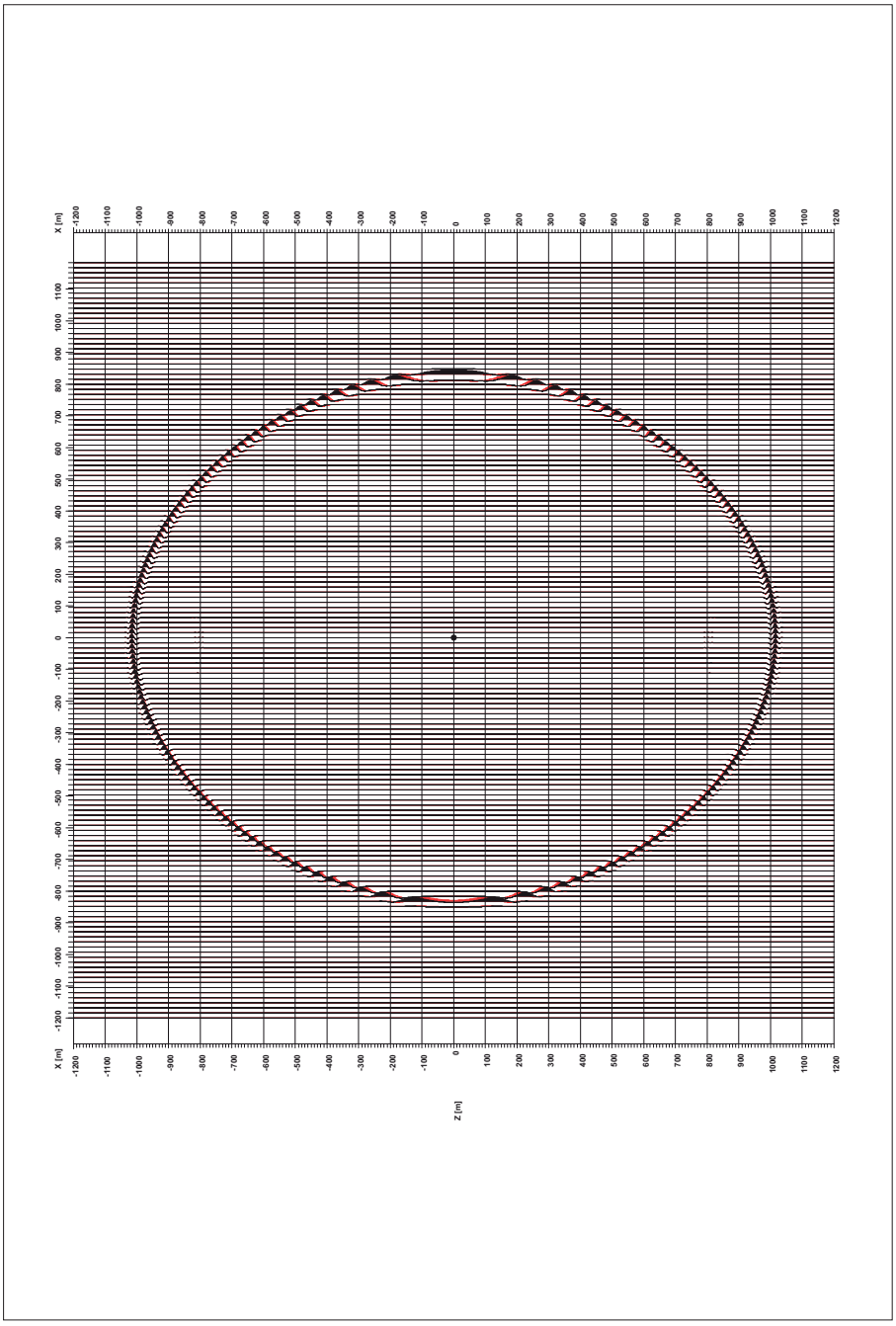

Fig. 2.60. Comparison of the versions (1.29) and (1.28) for $\Psi = 60°$; anisotropy parameters: $\varepsilon = 0.3$; $\delta = 0.1$; in moment time $t = 0.4$ s. The version (1.29) in red color differ slightly from image (1.28). Steps of computations: $\Delta x = \Delta z = 4$ m, $\Delta t = 0.5$ ms

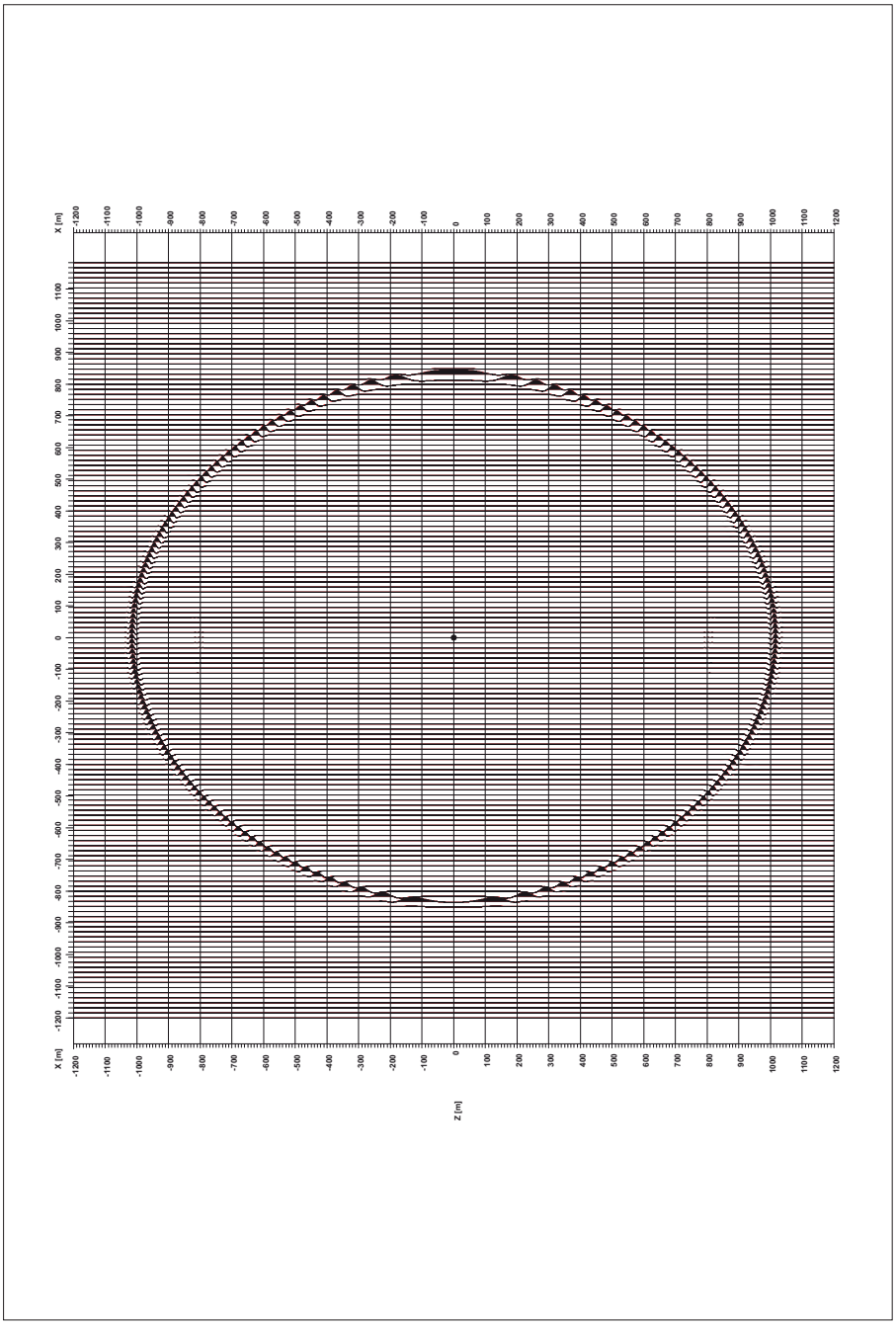

Fig. 2.61. Comparison of the versions (1.28) and (1.23) for $\Psi = 60°$; anisotropy parameters: $\varepsilon = 0.3$; $\delta = 0.1$; in moment time $t = 0.4$ s. The version (1.28) differ slightly (red color) from image (1.23). Steps of computations: $\Delta x = \Delta z = 4$ m, $\Delta t = 0.5$ ms

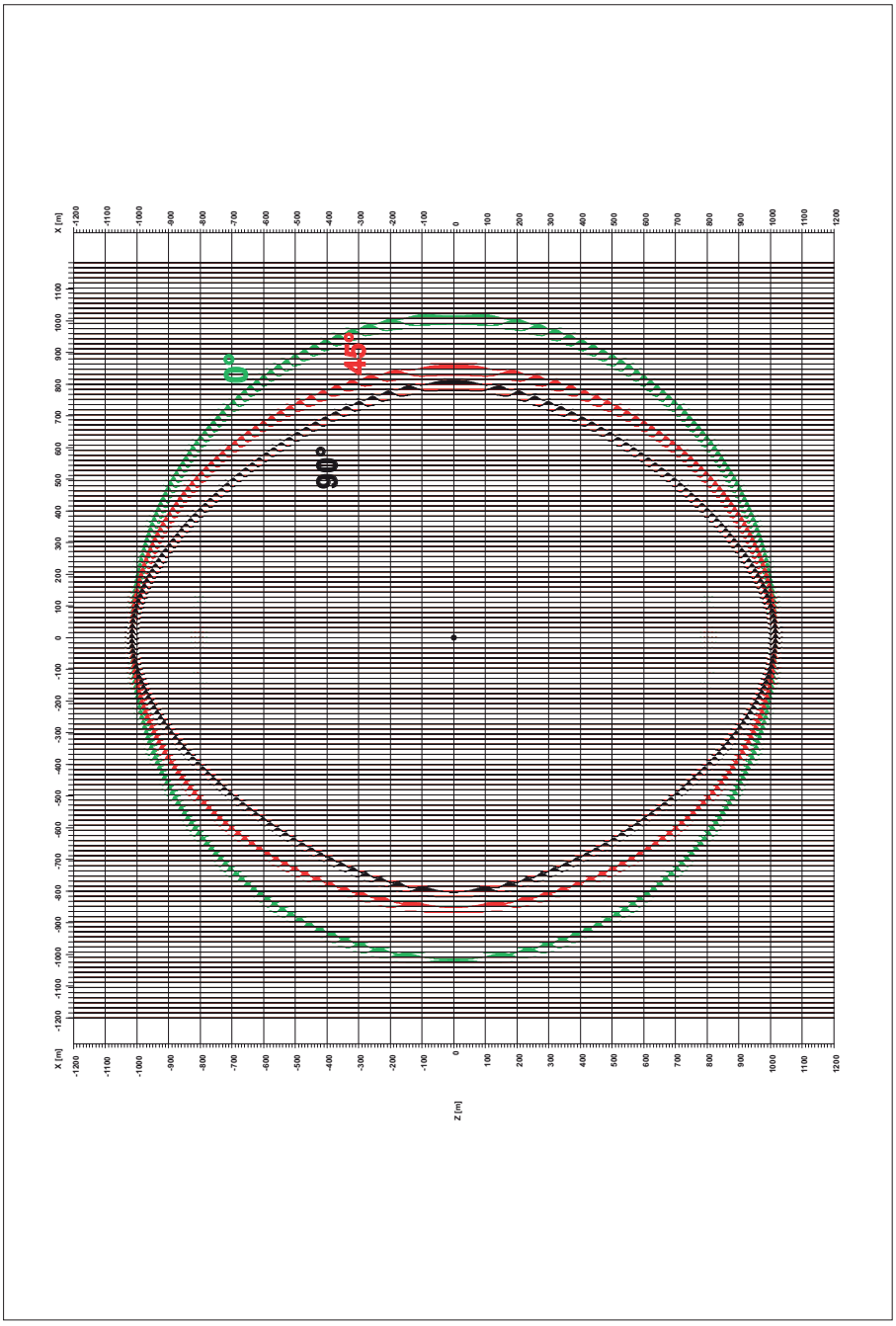

Fig. 2.62. Comparison of the propagation snapshots in time $t = 0.4$ s for version (1.23) for angle $\Psi = 0°, 45°$ and 90°; anisotropy parameters: $\varepsilon = 0.3$; $\delta = -0.1$

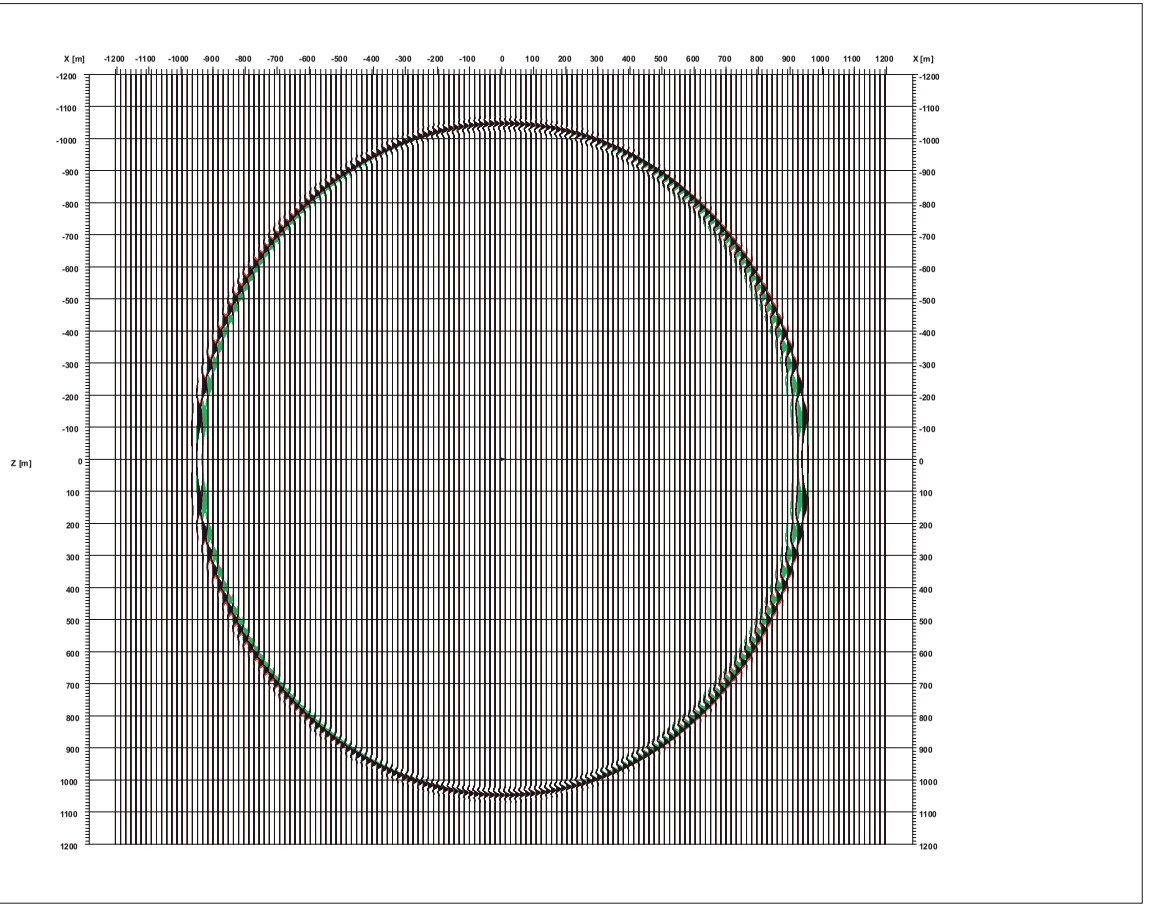

Fig. 2.63. Comparison of the propagation snapshots from (1.23) – in black, from (1.28) – in red and from (1.29) – in green; anisotropy parameters: $\varepsilon = 0.35$; $\delta = -0.1$ in moment time $t = 0.4$ s; azimuthal angle $\Psi = 30°$. Steps computations: $\Delta x = \Delta z = 4$ m, $\Delta t = 0.5$ ms

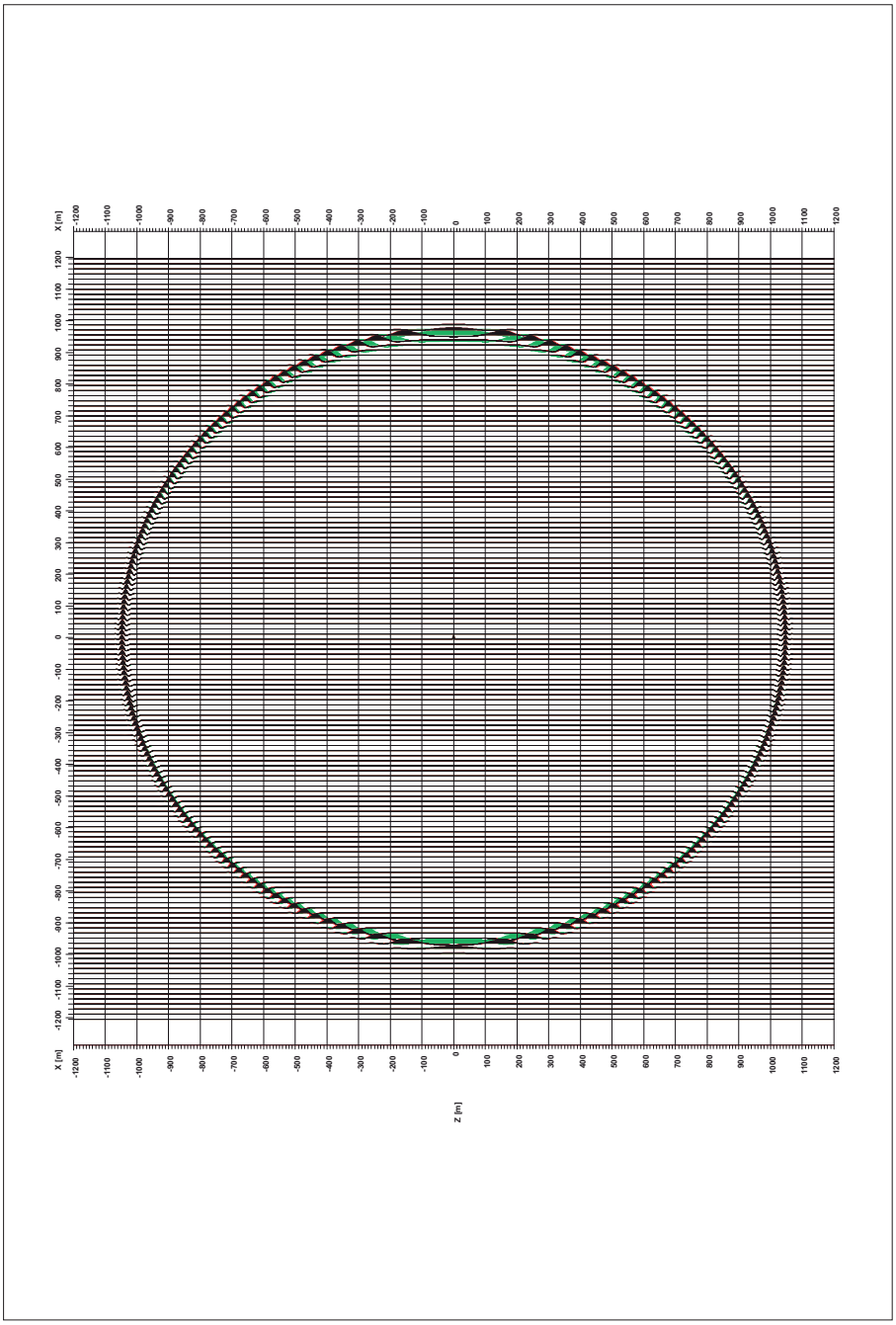

Fig. 2.64. Comparison of the propagation snapshots from (1.23) – in black, from (1.28) – in red and from (1.29) – in green for anisotropy parameters: $\varepsilon = 0.35$; $\delta = 0.1$ in moment time $t = 0.4$ s; azimuthal angle $\Psi = 30°$. Steps computations: $\Delta x = \Delta z = 4$ m, $\Delta t = 0.5$ ms

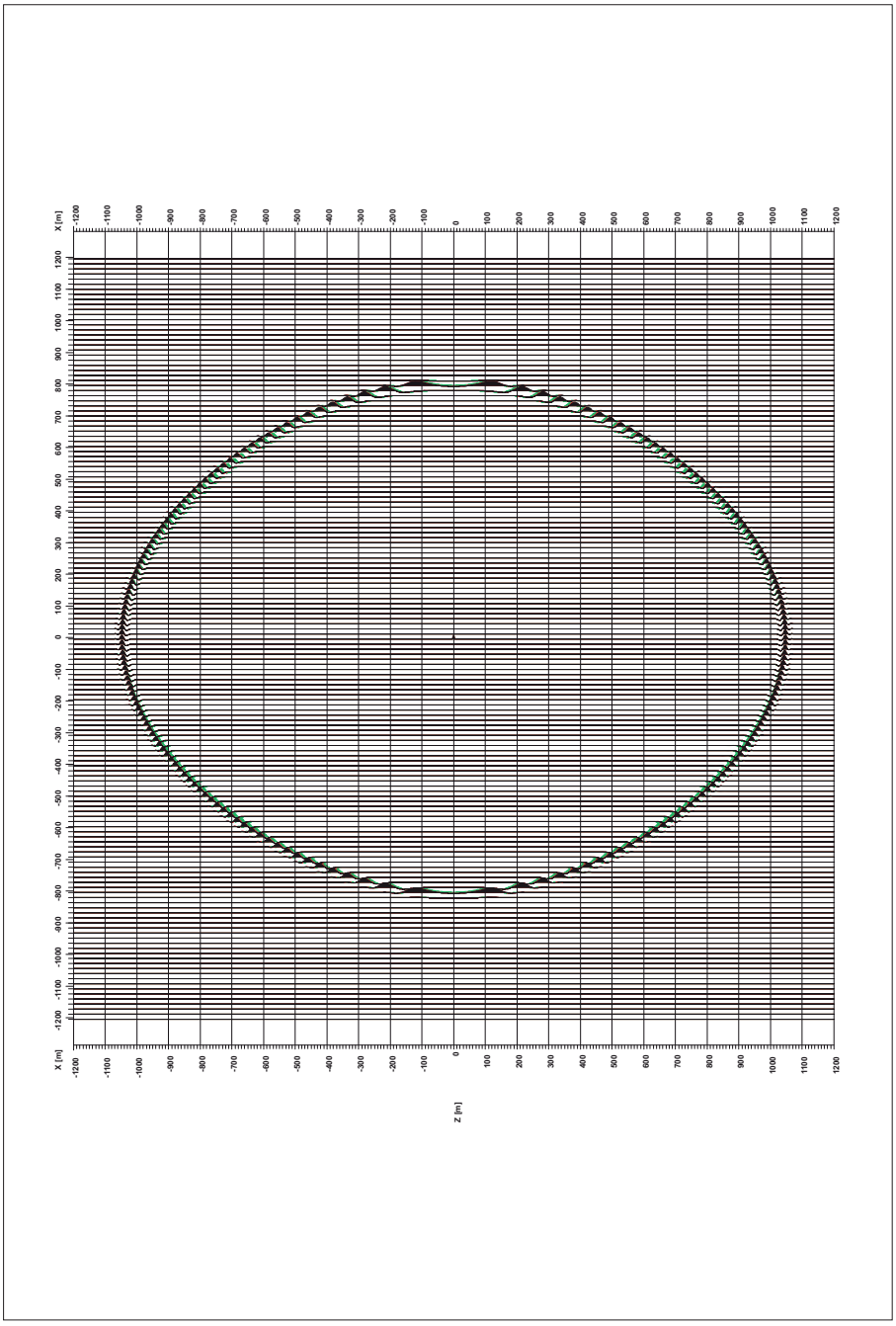

Fig. 2.65. Comparison of the propagation snapshots from (1.23) – in black, from (1.28) – in red and from (1.29) – in green for anisotropy parameters: $\varepsilon = 0.35$; $\delta = -0.1$ in moment time $t = 0.4$ s; azimuthal angle $\Psi = 60°$. Steps computations: $\Delta x = \Delta z = 4$ m; $\Delta t = 0.5$ ms

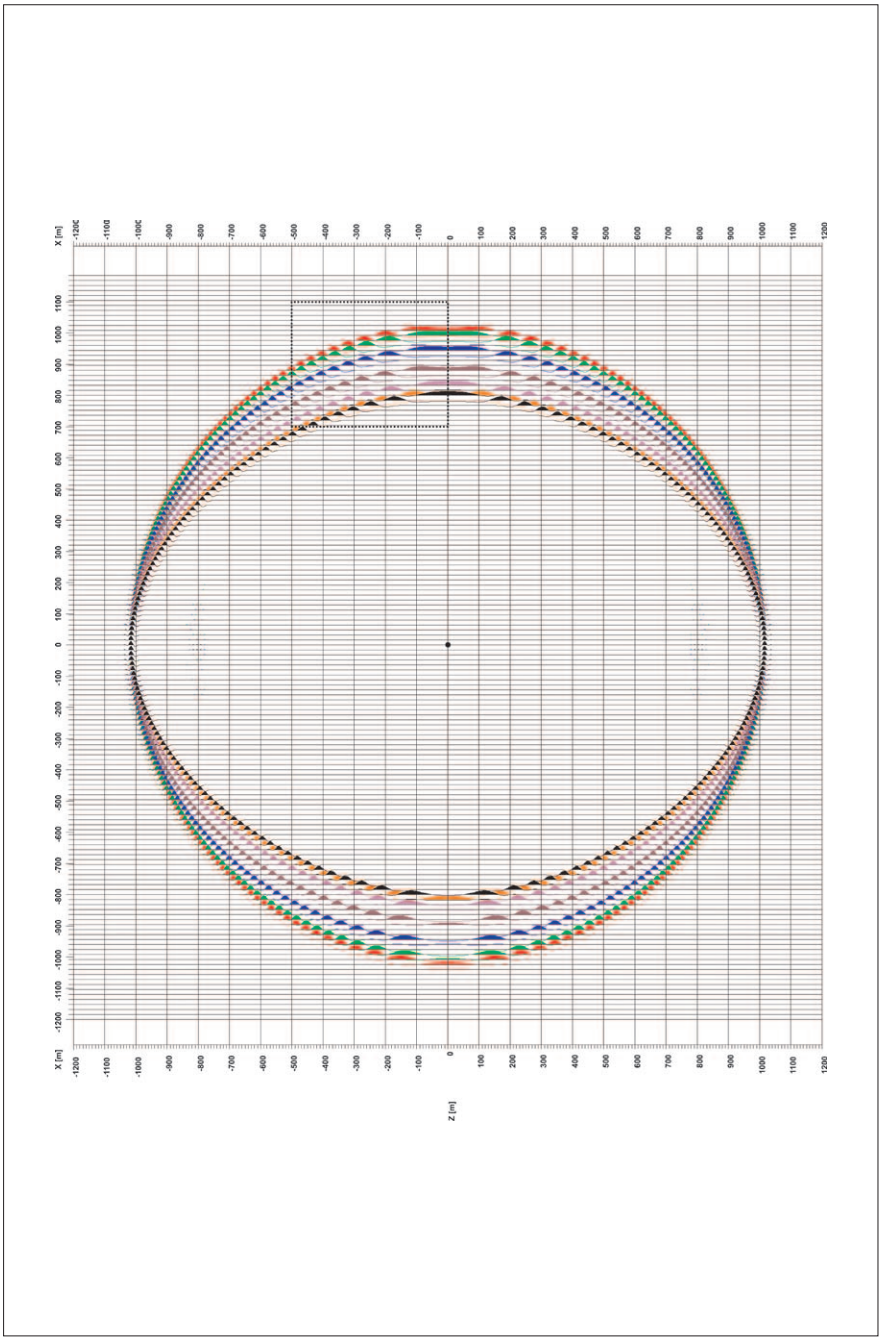

Fig. 2.66. Comparison of the propagation snapshots from (1.23) in moment time $t = 0.4$ s; anisotropy parameters: $\varepsilon = 0.3$; $\delta = 0.1$; for azimuthal angle: $\Psi = 0°$ – in red, $\Psi = 15°$ – in green, $\Psi = 30°$ – in blue, $\Psi = 45°$ – in crimson, $\Psi = 60°$ – in violet, $\Psi = 75°$ – in orange, $\Psi = 90°$ – in black

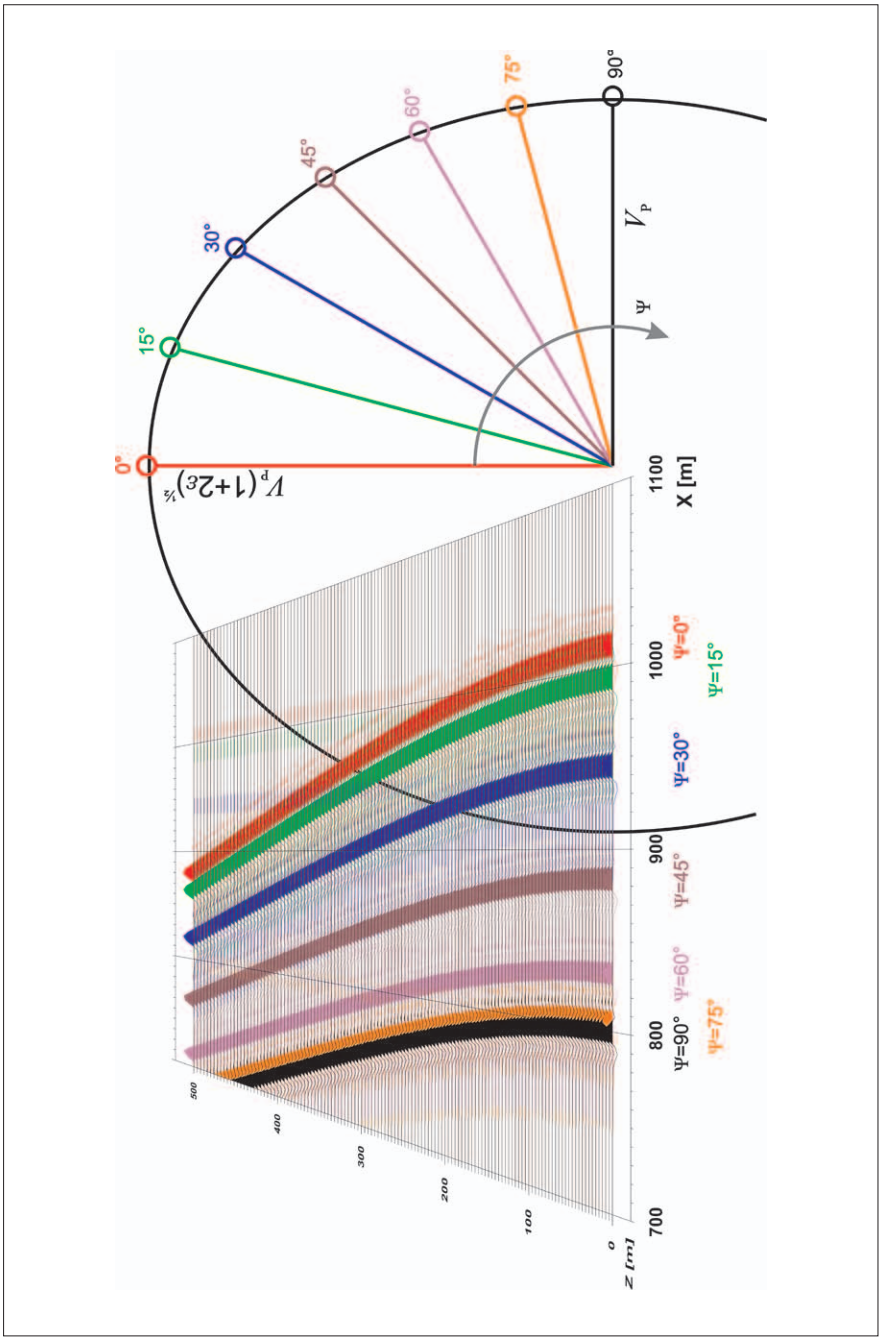

Fig. 2.67. Velocity as a function of the azimuthal angle Ψ in the first quarter of the clockwise polar coordinate system. The ellipsoid character of velocity (Ψ) is seen. In left part of figure we have a series of wavefronts which determine the length of propagation paths for time $t = 0.2$ s, $\varepsilon = 0.3$; $\delta = 0.1$

Chapter 3. Seismic migration in anisotropic media of type HTI(Ψ) in the function of azimuthal angle Ψ

Introduction

In media of the TI type most frequently Kirchhoff's migration is used in practice, because of the relative simplicity of this method. Kirchhoff's migration requires multipatching of seismic rays [46, 48, 47, 19, 11] or the application of the finite difference method [3]. Strong contrasts of velocity lead to some problems for both methods, which can create significant errors of depth imaging.

Podwin P. and Lecompte I. [41] proposed an algorithm for strong heterogeneous media in the case that the wavefront is approximated by a plane wave well. In monoclinal media with inclined axis of symmetry TTI, Kumar D., Sen M., Ferguson R. [36] developed algorithm by Faria and Stoffa [17] taking into account anisotropy parameters as a function of space coordinates. Reverse time migration takes a special position for effectiveness of imaging structures [6, 39, 16, 18, 57]. For TI type media algorithms were worked-out for VTI and TTI models.

In this chapter we present MG (F-K) migration in wavenumber – frequency which will be adapted to the imaging of 2D anisotropic media of the HTI(Ψ) type. This migration was created for compressional waves in pre-stack version [27, 28] and in post-stack version [28, 34], and as well for conversion waves P-S [29].

Basic equation for depth extrapolation of wavefields

Starting point for the migration process is the depth extrapolation of the wavefield $U(x, z_j, \omega)$ from level z_j to level $z_j + \Delta z$

$$U_{z_j+\Delta z} = F_j\left(x,\omega\right)U'\left(x, z_j + \Delta z, \omega\right) \tag{3.1}$$

where $U'(x, z_j + \Delta z, \omega)$ is Fourier transform ($k_x \rightarrow x$) of the wavefield

$$U'(k_x, z_j + \Delta z, \omega) = e^{-ik_{z_0}^{HTI}\Delta z}U(k_x, z_j, \omega) \tag{3.2}$$

and where: x is the horizontal coordinate along the measurements profile, j indicates the succeeding depth interval $z_{j+1} - z_j = \Delta z$, $k_{z_0}^{HTI}$ denotes the vertical wavenumber in homogeneous media HTI.

Relation

$$F_j(x,\omega) = [1 + \frac{i\omega^2}{2} \cdot \Delta z \cdot M_j(x,\omega)]^{-1} \tag{3.3}$$

determinates the correction of the wavefield and is the sum of Neumann's series and $M_j(x, \omega)$ denotes

$$M_j(x,\omega) = \sum_{k_x}(k_{z_0}^{HTJ})^{-1}[(k_{z_0}^{HTJ})^2 - (k_z^{HTJ})^2]e^{ik_x x}dk_x \tag{3.4}$$

where k_z^{HTJ} is the vertical wavenumber in heterogeneous media i.e. when velocity V_P and Thomsen's parameters ε and δ are functions of x space coordinate.

It follows from relation (3.1–3.3) that this migration has two stages. In the first stage, the extrapolation is made in homogeneous media for constant velocity V_P and parameters ε and δ in the range of measurements interval. From a practical point of view, it is conve-

nient to use average values in measurements interval. In the second stage, the correction of the wavefield proceeds by the application of the $F_j(x, z, \omega)$ function. The stability for down extrapolation process succeeds through the convergence of Neumann's series

$$\left[1+\frac{i\omega^2\Delta z}{2}M_j(x,\omega)\right]^{-1}$$

which is assured if condition

$$\left|\frac{i\omega^2\Delta z}{2}M_j(x,\omega)\right|<1 \tag{3.5}$$

is fulfilled.

As an option we can accept the operator

$$e^{\frac{-i\omega^2\Delta z}{2}M_j(x,\omega)} \tag{3.6}$$

which unconditionally assures stability of extrapolation.

Pre-stack migration

Equations (3.1–3.4) should be treated as a starting point for depth extrapolation process before the stack. The wavefield is exited by many sources and registered by many receivers, deployed along the profile. Imaging of the depth target is finished when the coincidence of sources and receivers position is fulfilled in time $t = 0$. It means that the sources and receivers should be displaced in depth until they reach the time-space coincidence. In the category of wave equations that means alternate use of extrapolation vs. source and receivers.

Denoting the coordinates of the sources positions by s and receivers by g we obtain the following relation for extrapolation:

$$U_j(g,s,z_j+\Delta z,\omega)=F_j(g,\Delta z,\omega)F_j(s,\Delta z,\omega)U'_j(g,s,z_j+\Delta z,\omega) \tag{3.7}$$

where $U'_j(g,s,z_j+\Delta z,\omega)$ is double Fourier transform ($k_g \to g$, $k_s \to s$) of the wavefield:

$$U'_j(k_g,k_s,z_j+\Delta z,\omega)=U_j(k_g,k_s,z_j,\omega)e^{-i(k_{z_g}^{HTJ}+k_{z_s}^{HTJ})\Delta z} \tag{3.8}$$

in other words the function of the horizontal wavenumber k_g and k_s which corresponds to space coordinates of source – s and receiver – g.

Corrections filters $F_j(g, \Delta z, \omega)$ and $F_j(s, \Delta z, \omega)$ relating to receivers and sources are expressed by analogical relations as (3.3) and (3.4) with such a difference that x coordinate should be substituted by s and g coordinates. These coordinates define slowness S and Thomsen's parameters in the expression of vertical wavenumbers $k_{z_s}^{HTJ}$ and $k_{z_g}^{HTJ}$

It is convenient to use common reference values of the vertical wavenumber in relations for $M_j(s)$ and $M_j(g)$.

The extrapolation procedure under relations (3.7–3.8) requires the application of double Fourier transform ($g \to k_g$, $s \to k_s$) to the wavefield in order to shift receivers and sources to subsequent level z_j of depth. Imaging of depth structures is made at the point of coincidence for sources and receivers when $s = g$ at time $t = 0$:

$$U_{j_{migr.}}(s=g,z_j+\Delta z,t=0)=\sum_{\omega}U_j(s=g,z_j+\Delta z,\omega)d\omega \tag{3.9}$$

where: $U_{j_{migr.}}$ stands for the wavefield at depth $z_j + \Delta z$.

The stability of the extrapolation algorithm requires the convergence of Neumann series:

$$\left|\frac{i\omega^2}{2}\Delta z\cdot M_j(s)\right|<1 \tag{3.10}$$

$$\left|\frac{i\omega^2}{2}\Delta z\cdot M_j(g)\right|<1$$

One can obtain unconditional stability by substituting corrections to functions $F_j(g, \Delta z, \omega)$ and $F_j(s, \Delta z, \omega)$ by exponential functions.

Then, we have:

$$U_j(s,g,z+\Delta z) = e^{-\frac{i\omega^2}{2}\Delta z \cdot M(g)} e^{-\frac{i\omega^2}{2}\Delta z \cdot M(s)} U'_j(s,g,z+\Delta z,\omega) \tag{3.11}$$

and the migration process is described by relation (3.9).

Zero-offset migration

In the case of zero-offset migration, one assumes that x on the profile is a coordinate of the source as well as the receiver.

The wavefield at registration level $z = 0$, one can obtain in the process of modeling, provided that at each point of velocity discontinuity wave is simultaneously excited at the time $t = 0$ and propagates into $z = 0$ level with velocity equal ½ of real velocity [38]. Therefore in the equations describing wave propagation, slowness $2S$ should be used instead of S. It should be pointed out that the approximation of the zero-offset section is in practice the stacked time section.

In the case of zero- offset migration, the depth extrapolation can be written as follows:

$$U_{z_j+\Delta z} = \left[1 + i2\omega^2 \Delta z M_j(x,\omega)\right]^{-1} U'(x, z_j + \Delta z, \omega) \tag{3.12}$$

where $U'(x, z_j + \Delta z, \omega)$ is defined by relation (3.2).

Imaging of depth structures is obtained as results of Fourier transform ($\omega \rightarrow t$) at $t = 0$ time:

$$U_{migr}\left(x, z_j + \Delta z, t = 0\right) = \sum_{\omega} U\left(x, z_j + \Delta z, \omega\right) \tag{3.13}$$

which leads to summation of the wavefield for a useful range of frequency.

Depth extrapolation operators

Vertical wavenumber $k_{z_s}^{HTJ}$ and $k_{z_g}^{HTJ}$ for pre-stack migration and k_z^{HTJ} for zero-offset migration are solutions of dispersion relation (1.23) and they can be determined by relation:

$$k_z^{HTI} = \left\{ \frac{\omega^6 - \omega^4 k_x^2 \left(d_{11} + d_{66}\right) + \omega^2 k_x^4 \left(d_{11} d_{66} - d_{16}^2\right)}{\omega^4 d_{33} - \omega^2 k_x^2 N_1 + k_x^4 N_2} \right\}^{1/2} \tag{3.14}$$

where

$$\begin{aligned} N_1 &= d_{33}\left(d_{11} + d_{66}\right) - d_{63}{}^2 - d_{13}{}^2 \\ N_2 &= d_{11}[d_{33} d_{66} - d_{63}^2] - d_{16}^2 d_{33} + d_{13} d_{16} d_{63} - d_{13}^2 d_{66} \end{aligned} \tag{3.14a}$$

(see appendix 4).

Neglecting d_{66}, d_{63}, d_{16} components of elasticity tensor $D^{90°.\Psi}$as small values in comparison to d_{11}, d_{33}, d_{13}, we have approximation:

$$\begin{aligned} k_z^{HTI} &= \{ \frac{\omega^4 - \omega^2 k_x^2 d_{11}}{\omega^2 d_{33} - k_x^2 (d_{11} d_{33} - d_{13}{}^2)} \}^{1/2} \\ &= \left\{ \frac{\omega^4 S^4 - \omega^2 S^2 k_x^2 [(1+2\varepsilon)\cos^4 \Psi + \sin^4 \Psi + \frac{1}{2}(1+\delta)\sin^2(2\Psi)]}{\omega^2 S^2 (1+2\varepsilon) - k_x^2 \sin^4 \Psi \cdot \eta_a} \right\}^{1/2} \end{aligned} \tag{3.15}$$

where $S = V_P^{-1}$; $\eta_a = 2(\varepsilon - \delta)$

Modeling and migration of zero-offset time sections

The subject of numerical experiments was an inhomogeneous four layers model of anticline covered by a 500 m thick horizontal layer (Fig. 3.1). The velocity of compressional waves, constant in each layer, changes from 3.0 km/s to 5.0 km/s.

The wavefield for this zero-offset time section was computed by a simultaneously exited reflectors method at $t = 0$ [38]. The pseudo-spectral version of one-way equation was used (2.14) in view of lateral inhomogeneity. Wavefields were computed for sequence of parameters ε and δ [0.3; 0.1] (Fig. 3.2, Fig. 3.5, Fig. 3.8, Fig. 3.11, Fig. 3.14, Fig. 3.17, Fig. 3.20, Fig. 3.23, Fig. 3.26 and Fig. 3.29); [0.35; 0.1] (Fig. 3.47, Fig. 3.50 and Fig. 3.53); [0.5; 0.1] (Fig. 3.32); [0.5; 0.3] (Fig. 3.39); [0.35; –0.2] (Fig. 3.42 and Fig. 3.44). Analyzing time sections for $\varepsilon = 0.3$ and $\delta = 0.1$, one can easily note the conformity in the central part (the summits of anticline) and in the right side (flat runtime), whereas in the left side one can observe the differentiation according to azimuthal angle Ψ. An analogical situation one can observe for sequence parameters $\varepsilon = 0.35$; $\delta = 0.1$ and for $\varepsilon = 0.35$; $\delta = -0.2$. In this case, the build-up of ε value results in the reduction of minimal runtimes in the anticlinal part. The observations of those runtimes find full justification in the characteristics for $\varepsilon = 0.5$; $\delta = 0.1$ and $\varepsilon = 0.5$; $\delta = 0.3$ for dependence of compressional waves velocity $V(\Psi)$ on azimuthal angle Ψ. In this case vertical velocity reaches maximal value independently from the azimuthal angle, therefore in central parts of the anticline and in its right slope, one can observe similar runtimes in the vertical and near to vertical directions which shapes time sections in this fragment of image. Horizontal velocities, which depend only on the azimuthal angle Ψ and parameter ε, and velocities near to horizontal directions depending even on parameter δ, form characteristic branches of runtimes for zero-offset times and are decisive for their differentiation.

Depth migrations (relations 3.14) from the time the zero-offset section obtained from exact relations (1.23) [Fig. 3.3, Fig. 3.6, Fig. 3.9, Fig. 3.12, Fig. 3.15 and Fig. 3.18] for sequences: $\varepsilon = 0.3$; $\delta = 0.1$ and for $\varepsilon = 0.35$; $\delta = 0.1$ [Fig. 3.48, Fig. 3.49, Fig. 3.51, Fig. 3.52 and Fig. 3.54] present, according to expectations, invariable images for different azimuthal angles Ψ.

Comparing images from the approximate version (3.15) in Fig. 3.25, Fig. 3.28, Fig. 3.31, Fig. 3.34, Fig. 3.36 and Fig. 3.41 with relevant migrations from relations (3.14), one can see that both versions give similar results. The convergence of migrations Fig. 3.21, Fig. 3.24 and Fig. 3.22, Fig. 3.25 for $\Psi = 30°$, obtained from frequencies ω_a for equations (1.28) and (1.29), confirms results of signal propagation comparative experiments in Fig. 2.63, Fig. 2.64 and Fig. 2.65. For error evaluation of imaging, resulting from the use of incorrect parameters,

we show post-stack migration in Fig. 3.35 for parameters $\varepsilon = 0.4$; $\delta = 0.2$; $\Psi = 45°$ and for the time section with parameters $\varepsilon = 0.5$; $\delta = 0.1$; $\Psi = 45°$ (Fig. 3.32). Then one can see the shift of the anticline reflectors in the direction of the registration level that reaches about 100 m (for deepest reflector). This effect is caused by the reduction of parameter ε about 0.1, which generated the depression of reflectors. The confirmation that parameter ε is decisive in this case, one can obtain from the practical indifference of images in the central part of the model, while one compare images for parameters $\varepsilon = 0.5$; $\delta = 0.3$; $\Psi = 45°$ (Fig. 3.37) and for parameters $\varepsilon = 0.5$; $\delta = 0.1$ (Fig. 3.34).

The analysis of zero-offset time sections shows little sensibility of kinematic characteristics described by relations (2.25). For example, images in Fig. 3.52 and Fig. 3.54 are similar, despite the fact that the zero-offset time sections were computed for $\Psi = 60°$ (Fig. 3.52) and for $\Psi = 90°$ (Fig. 3.54).

The second test object of zero-offset modeling and migration was the fault in symmetrical form – vertical horst (Fig. 3.55), with the velocity of compressional waves changing from 3.0 km/s in the elevated part to 4.5 km/s at the floor of model. A series of experiments were executed for different sequences of Thomsen's parameters ε and δ. For comparative purpose we executed also computations for VTI and TTI models. The zero-offset migrations, presented in Fig. 3.57 and Fig. 3.59 for isotropic and anisotropic models, are in practice indistinguishable and exactly image the zone of the horst. This effect is justified by identical vertical velocity for both models, which places the horizontal elements of thrust in the same positions in the time t domain. One can notice that in zero-offset time sections (Fig. 3.56 and Fig. 3.58), where slight differences occur only for diffraction curves adjoining the block edges of the thrust.

The migration series for TTI media for parameters $\varepsilon = 0.3$ and $\delta = 0.1$ (Fig. 3.61, Fig. 3.63, Fig. 3.65 and Fig. 3.67) and dip angles $\theta = 30°, 45°, 60°, 90°$ image satisfactorily geometrical positions of the horst, however in dip angle range $\theta = 30° \rightarrow 60°$, one can notice some artifacts in discontinuities of reflectors. In the TTI model case for $\theta = 90°$, exact, high quality horst image is obtained.

A series of zero-offset time sections and depth migrations for HTI models were performed for Thomsen's parameters sequence: $\varepsilon = 0.25$; $\delta = 0.1$ and for azimuthal angles $\Psi = 0°$ (Fig. 3.68, Fig. 3.69), $\Psi = 30°$ (Fig. 3.70, Fig. 3.71), $\Psi = 60°$ (Fig. 3.72, Fig. 3.73), $\Psi = 90°$ (Fig. 3.74, Fig. 3.75). The obvious result was independence of the migration on azimuthal angle Ψ according to the vertical velocity independence versus the angle.

In general, those zero-offset modeling and migration experiments have shown the correctness of algorithmic and numerical solutions and high precision and quality imaging of the complex geometry of velocity models.

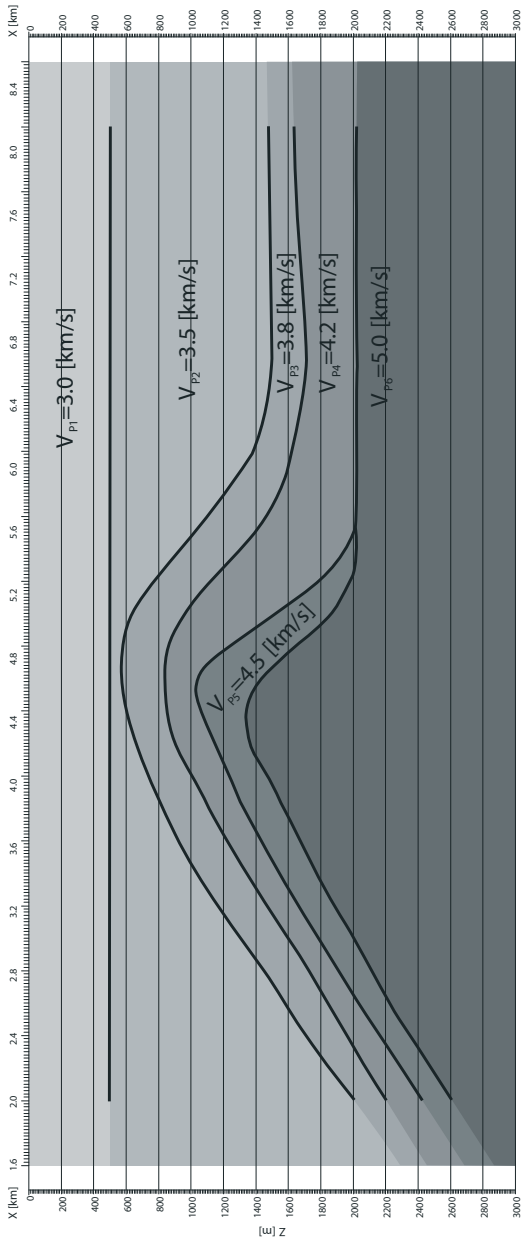

Fig. 3.1. The geometry of velocity anticline model

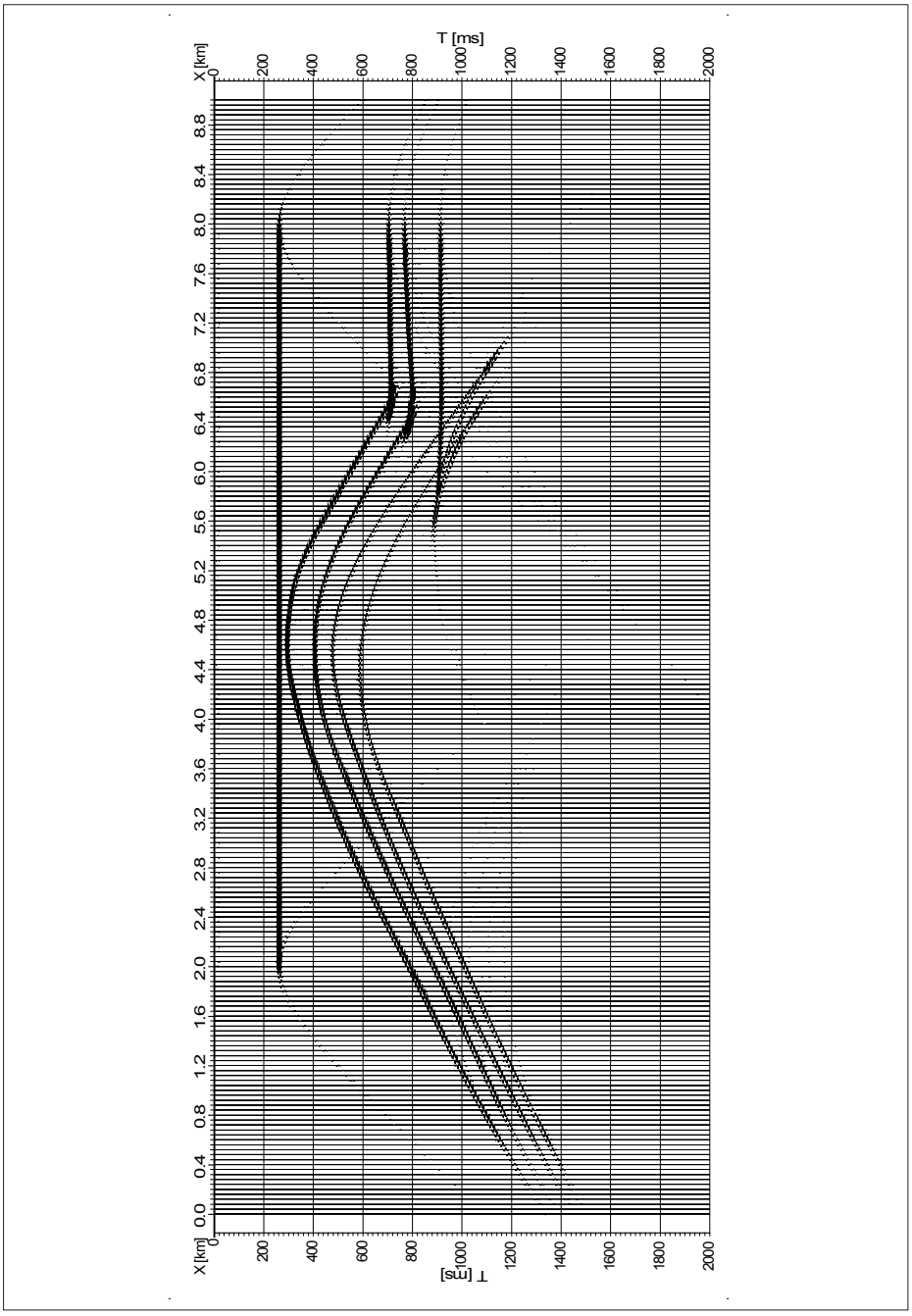

Fig. 3.2. The zero-offset time section from relations (1.23); anisotropy parameters $\varepsilon = 0.3$; $\delta = 0.1$; azimuthal angle $\Psi = 15°$

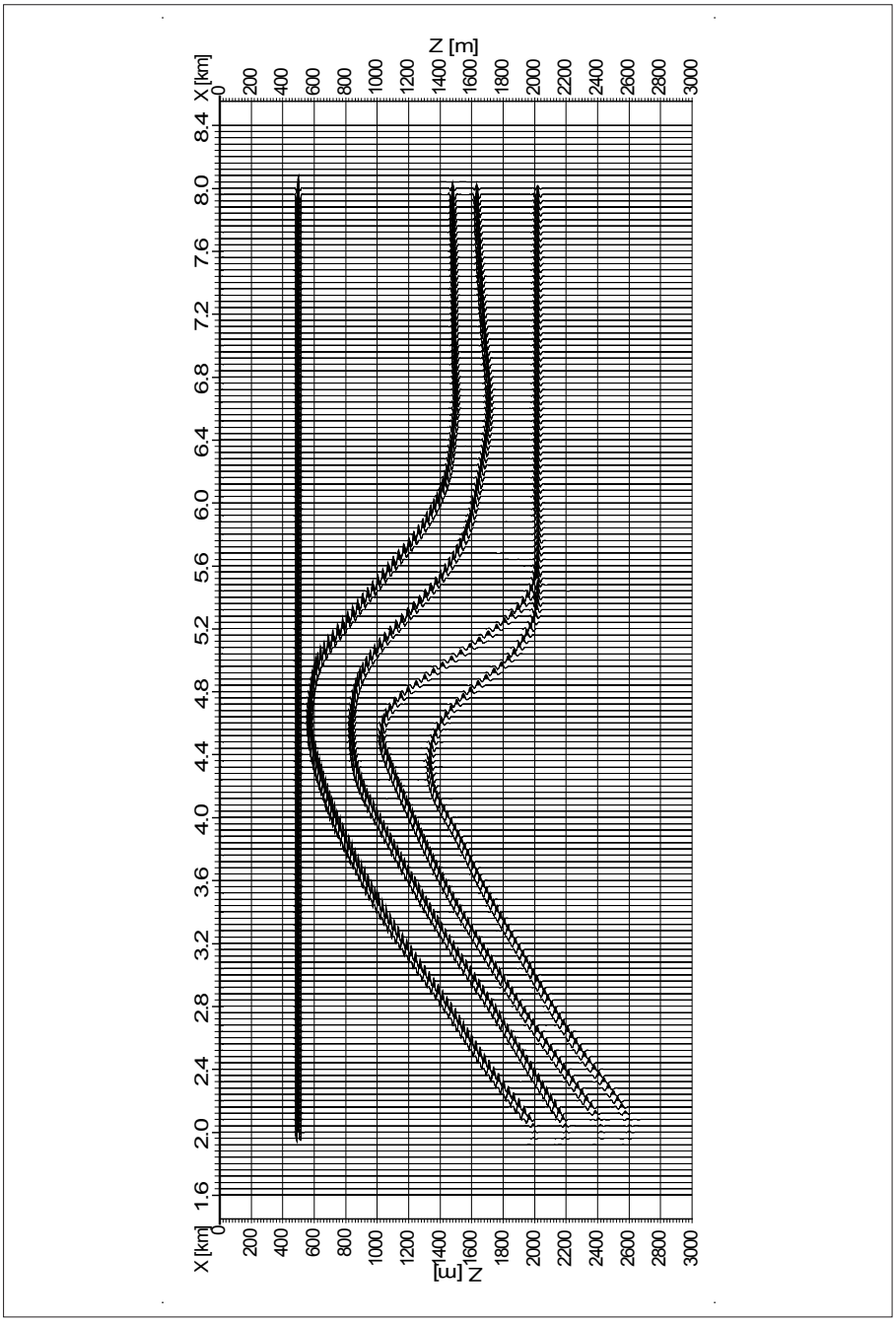

Fig. 3.3. The migration from (3.14) for the zero-offset time section from relation (1.23); anisotropy parameters $\varepsilon = 0.3$; $\delta = 0.1$; azimuthal angle $\Psi = 15°$ (Fig. 3.2)

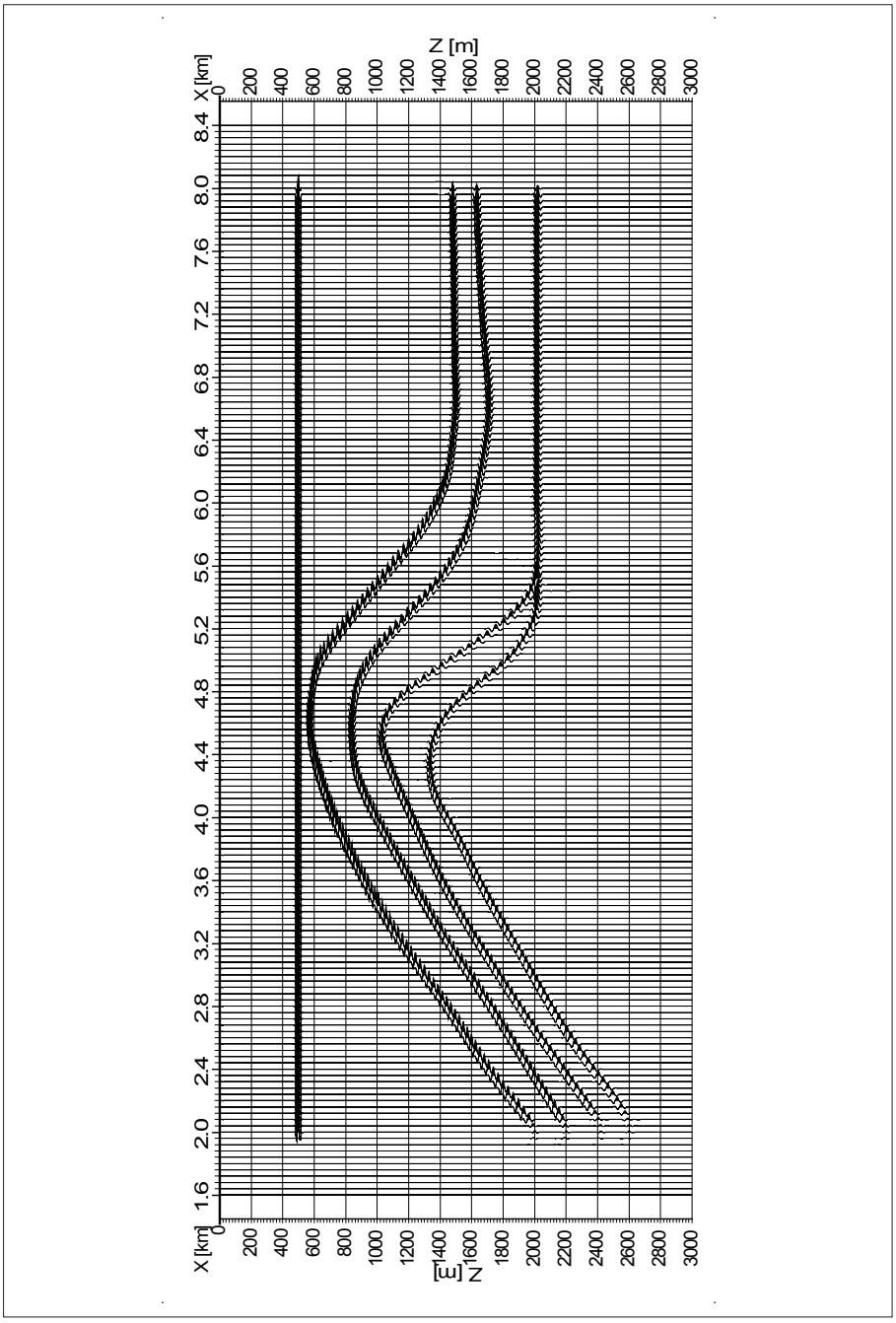

Fig. 3.4. The migration from (3.15) for the zero-offset time section from relation (1.23); anisotropy parameters $\varepsilon = 0.3$; $\delta = 0.1$; azimuthal angle $\Psi = 15°$ (Fig. 3.2)

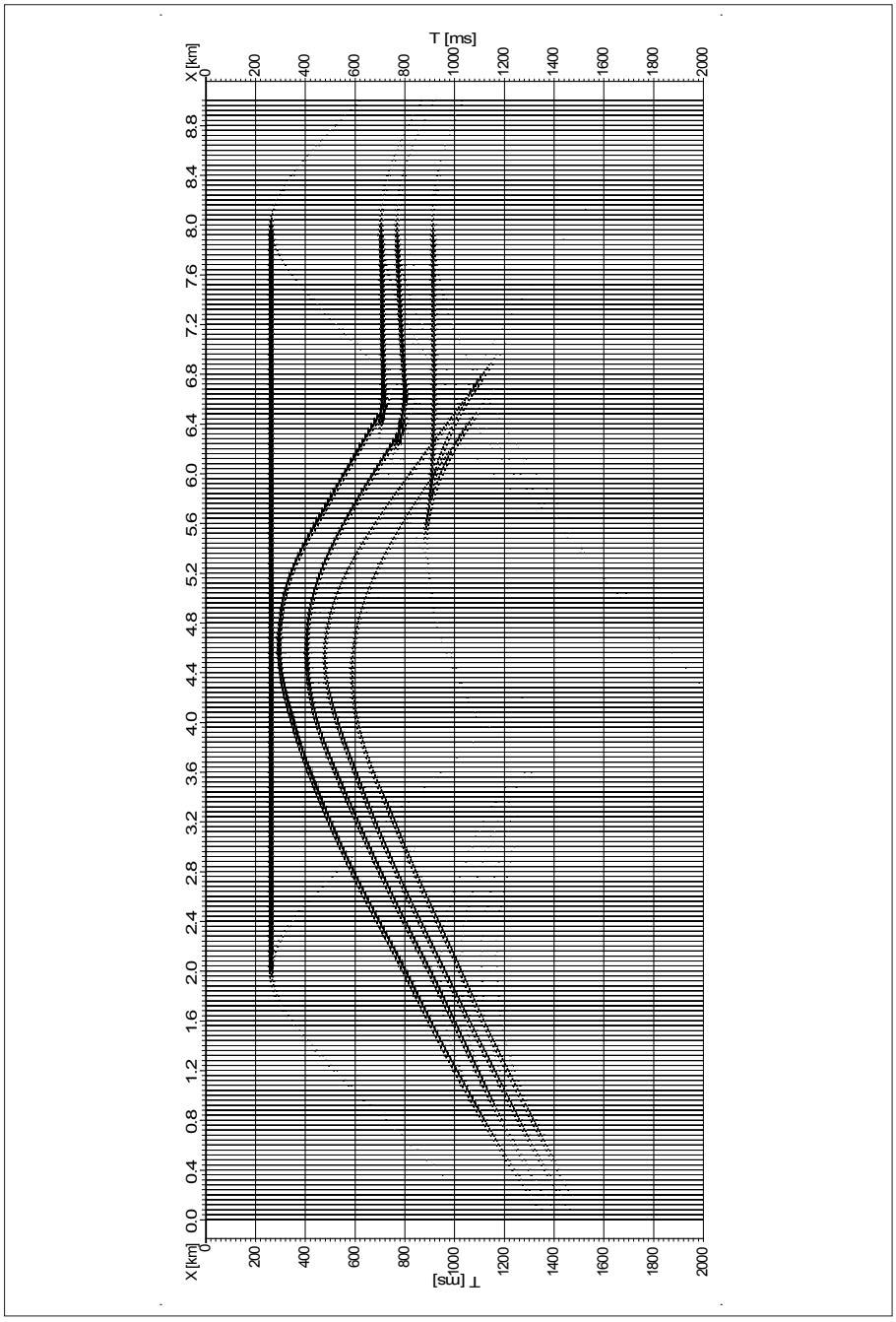

Fig. 3.5. The zero-offset time section from relation (1.23); anisotropy parameters $\varepsilon = 0.3$; $\delta = 0.1$; azimuthal angle $\Psi = 30°$

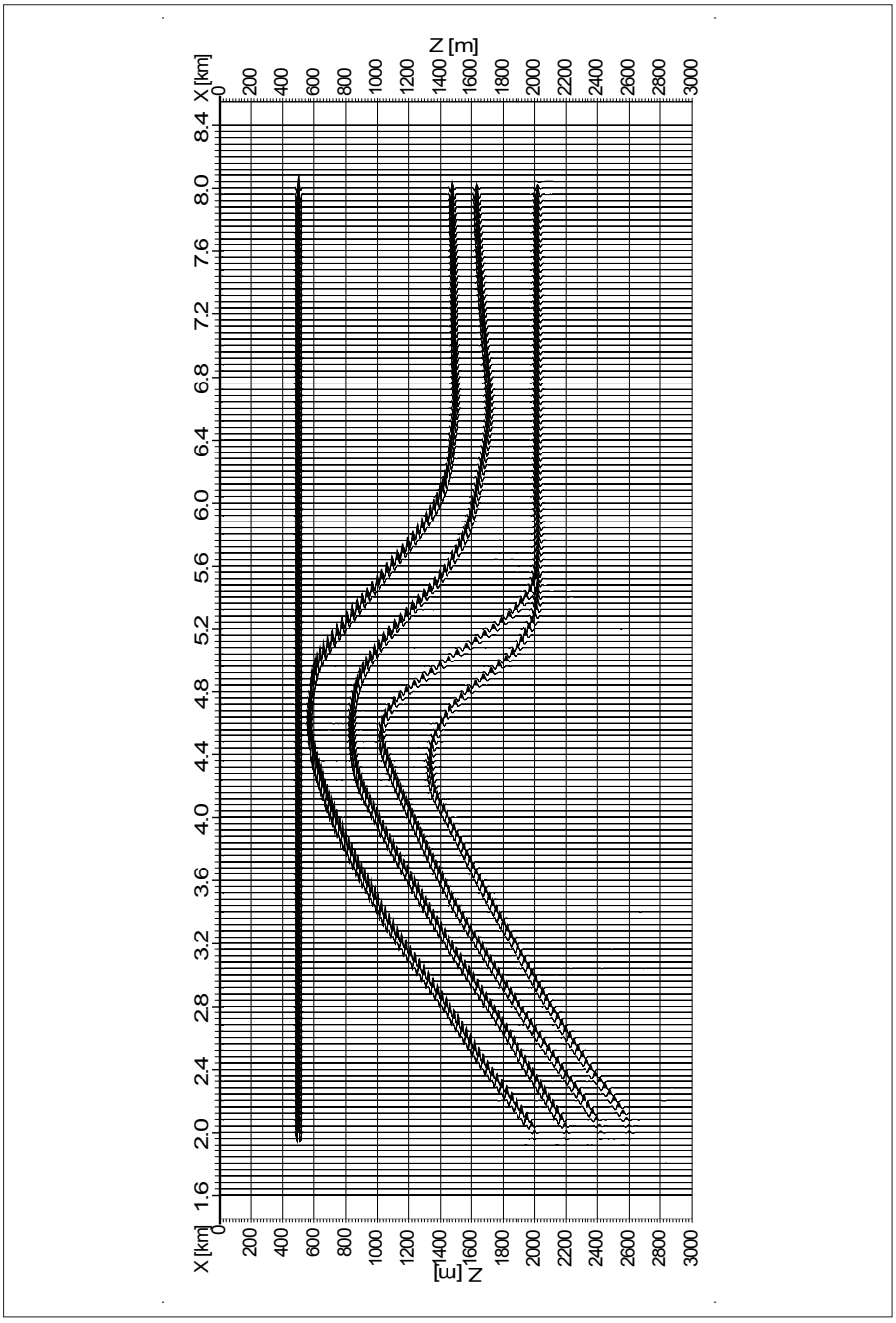

Fig. 3.6. The migration from (3.14) for the zero-offset time section from relation (1.23); anisotropy parameters $\varepsilon = 0.3$; $\delta = 0.1$; azimuthal angle $\Psi = 30°$ (Fig. 3.5)

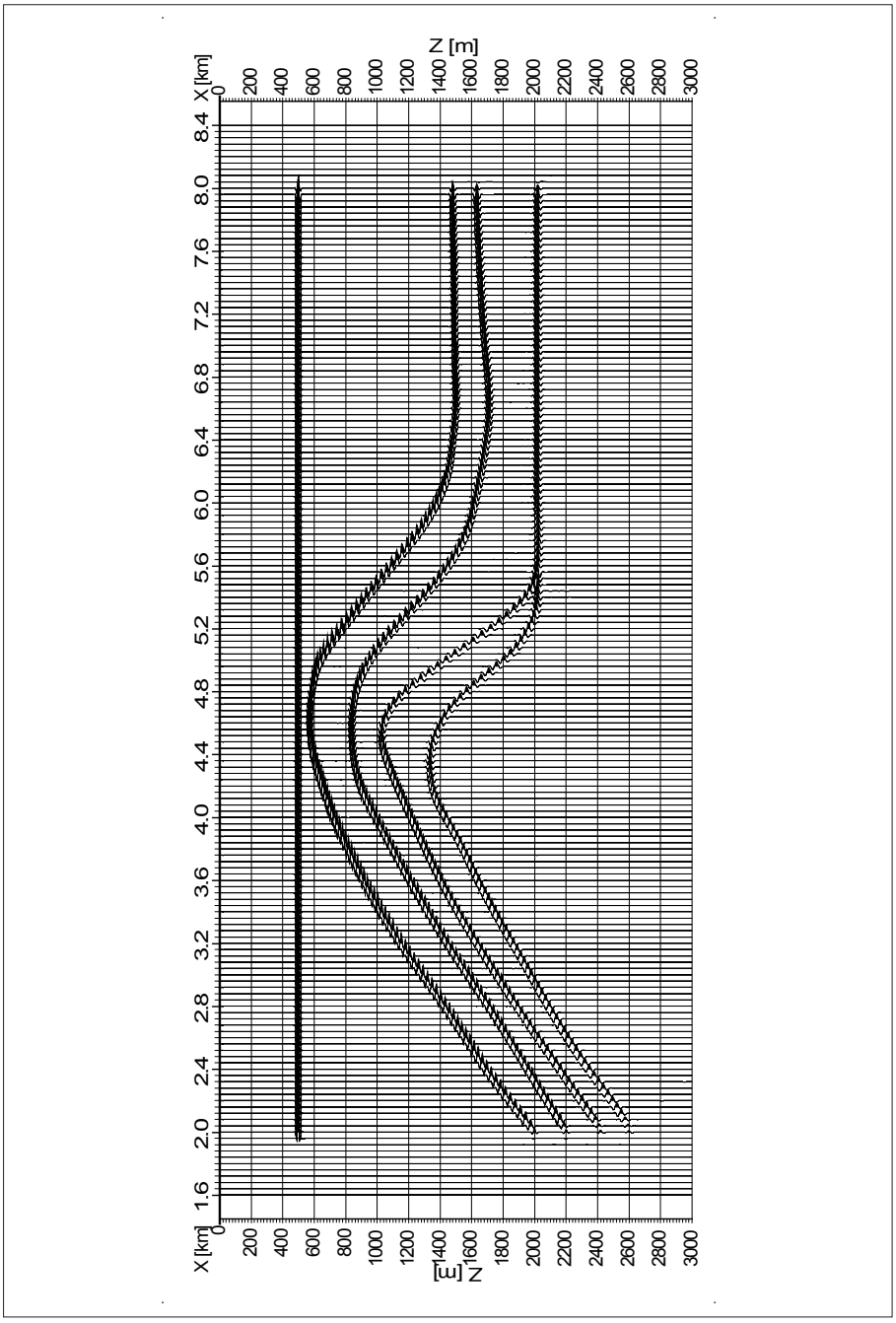

Fig. 3.7. The migration from (3.15) for the zero-offset time section from relation (1.23); anisotropy parameters $\varepsilon = 0.3$; $\delta = 0.1$; azimuthal angle $\Psi = 30°$ (Fig. 3.5)

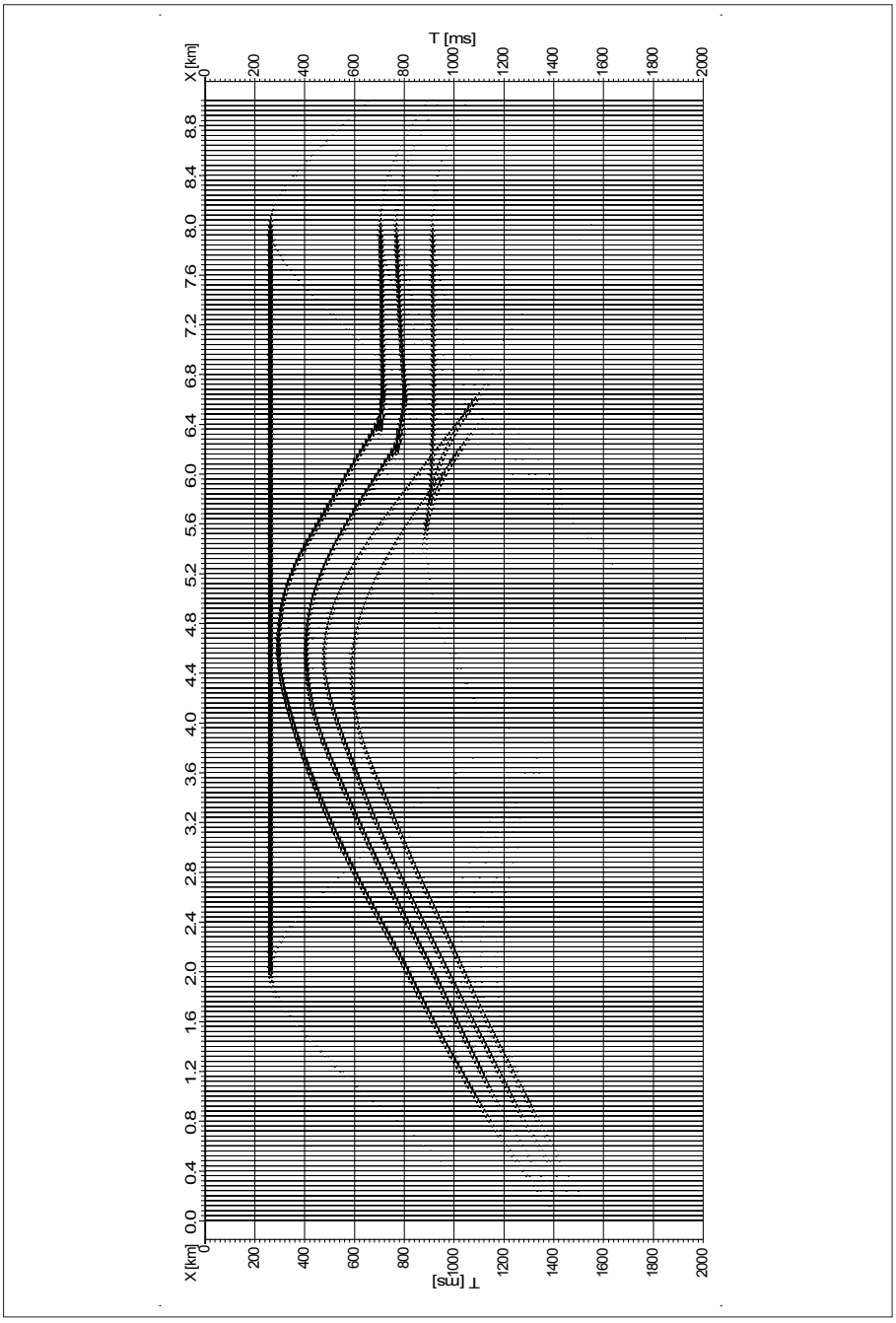

Fig. 3.8. The zero-offset time section from relation (1.23); anisotropy parameters $\varepsilon = 0.3$; $\delta = 0.1$; azimuthal angle $\Psi = 45°$

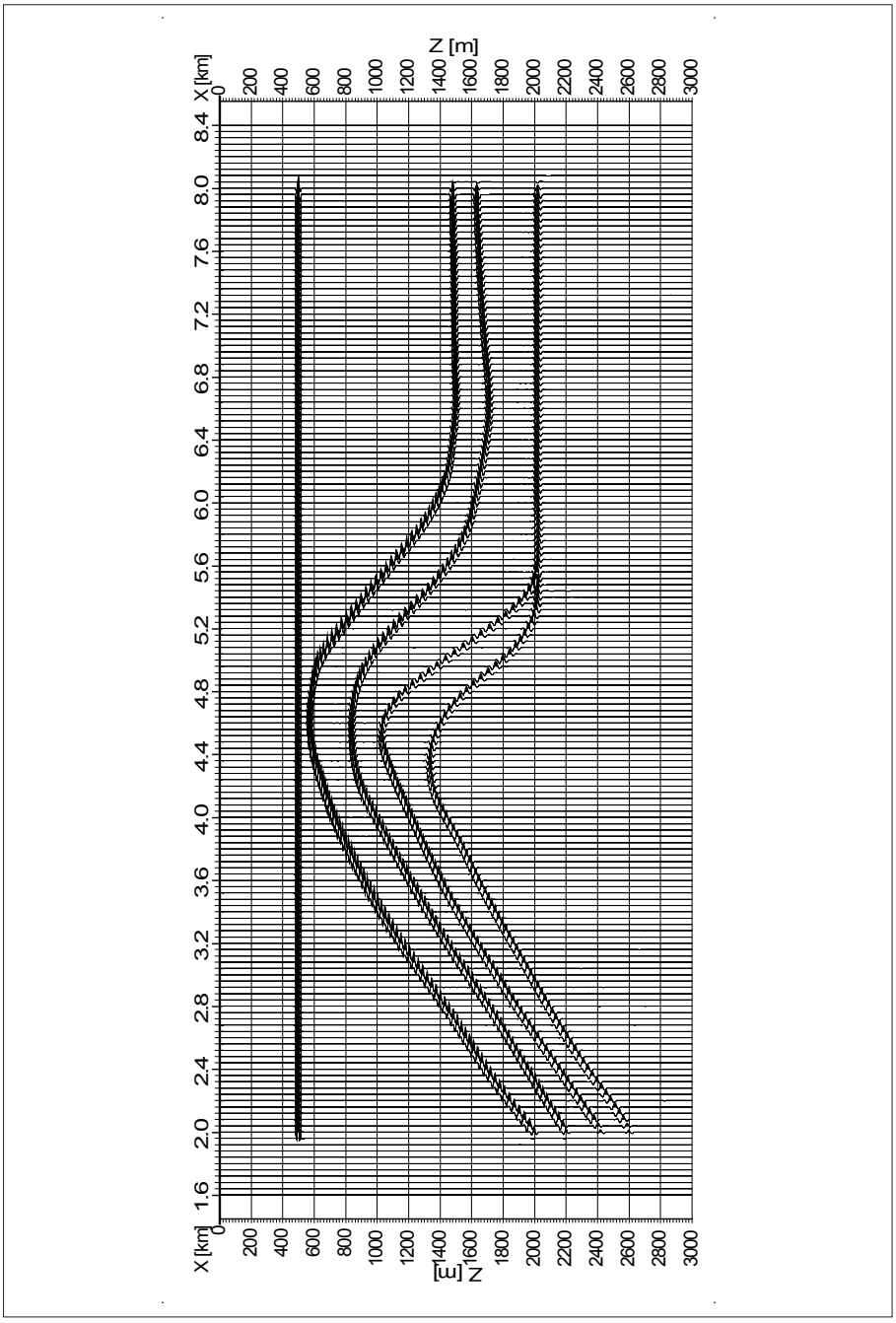

Fig. 3.9. The migration from (3.14) for the zero-offset time section from relation (1.23); anisotropy parameters $\varepsilon = 0.3$; $\delta = 0.1$; azimuthal angle $\Psi = 45°$ (Fig. 3.8)

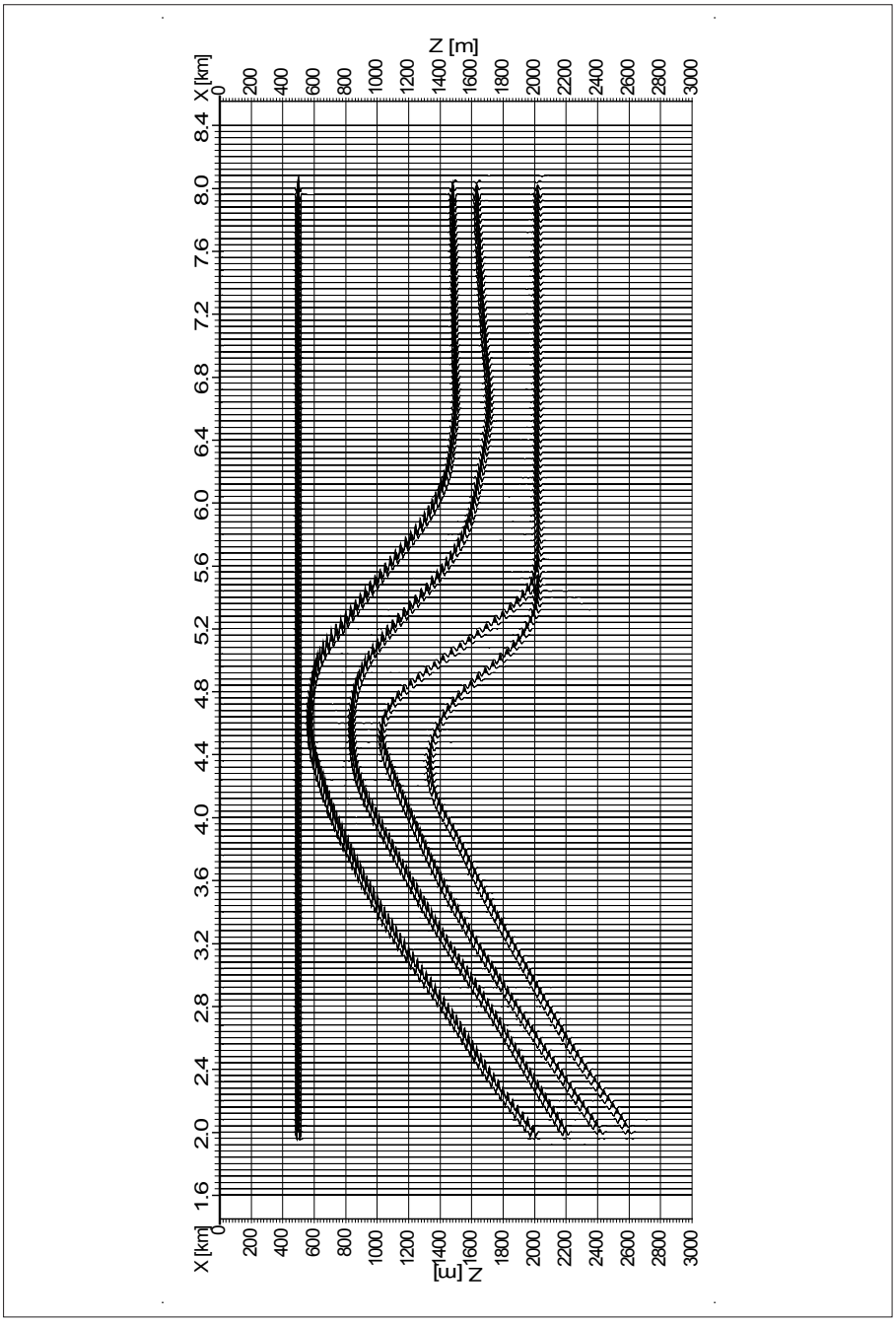

Fig. 3.10. The migration from (3.15) for the zero-offset time section from relation (1.23); anisotropy parameters $\varepsilon = 0.3$; $\delta = 0.1$; azimuthal angle $\Psi = 45°$ (Fig. 3.8)

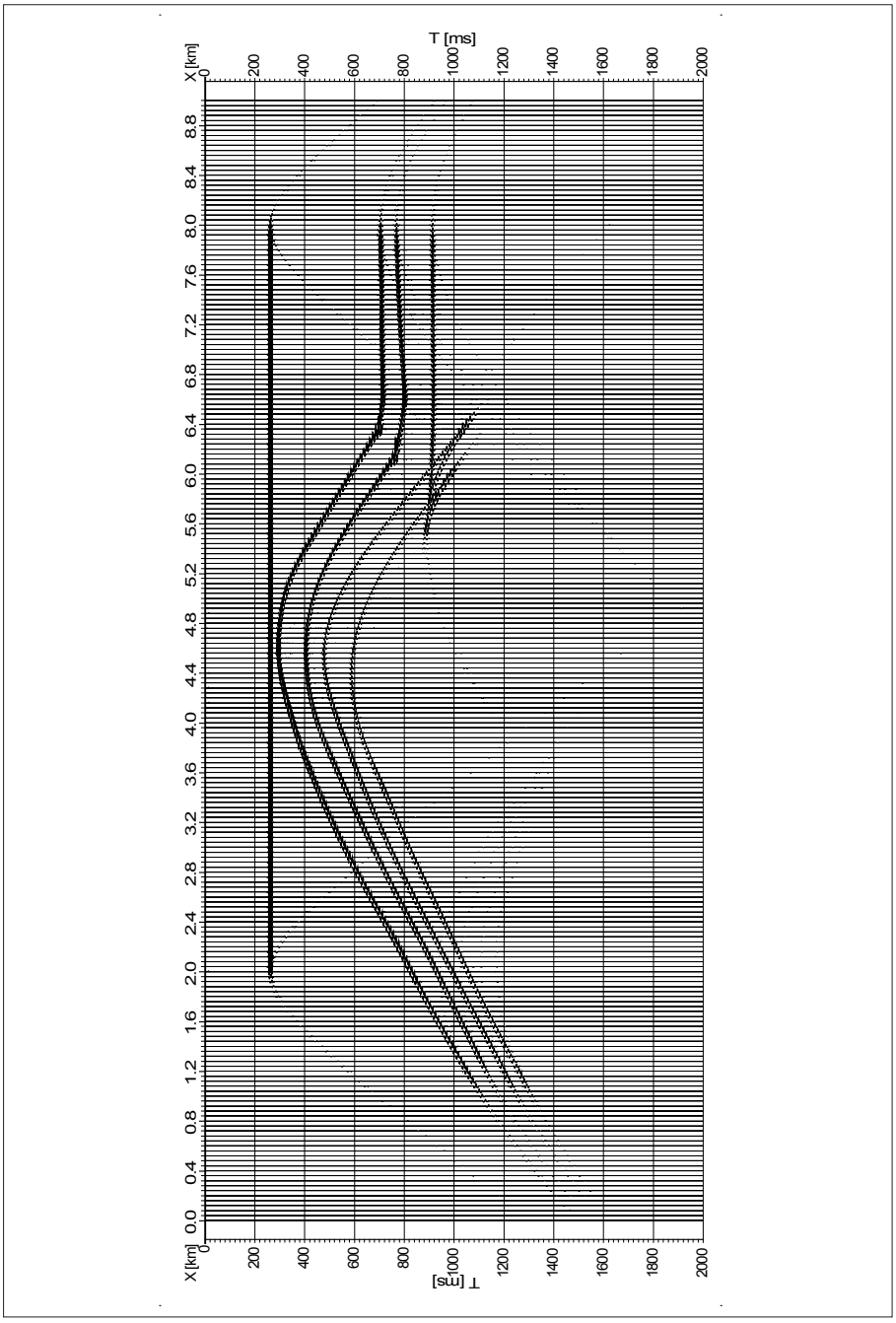

Fig. 3.11. The zero-offset time section from relation (1.23); anisotropy parameters $\varepsilon = 0.3$; $\delta = 0.1$; azimuthal angle $\Psi = 60°$

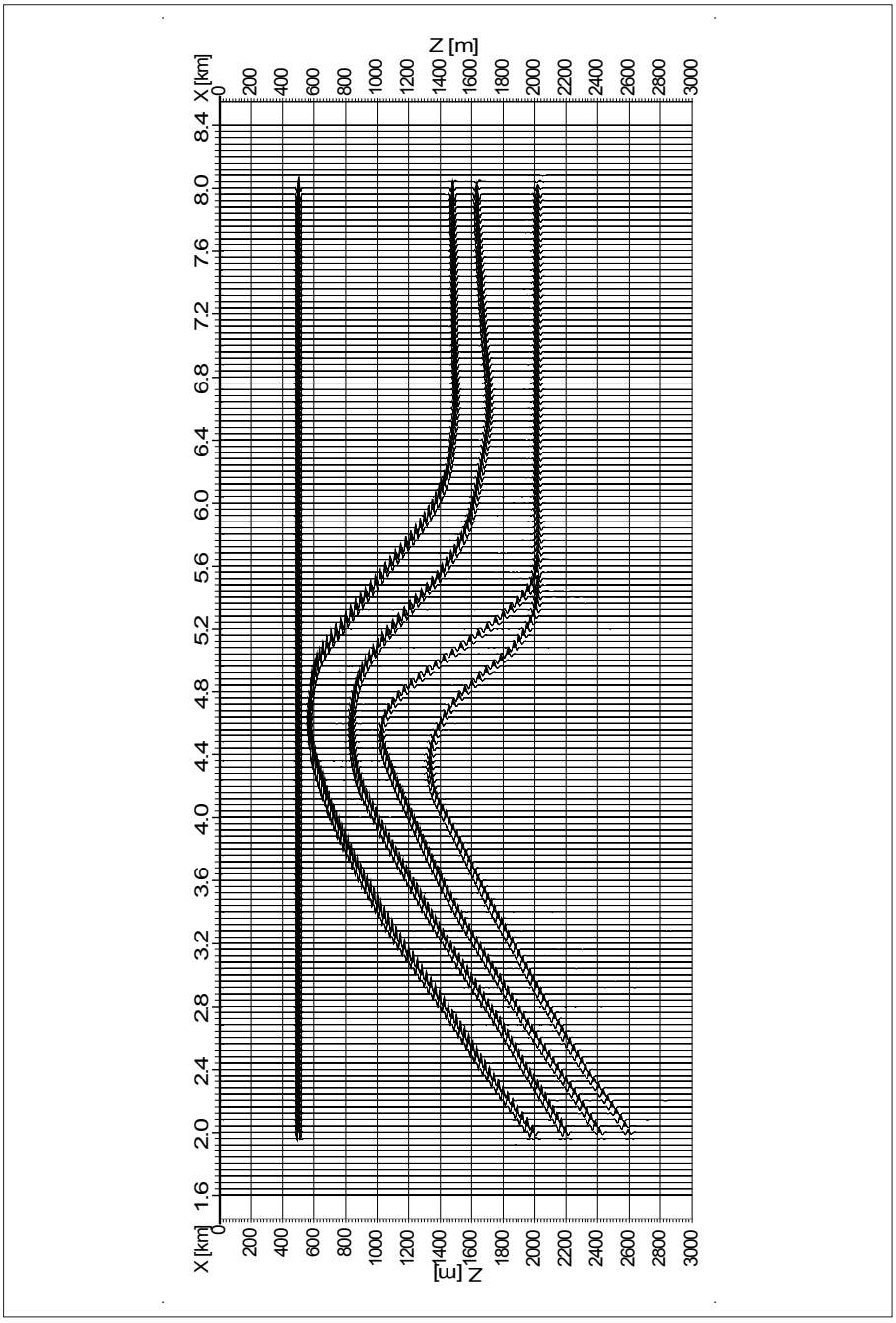

Fig. 3.12. The migration from (3.14) for the zero-offset time section from relation (1.23); anisotropy parameters $\varepsilon = 0.3$; $\delta = 0.1$; azimuthal angle $\Psi = 60°$ (Fig. 3.11)

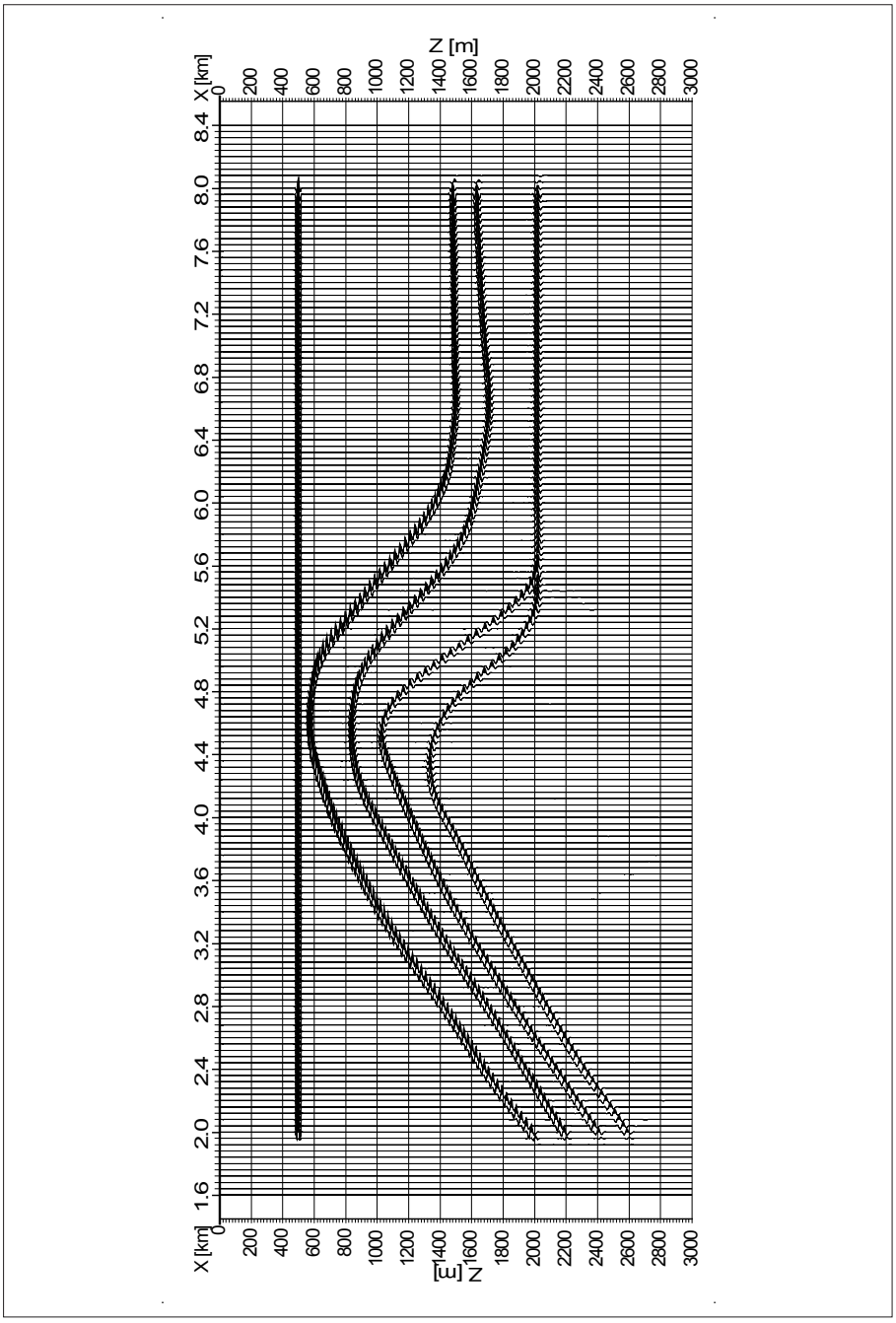

Fig. 3.13. The migration from (3.15) for the zero-offset time section from relation (1.23); anisotropy parameters $\varepsilon = 0.3$; $\delta = 0.1$; azimuthal angle $\Psi = 60°$ (Fig. 3.11)

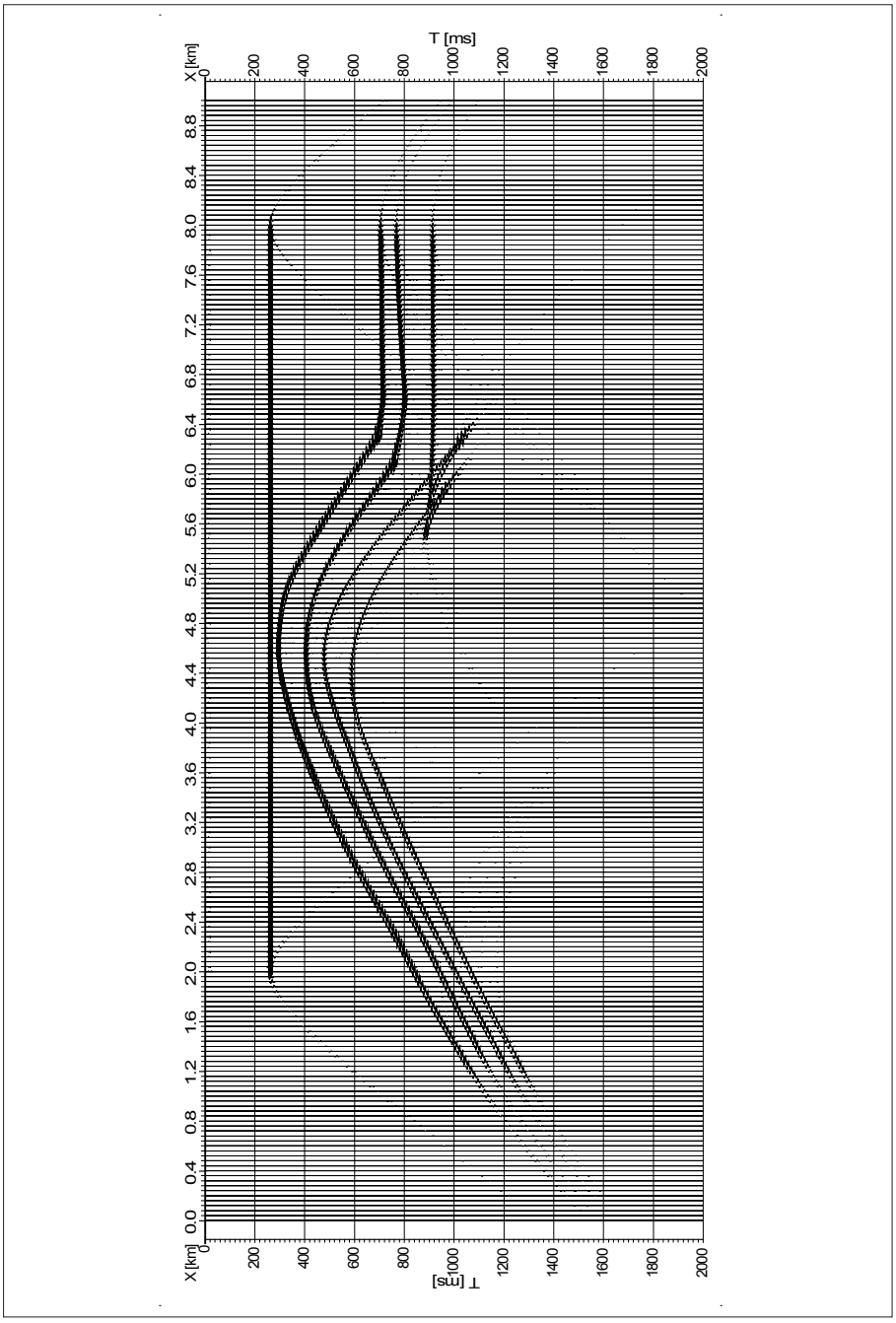

Fig. 3.14. The zero-offset time section from relation (1.23); anisotropy parameters $\varepsilon = 0.3$; $\delta = 0.1$; azimuthal angle $\Psi = 75°$

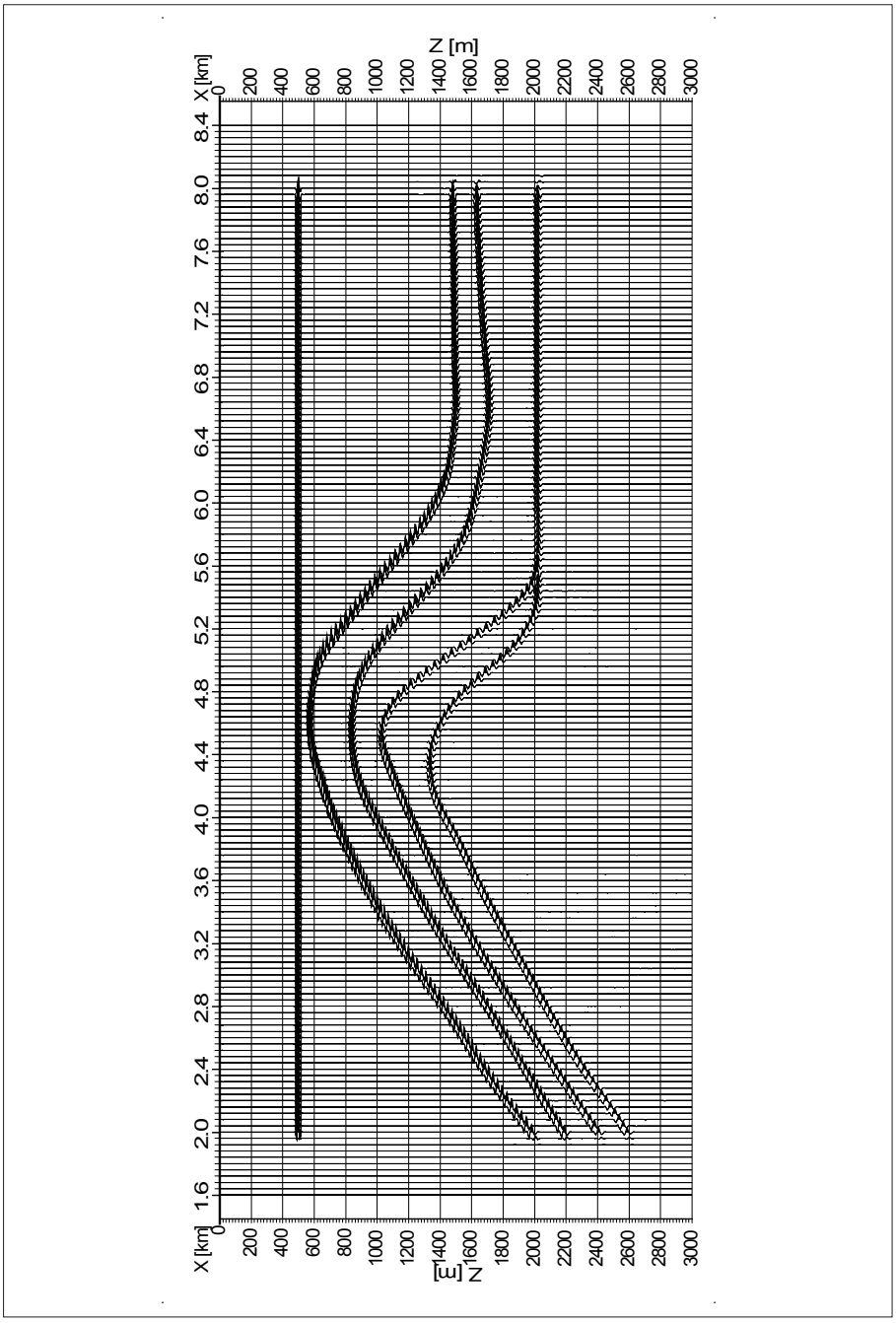

Fig. 3.15. The migration from (3.14) for the zero-offset time section from relation (1.23); anisotropy parameters $\varepsilon = 0.3$; $\delta = 0.1$; azimuthal angle $\Psi = 75°$ (Fig. 3.14)

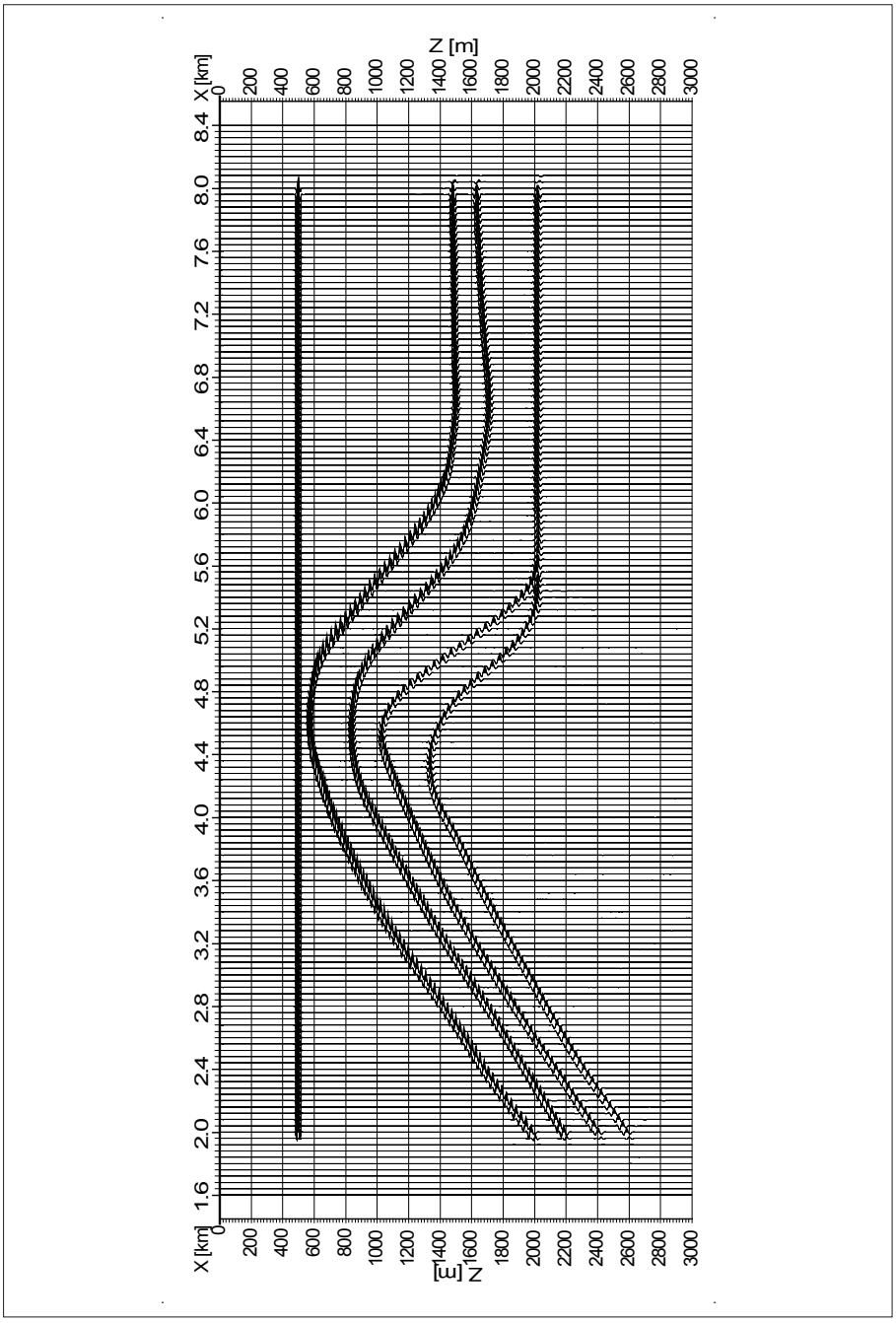

Fig. 3.16. The migration from (3.15) for the zero-offset time section from relation (1.23); anisotropy parameters $\varepsilon = 0.3$; $\delta = 0.1$; azimuthal angle $\Psi = 75°$ (Fig. 3.14)

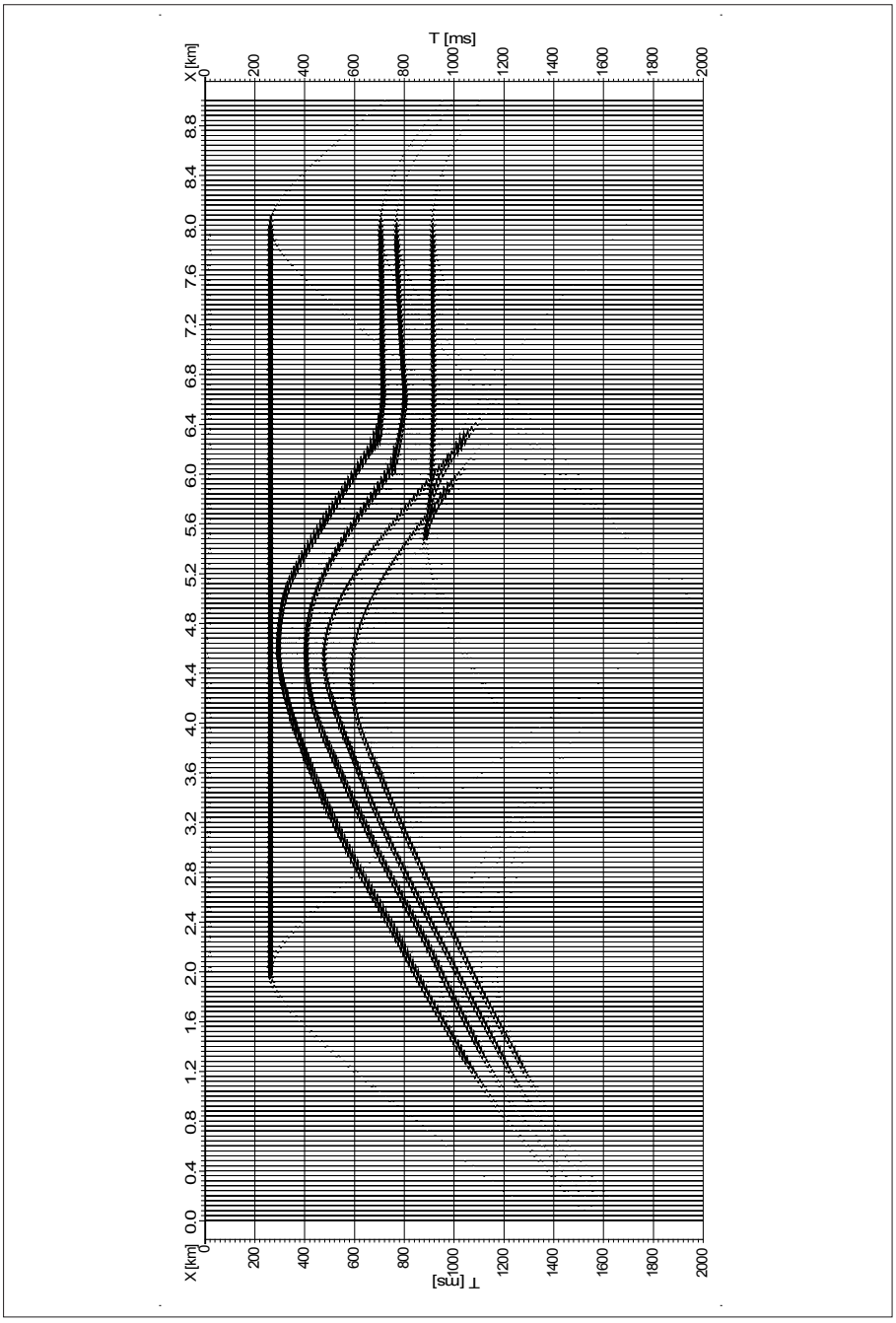

Fig. 3.17. The zero-offset time section from relation (1.23); anisotropy parameters $\varepsilon = 0.3$; $\delta = 0.1$; azimuthal angle $\Psi = 90°$

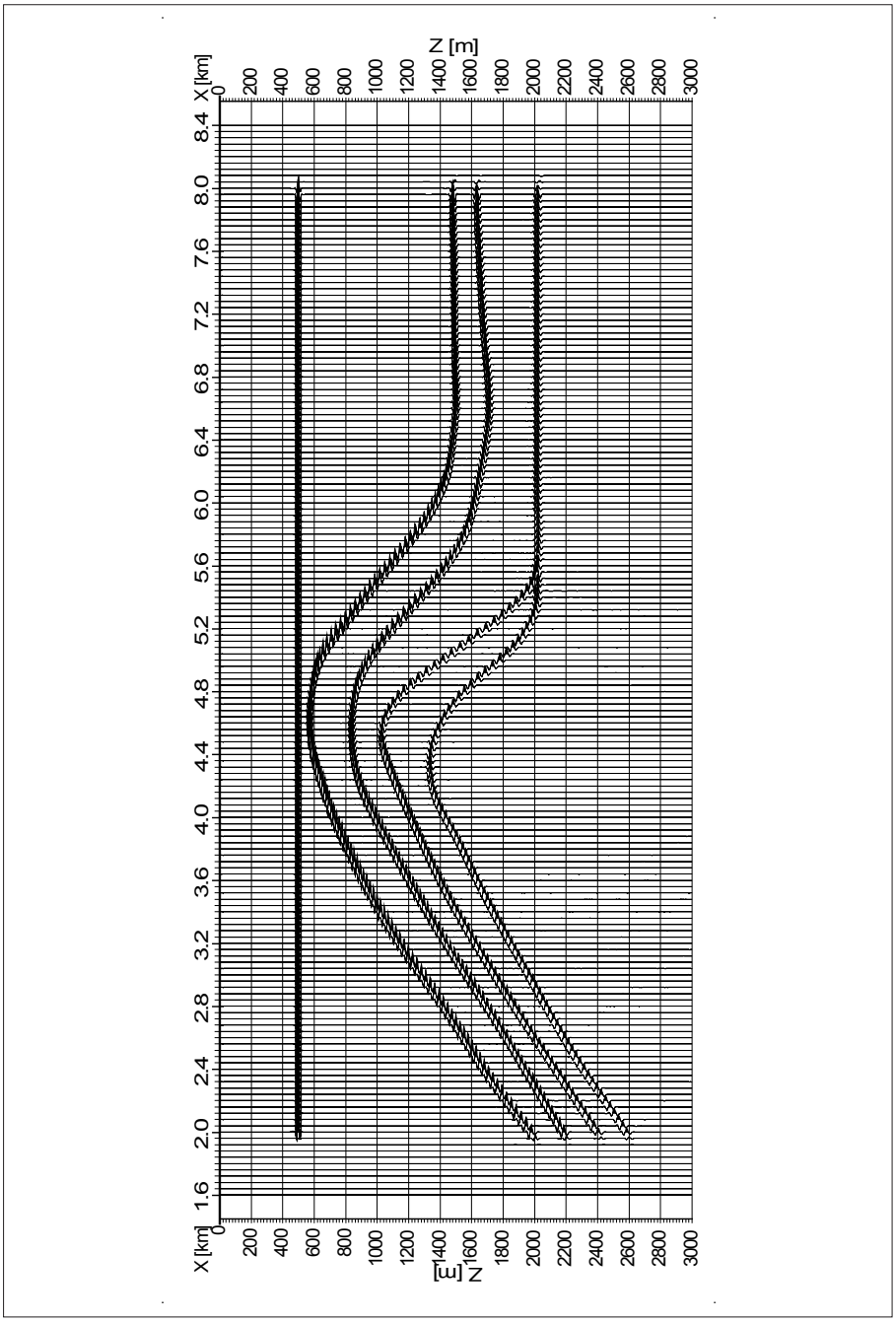

Fig. 3.18. The migration from (3.14) for the zero-offset time section from relation (1.23); anisotropy parameters $\varepsilon = 0.3$; $\delta = 0.1$; azimuthal angle $\Psi = 90°$ (Fig. 3.17)

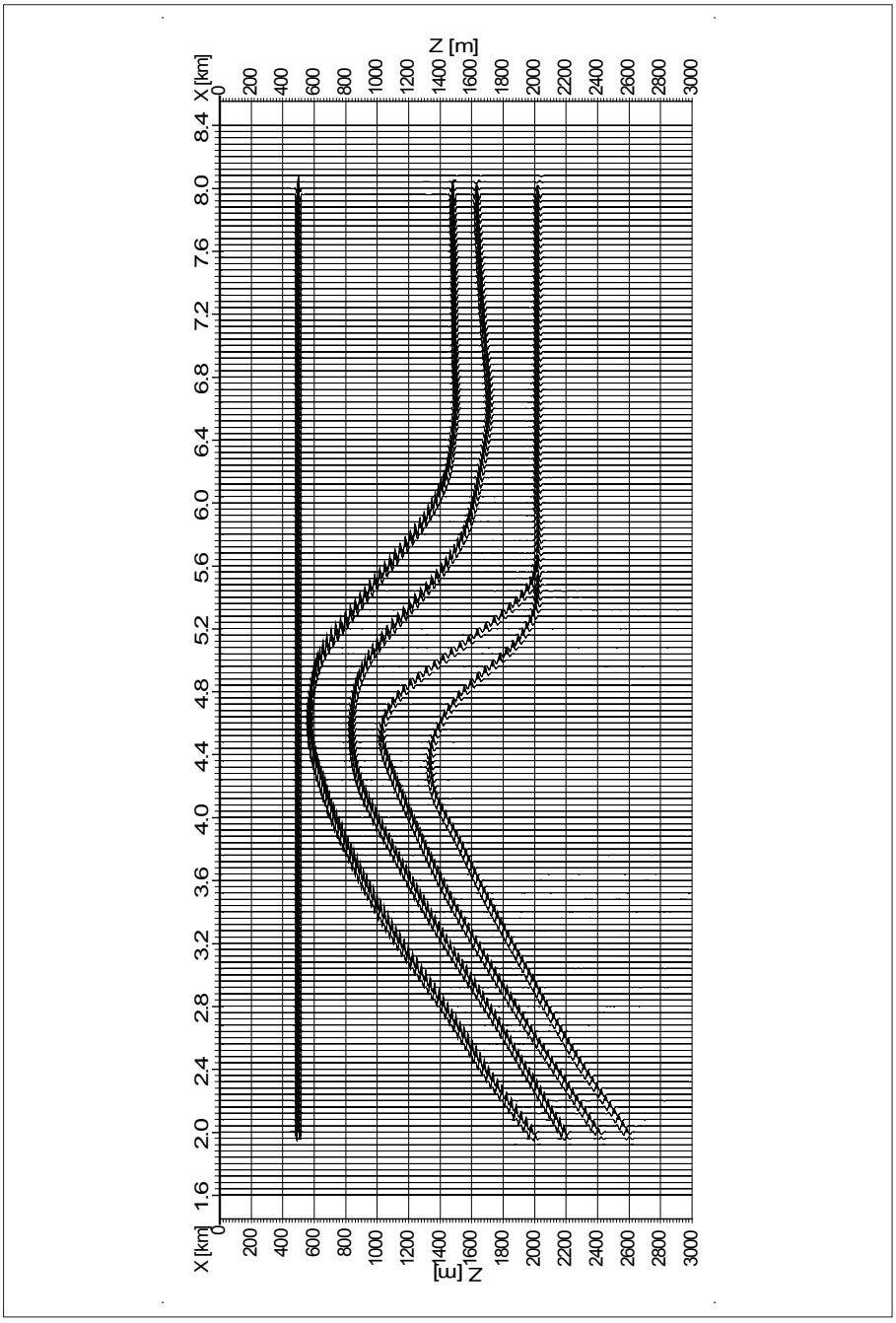

Fig. 3.19. The migration from (3.15) for the zero-offset time section from relation (1.23); anisotropy parameters $\varepsilon = 0.3$; $\delta = 0.1$; azimuthal angle $\Psi = 90°$ (Fig. 3.17)

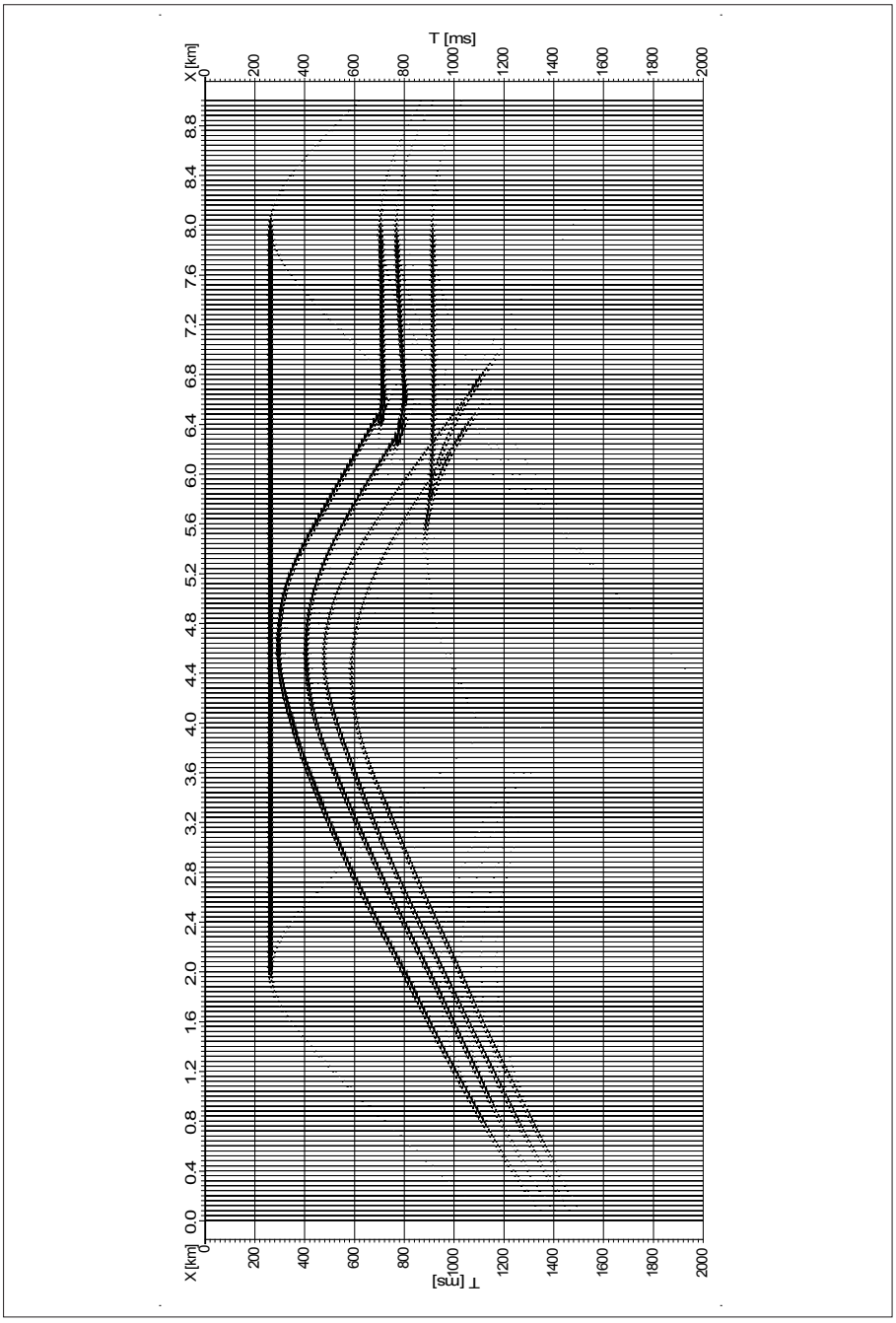

Fig. 3.20. The zero-offset time section from relation (1.28); anisotropy parameters $\varepsilon = 0.3$; $\delta = 0.1$; azimuthal angle $\Psi = 30°$

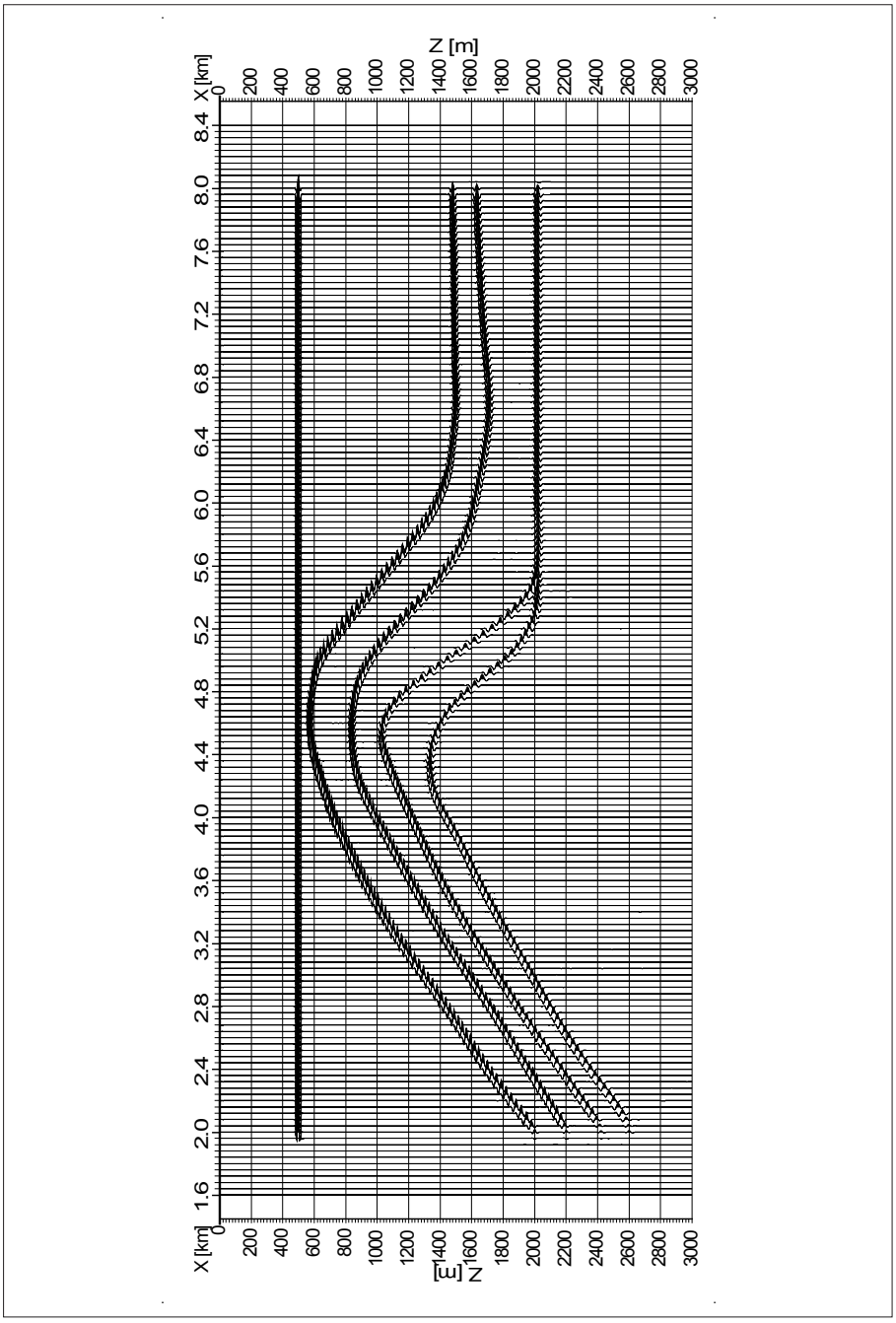

Fig. 3.21. The migration from (3.14) for the zero-offset time section from relation (1.28); anisotropy parameters $\varepsilon = 0.3$; $\delta = 0.1$; azimuthal angle $\Psi = 30°$ (Fig. 3.20)

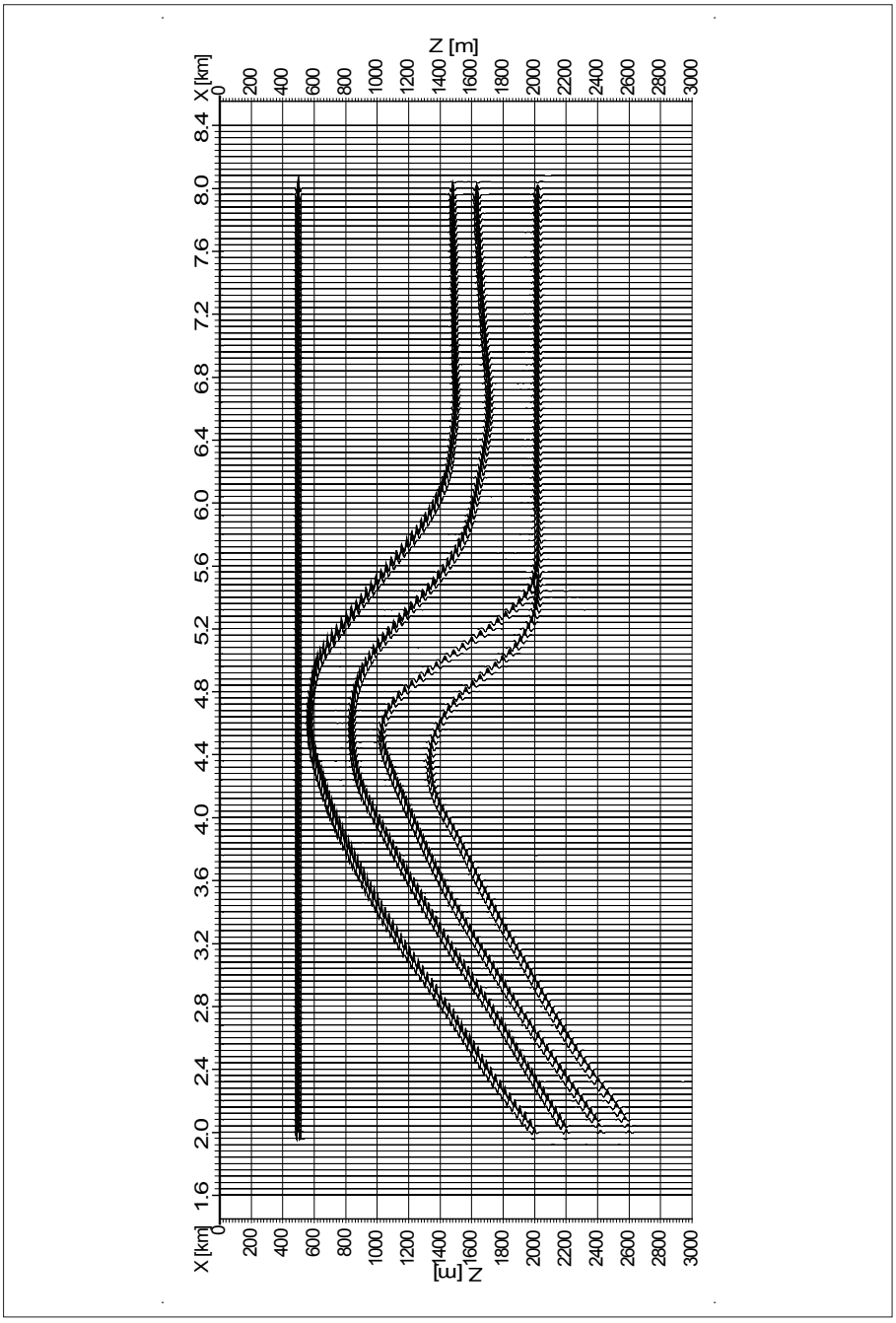

Fig. 3.22. The migration from (3.15) for the zero-offset time section from relation (1.28); anisotropy parameters $\varepsilon = 0.3$; $\delta = 0.1$; azimuthal angle $\Psi = 30°$ (Fig. 3.20)

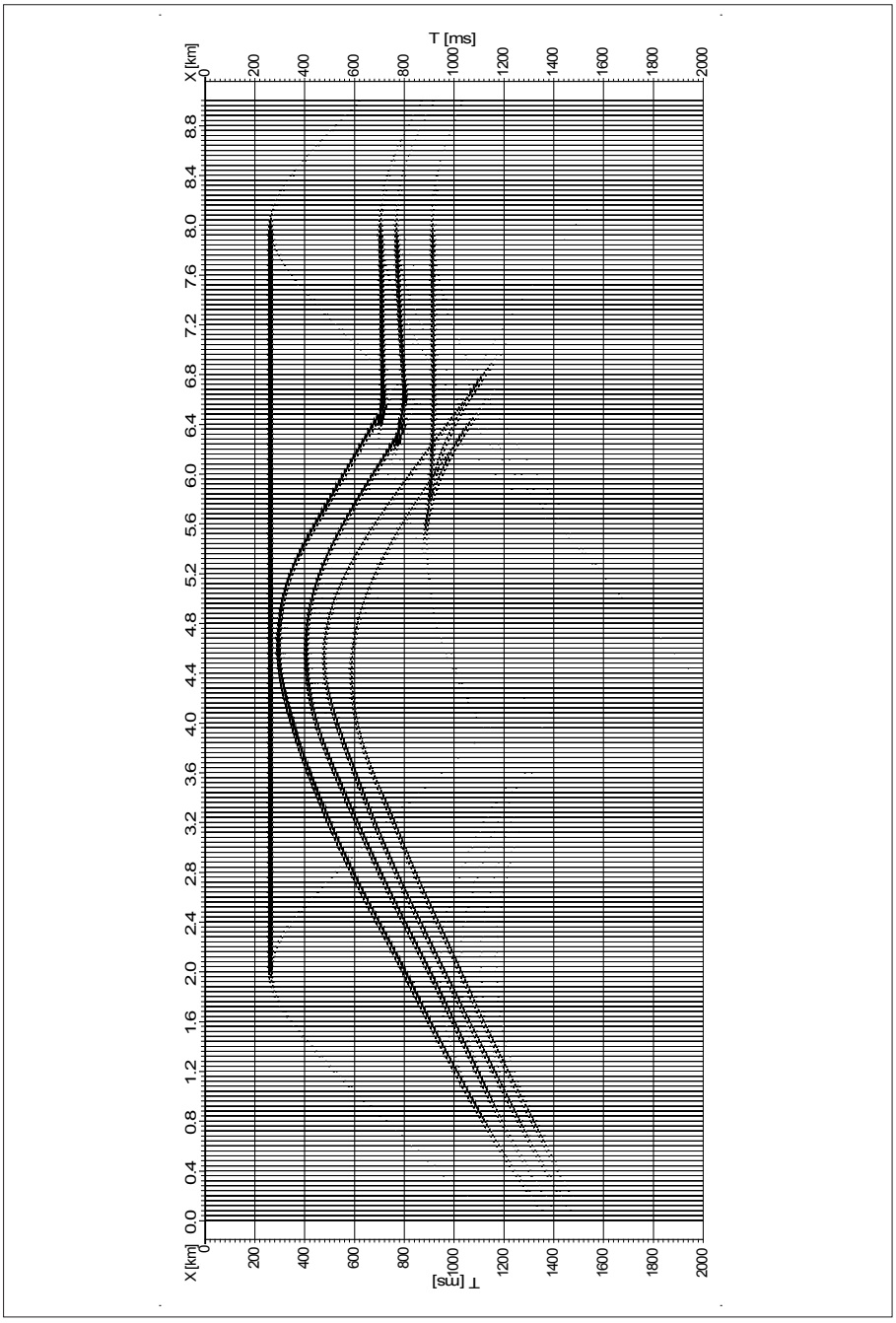

Fig. 3.23. The zero-offset time section from relation (1.29); anisotropy parameters $\varepsilon = 0.3$; $\delta = 0.1$; azimuthal angle $\Psi = 30°$

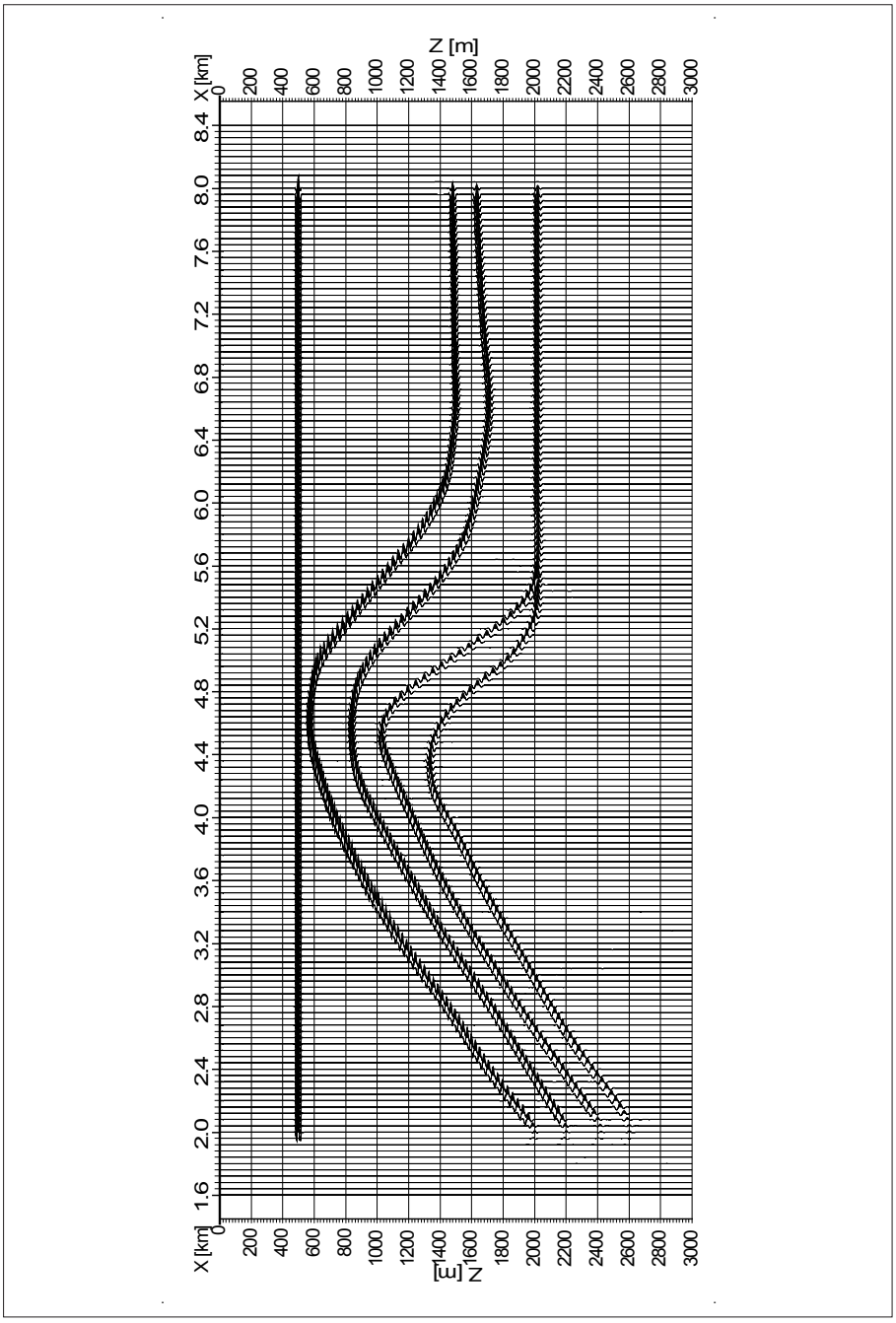

Fig. 3.24. The migration from (3.14) for the zero-offset time section from relation (1.29); anisotropy parameters $\varepsilon = 0.3$; $\delta = 0.1$; azimuthal angle $\Psi = 30°$ (Fig. 3.23)

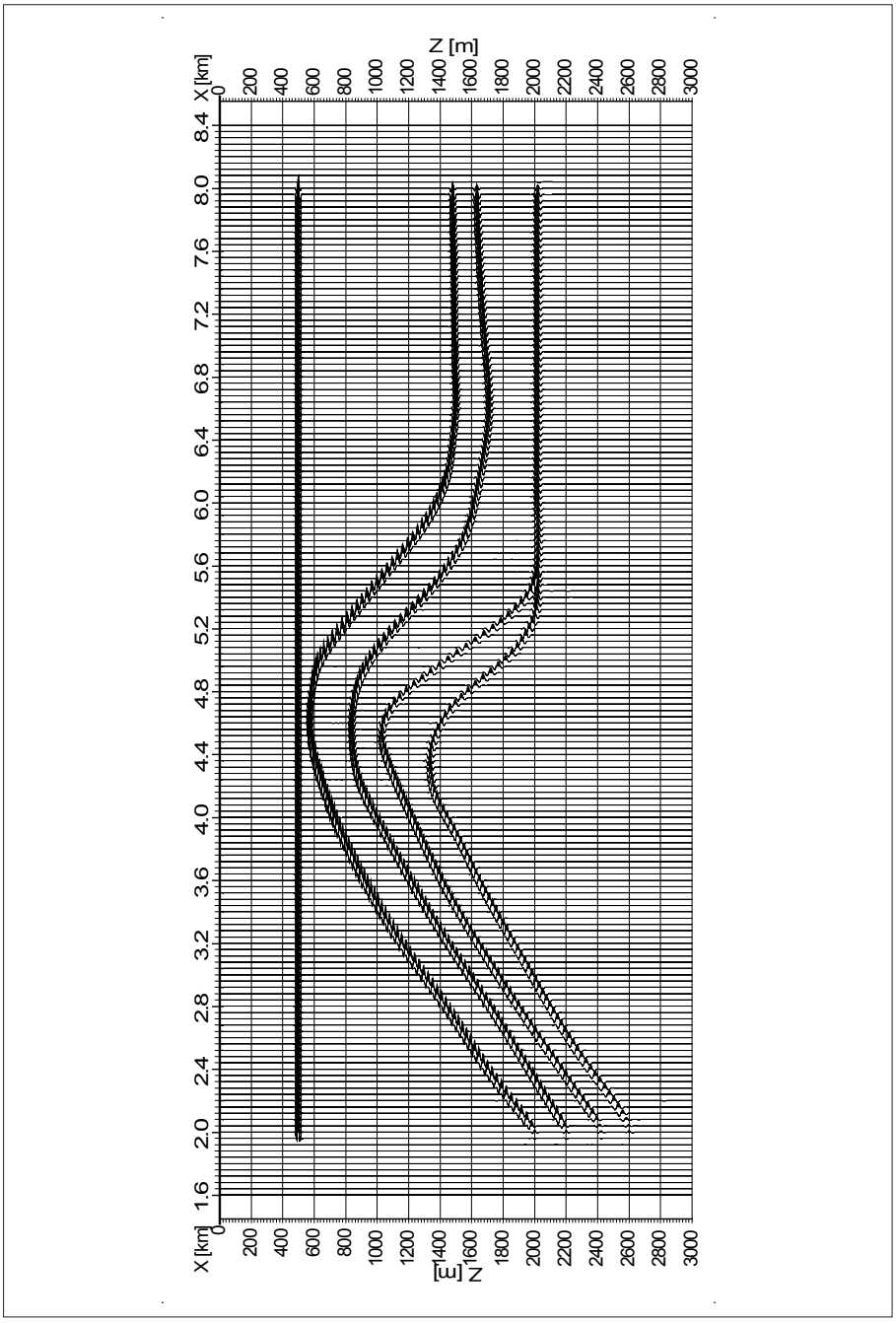

Fig. 3.25. The migration from (3.15) for the zero-offset time section from relation (1.29); anisotropy parameters $\varepsilon = 0.3$; $\delta = 0.1$; azimuthal angle $\Psi = 30°$ (Fig. 3.23)

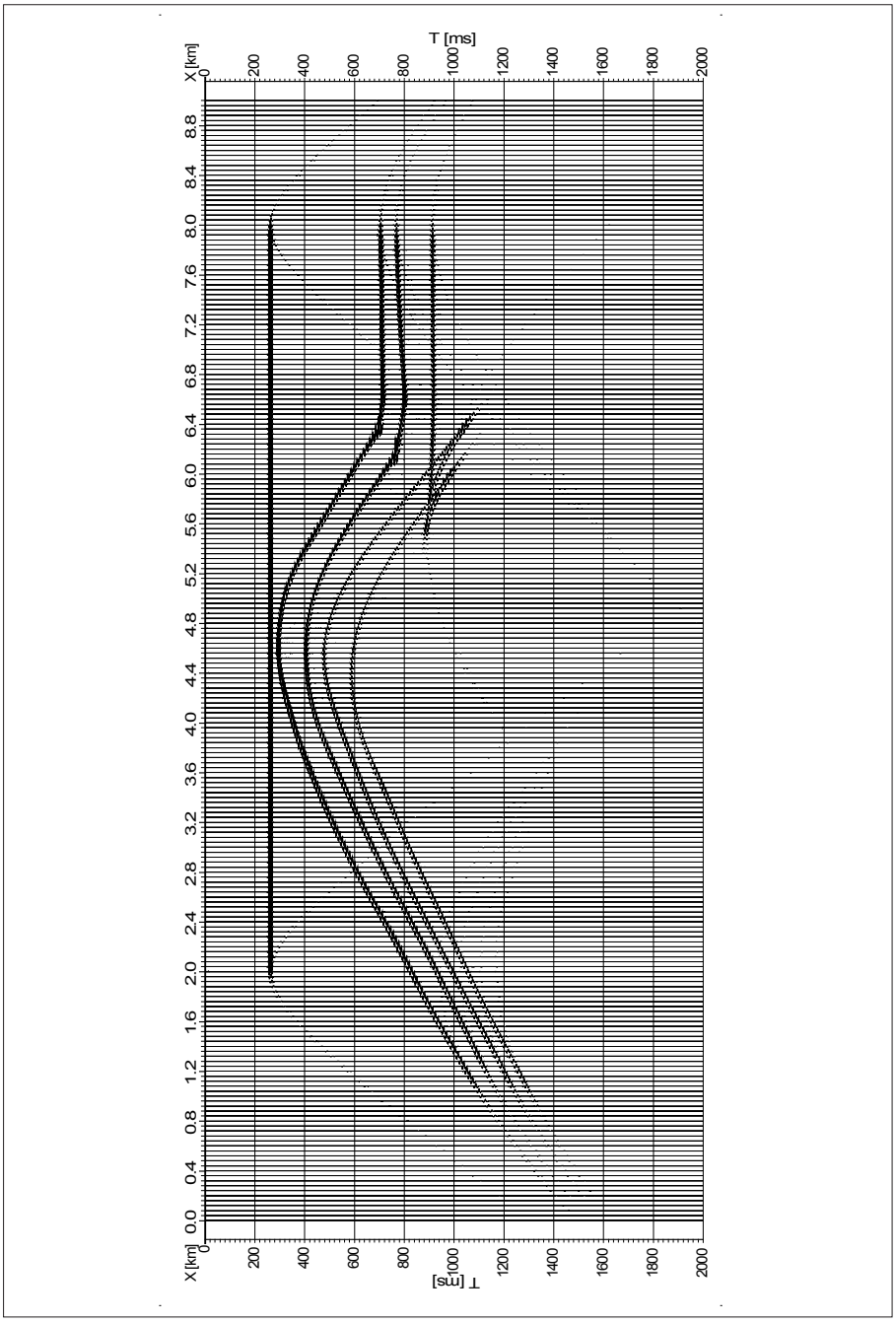

Fig. 3.26. The zero-offset time section from relation (1.28); anisotropy parameters $\varepsilon = 0.3$; $\delta = 0.1$; azimuthal angle $\Psi = 60°$

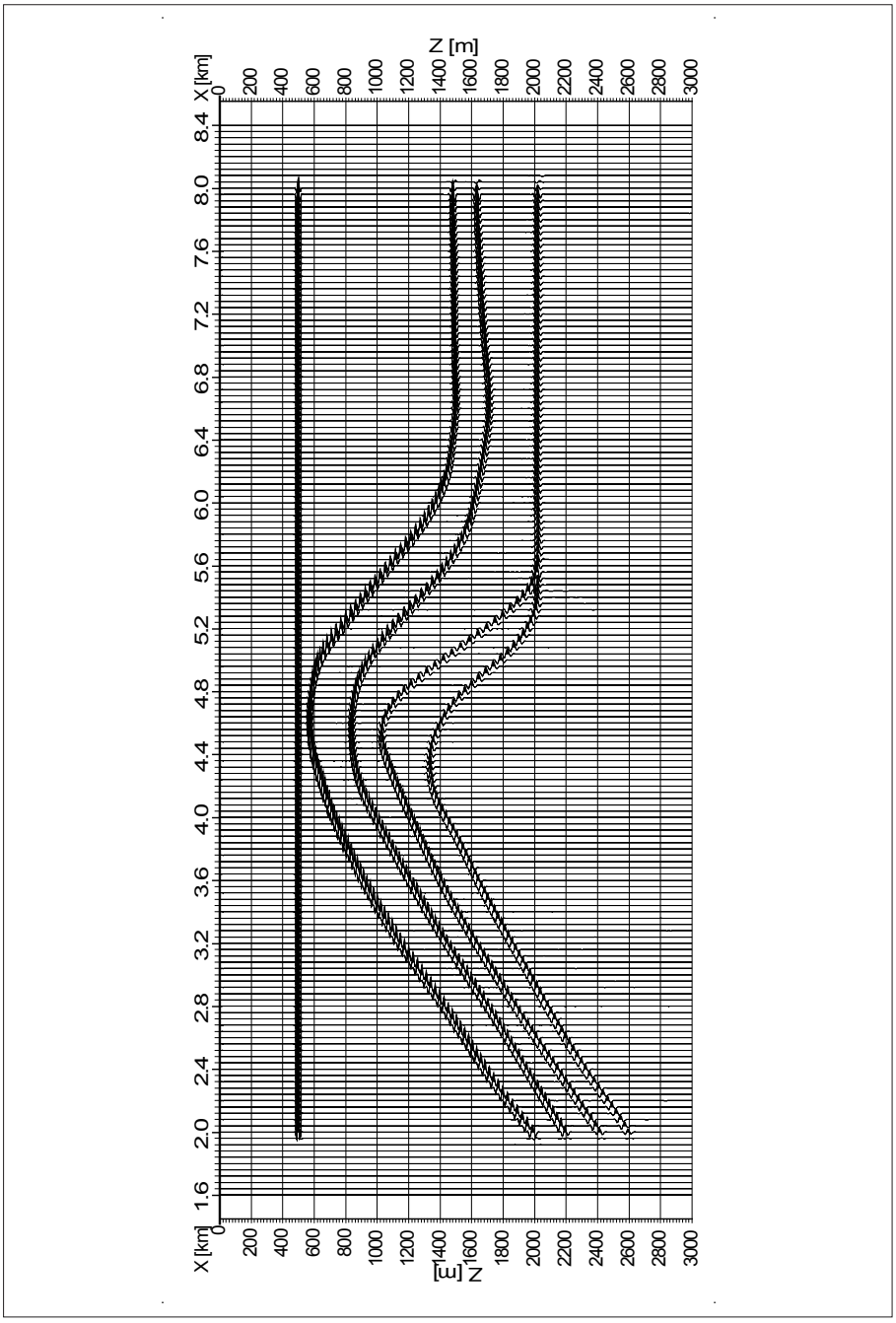

Fig. 3.27. The migration from (3.14) for the zero-offset time section from relation (1.28); anisotropy parameters $\varepsilon = 0.3$; $\delta = 0.1$; azimuthal angle $\Psi = 60°$ (Fig. 3.26)

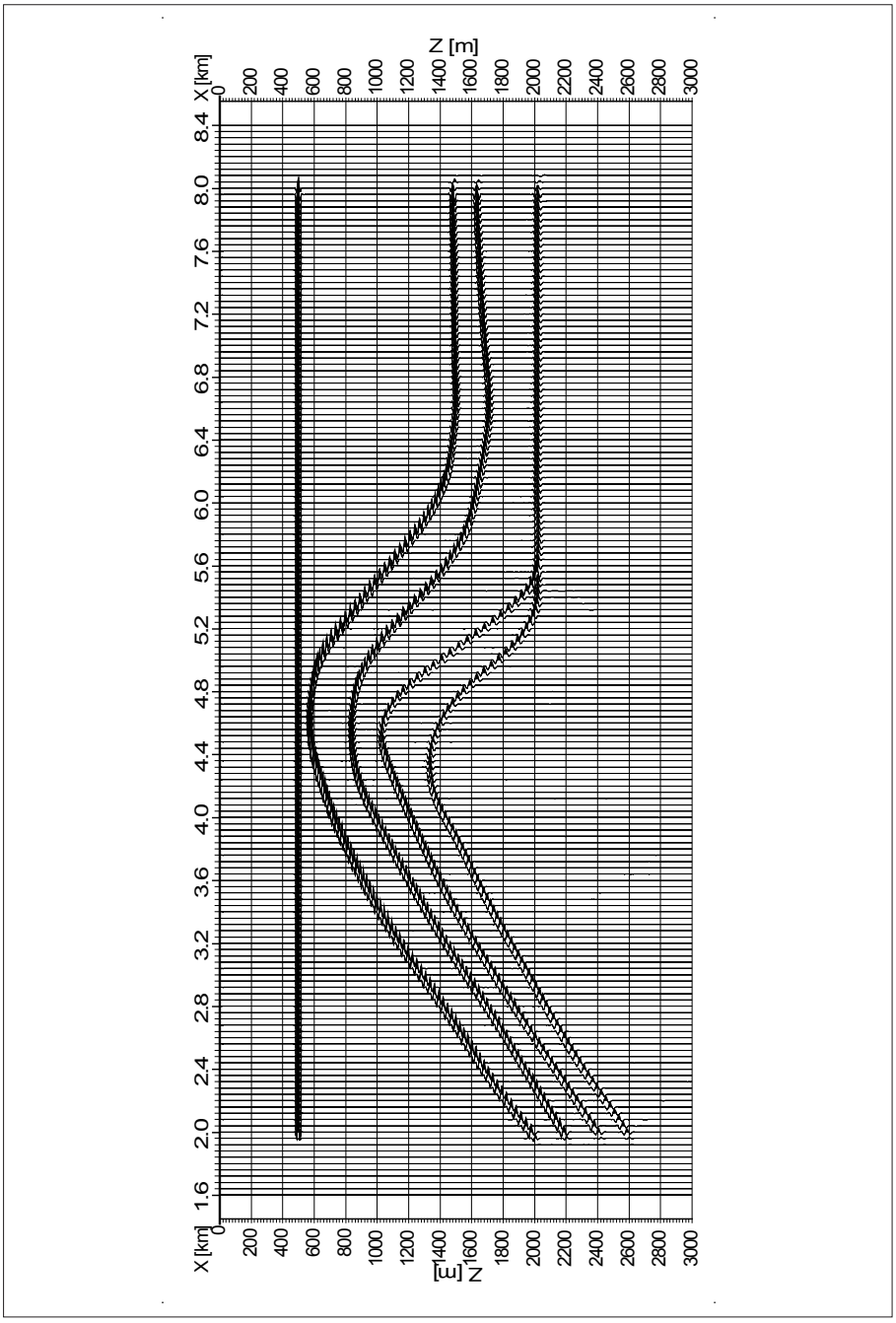

Fig. 3.28. The migration from (3.15) for the zero-offset time section from relation (1.28); anisotropy parameters $\varepsilon = 0.3$; $\delta = 0.1$; azimuthal angle $\Psi = 60°$ (Fig. 3.26)

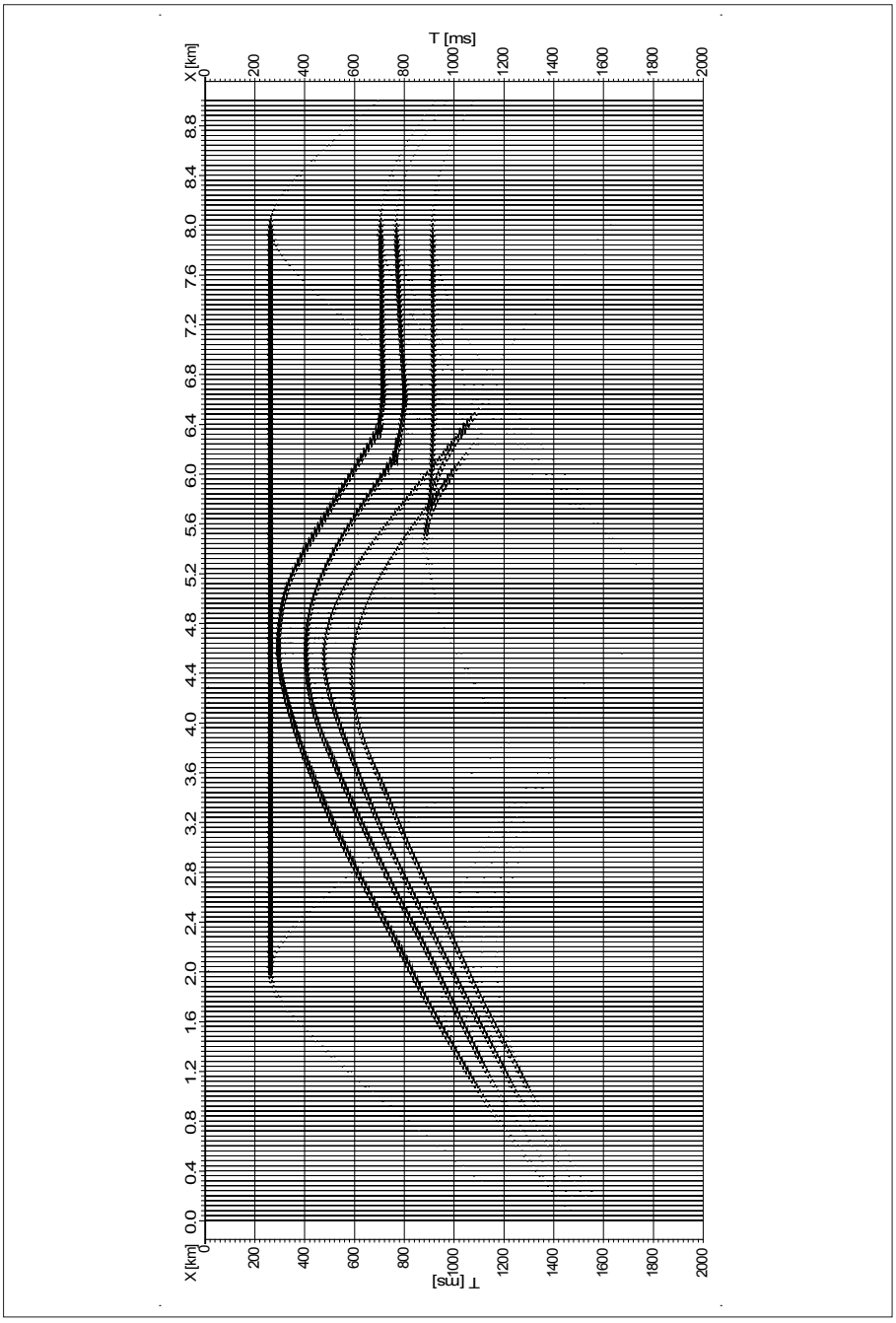

Fig. 3.29. The zero-offset time section from relation (1.29); anisotropy parameters $\varepsilon = 0.3$; $\delta = 0.1$; azimuthal angle $\Psi = 60°$

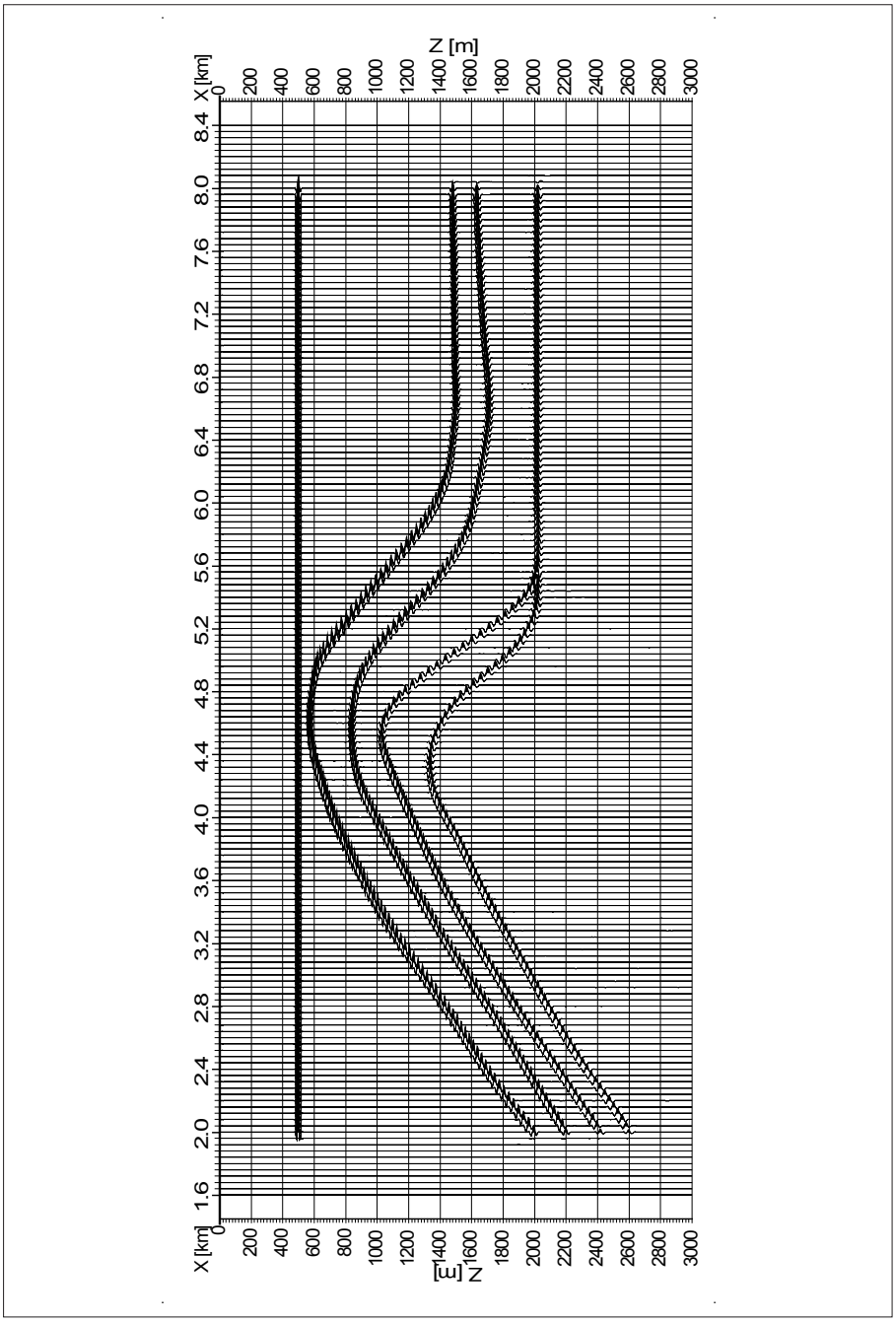

Fig. 3.30. The migration from (3.14) for the zero-offset time section from relation (1.29); anisotropy parameters $\varepsilon = 0.3$; $\delta = 0.1$; azimuthal angle $\Psi = 60°$ (Fig. 3.29)

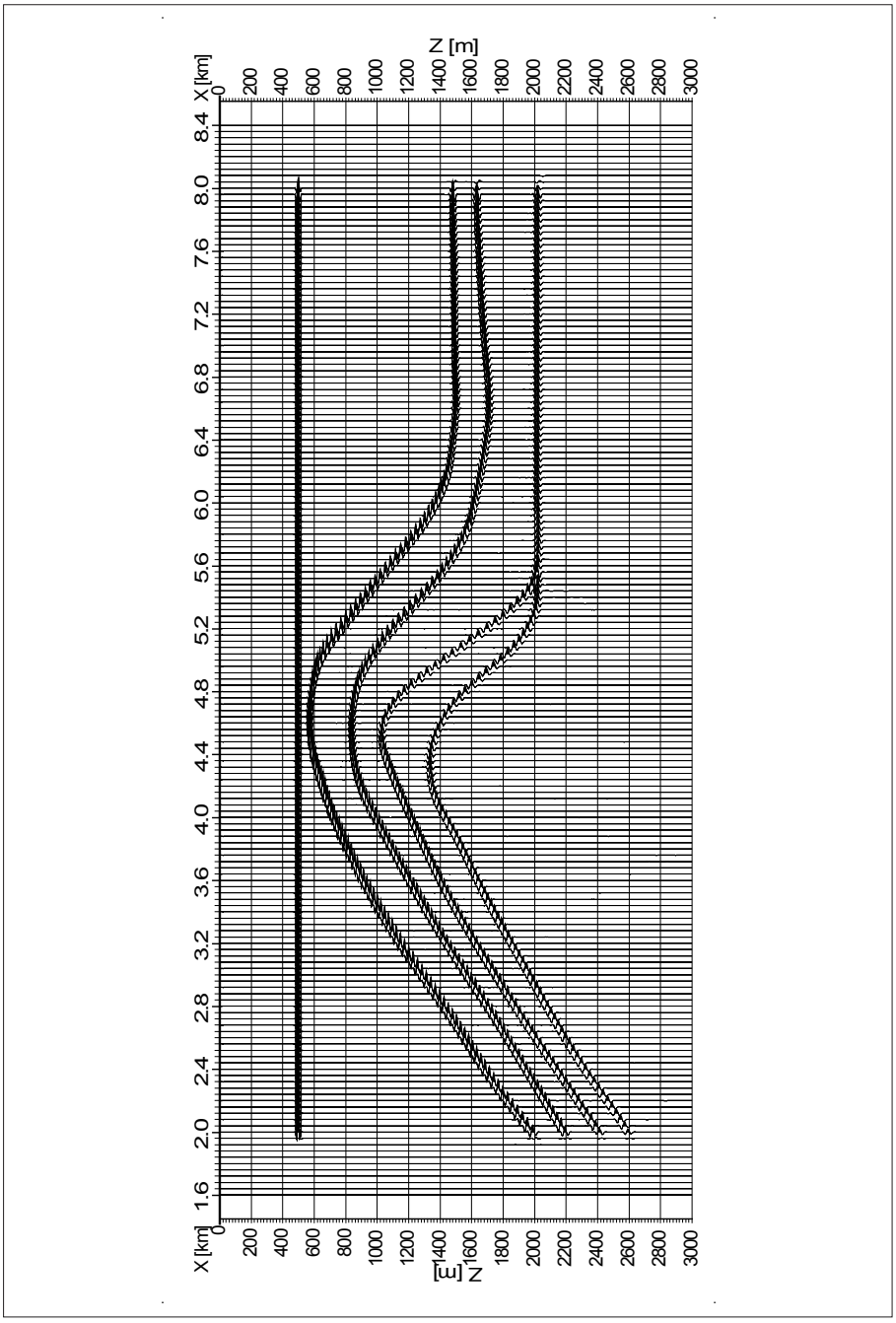

Fig. 3.31. The migration from (3.15) for the zero-offset time section from relation (1.29); anisotropy parameters $\varepsilon = 0.3$; $\delta = 0.1$; azimuthal angle $\Psi = 60°$ (Fig. 3.29)

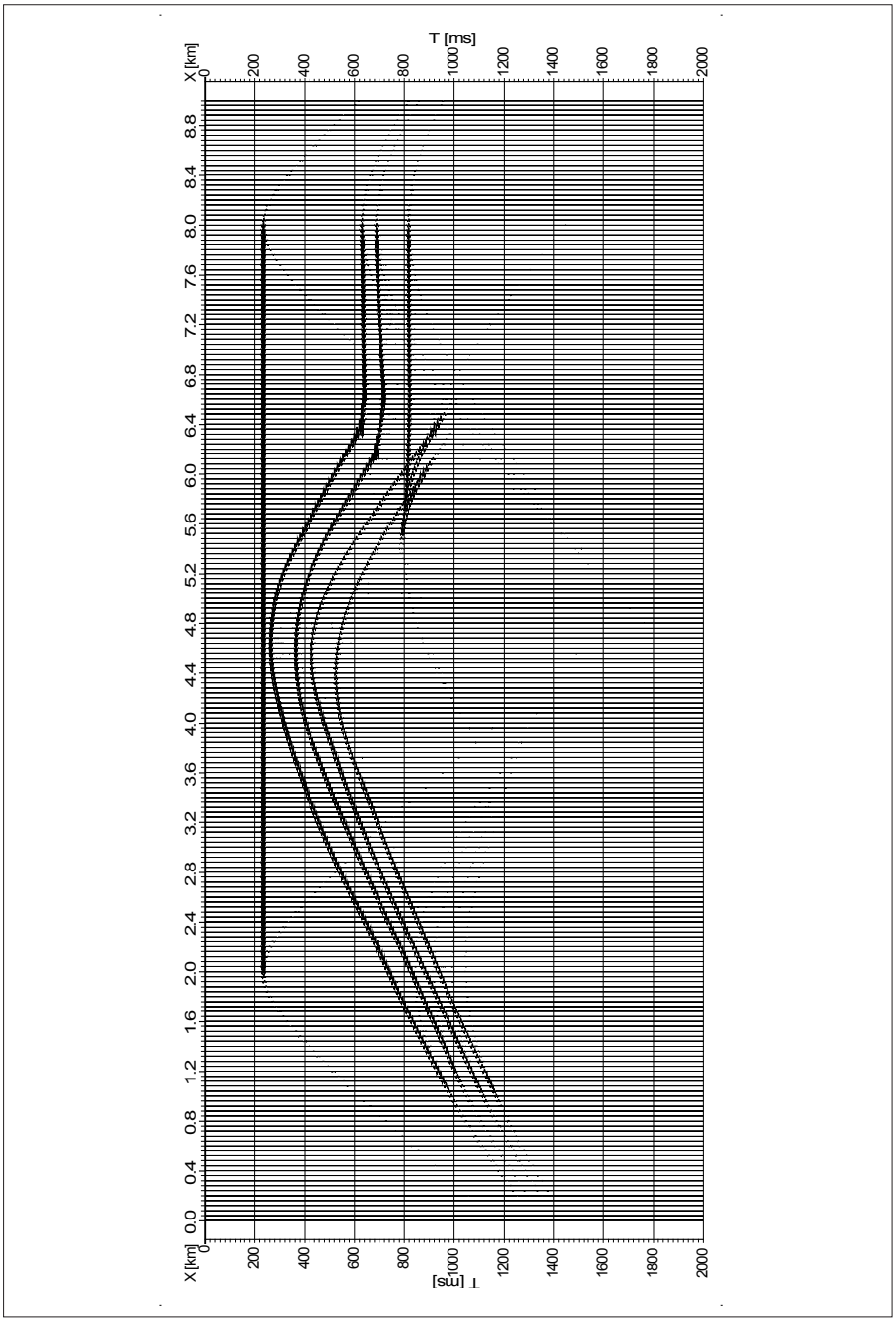

Fig. 3.32. The zero-offset time section from relation (1.23); anisotropy parameters $\varepsilon = 0.5$; $\delta = 0.1$; azimuthal angle $\Psi = 45°$

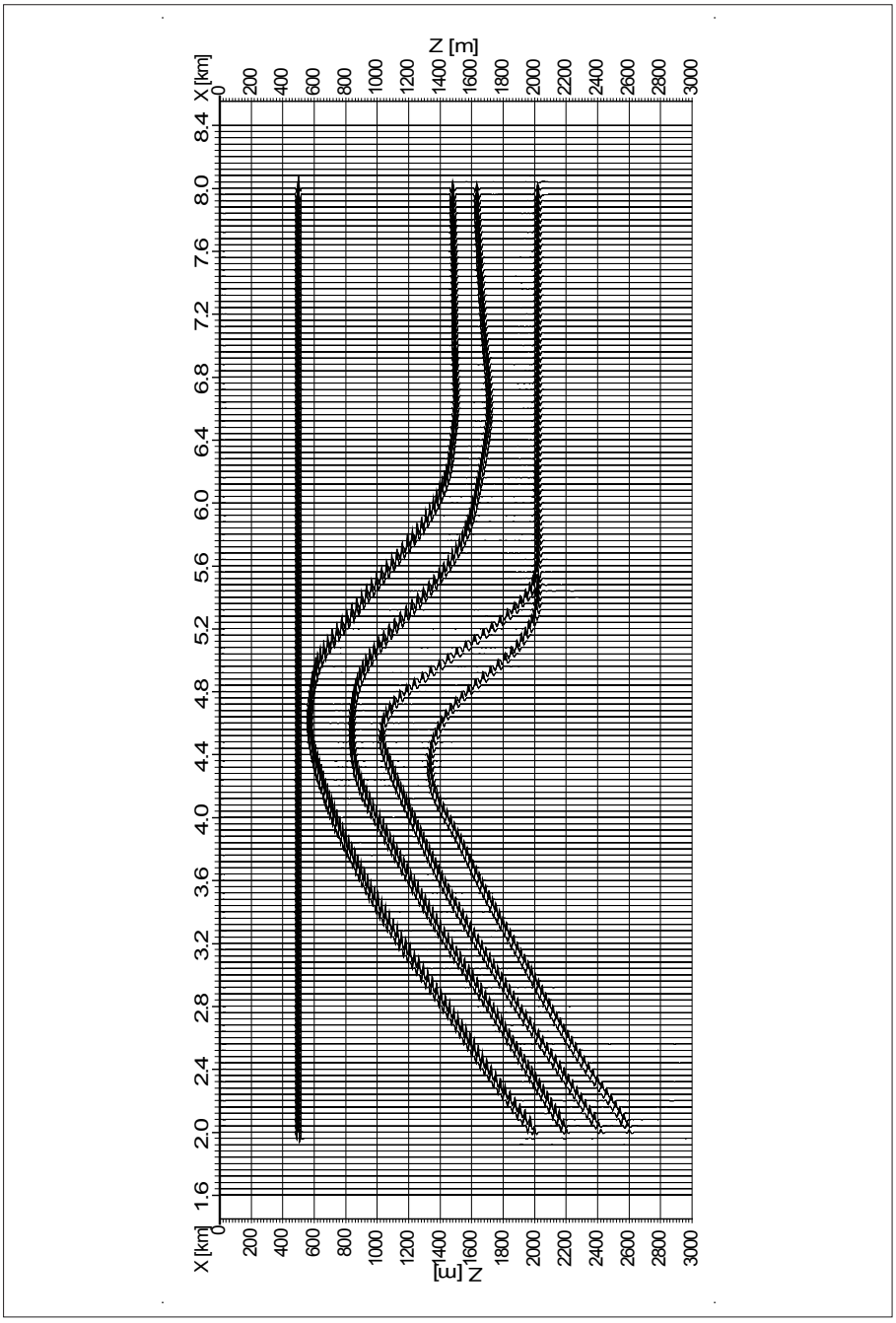

Fig. 3.33. The migration from (3.14) for the zero-offset time section from relation (1.23); anisotropy parameters $\varepsilon = 0.5$; $\delta = 0.1$; azimuthal angle $\Psi = 45°$ (Fig. 3.32)

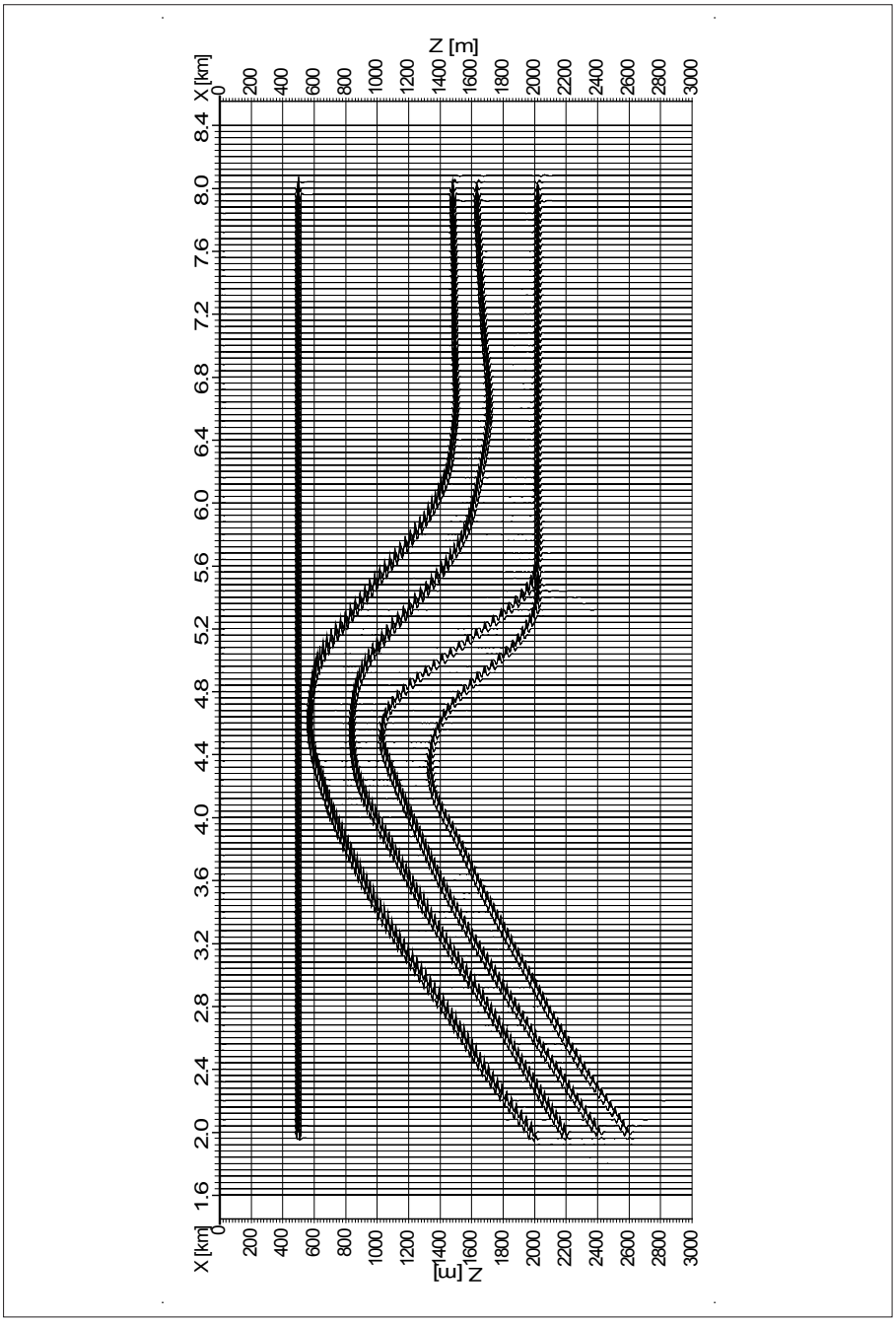

Fig. 3.34. The migration from (3.15) for the zero-offset time section from relation (1.23); anisotropy parameters $\varepsilon = 0.5$; $\delta = 0.1$; azimuthal angle $\Psi = 45°$ (Fig. 3.32)

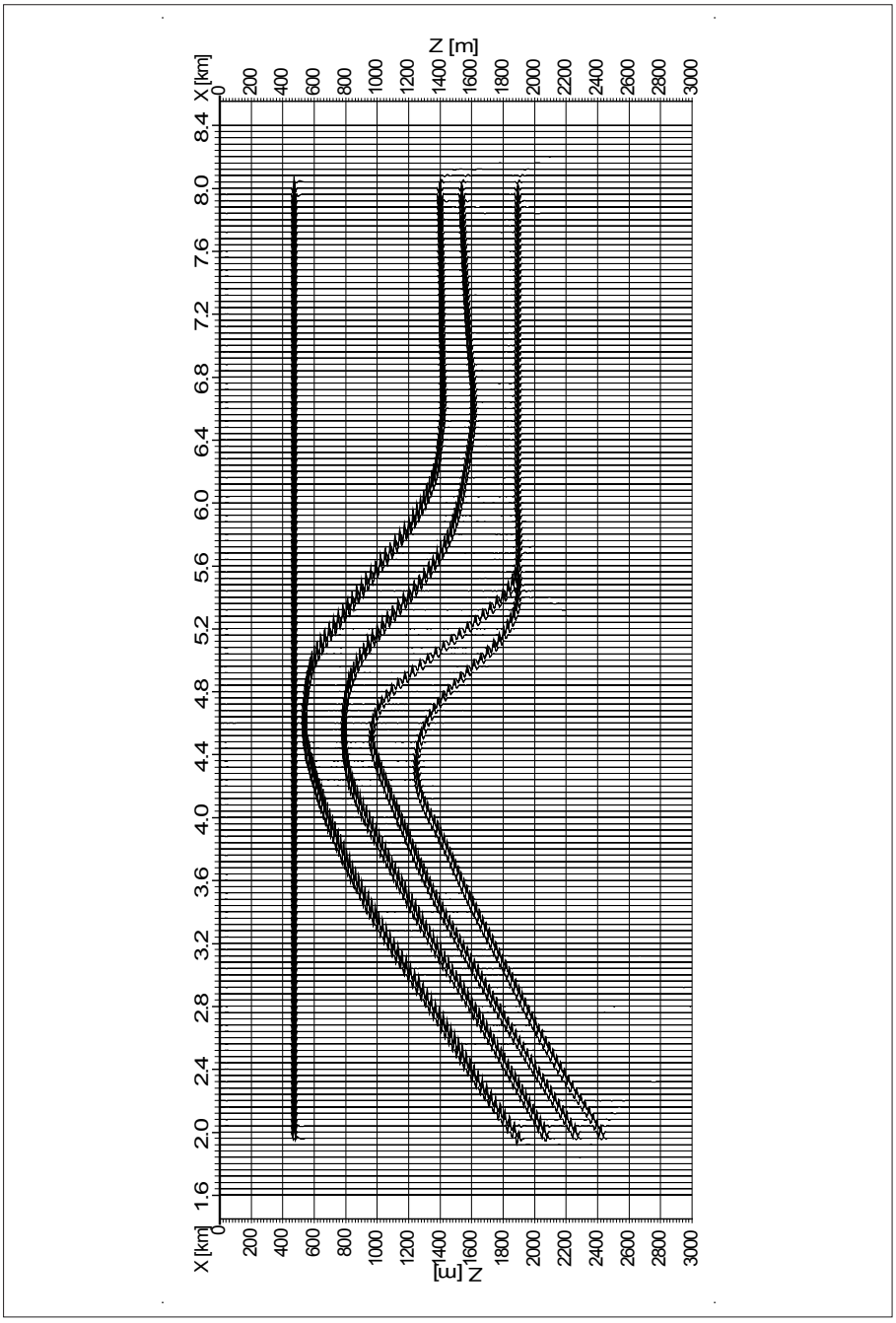

Fig. 3.35. The migration from (3.14) for anisotropy parameters $\varepsilon = 0.4$; $\delta = 0.2$; azimuthal angle $\Psi = 45°$ for the zero-offset time section from relation (1.23) for anisotropy parameters $\varepsilon = 0.5$; $\delta = 0.1$; azimuthal angle $\Psi = 45°$ (Fig. 3.32)

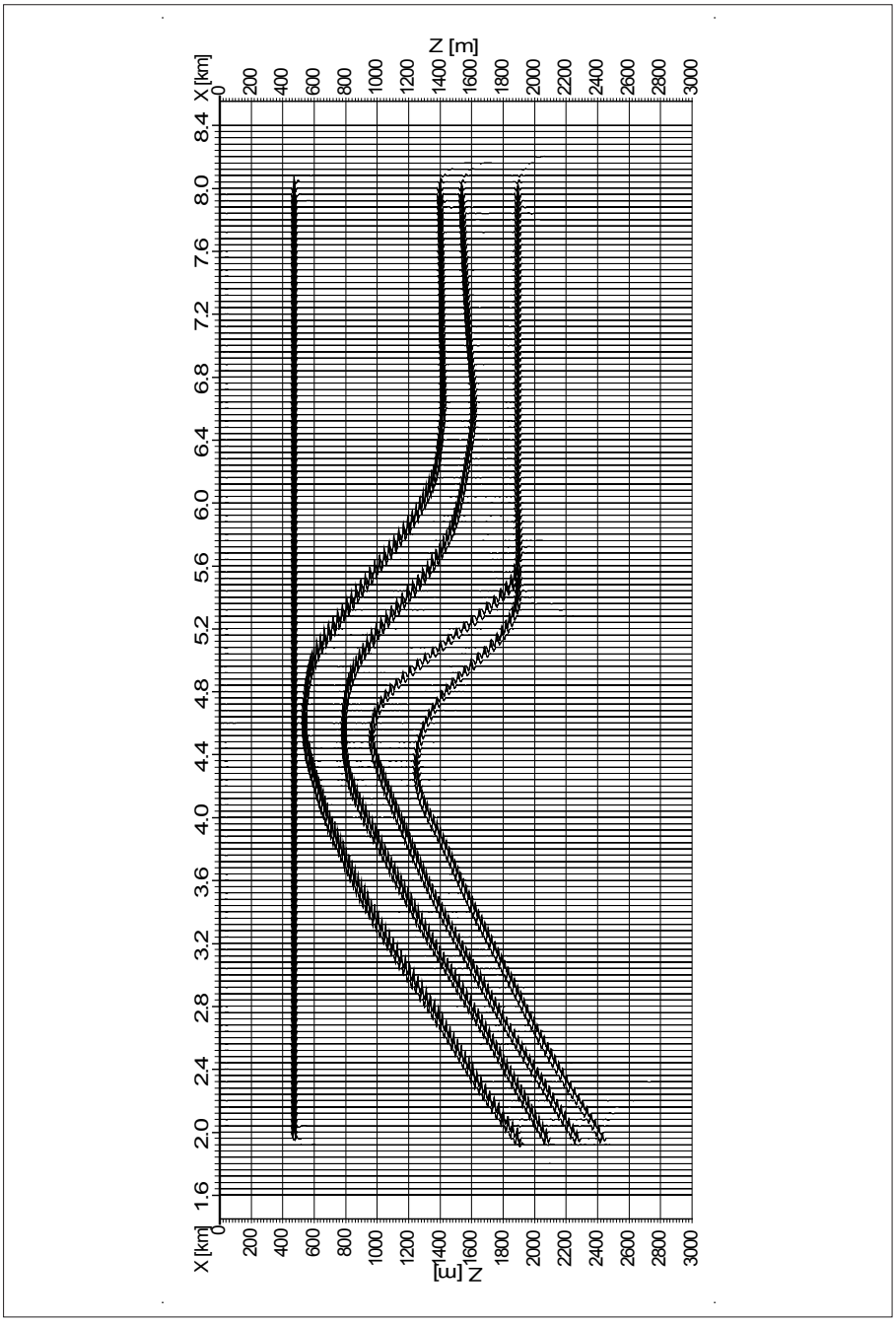

Fig. 3.36. The migration from (3.15) for anisotropy parameters $\varepsilon = 0.4$; $\delta = 0.2$; azimuthal angle $\Psi = 45°$ for the zero-offset time section from relation (1.23) for anisotropy parameters $\varepsilon = 0.5$; $\delta = 0.1$; azimuthal angle $\Psi = 45°$ (Fig. 3.32)

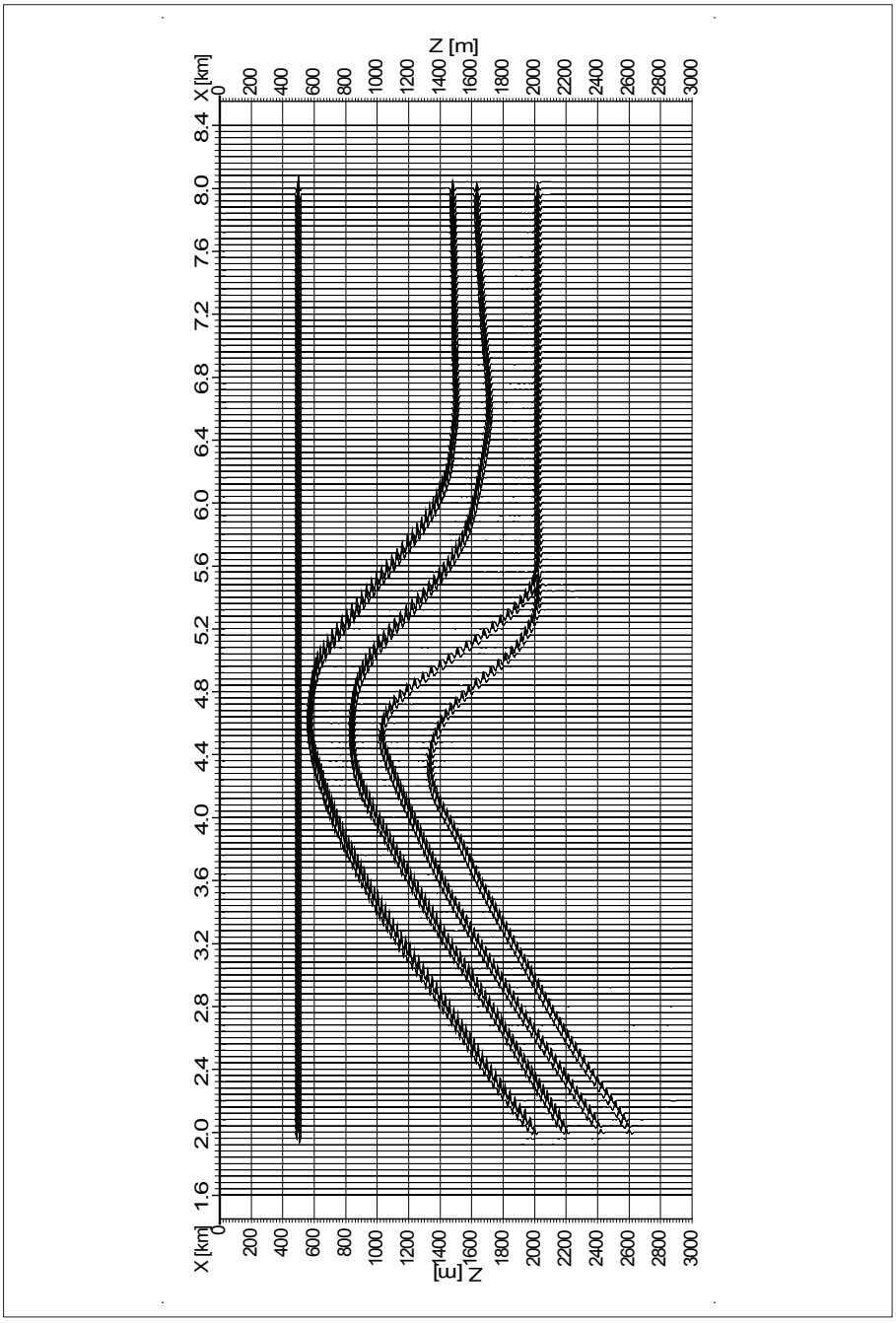

Fig. 3.37. The migration from (3.14) for anisotropy parameters $\varepsilon = 0.5$; $\delta = 0.3$; azimuthal angle $\Psi = 45°$ for the zero-offset time section from relation (1.23) for anisotropy parameters $\varepsilon = 0.5$; $\delta = 0.1$; azimuthal angle $\Psi = 45°$ (Fig. 3.32)

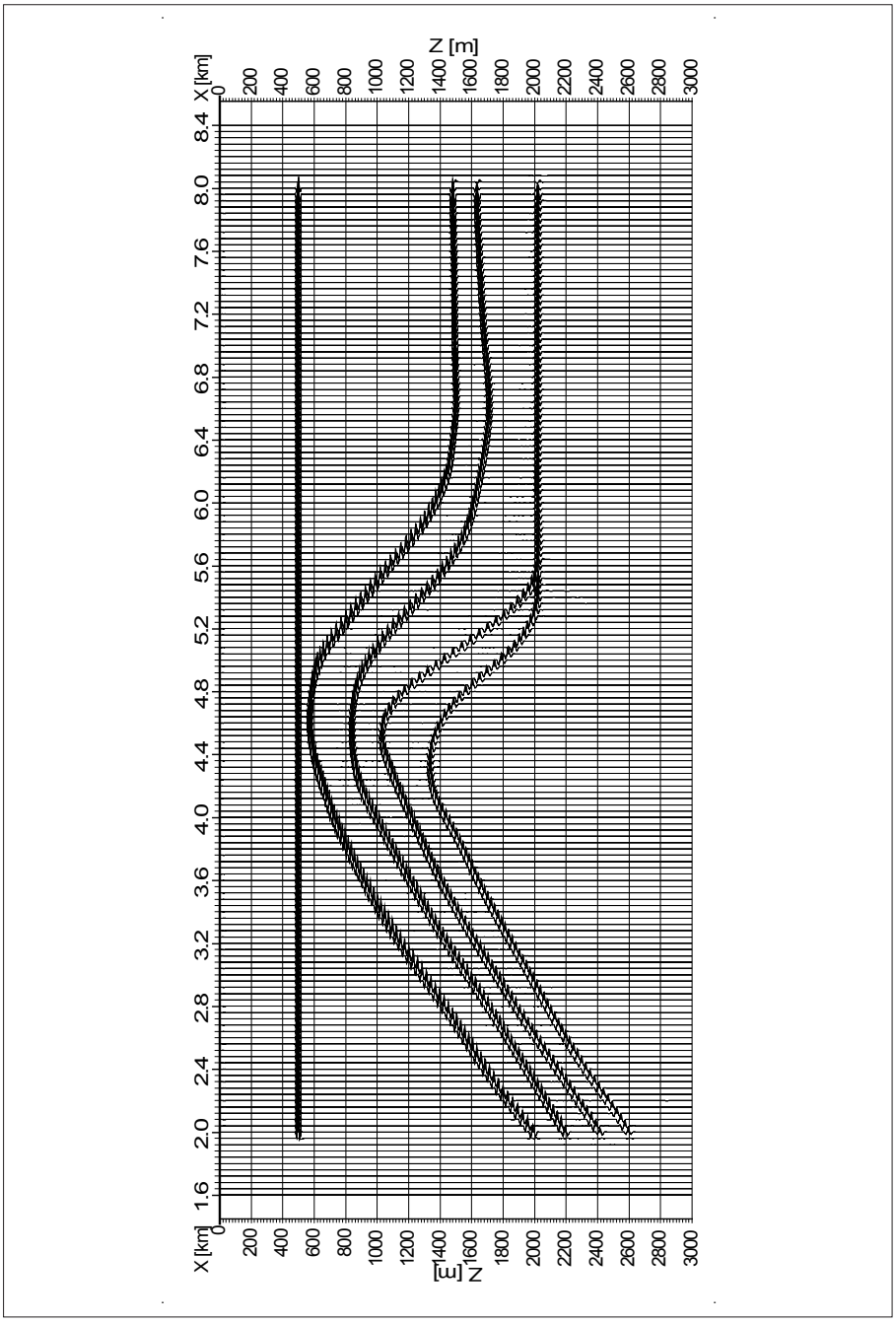

Fig. 3.38. The migration from (3.15) for anisotropy parameters ε = 0.5; δ = 0.3; azimuthal angle Ψ = 45° for the zero-offset time section from relation (1.23) for anisotropy parameters ε = 0.5; δ = 0.1; azimuthal angle Ψ = 45° (Fig. 3.32)

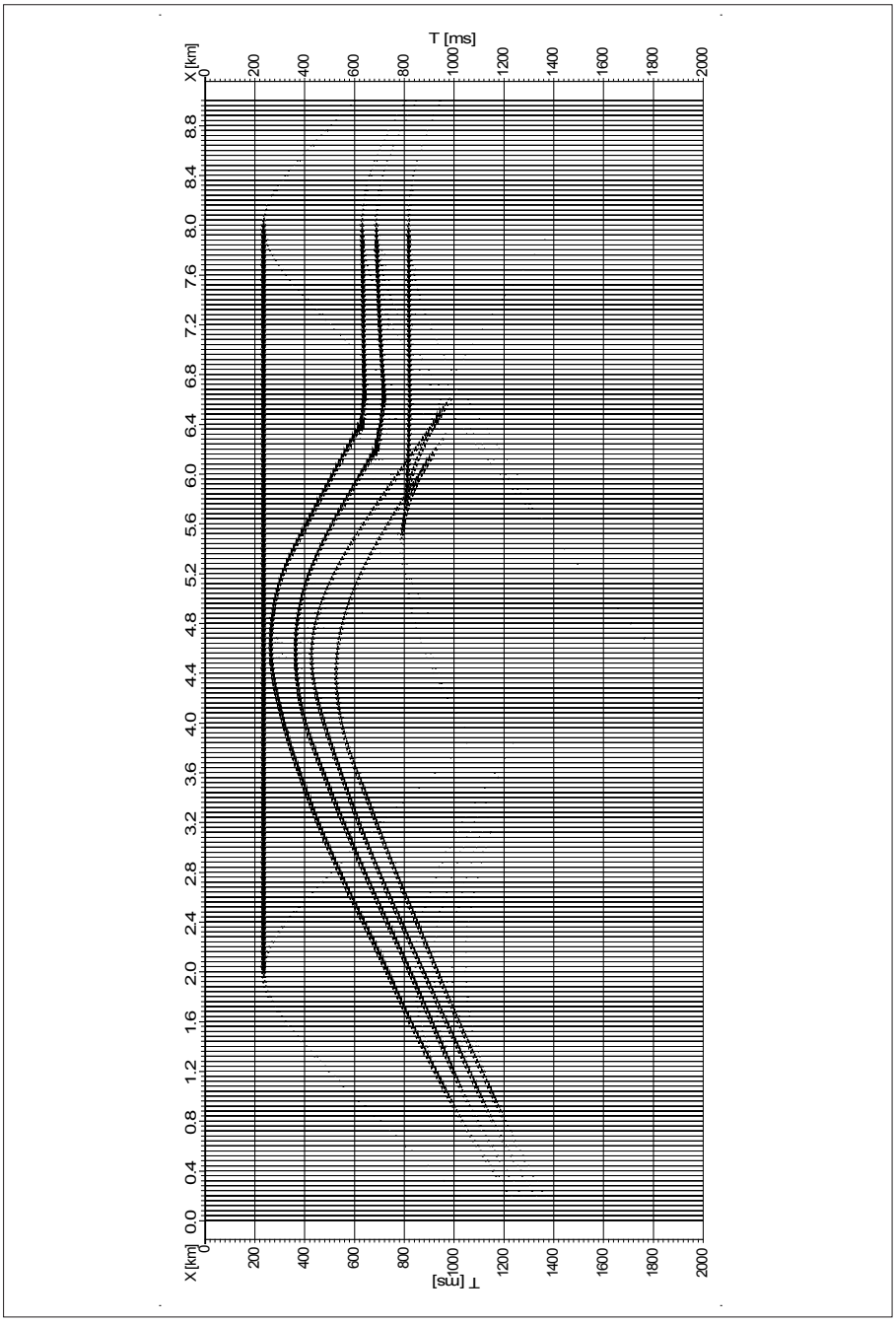

Fig. 3.39. The zero-offset time section from relation (1.23); anisotropy parameters $\varepsilon = 0.5$; $\delta = 0.3$; azimuthal angle $\Psi = 45°$

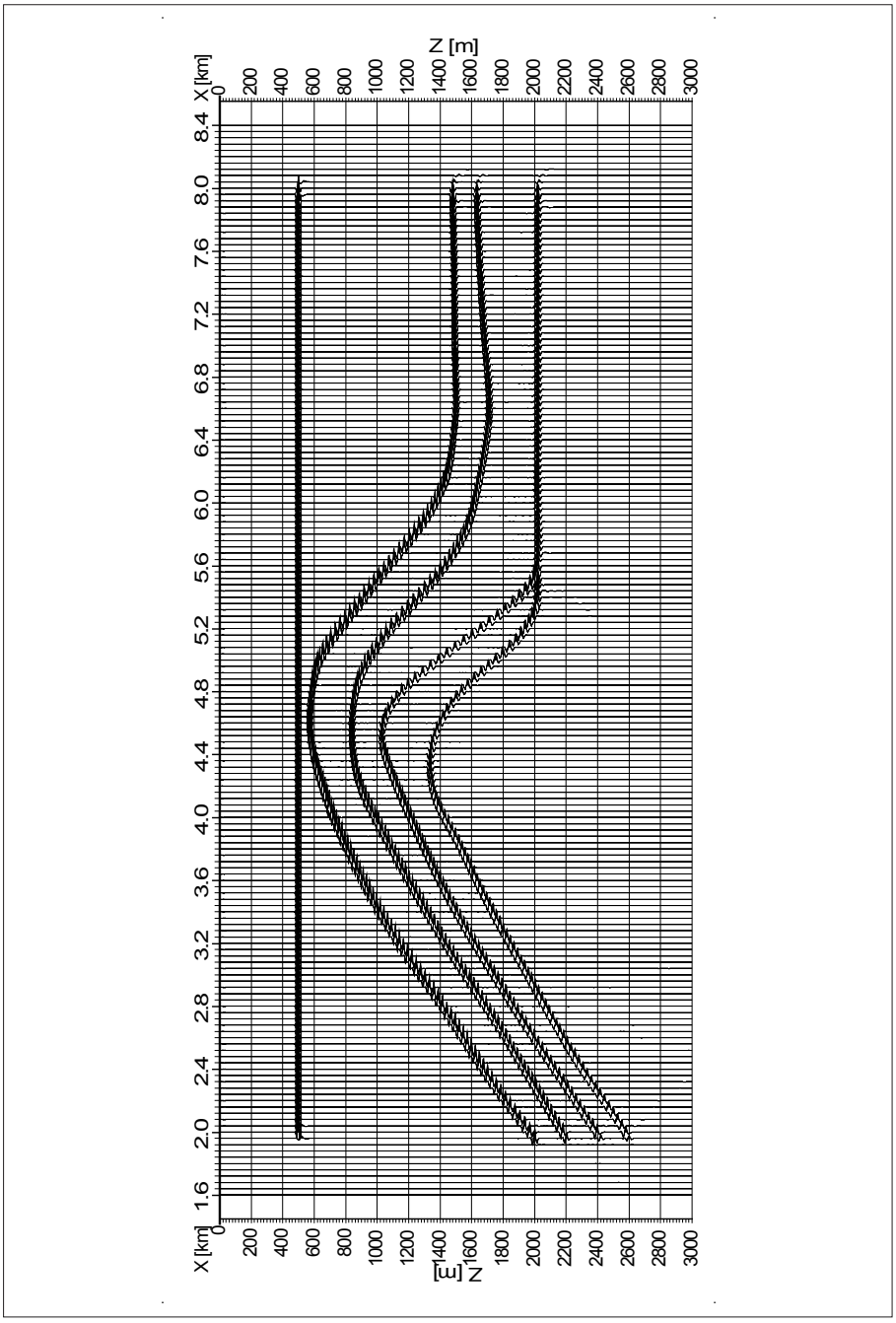

Fig. 3.40. The migration from (3.14) for the zero-offset time section from relation (1.23); anisotropy parameters $\varepsilon = 0.5$; $\delta = 0.3$; azimuthal angle $\Psi = 45°$ (Fig. 3.39)

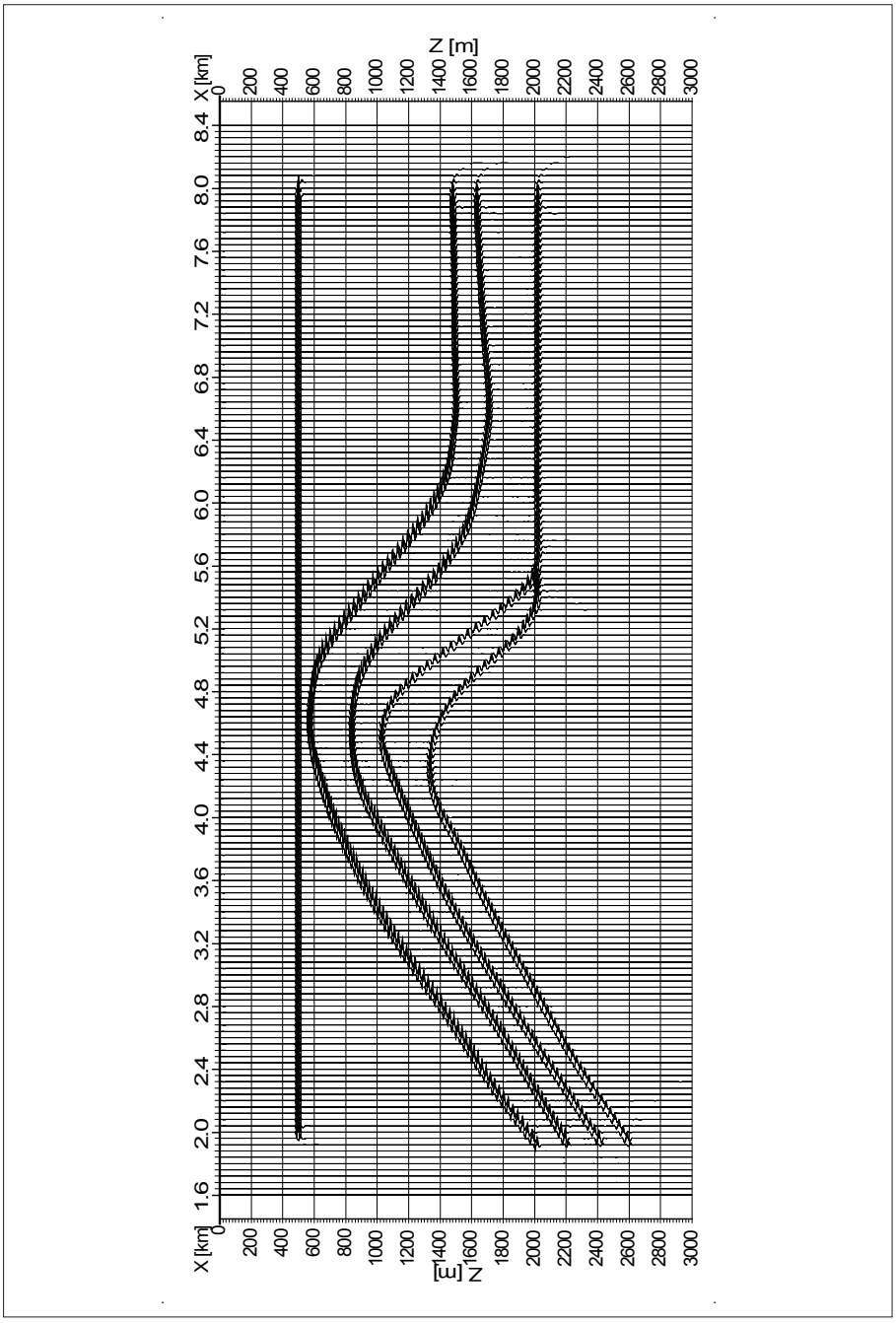

Fig. 3.41. The migration from (3.15) for the zero-offset time section from relation (1.23); anisotropy parameters $\varepsilon = 0.5$; $\delta = 0.3$; azimuthal angle $\Psi = 45°$ (Fig. 3.39)

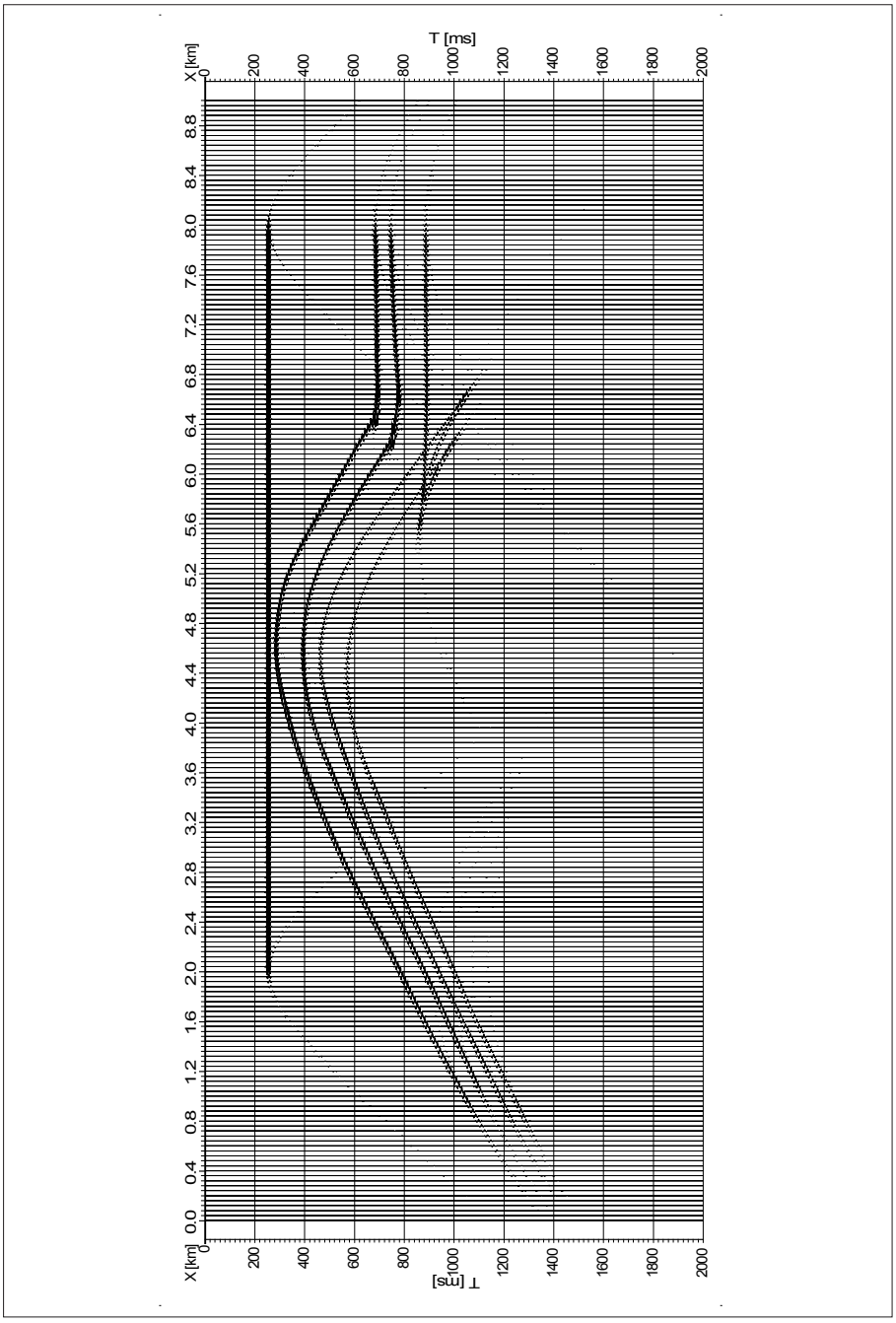

Fig. 3.42. The zero-offset time section from relation (1.23); anisotropy parameters $\varepsilon = 0.35$; $\delta = -0.2$; azimuthal angle $\Psi = 30°$

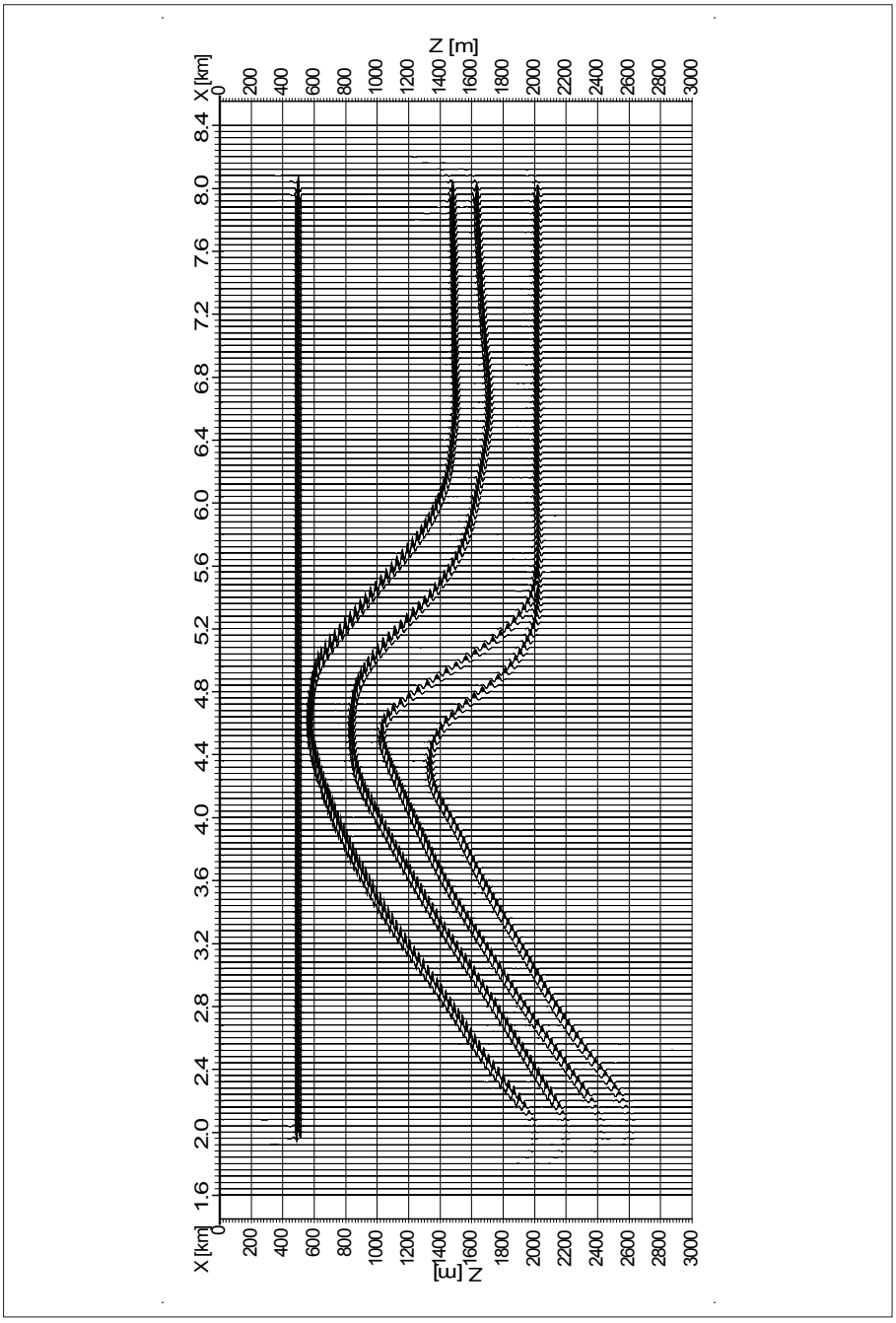

Fig. 3.43. The migration from (3.14) for the zero-offset time section from relation (1.23); anisotropy parameters $\varepsilon = 0.35$; $\delta = -0.2$; azimuthal angle $\Psi = 30°$ (Fig. 3.42)

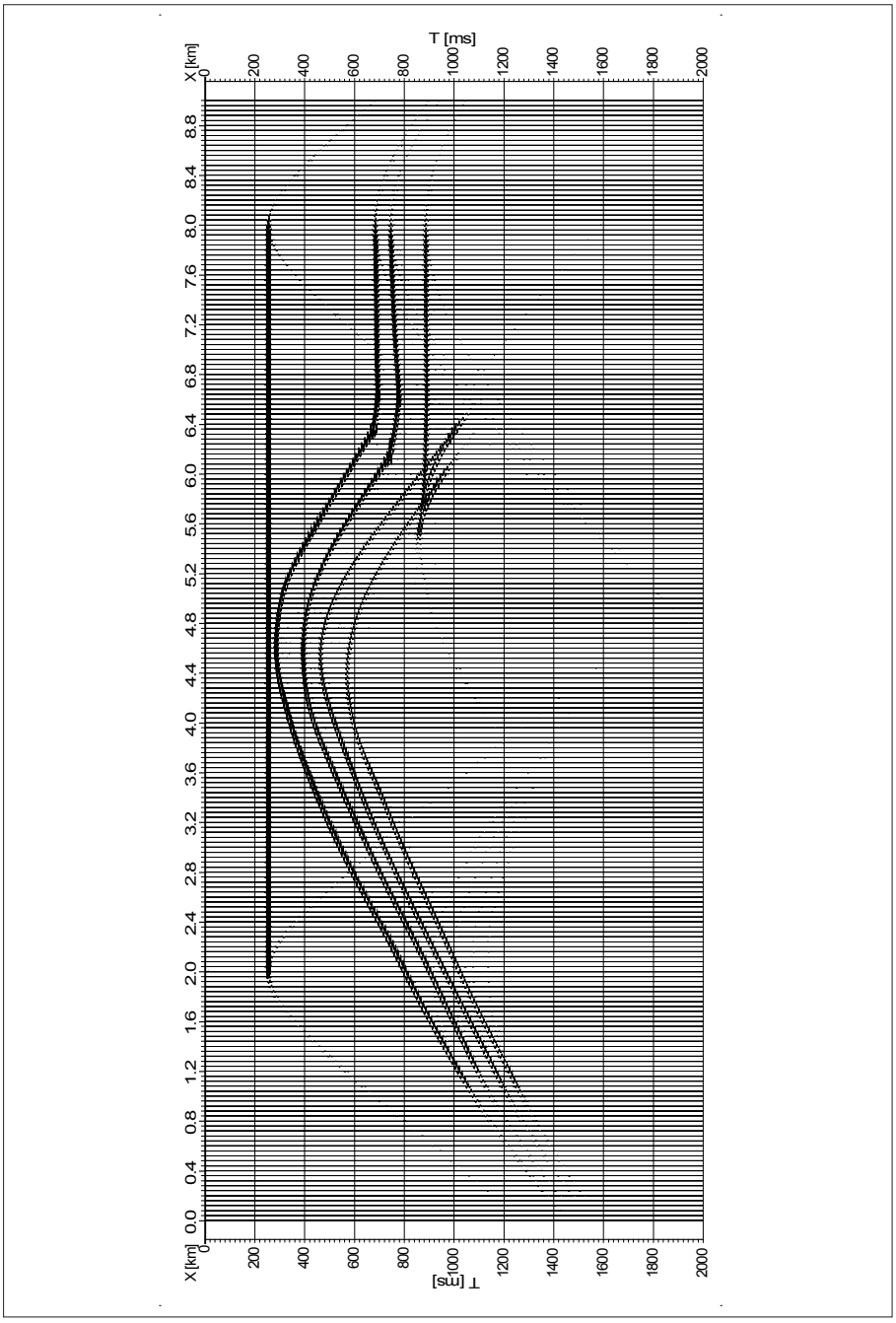

Fig. 3.44. The zero-offset time section from relation (1.23); anisotropy parameters $\varepsilon = 0.35$; $\delta = -0.2$; azimuthal angle $\Psi = 45°$

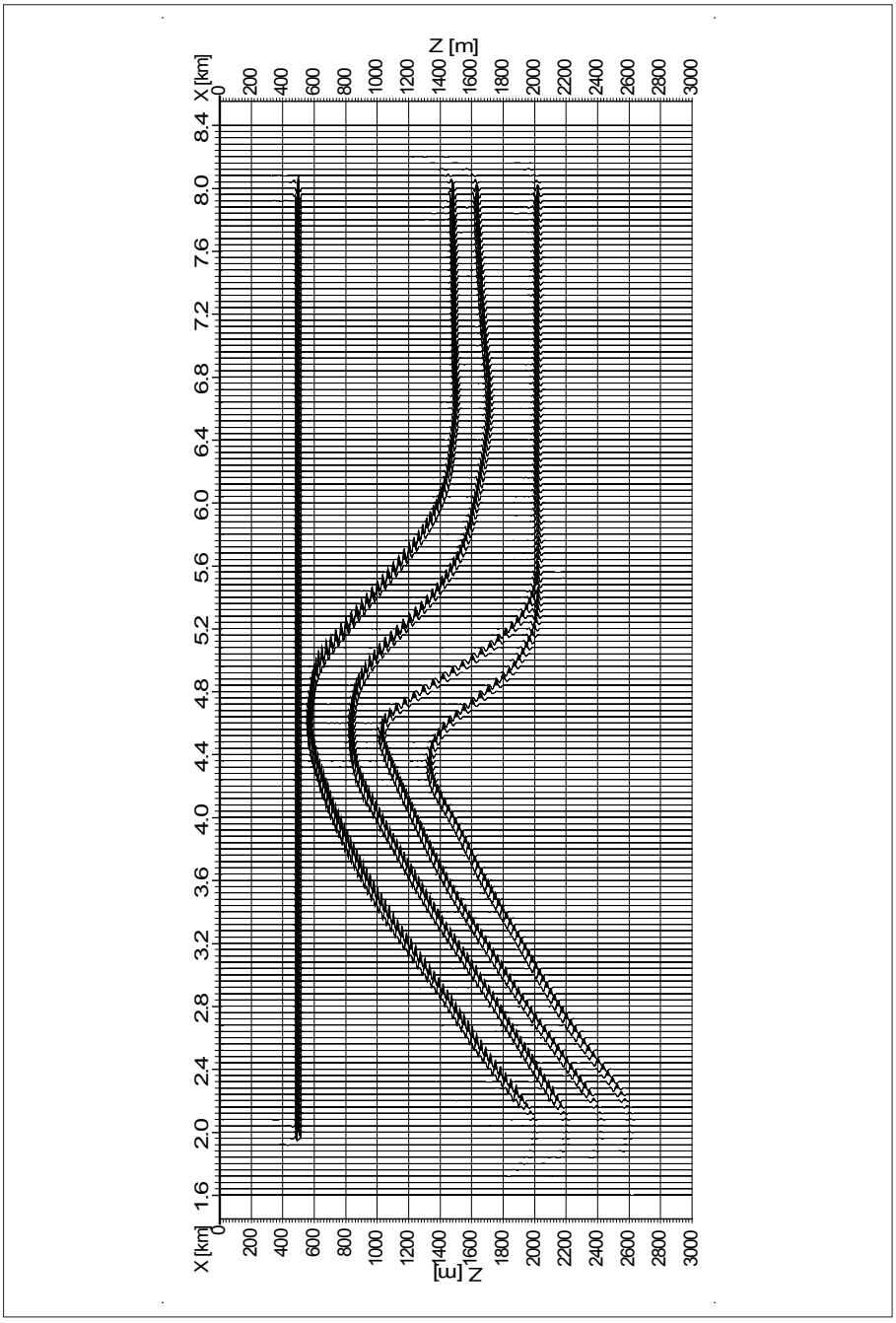

Fig. 3.45. The migration from (3.14) for the zero-offset time section from relation (1.23); anisotropy parameters $\varepsilon = 0.35$; $\delta = -0.2$; azimuthal angle $\Psi = 45°$ (Fig. 3.44)

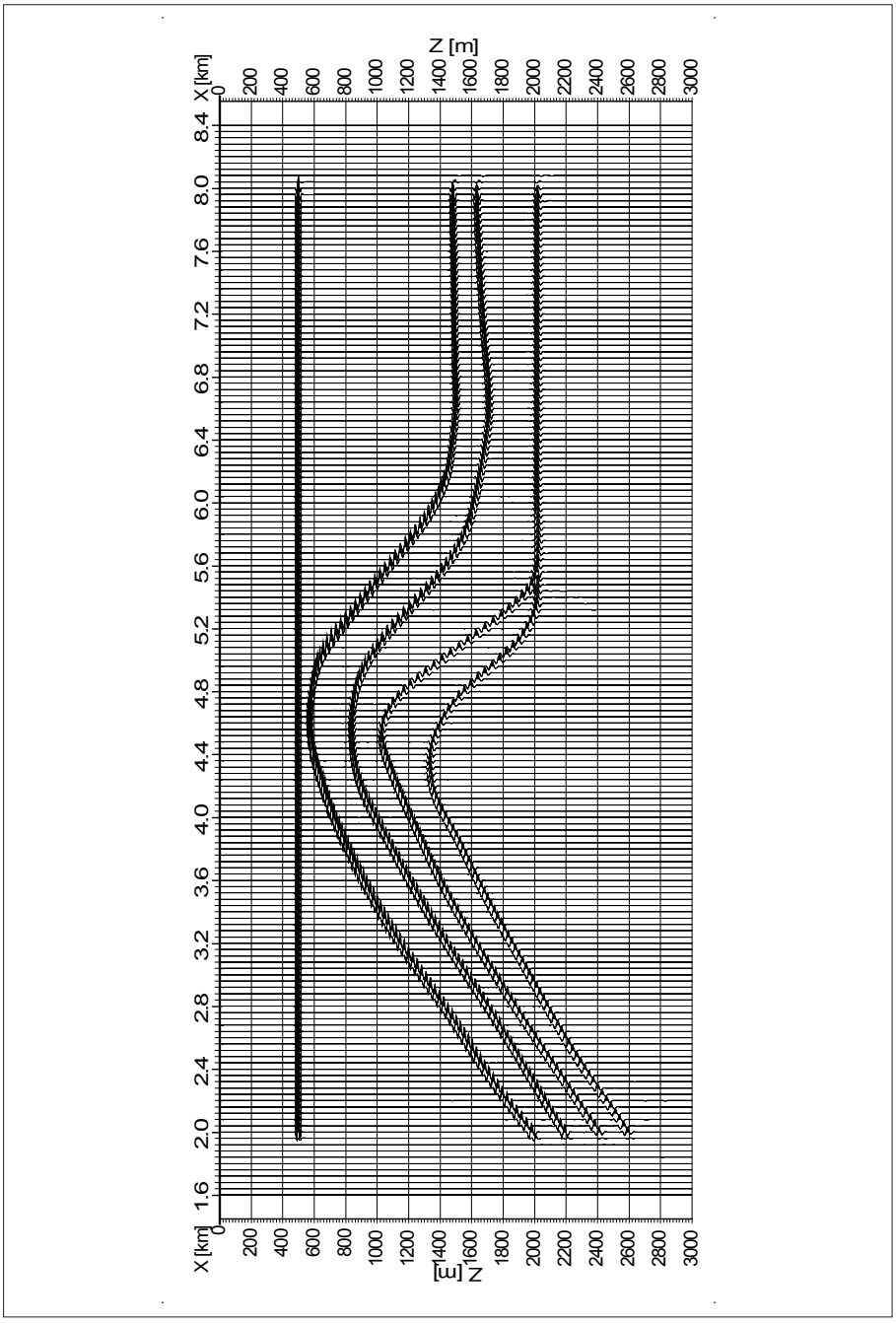

Fig. 3.46. The migration from (3.14) for anisotropy parameters ε = 0.35; δ = –0.2; azimuthal angle Ψ = 60° for the zero-offset time section from relation (1.23) for anisotropy parameters ε = 0.35; δ = –0.2; azimuthal angle Ψ = 45° (Fig. 3.44)

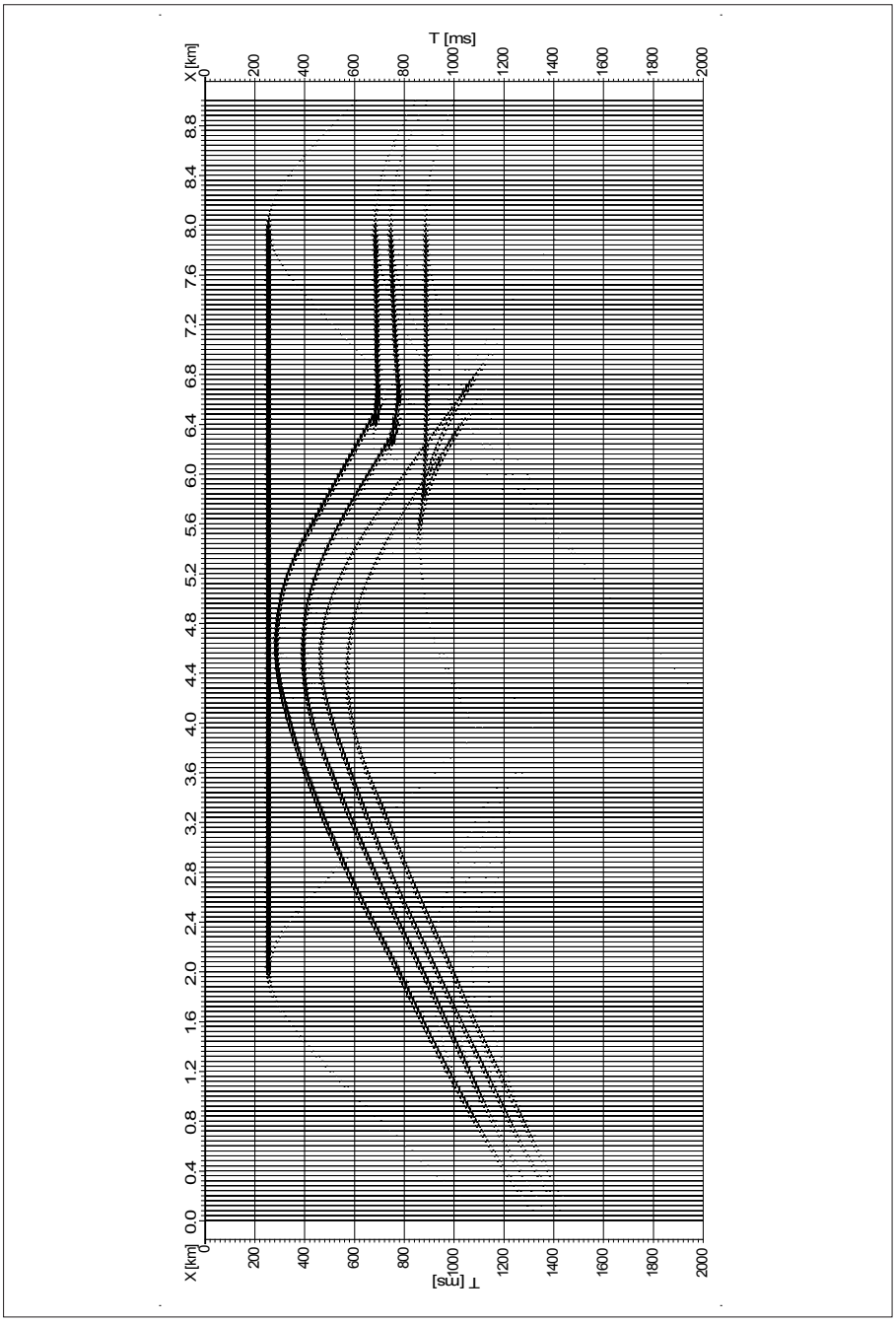

Fig. 3.47. The zero-offset time section from relation (1.23); anisotropy parameters $\varepsilon = 0.35$; $\delta = 0.1$; azimuthal angle $\Psi = 30°$

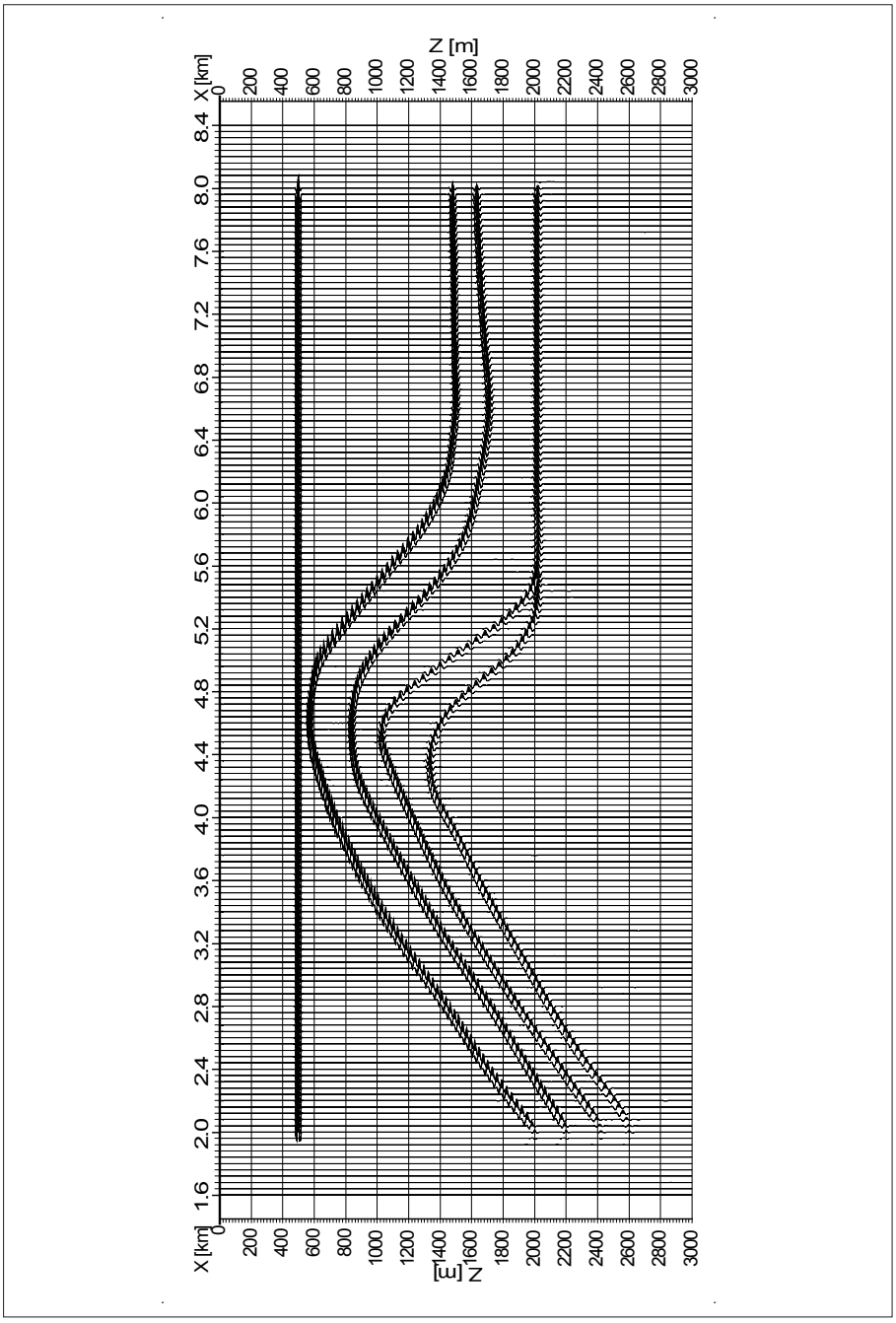

Fig. 3.48. The migration from (3.14) for the zero-offset time section from relation (1.23); anisotropy parameters $\varepsilon = 0.35$; $\delta = 0.1$; azimuthal angle $\Psi = 30°$ (Fig. 3.47)

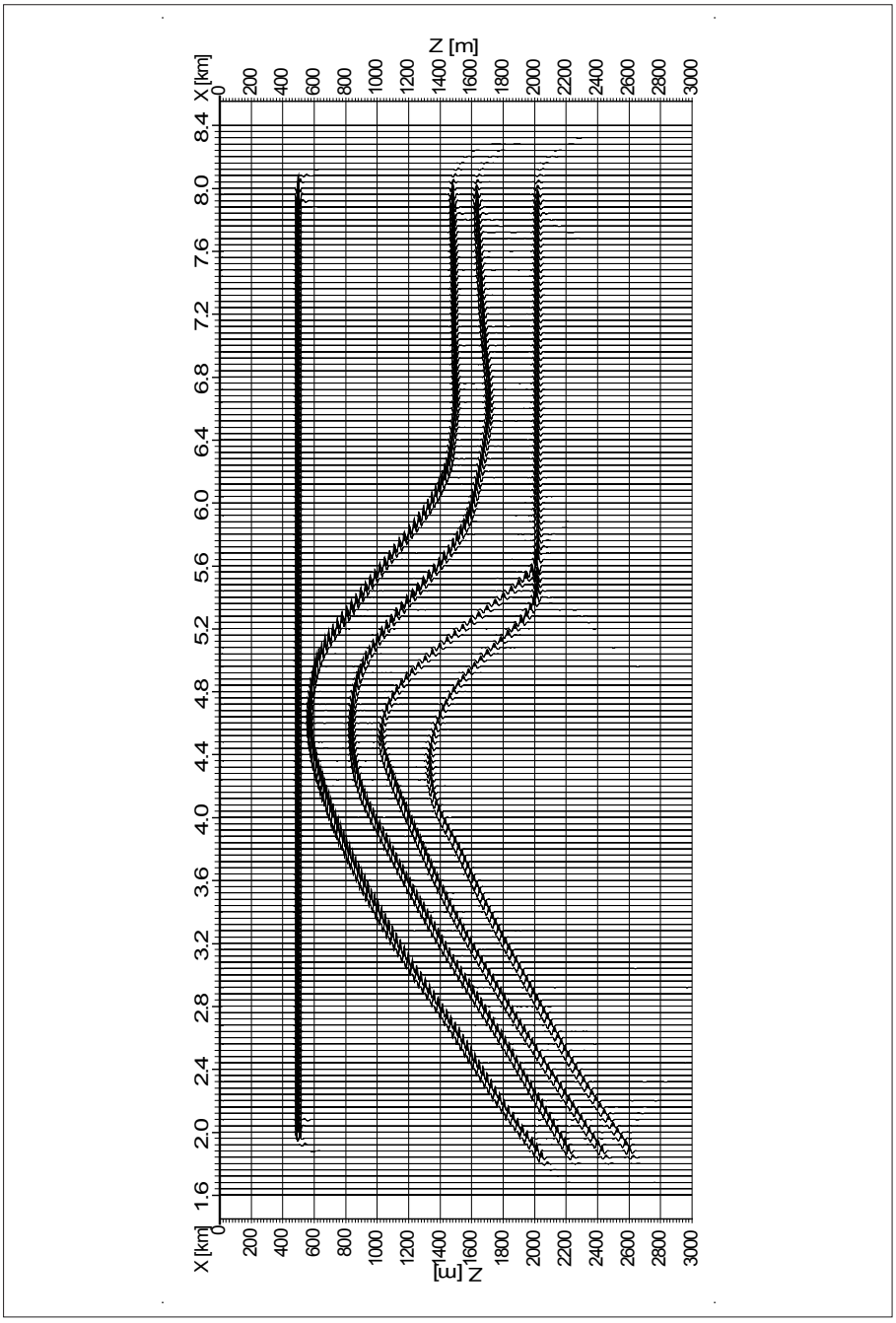

Fig. 3.49. The migration from (3.14) for anisotropy parameters $\varepsilon = 0.35$; $\delta = 0.1$; azimuthal angle $\Psi = 45°$ for the zero-offset time section from relation (1.23) for anisotropy parameters $\varepsilon = 0.35$; $\delta = 0.1$; azimuthal angle $\Psi = 30°$ (Fig. 3.47)

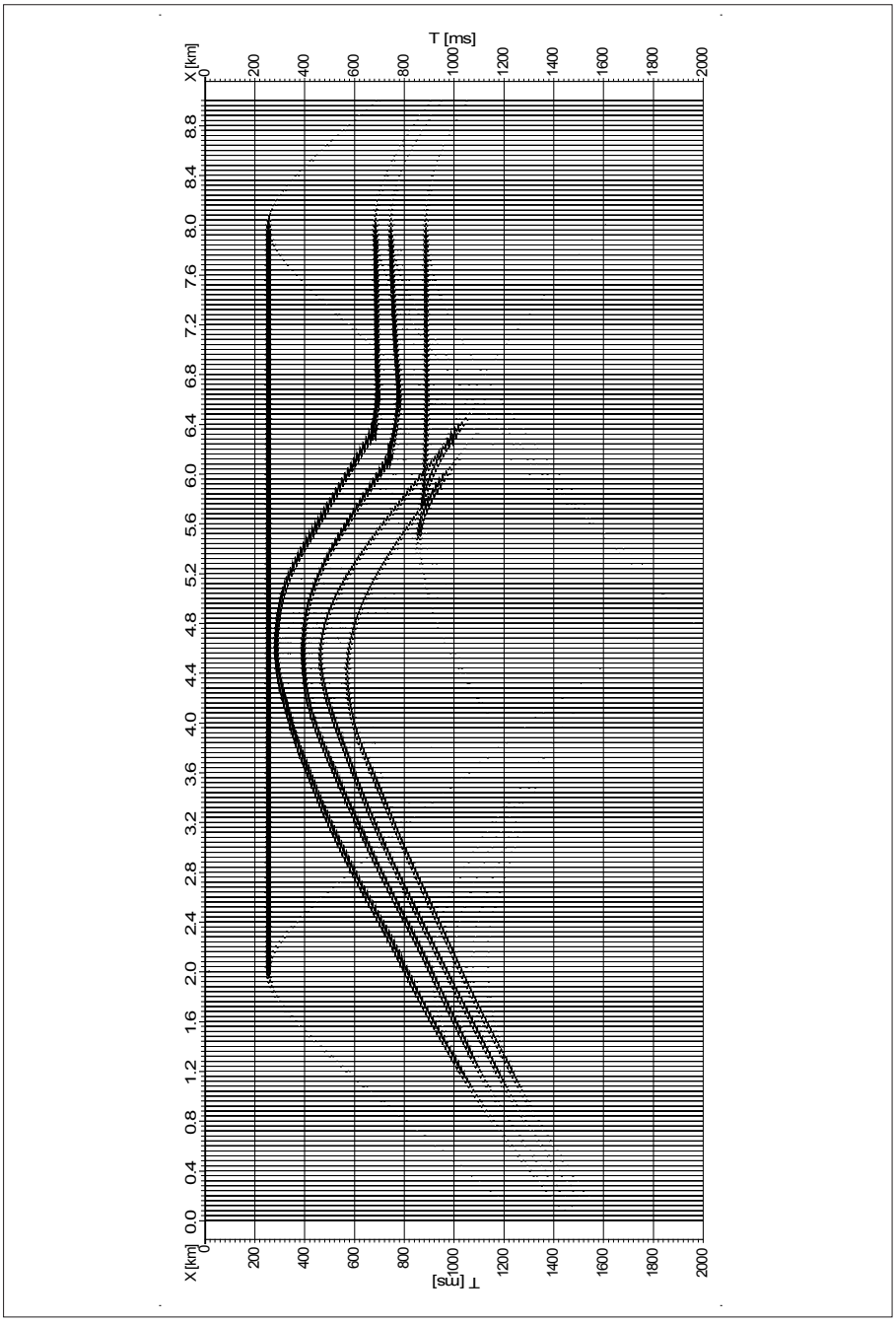

Fig. 3.50. The zero-offset time section from relation (1.23); anisotropy parameters $\varepsilon = 0.35$; $\delta = 0.1$; azimuthal angle $\Psi = 60°$

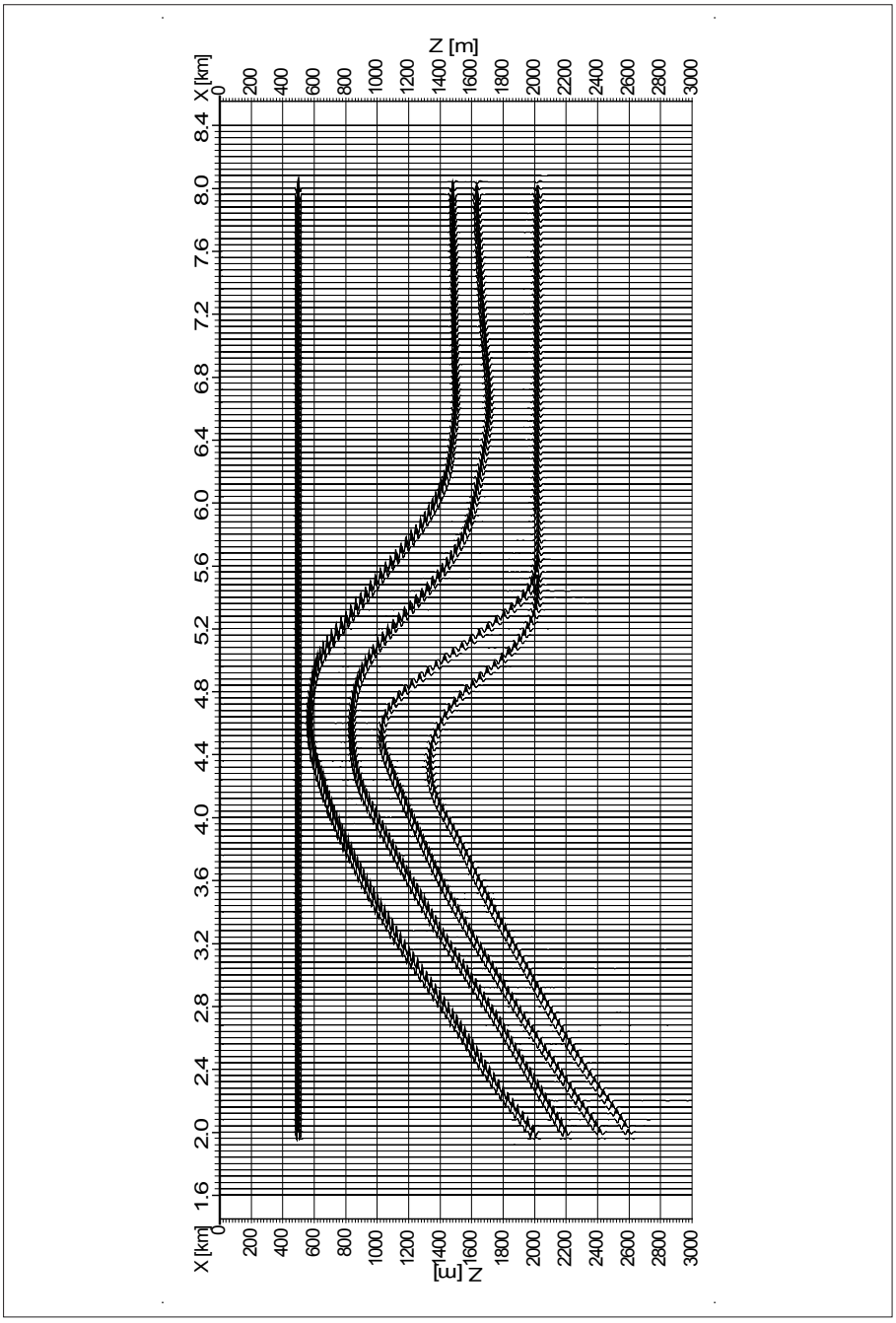

Fig. 3.51. The migration from (3.14) for the zero-offset time section from relation (1.23); anisotropy parameters $\varepsilon = 0.35$; $\delta = 0.1$; azimuthal angle $\Psi = 60°$ (Fig. 3.50)

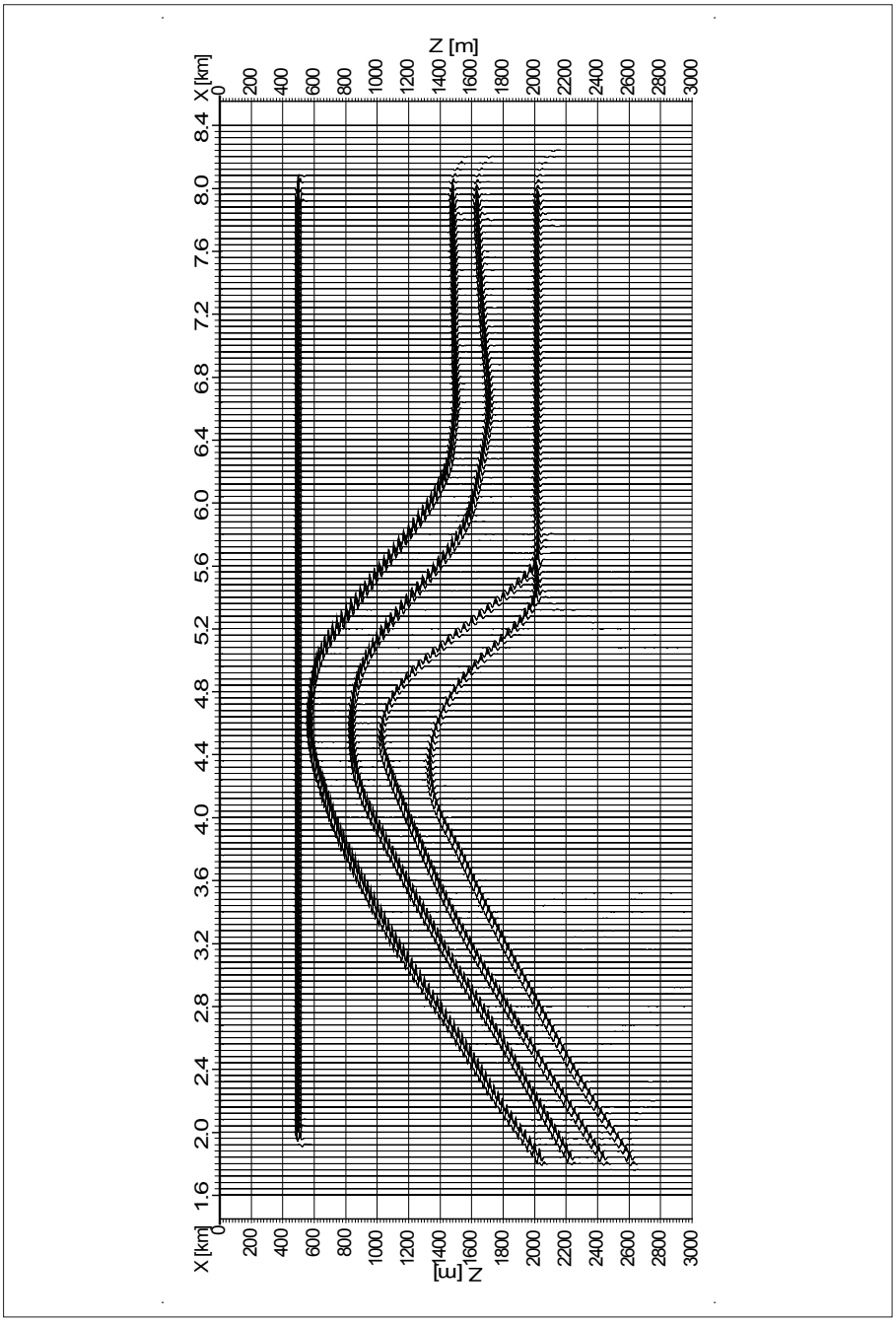

Fig. 3.52. The migration from (3.14) for anisotropy parameters ε = 0.35; δ = 0.1; azimuthal angle Ψ = 90° for the zero-offset time section from relation (1.23) for anisotropy parameters ε = 0.35; δ = 0.1; azimuthal angle Ψ = 60° (Fig. 3.50)

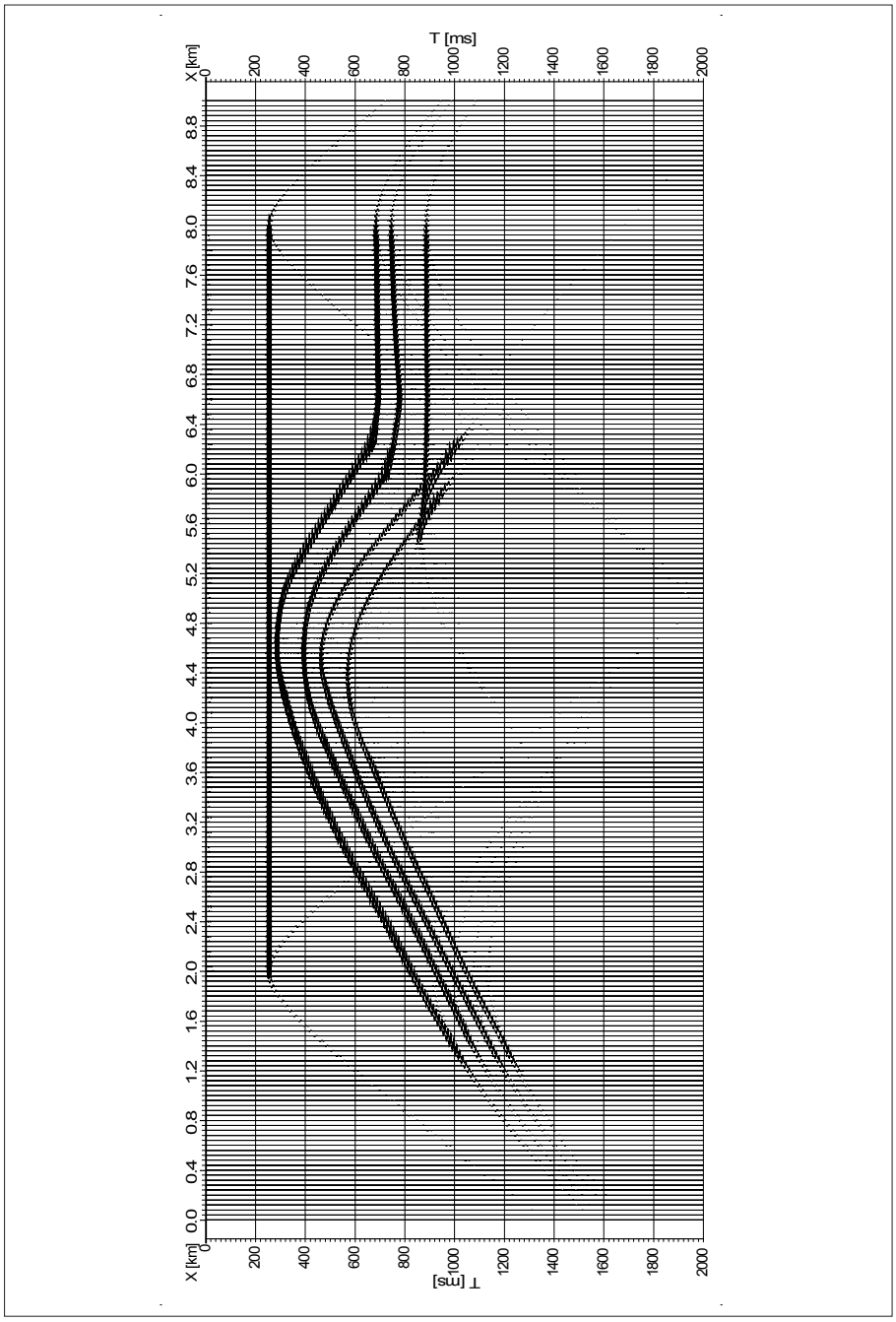

Fig. 3.53. The zero-offset time section from relation (1.23); anisotropy parameters $\varepsilon = 0.35$; $\delta = 0.1$; azimuthal angle $\Psi = 90°$

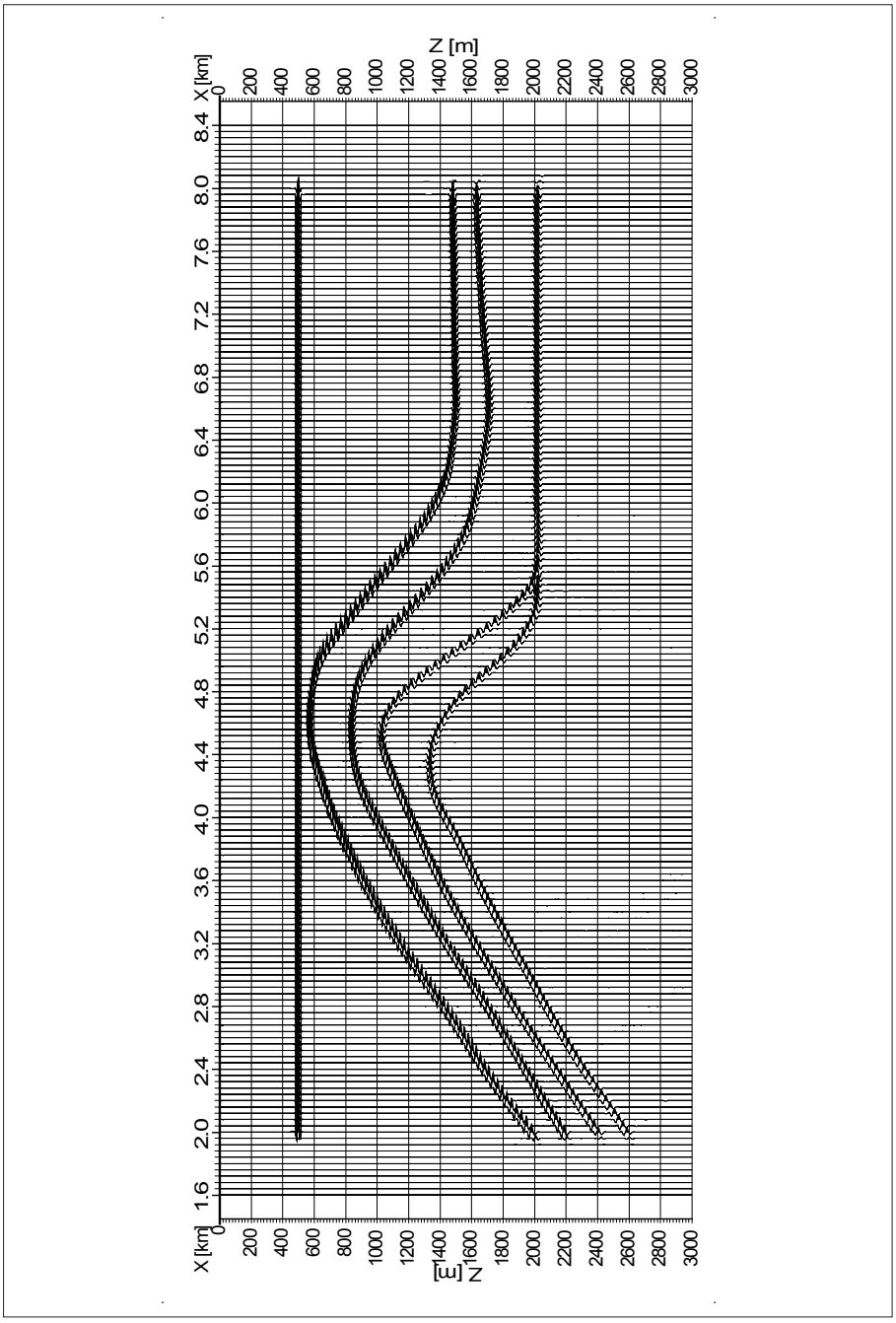

Fig. 3.54. The migration from (3.14) for the zero-offset time section from relation (1.23); anisotropy parameters $\varepsilon = 0.35$; $\delta = 0.1$; azimuthal angle $\Psi = 90°$ (Fig. 3.53)

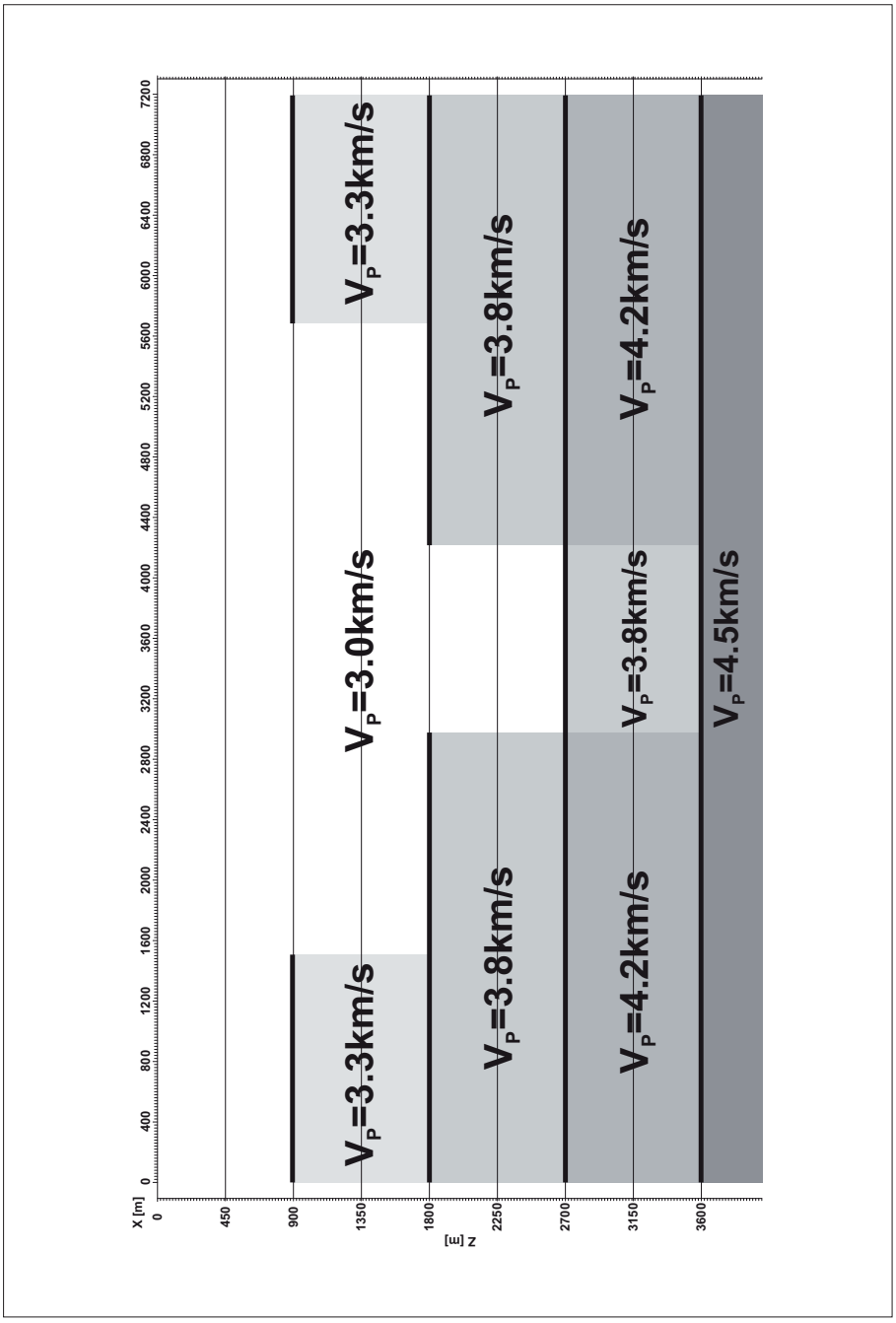

Fig. 3.55. The geometry of velocity horst model

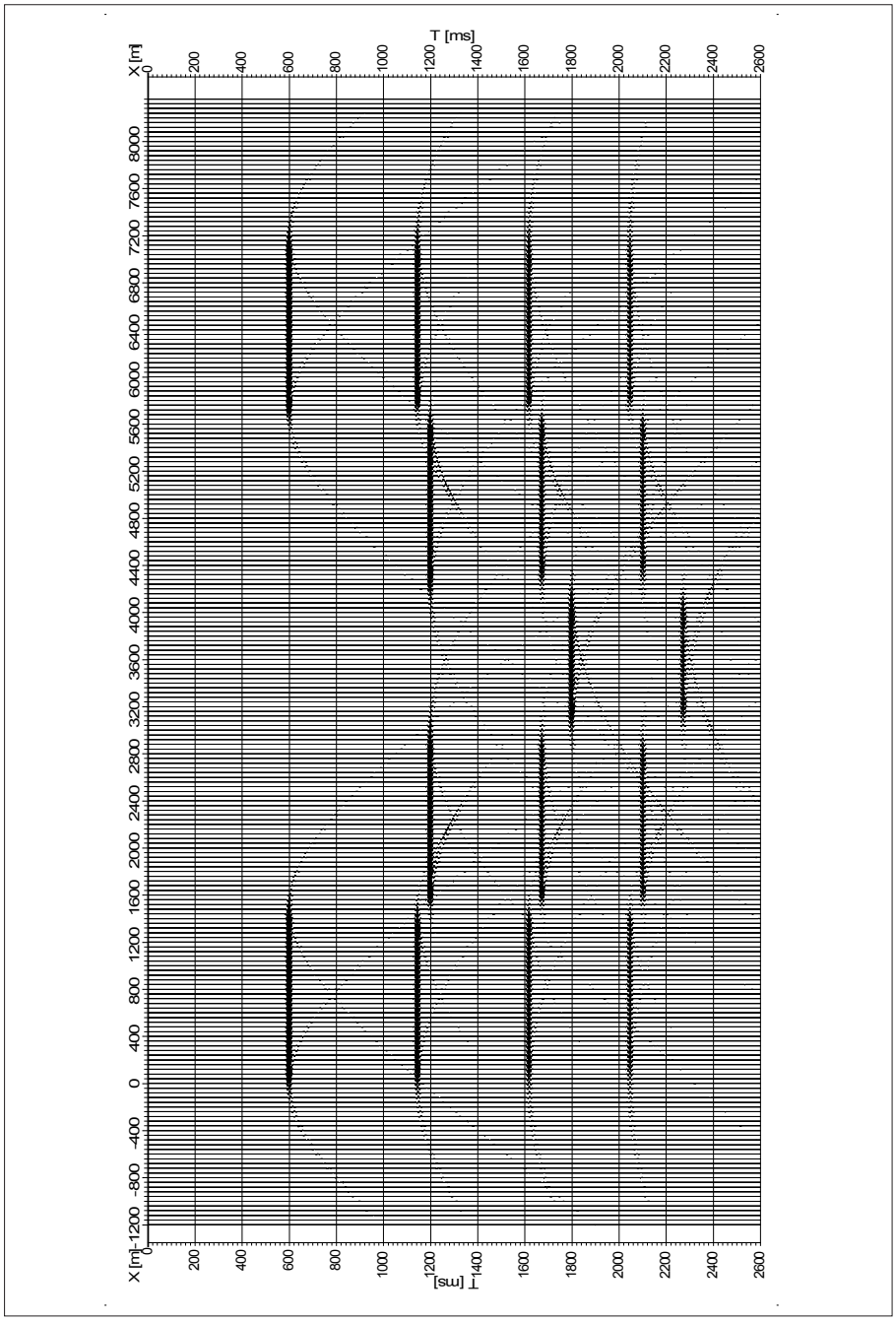

Fig. 3.56. The zero-offset time section from relation (1.23) for isotropic model

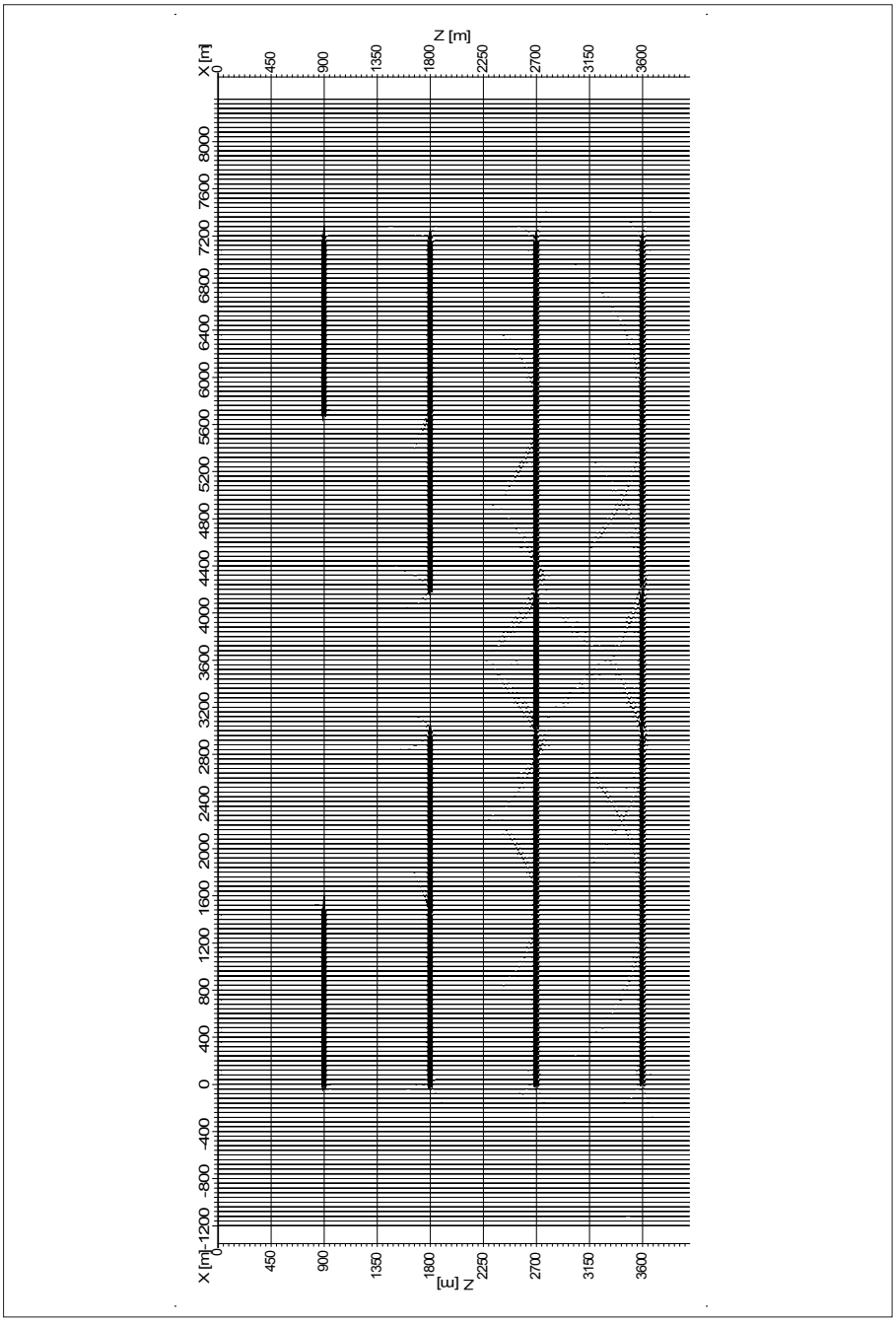

Fig. 3.57. The zero-offset migration for the isotropic model (Fig. 3.56)

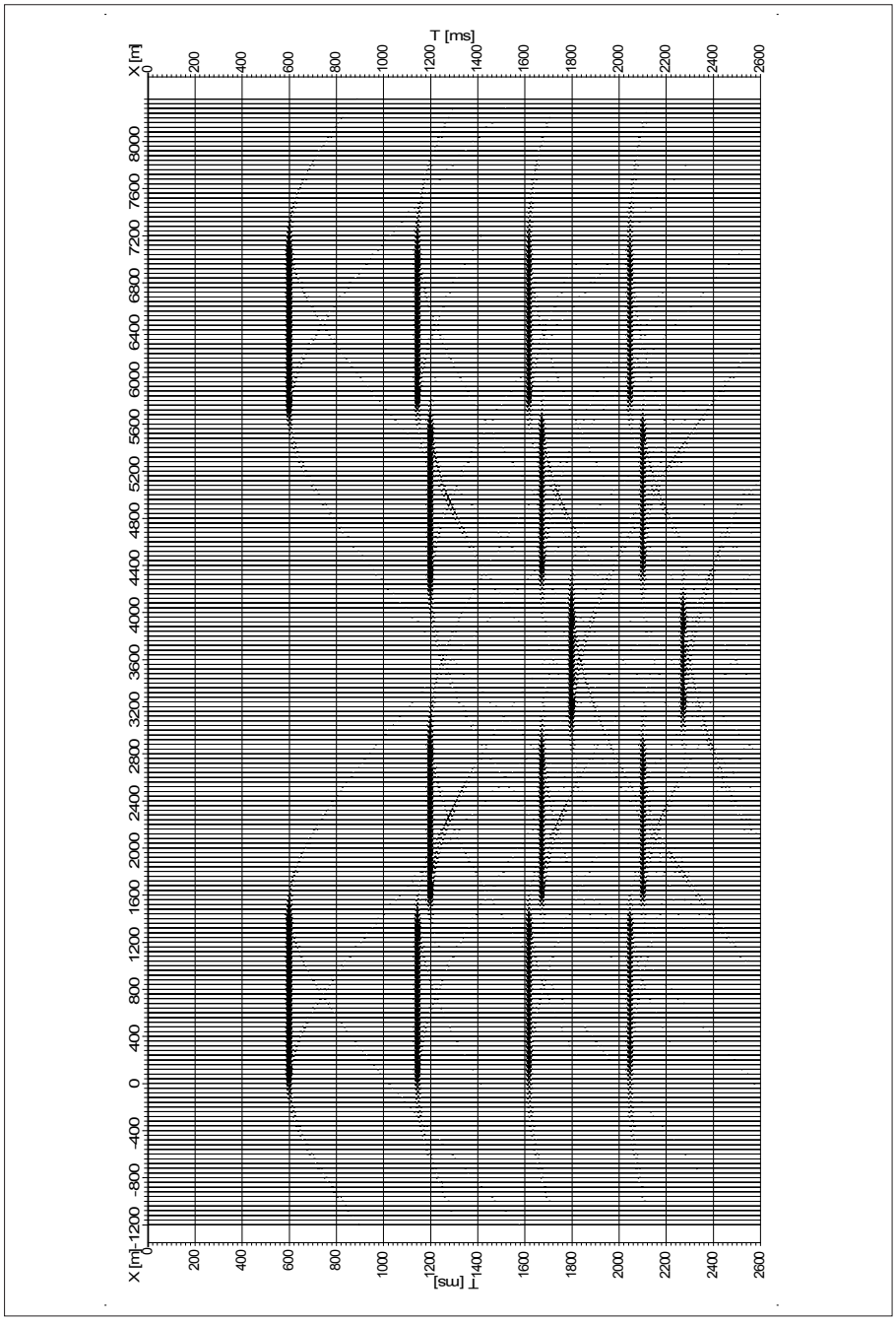

Fig. 3.58. The zero-offset time section for anisotropic VTI model; anisotropy parameters $\varepsilon = 0.3$; $\delta = 0.1$

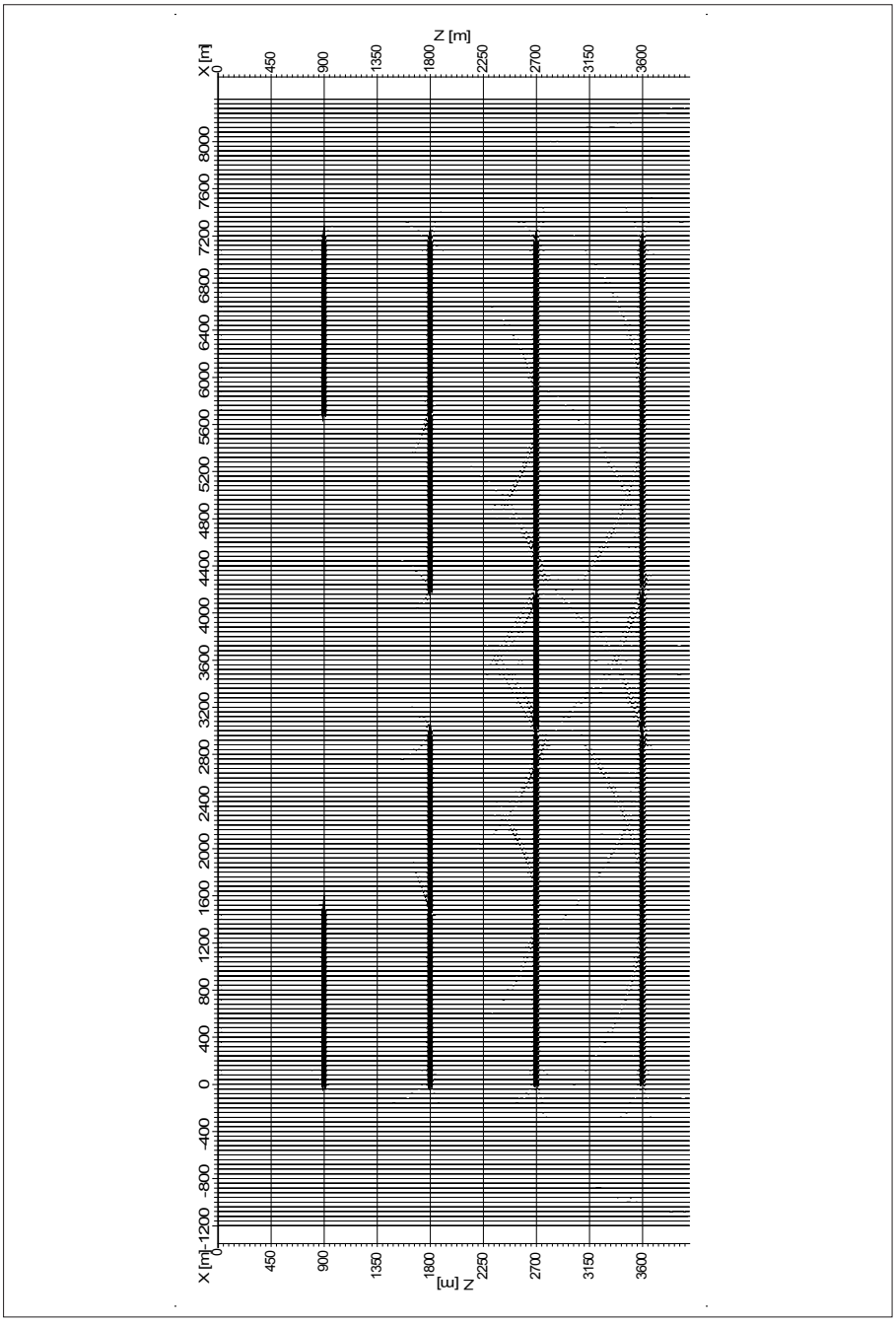

Fig. 3.59. The zero-offset migration for the anisotropic VTI model (Fig. 3.58); anisotropy parameters $\varepsilon = 0.3$; $\delta = 0.1$

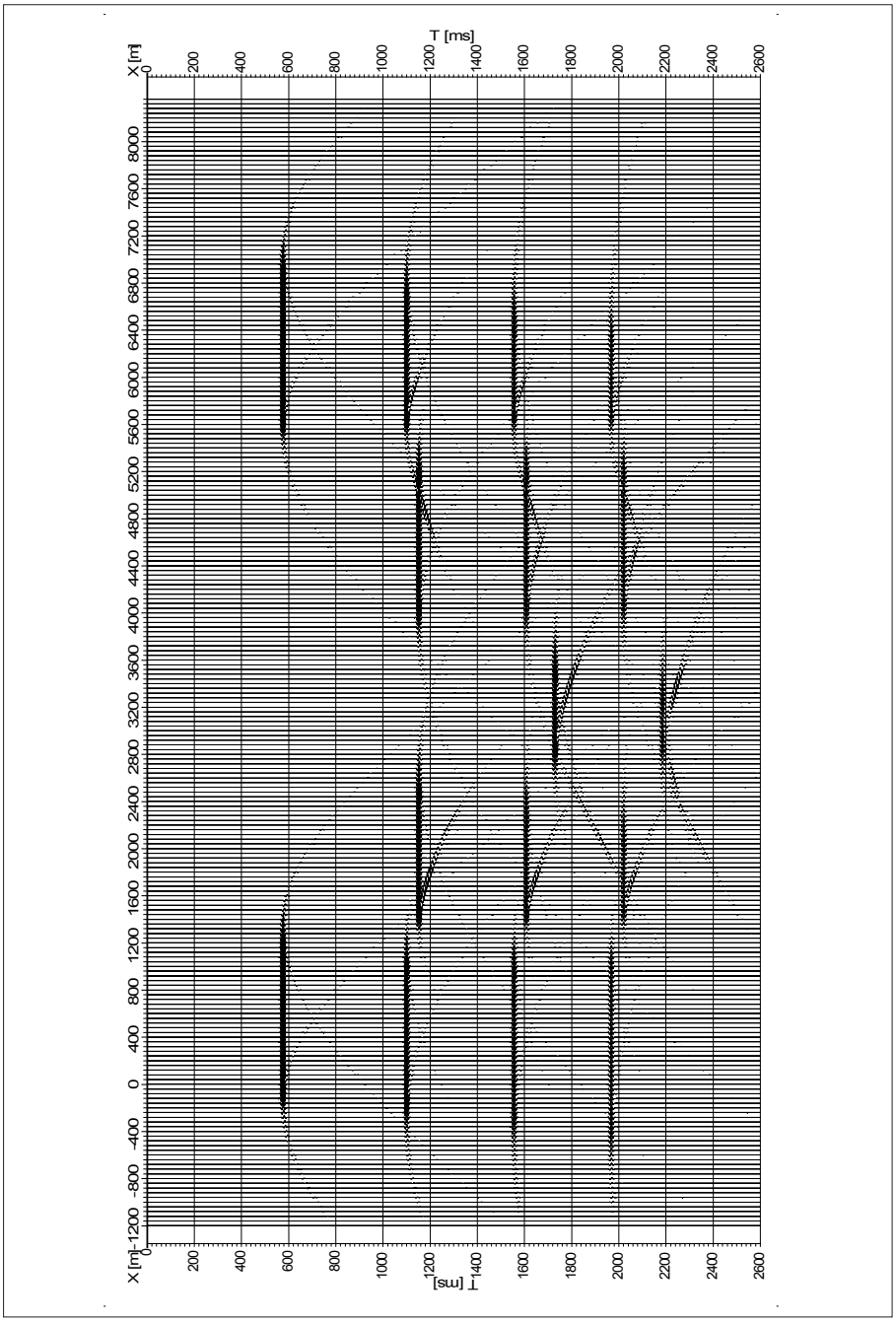

Fig. 3.60. The zero-offset time section for anisotropic TTI model; anisotropy parameters $\varepsilon = 0.3$; $\delta = 0.1$; dip angle $\theta = 30°$

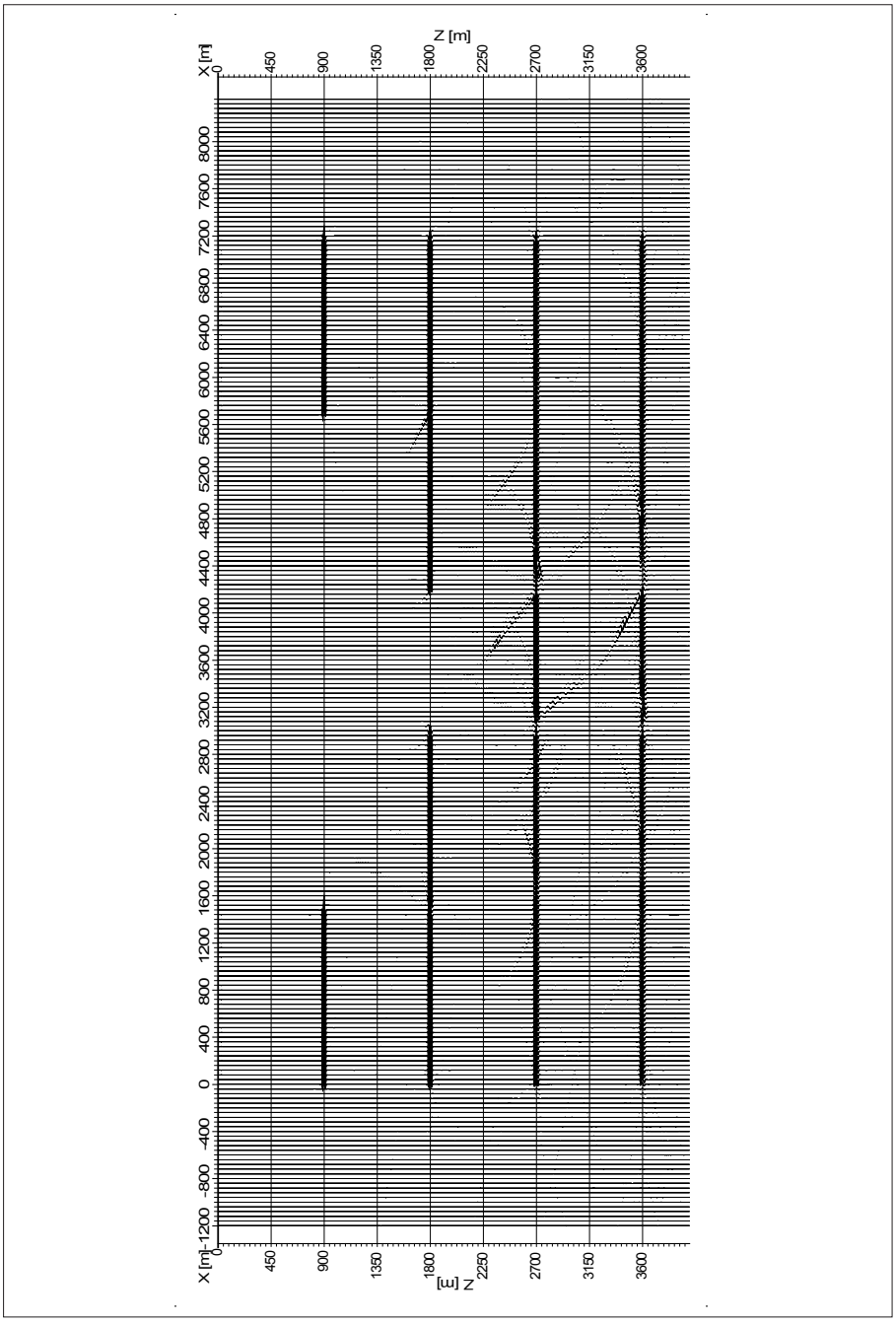

Fig. 3.61. The zero-offset migration for the anisotropic TTI model (Fig. 3.60); anisotropy parameters $\varepsilon = 0.3$; $\delta = 0.1$; dip angle $\theta = 30°$

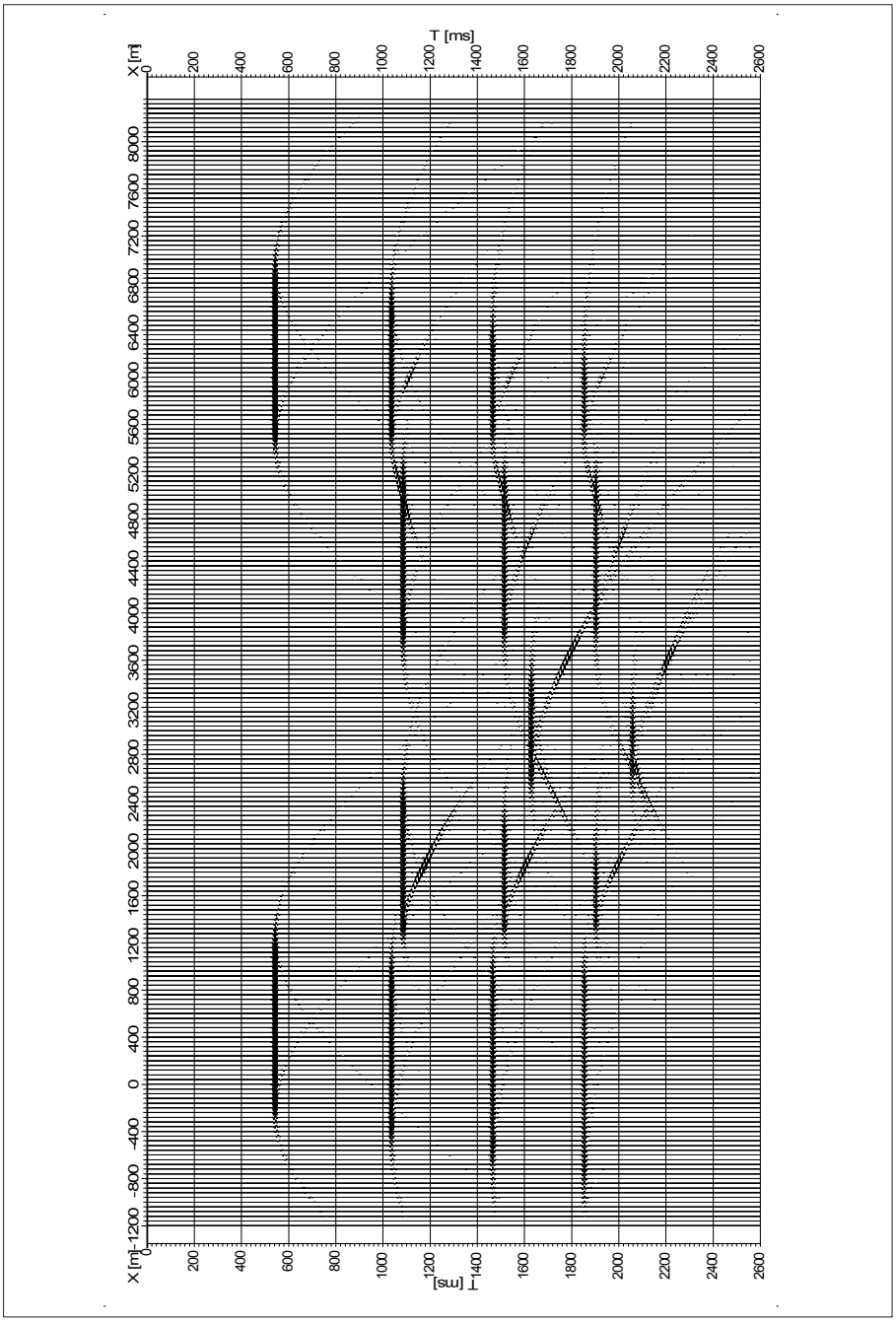

Fig. 3.62. The zero-offset time section for anisotropic TTI model; anisotropy parameters $\varepsilon = 0.3$; $\delta = 0.1$; dip angle $\theta = 45°$

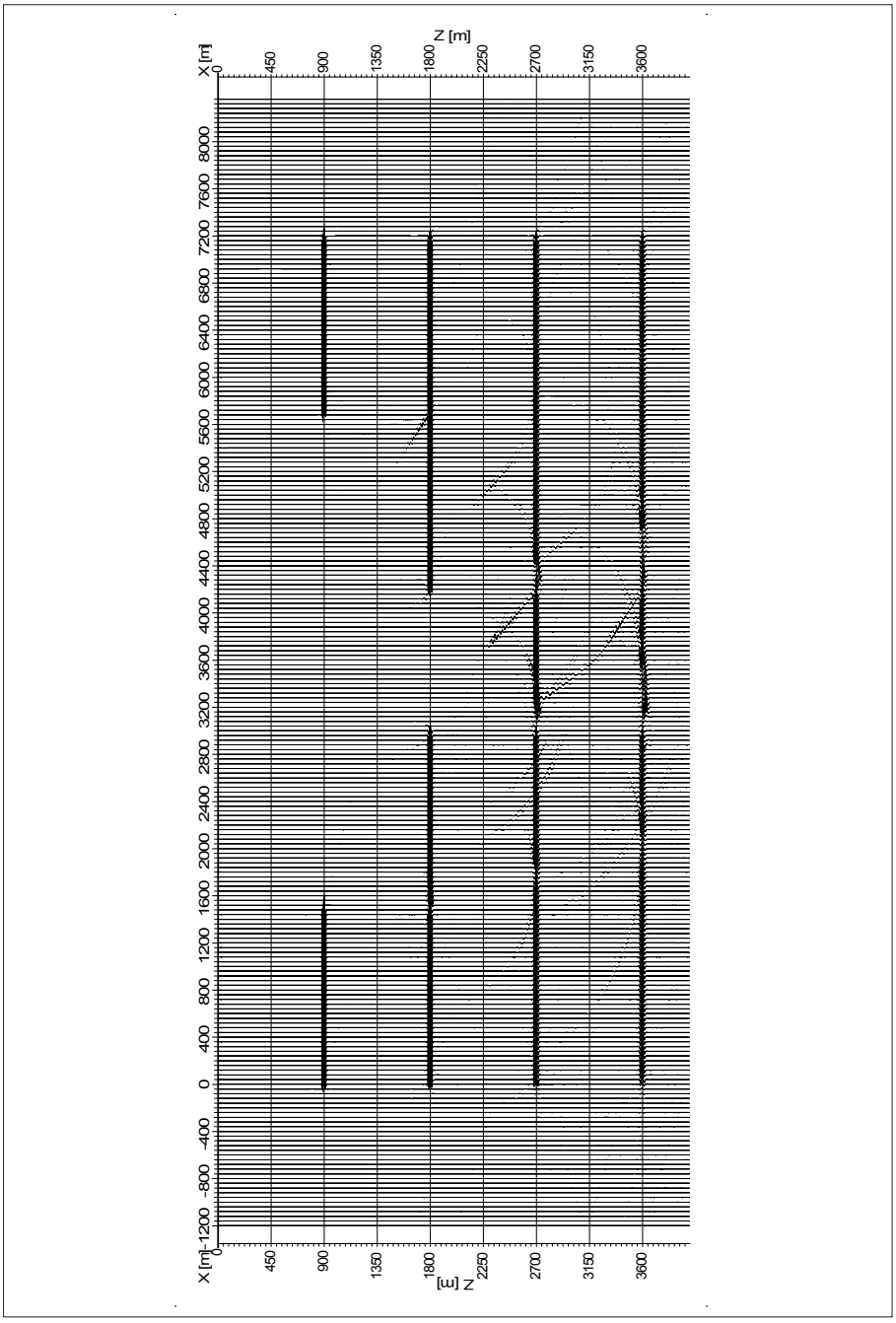

Fig. 3.63. The zero-offset migration for the anisotropic TTI model (Fig. 3.62); anisotropy parameters $\varepsilon = 0.3$; $\delta = 0.1$; dip angle $\theta = 45°$

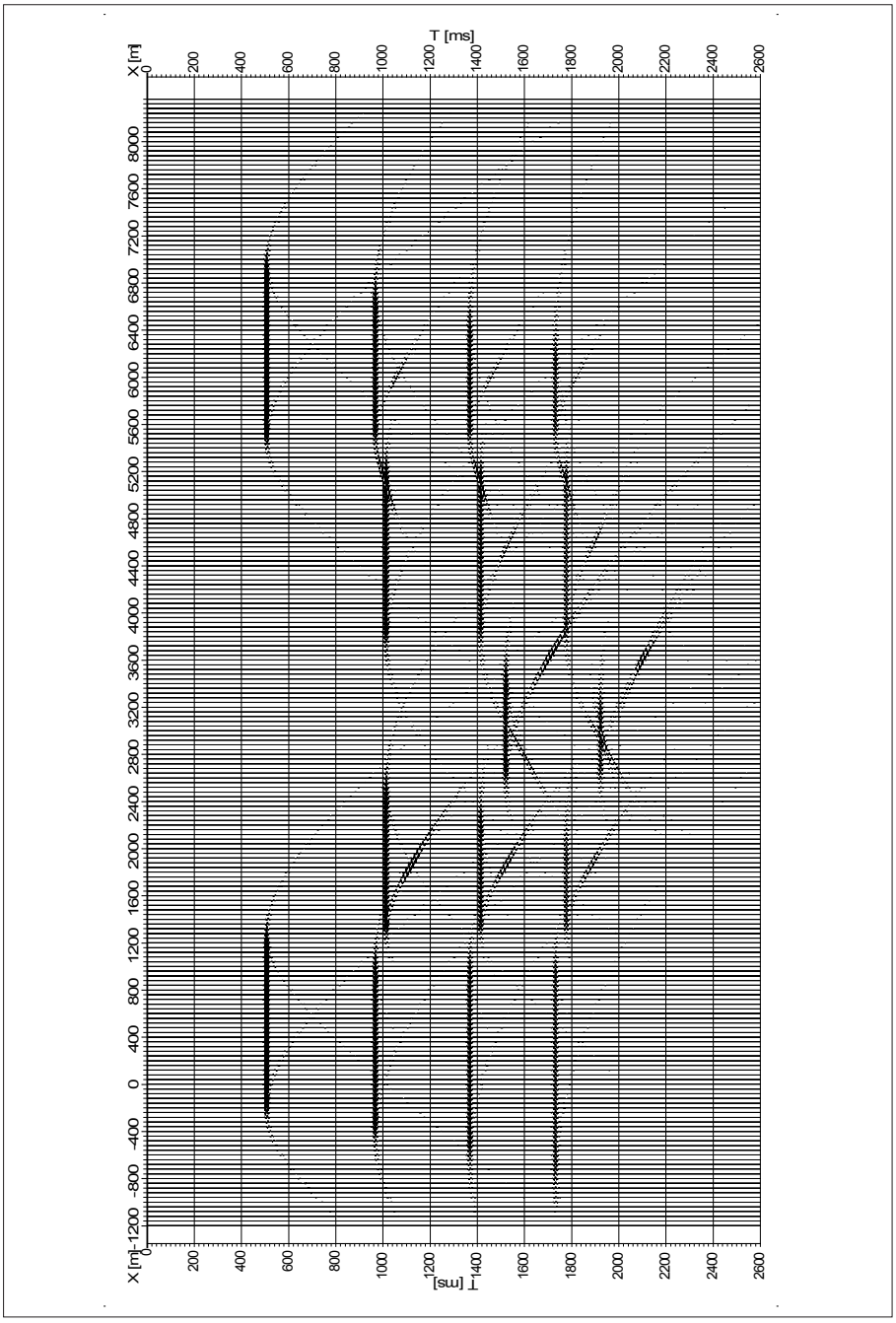

Fig. 3.64. The zero-offset time section for anisotropic TTI model; anisotropy parameters $\varepsilon = 0.3$; $\delta = 0.1$; dip angle $\theta = 60°$

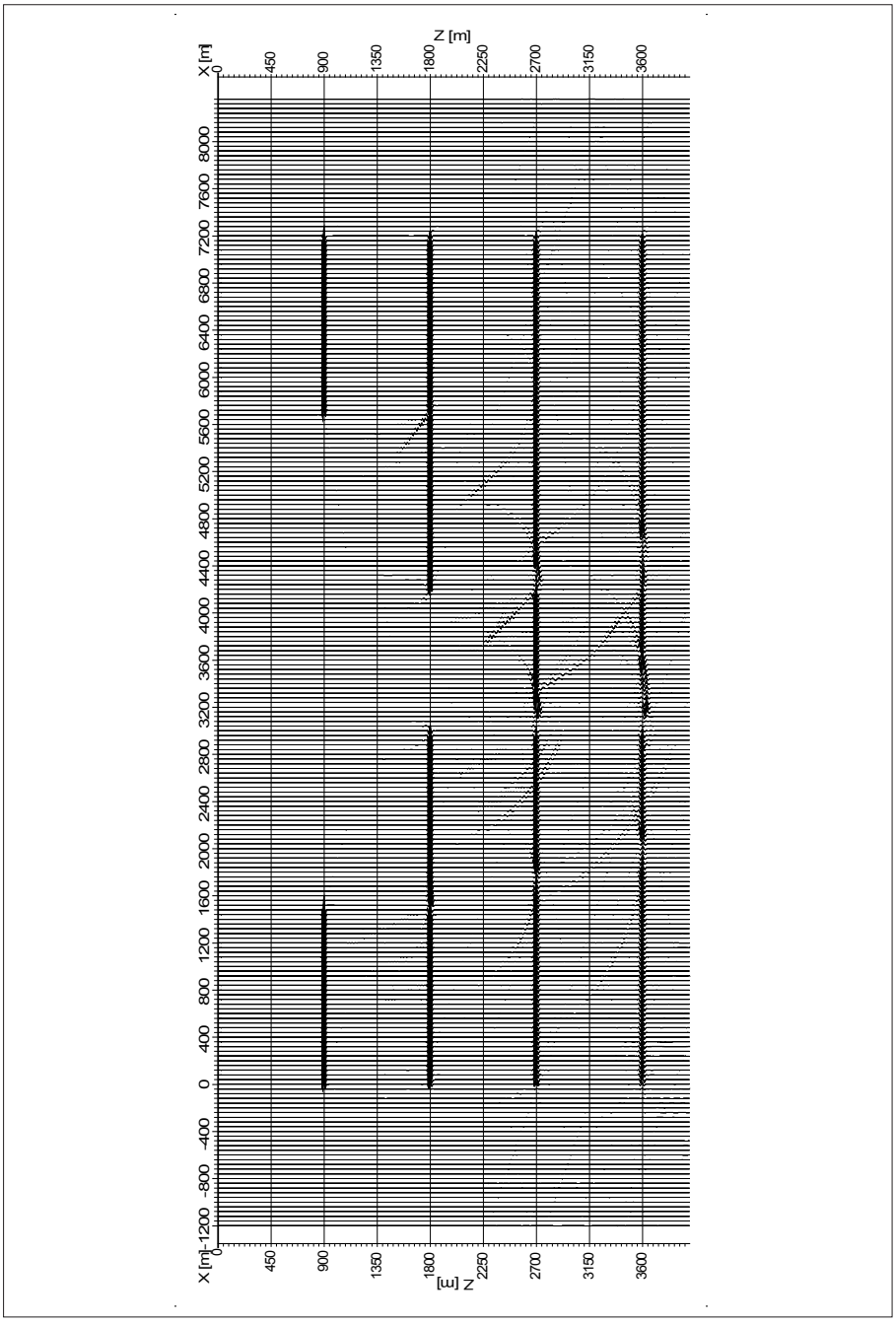

Fig. 3.65. The zero-offset migration for the anisotropic TTI model (Fig. 3.64); anisotropy parameters $\varepsilon = 0.3$; $\delta = 0.1$; dip angle $\theta = 60°$

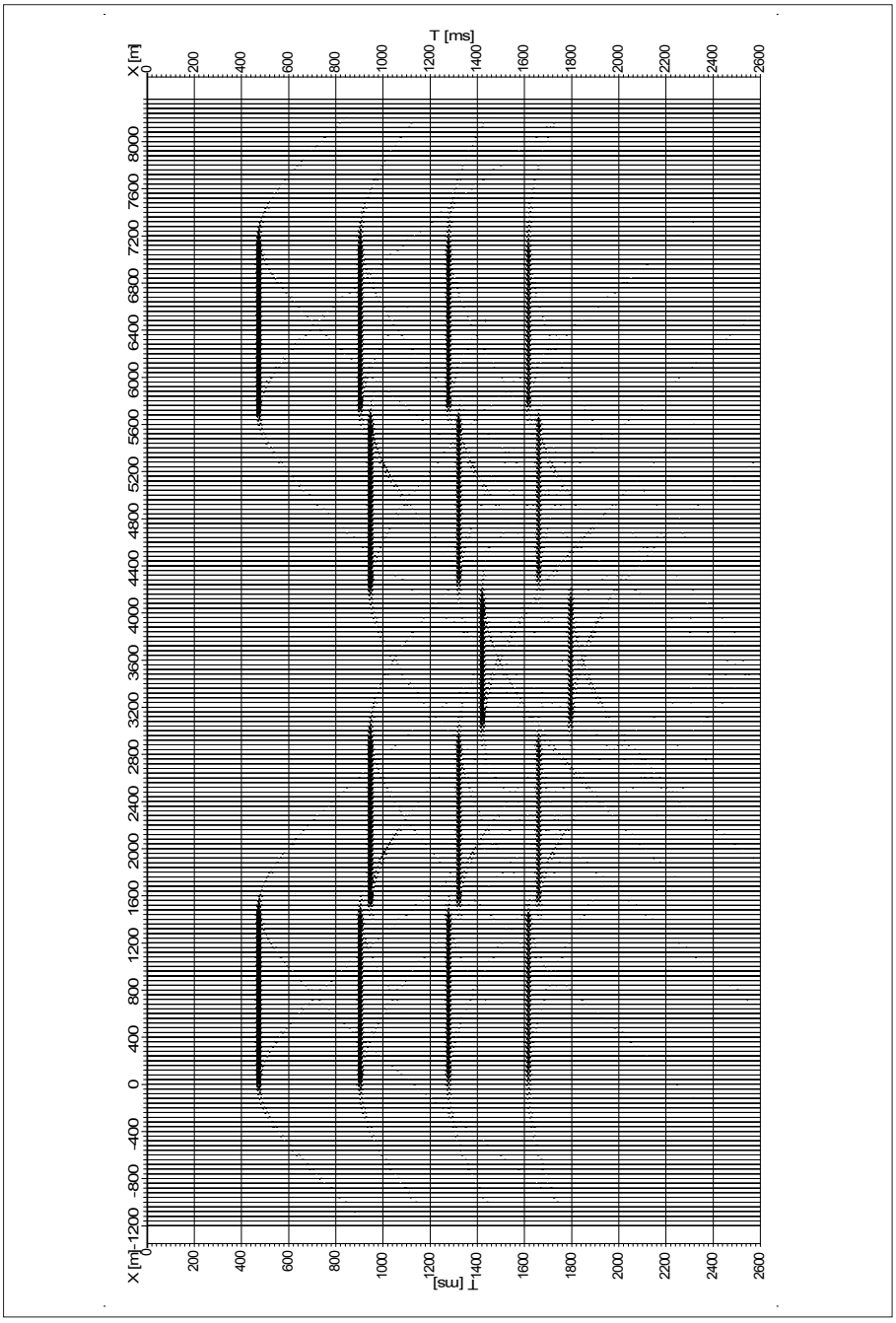

Fig. 3.66. The zero-offset time section for anisotropic TTI model; anisotropy parameters $\varepsilon = 0.3$; $\delta = 0.1$; dip angle $\theta = 90°$

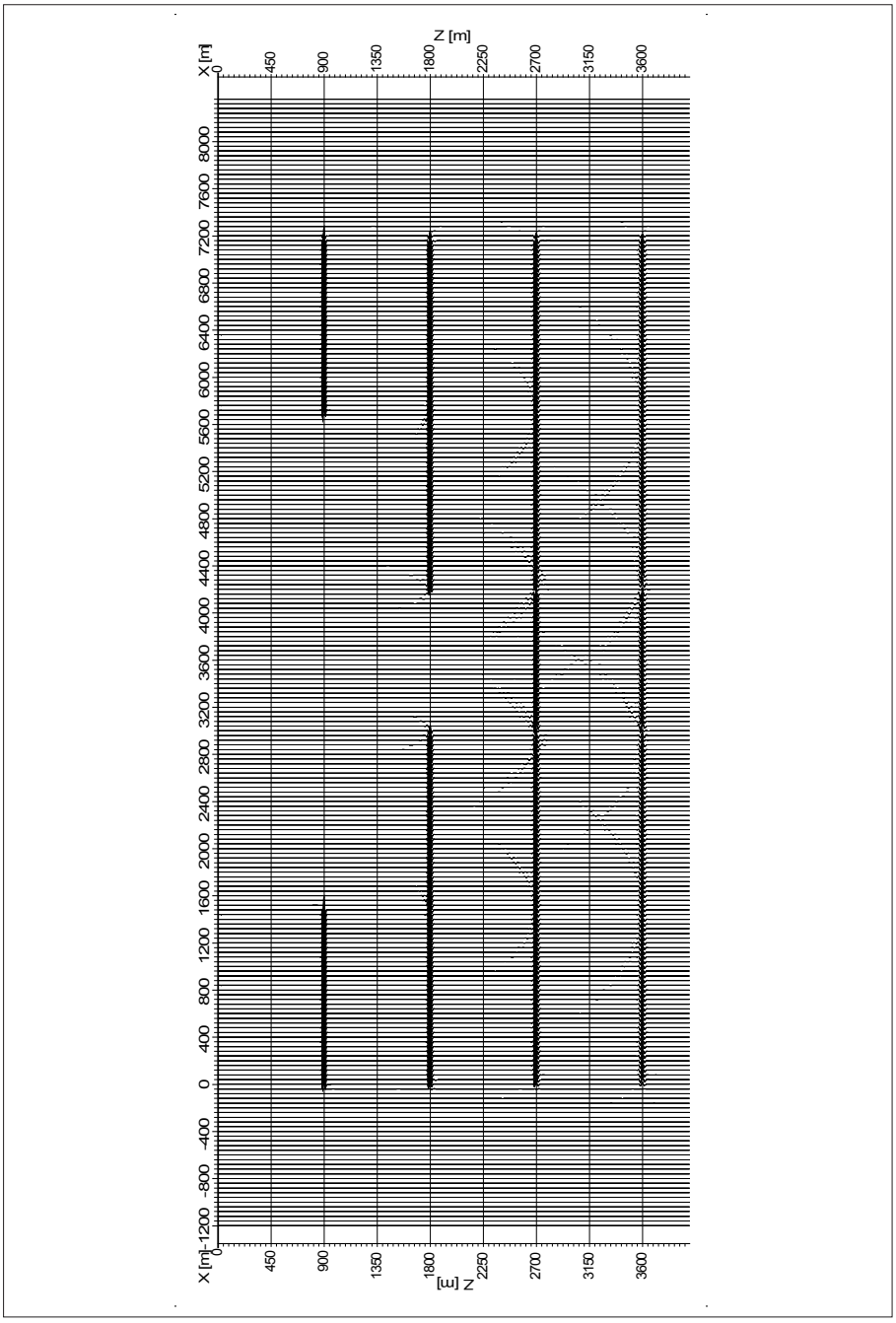

Fig. 3.67. The zero-offset migration for the anisotropic TTI model (Fig. 3.66); anisotropy parameters $\varepsilon = 0.3$; $\delta = 0.1$; dip angle $\theta = 90°$

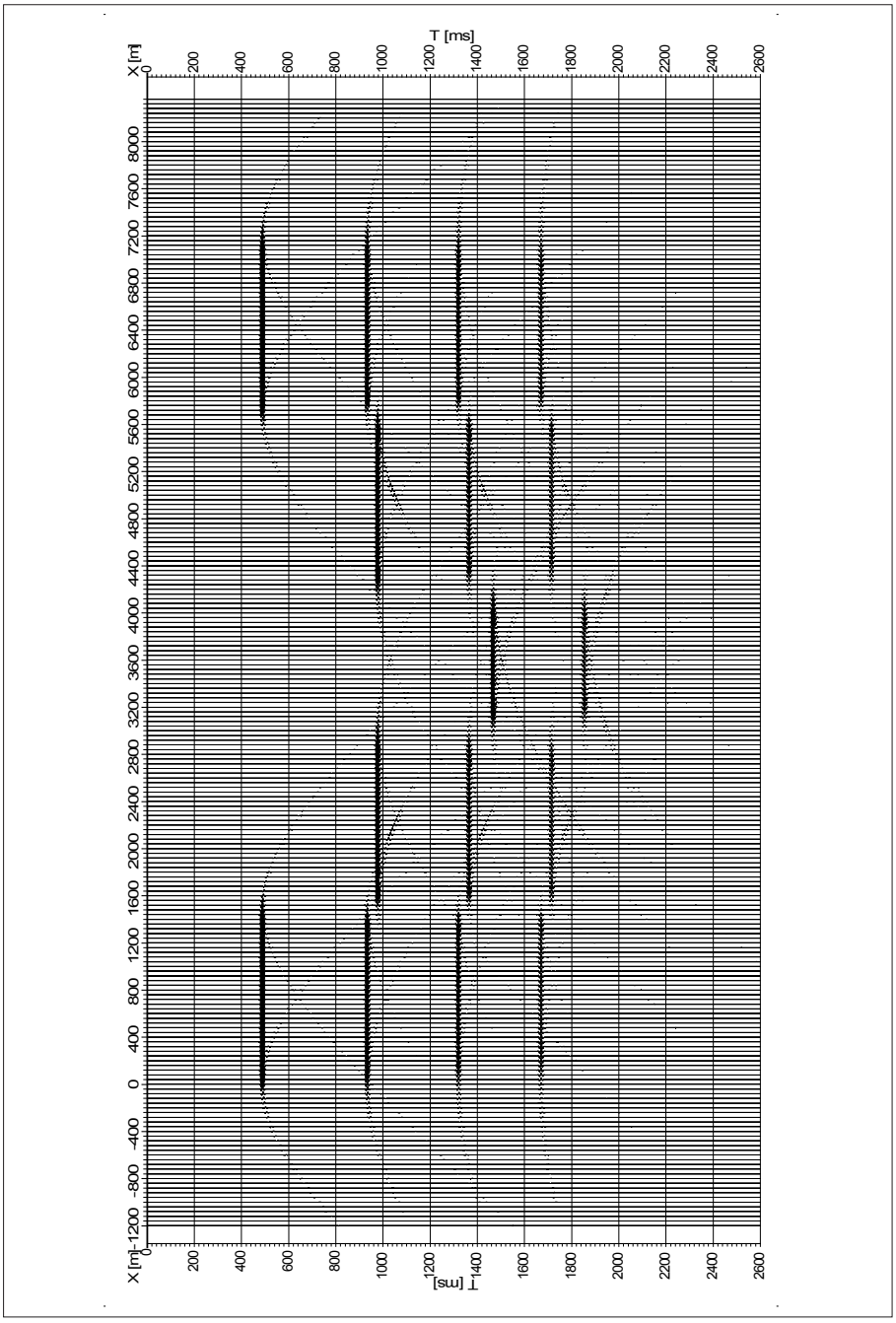

Fig. 3.68. The zero-offset time section for anisotropic HTI model; anisotropy parameters $\varepsilon = 0.25$; $\delta = 0.1$; azimuthal angle $\Psi = 0°$

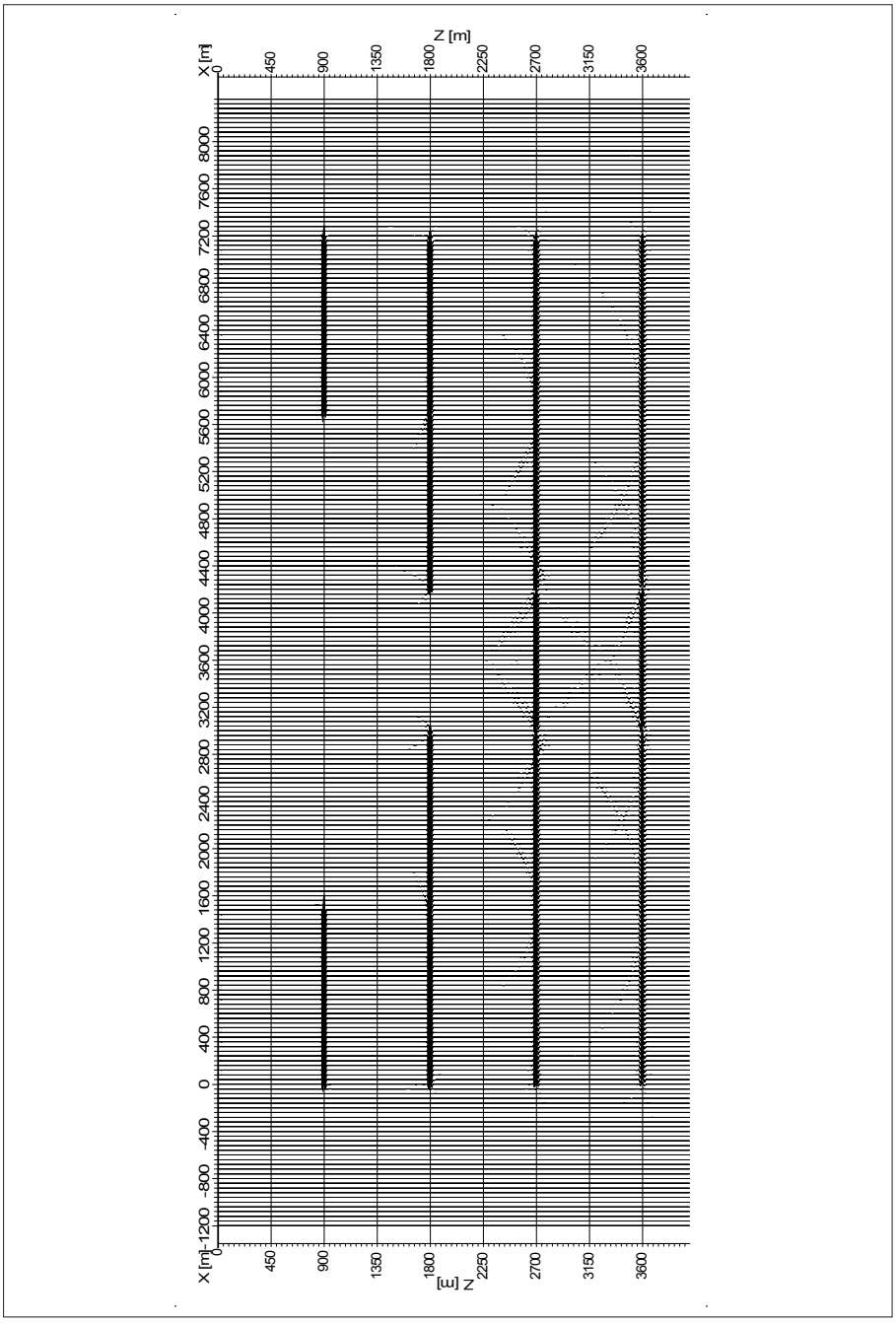

Fig. 3.69. The zero-offset migration for the anisotropic HTI model (Fig. 3.68); anisotropy parameters $\varepsilon = 0.25$; $\delta = 0.1$; azimuthal angle $\Psi = 0°$

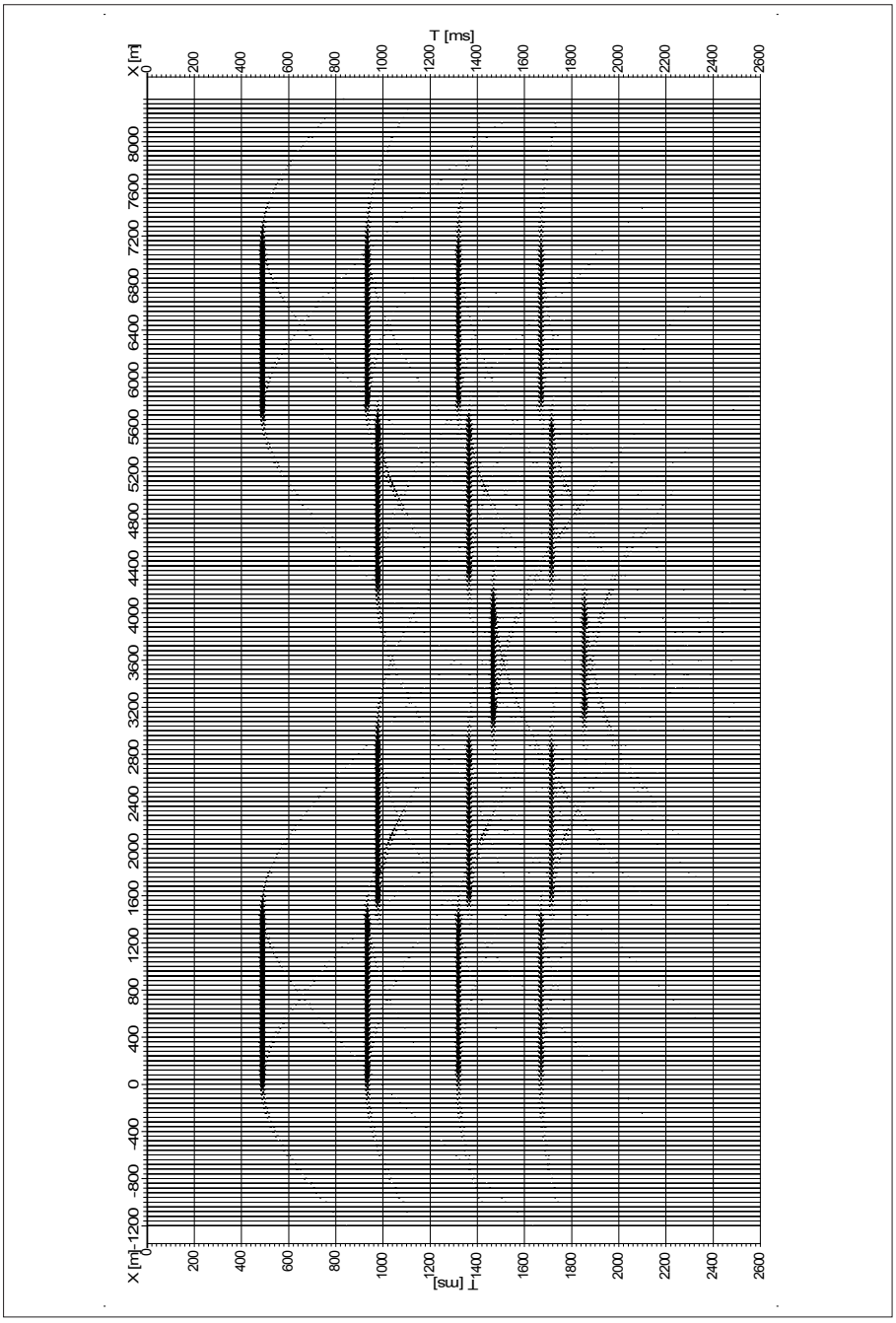

Fig. 3.70. The zero-offset time section for anisotropic HTI model; anisotropy parameters $\varepsilon = 0.25$; $\delta = 0.1$; azimuthal angle $\Psi = 30°$

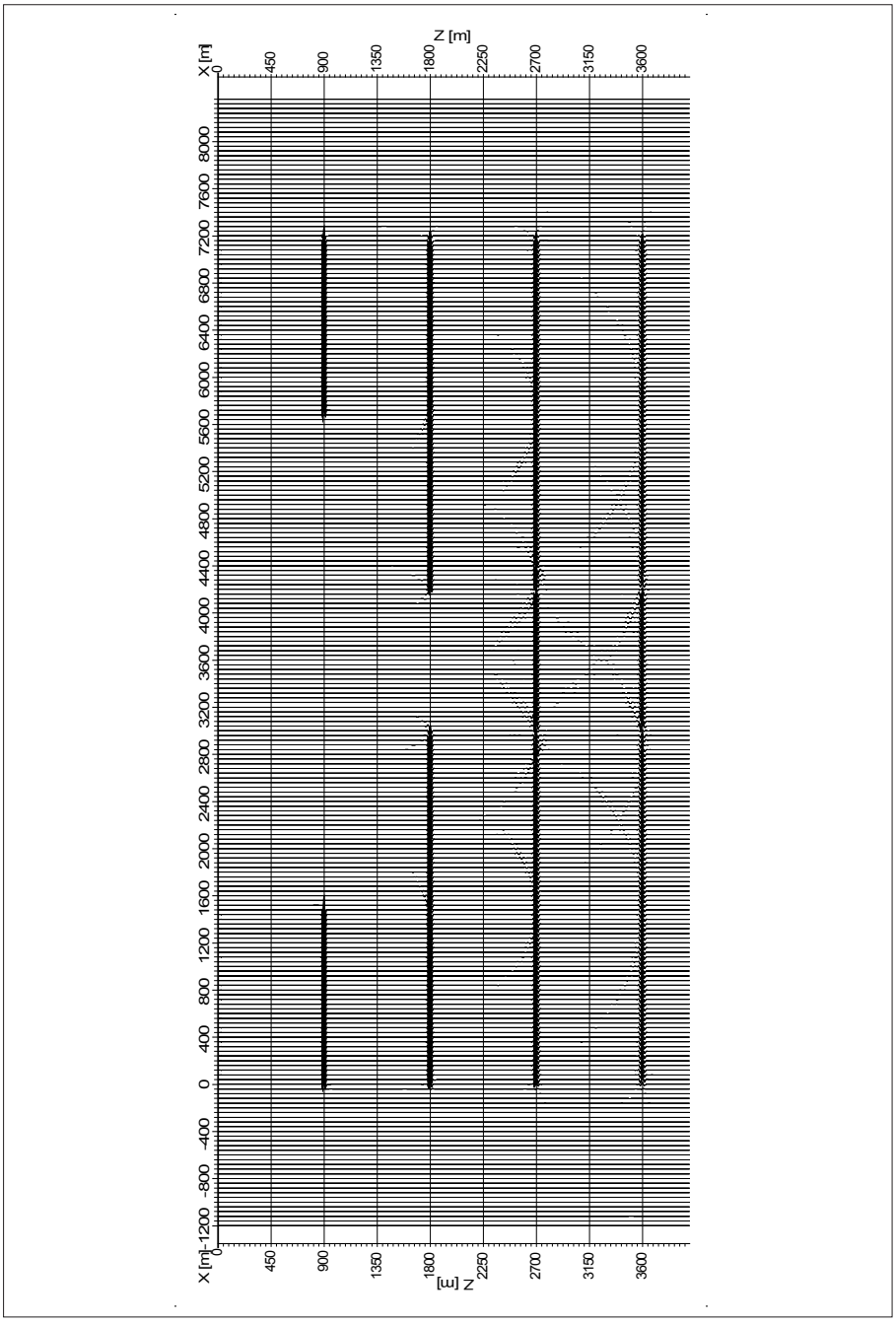

Fig. 3.71. The zero-offset migration for the anisotropic HTI model (Fig. 3.70); anisotropy parameters $\varepsilon = 0.25$; $\delta = 0.1$; azimuthal angle $\Psi = 30°$

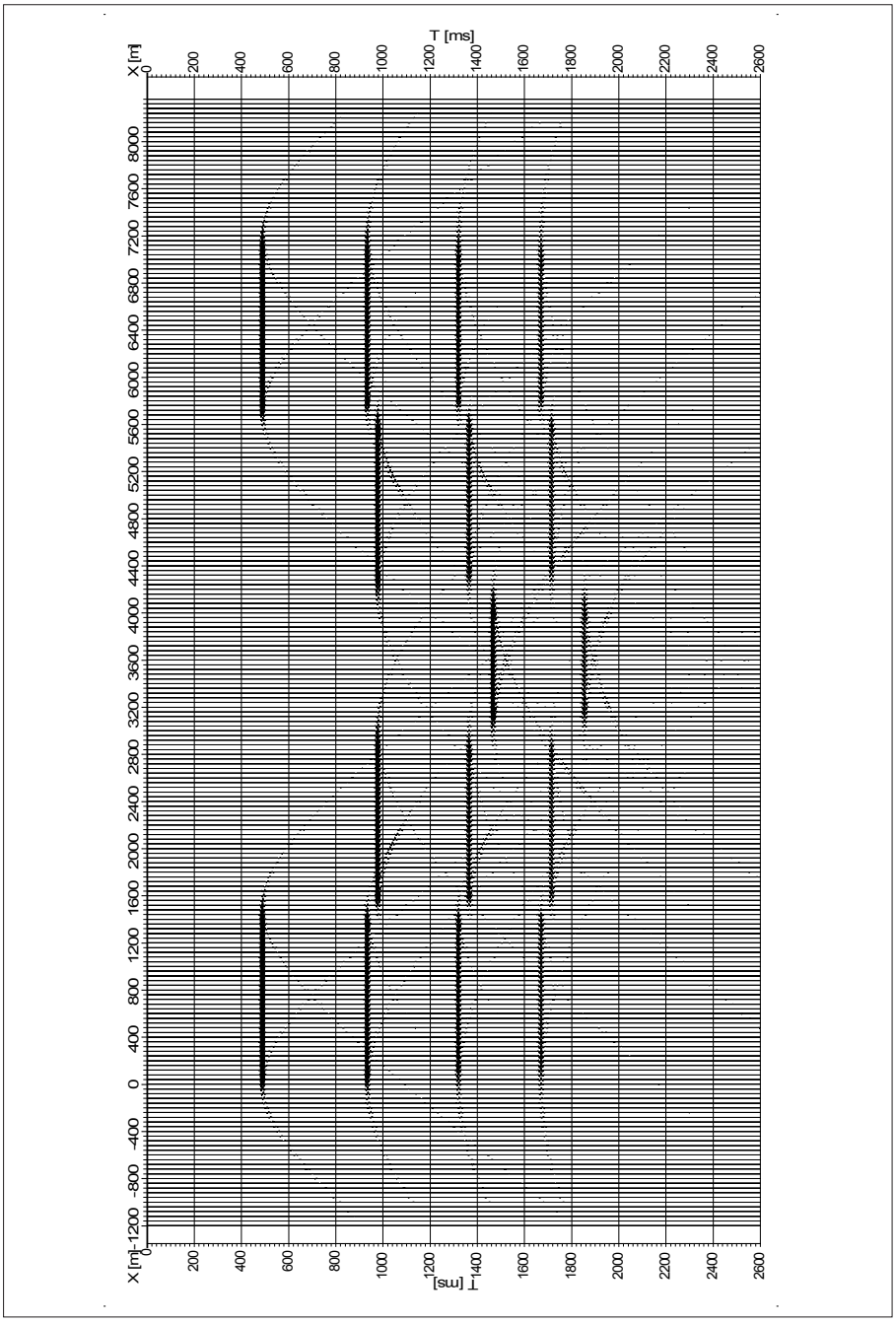

Fig. 3.72. The zero-offset time section for anisotropic HTI model; anisotropy parameters $\varepsilon = 0.25$; $\delta = 0.1$; azimuthal angle $\Psi = 60°$

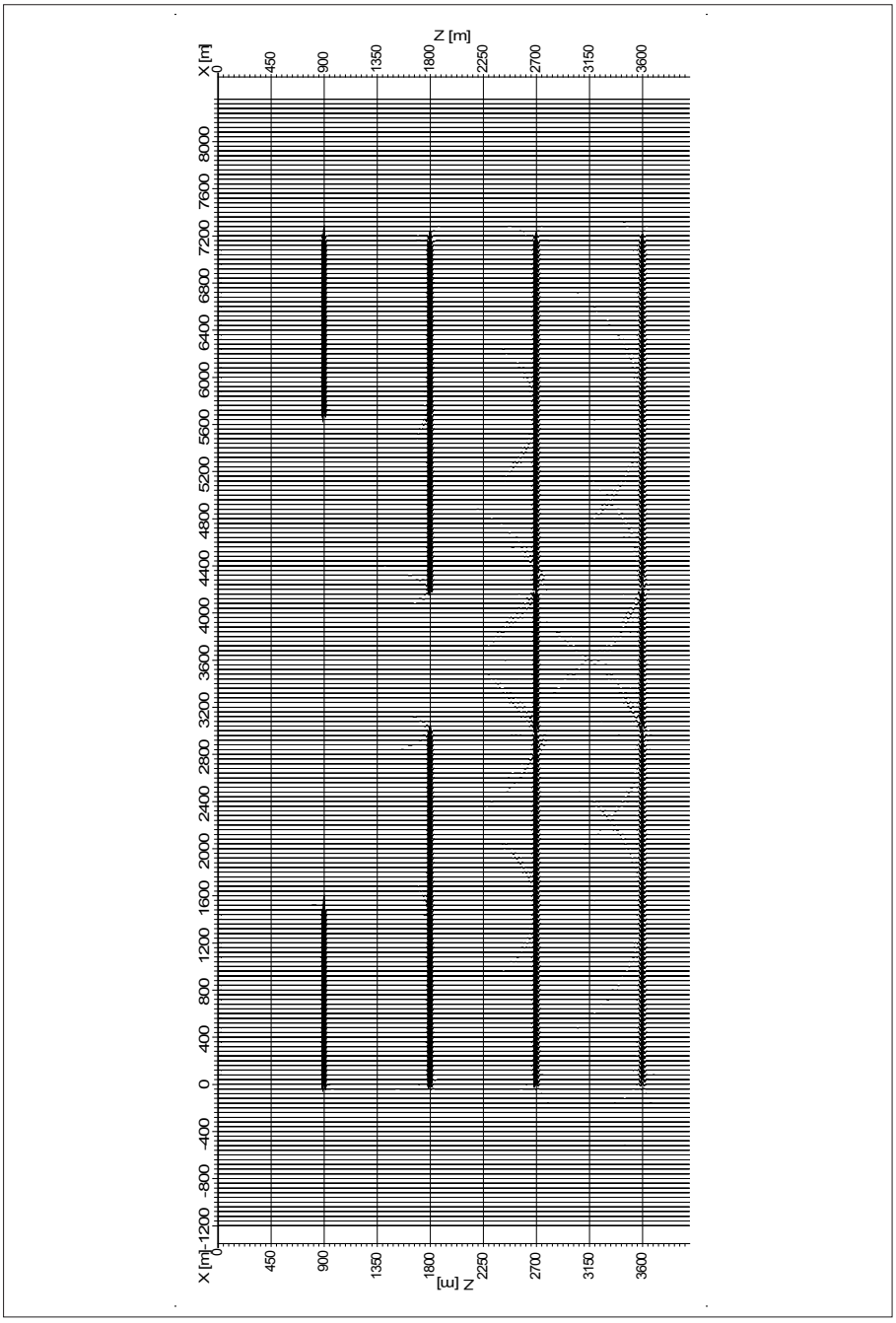

Fig. 3.73. The zero-offset migration for the anisotropic HTI model (Fig. 3.72); anisotropy parameters $\varepsilon = 0.25$; $\delta = 0.1$; azimuthal angle $\Psi = 60°$

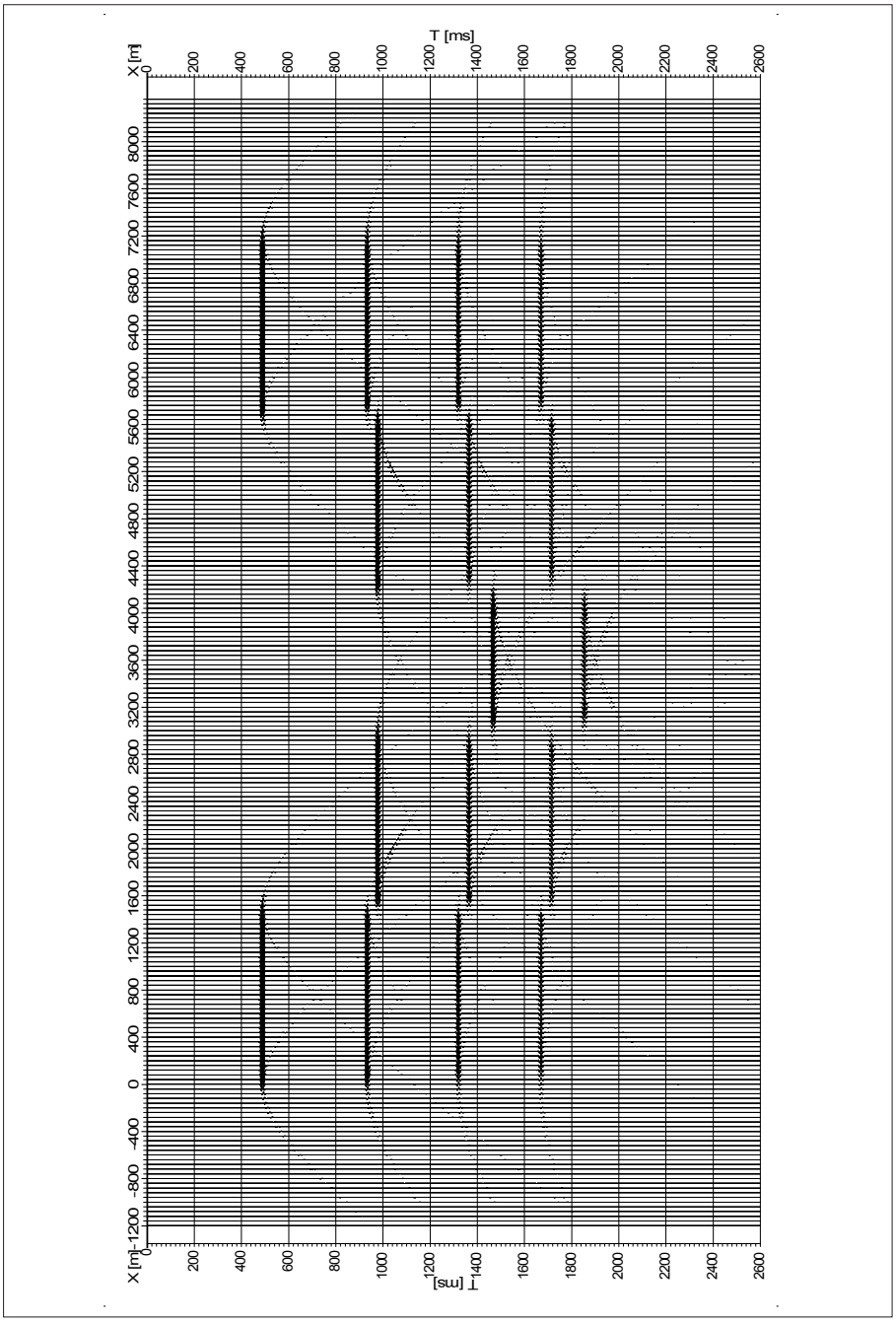

Fig. 3.74. The zero-offset time section for anisotropic HTI model; anisotropy parameters $\varepsilon = 0.25$; $\delta = 0.1$; azimuthal angle $\Psi = 90°$

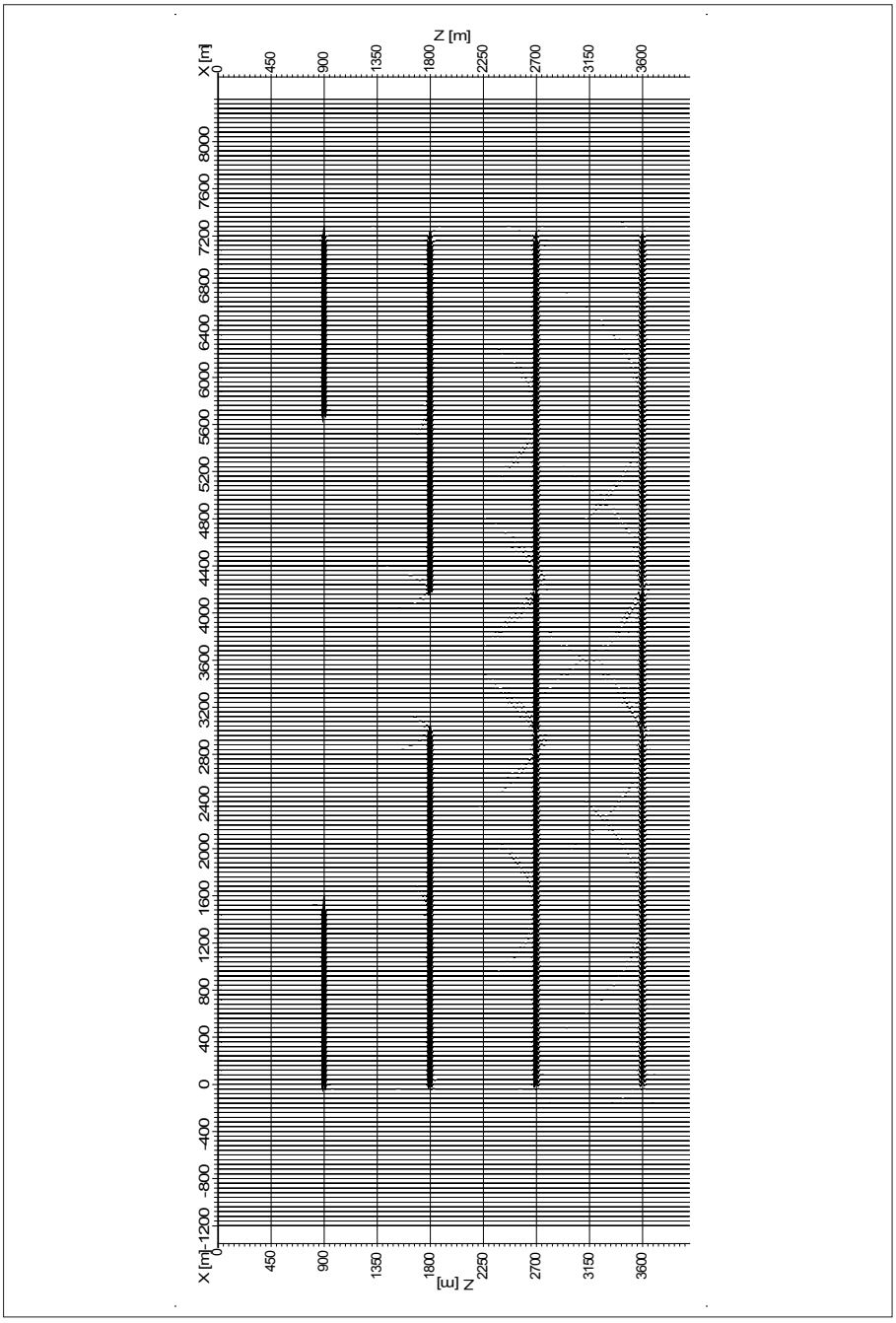

Fig. 3.75. The zero-offset migration for the anisotropic HTI model (Fig. 3.74); anisotropy parameters $\varepsilon = 0.25$; $\delta = 0.1$; azimuthal angle $\Psi = 90°$

Conclusions

In this study, we presented a new method of pseudo-acoustic wave's propagation in anisotropic, azimuthal media. Waves propagation described in wavenumbers domain was derived from a dispersion relation, as the outcome of the resolving of the full system of elastic equations by use of multidimensional Fourier's transform. In this equation system one assumed that the velocity of shear waves $V_{SV} = 0$, that these waves has little influence on compressional wave velocity, which legitimates the name – pseudo-acoustic waves.

Propagation of pseudo-acoustic waves in one-way and two-sided equation is based on determination of eigenvalues in a dispersion relation, i.e. time frequency as a function of wavenumbers, compressional velocity, Thomsen's anisotropy parameters and dip angle θ and azimuthal angle Ψ. The eigenvalue of a dispersion relation has the universal characteristic of separability of the compressional velocity. This property is suitable for all transverse isotropic media types (VTI, TTI(θ), HTI(Ψ)), which directly allows the construction of waves equations of first and second order. For isotropy media these equations transform into generally used acoustic equations.

A wide range of experiments for waves propagations generated by point source in homogeneous HTI(Ψ) media was performed. We used the exact solution (Cardano for cubic equation – (1.23)) and two approximations – the solution of biquadratic equations (1.28 and 1.29). With the use of "spike signal" for the exact solution (1.23) a high accuracy of propagation (error ≈ 0.2%) and very good standard snapshots was obtained for a wide range of Ψ angle. Those snapshots are deprived of the "diamond shape" type of noise, which is characteristic for propagation of pseudo-acoustic waves according to the space coordinates formula. The experiments of pseudo-acoustic wave propagation in the xz-plane in dependency to azimuthal angle Ψ, have shown that the velocity of compressional waves are expressed by relation $V(\Psi) = V_P(1 + 2\varepsilon \cos^2\Psi)^{½}$ which indicates the ellipsoidal character of horizontal velocity and confirms indirectly, the dependence of velocity $V_{NMO}^{-2}(\Psi)$ according to Grechka V. and Tsvankin I. [21].

For depth imaging of azimuthal anisotropic media, one used back propagation, i.e. zero-offset migration in the MG(F-K) version, working in wavenumbers (K) and frequency (F) domain, which was successfully adapted for transverse isotropy (TI) [32] media, for TTI and VTI as well. Algorithmic structures for every migration type are similar, whereas depth extrapolation expressed by an exponential function, which exponent, vertical wavenumber is separately derived from the dispersion relation for each migration type. Essential MG(F-K) migration property is the ability to take into consideration the variability of a compressional wave's velocity as well as Thomsen's anisotropy parameters, ε and δ, with the use of Neumann's series.

The tests of zero-offset migration executed on an inhomogeneous, multilayered anticline model, have shown independence of imagined structures on azimuthal angle, i.e. the expected result. One can notice a relatively low sensitivity of imaging on azimuthal angle variability conditioned by the effect of horizontal velocity dependence on azimuthal angle. Strong dependence of vertical shifts of the reflector on ε parameter, was confirmed in the second experiment of zero-offset migration for vertical thrusts. In this case, one can notice that the zero-offset wavefield is independent of the azimuthal angle because it is shaped by vertical compressional waves, propagating with their maximum velocities.

In general, the method of waves propagation in azimuthal anisotropic medium presented here, has shown high precision in the process of modeling and migration.

References

[1] Alkhalifah T.: *Acoustic approximation for processing in transversely isotropic medi*a. Geophysics 1998, vol. 63, no. 2, p. 623–631.

[2] Alkhalifah T.: *An acoustic wave equation for anisotropic media*. Geophysics 2000, vol. 65, no. 4, p. 1239–1250.

[3] Alkhalifah T.: *Traveltime computation with the linearized eikonal equation for anisotropic media*. Geophysical Prospecting 2002, vol. 50, p. 373–382.

[4] Auld B.: *Acoustic field and waves in solid*. Krieger Publishing Company 1990, vol. 1.

[5] Banik N. C.: *Velocity of anisotropy of shales and depth estimation in the North Sea basin*. Geophysics 1984, vol. 49, no. 9, p. 1411–1419.

[6] Baysal E., Kosloff D. D., Sherwood J. W.: *Reverse time migration*. Geophysics 1984, vol. 48, no. 9, p. 1411–1419.

[7] Bonsal R., Sen M. K.: *Finite – difference modeling of S-wave splitting in anisotropic media*. Geophysical Prospecting 2008, vol. 56, p. 293–312.

[8] Boore D.: *Finite difference methods for seismic wave propagation in heterogeneous materials*. Methods in computational physics 1972, vol. 11, Academic Press Inc.

[9] Bube K., Nemeth T., Stefani J., Ergas R., Wei Liu, Nihei K., Linbin Zhang: *On the instability in second – order systems for acoustic VTI and TTI media*. Geophysics 2012a, vol. 77, no. 5, p. T171–T186.

[10] Bube K., Nemeth T., Stefani J., Wei Liu, Nihei K., Ergas R., Zhang L.: *First-order systems of elastic and acoustic variable-tilt TI media*. Geophysics 2012, vol. 77, no. 5, p. T157–T170.

[11] Ĉerveny W.: *Seismic ray theory*. Cambridge University Press 2001.

[12] Crampin S.: *Evaluation of anisotropy by shear-wave splitting*. Geophysics 1985, vol. 50, p. 142–152.

[13] Daley P., Hron F.: *Reflection and transmission coefficients for transversely isotropic solid*s. Bull. Seis. Soc. Am. 1977, vol. 67, p. 661–675.

[14] Danek T., Leśniak A., Pięta A.: *Numerical modeling of seismic wave propagating in selected anisotropic media*. Studia, Rozprawy, Monografie Nr 162, Instytut Gosp. Surowcami Mineralnymi i Energią PAN, 2010.

[15] Du X., Fletcher R., Fowler P. J.: *A new pseudo-acoustic wave equation for TI media*. 70th Annual International Conference and Exhibition 2008, EAGE, Extended Abstracts, H033.

[16] Duveneck E., Bakker P. M.: *Stable P-wave modeling for reverse time migration in tilted media*. Geophysics 2011, vol. 76, no. 2, p. 565–575, doi: 10.1190/1.3533964.

[17] Faria E., Stoffa P.: *Traveltime computation in transversely isotropic media*. Geophysics 1994, vol. 59, p. 272–281.

[18] Fletcher R., Du X., Fowler P. J.: *A new pseudo-acoustic wave equation for TI media*. Annual Meeting 2008, Las Vegas, SEG, Extended Abstracts.

[19] Gajewski D., Pŝencik V.: *Computation of high–frequency seismic wavefield in 3D-laterally inhomogeneous anisotropic media*. Geophysical Journal of the Royal Astronomical Society 1987, 91, p. 381–411.

[20] Gazdag J.: *Modeling of the acoustic wave equation with transform methods*. Geophysics 1981, vol. 46, p. 854–859.

[21] Grechka V., Tsvankin I.: *3D description of normal moveout in anisotropic inhomogeneous media*. Geophysics 1998, vol. 63, p. 1079–1092.

[22] Han Q., Wu R. S.: *A one-way dual-domain propagator for scalar qP-waves in VTI media*. Geophysics 2005, vol. 70, no. 2, D9–D17.

[23] Kendall R., Gray S., Xiaogui Miao: *Anisotropic prestack depth migration for multicomponent data-methodology and examples*. Extended Abstracts 63th EAGE Conference 2001.

[24] Kitchenside P. W.: *Phase shift-based migration for transverse isotropy*. Proc 61st SEG Annual Meeting 1991, Expanded Abstracts, p. 993–998.

[25] Koren Z., Ravve I.: *Full-azimuth subsurface angle domain wavefield decomposition and imaging: Part I – Directional and reflection image gathers*. Geophysics 2011, vol. 76, no. 1 p. S1–S13, doi: 10.1190/1.3511352.

[26] Kosloff D., Filho Q., Tessmer E., Behle A.: *Numerical solution of the acoustic and elastic wave equation by new rapid extension method*. Geophysical Prospecting 1989, vol. 37, p. 983–994.

[27] Kostecki A.: *Algorithm of prestack migration of wavefield*. Proc. First Science-Tech. Conf. The Seismic Problems of the Interpretation" 1994, Cracow/ Poland (in polish).

[28] Kostecki A., Półchłopek A.: *Stable depth extrapolation of seismic wavefields by a Neumann series*. Geophysics 1998, vol. 63, no. 6, p. 2063–2071.

[29] Kostecki A., Półchłopek A.: *Prestack depth migration using converted waves*. Acta Geophysica 2003, vol. 53, no. 1, p. 73–84.

[30] Kostecki A.: *Tilted Transverse Isotropy*. Nafta-Gaz 2011, no. 11, p. 769–776.

[31] Kostecki A., Półchłopek A.: *Generalized migration in frequency – wavenumber domain MG(F-K) in anisotropic media*. Acta Geophysica 2013, vol. 61, no. 3, p. 624–637.

[32] Kostecki A., Półchłopek A., Żuławiński K.: *Odwzorowanie struktur wgłębnych w ośrodkach anizotropowych metodą migracji sejsmicznej. The imaging structures in anisotropic media by seismic migration*. Prace Naukowe Instytutu Nafty i Gazu – Państwowego Instytutu Badawczego Nr 191, 2013. 134 p. Monograph (in polish).

[33] Kostecki A., Żuławiński K.: *Modeling of zero – offset time sections In TTI (Tilted Transverse Isotropy) media by pseudospectral method*. Proc. EAGE Conference St. Petersburg 2013.

[34] Kostecki A., Żuławiński K.: *Modeling and migration of zero-offset time sections in TTI media by pseudo-spectral method*. Nafta-Gaz 2014, no. 12, p. 855–860.

[35] Kostecki A., Żuławiński K.: *The pseudo-acoustic equations of the scalar wavefield in anisotropic media*. Nafta-Gaz 2015, no. 11, p. 811–815.

[36] Kumar D., Sen M., Ferguson R.: *Traveltime calculation and prestack migration in tilted transversely isotropic media*. Geophysics 2004, vol. 69, p. 37–44. doi: 10.1190/1.1649373.

[37] Levander A.: *Fourth – order finite – difference P-SV seismograms*. Geophysics 1988, vol. 53, no. 11.

[38] Loewenthal D., Lu L., Robertson R., Sherwod I.: *The wave equation applied to migration*. Geophysical Prospecting 1976, vol. 24, no. 2, p. 380–399.

[39] McMechan G. A.: *Migration by extrapolation of time dependent boundary values*. Geophysical Prospecting 1983, vol. 31, no. 4, p. 413–420.

[40] Pech A., Tsvankin I. and Grechka V.: *Quartic moveout coefficient: 3D description and application to tilted TI media*. Geophysics 2003, vol. 68, p. 1600–1610, doi: 10.1190/1.162.0634.

[41] Podvin P., Lecomte I.: *Finite difference computation of traveltimes in very contrasted velocity models. A massively parallel approach and its associated tools*. Geophysical Journal International 1991, vol. 105, p. 272–284.

[42] Postma G. M.: *Wave propagation in a stratified medium*. Geophysics 1955, vol. 20, no. 4.

[43] Ravve I. and Koren Z.: *Full-azimuth subsurface angle domain wavefield decomposition and imaging. Part 2 – Local angle domain*. Geophysics 2011, vol. 76, no. 2, p. S51–S64, doi: 10.1190/1.3549742.

[44] Ristow D., Rühl T.: *Fourier finite-difference migration*. Geophysics 1994, vol. 59, no. 12, p. 1882–1893.

[45] Rousseau J. H.: *Depth migration in heterogeneous transversely isotropic media with the phase-shift-plus interpolation method*. 67-th Meeting SEG 1997, Expanded Abstracts, p. 1703–1706.

[46] Schneider W. A.: *Integral formulation for migration in two and three dimensions*. Geophysics 1978, vol. 43, no. 1, p. 49–76.

[47] Sena A., Tőksoz M. N.: *Kirchoff migration and velocity analysis for converted and nonconverted waves in anisotropic media*. Geophysics 1993, vol. 58, p. 265-276.

[48] Shearer P., Chapman C.: *Ray tracing in anisotropic media with linear gradient*. Geoph. Inter. 1988, 94, p. 575–580.

[49] Sun X. and Sun S. Z.: *Full-azimuth anisotropic prestack time migration in the local--angle domain and its application in fracture detection*. Geophysics 2015, vol. 80, no. 2, C37–C47.

[50] Taner M. T. and Koehler F.: *Velocity spectra- digital computer derivation and application of velocity functions*. Geophysics 1969, vol. 34, p. 859–881, doi: 10.1190/1.1440058.

[51] Thomsen L.: *Weak elastic anisotropy*. Geophysics 1986, vol. 51, no. 10, p. 1954–1966.

[52] Tsingas C., Wafidis A., Kanasewich E.: *Elastic wave propagation in transversely isotropic media using finite-differences*. Geophysical Prospecting 1990, vol. 38, p. 933–949.

[53] Tsvankin I., Grechka V.: *Seismology of azimuthally anisotropic media and seismic fracture characterization*. Geophysical Reference Series 17:SEG, 2011.

[54] Uzcategui O.: *2-D depth migration in transversely isotropic media using explicit operators*. Geophysics 1995, vol. 60, p. 1819–1829.

[55] Virieux J.: *P-SV wave propagation in heterogeneous media; velocity-stress finite-difference method*. Geophysics 1986, vol. 51, p. 889–901.

[56] Wang D., Sun S. Z., Zhou I., Wang I., Yue H., Liu Y.: *3D amplitude – preserved full-azimuth anisotropic imaging: Offering more reliable azimuthal AVO for fracture detection*. 75 Conference AEGE 2013, Abstracts, P1305.

[57] Xie W., Yang D., Liu F., Li J.: *Reverse – time migration in acoustic VTI media using a high-order stereo – operator*. Geophysics 2014, vol. 79, no. 3, p. WA3–WA13.

[58] Yang D., Liu E., Zhang Z., Teng J.: *Finite-difference modeling in two-dimensional anisotropic media using a flux-corrected technique*. Geophysical Journal Int. 2002, vol. 148, p. 320–328.

[59] Zhan G., Pestana R. C., Stoffa P. L.: *Decoupled equations for reverse time migration in tilted transversely isotropic media*. Geophysics 2012, vol. 77, no. 2, T37–T45, doi: 101190GEO2011-175.1.

[60] Zhang L., Rector III J. W., Hoversten M.: *Finite-difference modeling of wave propagation in acoustic tilted TI media*. Geophysical Prospecting 2005, vol. 53, p. 843–852.

[61] Zhang H., Zhang Y.: *Reverse time migration in 3D heterogeneous TTI media*. 78th Annual Inter. Meeting SEG 2008. Expanded Abstracts, 27, p. 2196–2200.

[62] Zhou H., Zhang G., Bloor R.: *An anisotropic acoustic wave equation for VTI media*. 68th Annual International Conference EAGE 2006a, Extended Abstracts.

[63] Zhou H., Zhang G. and Bloor R.: *An anisotropic acoustic wave equation for modeling and migration in 2D TTI media*. 76th Annual International Meeting SEG 2006b, Expanded Abstracts 25, p. 194–198.

[64] Zhu J., Dorman J.: *Two-dimensional, three-component wave propagation in a transversely isotropic medium with arbitrary-orientation-finite element modeling*. Geophysics 2000, vol. 65, p. 934–942.

Table of figures

Fig. 1.1. Right-handed coordinate measurement system x, y, z and x', y', z' system tied with inclined, inter bedding layering simulating tilted media TTI (Titled Transverse Isotropy) 20

Fig. 2.1. The forms of signal used in testing experiment 37

Fig. 2.2. Snapshot of signal Ricker's 60 Hz propagation from relation (1.29) in moment time $t = 0.2$ s; anisotropy parameter's: $\varepsilon = 0.3$; $\delta = 0.1$; azimuthal angle Ψ=0°; steps of computations: $\Delta x = \Delta z = 4$ m, $\Delta t = 0.5$ ms 38

Fig. 2.3. Snapshot of zero-phase signal propagation from relation (1.29) in moment time $t = 0.2$ s; anisotropy parameter's: $\varepsilon = 0.3$; $\delta = 0.1$; azimuthal angle $\Psi = 0°$; steps of computations: $\Delta x = \Delta z = 4$ m, $\Delta t = 0.5$ ms 39

Fig. 2.4. Snapshot of spike signal propagation from relation (1.29) in moment time $t = 0.2$ s; anisotropy parameter's: $\varepsilon = 0.3$; $\delta = 0.1$; azimuthal angle $\Psi = 0°$; steps of computations: $\Delta x = \Delta z = 4$ m, $\Delta t = 0.5$ ms 40

Fig. 2.5. Snapshot of spike signal propagation from relation (1.29) in moment time $t = 0.2$ s; anisotropy parameter's: $\varepsilon = 0.3$; $\delta = 0.2$; azimuthal angle $\Psi = 30°$; steps of computations: $\Delta x = \Delta z = 4$ m, $\Delta t = 0.5$ ms 41

Fig. 2.6. Snapshot of spike wave propagation from algorithm (1.29) for parameters: $\varepsilon = 0.3$; $\delta = -0.1$ azimuthal angle $\Psi = 0°$; in moment time $t = 0.4$ s; steps of computation: $\Delta x = \Delta z = 4$ m, $\Delta t = 0.5$ ms 44

Fig. 2.7. Snapshot of spike wave propagation from algorithm (1.29) for parameters: $\varepsilon = 0.3$; $\delta = -0.1$ azimuthal angle $\Psi = 30°$; in moment time $t = 0.4$ s; steps of computation: $\Delta x = \Delta z = 4$ m, $\Delta t = 0.5$ ms 45

Fig. 2.8. Snapshot of spike wave propagation from algorithm (1.29) for parameters: $\varepsilon = 0.3$; $\delta = -0.1$ azimuthal angle $\Psi = 45°$; in moment time $t = 0.4$ s; steps of computation: $\Delta x = \Delta z = 4$ m, $\Delta t = 0.5$ ms 46

Fig. 2.9. Snapshot of spike wave propagation from algorithm (1.29) for parameters: $\varepsilon = 0.3$; $\delta = -0.1$ azimuthal angle $\Psi = 60°$; in moment time $t = 0.4$ s; steps of computation: $\Delta x = \Delta z = 4$ m, $\Delta t = 0.5$ ms 47

Fig. 2.10. Snapshot of spike wave propagation from algorithm (1.29) for parameters: ε = 0.3; δ = –0.1 azimuthal angle Ψ = 90°; in moment time t = 0.4 s; steps of computation: Δx = Δz = 4 m, Δt = 0.5 ms 48
Fig. 2.11. Snapshot of spike wave propagation from algorithm (1.29) for parameters: ε = 0.3; δ = –0.1 azimuthal angle Ψ = 120°; in moment time t = 0.4 s; steps of computation: Δx = Δz = 4 m, Δt = 0.5 ms 49
Fig. 2.12. Snapshot of spike wave propagation from algorithm (1.28) for parameters: ε = 0.3; δ = –0.1 azimuthal angle Ψ = 0°; in moment time t = 0.4 s; steps of computation: Δx = Δz = 4 m, Δt = 0.5 ms 50
Fig. 2.13. Snapshot of spike wave propagation from algorithm (1.28) for parameters: ε = 0.3; δ = –0.1 azimuthal angle Ψ = 30°; in moment time t = 0.4 s; steps of computation: Δx = Δz = 4 m, Δt = 0.5 ms 51
Fig. 2.14. Snapshot of spike wave propagation from algorithm (1.28) for parameters: ε = 0.3; δ = –0.1 azimuthal angle Ψ = 45°; in moment time t = 0.4 s; steps of computation: Δx = Δz = 4 m, Δt = 0.5 ms 52
Fig. 2.15. Snapshot of spike wave propagation from algorithm (1.28) for parameters: ε = 0.3; δ = –0.1 azimuthal angle Ψ = 60°; in moment time t = 0.4 s; steps of computation: Δx = Δz = 4 m, Δt = 0.5 ms 53
Fig. 2.16. Snapshot of spike wave propagation from algorithm (1.28) for parameters: ε = 0.3; δ = –0.1 azimuthal angle Ψ = 90°; in moment time t = 0.4 s; steps of computation: Δx = Δz = 4 m, Δt = 0.5 ms 54
Fig. 2.17. Snapshot of spike wave propagation from algorithm (1.28) for parameters: ε = 0.3; δ = –0.1 azimuthal angle Ψ = 120°; in moment time t = 0.4 s; steps of computation: Δx = Δz = 4 m, Δt = 0.5 ms 55
Fig. 2.18. Snapshot of spike wave propagation from algorithm (1.23) for parameters: ε = 0.3; δ = –0.1 azimuthal angle Ψ = 0°; in moment time t = 0.4 s; steps of computation: Δx = Δz = 4 m, Δt = 0.5 ms 56
Fig. 2.19. Snapshot of spike wave propagation from algorithm (1.23) for parameters: ε = 0.3; δ = –0.1 azimuthal angle Ψ = 30°; in moment time t = 0.4 s; steps of computation: Δx = Δz = 4 m, Δt = 0.5 ms 57
Fig. 2.20. Snapshot of spike wave propagation from algorithm (1.23) for parameters: ε = 0.3; δ = –0.1 azimuthal angle Ψ = 45°; in moment time t = 0.4 s; steps of computation: Δx = Δz = 4 m, Δt = 0.5 ms 58
Fig. 2.21. Snapshot of spike wave propagation from algorithm (1.23) for parameters: ε = 0.3; δ = –0.1 azimuthal angle Ψ = 60°; in moment time t = 0.4 s; steps of computation: Δx = Δz = 4 m, Δt = 0.5 ms 59
Fig. 2.22. Snapshot of spike wave propagation from algorithm (1.23) for parameters: ε = 0.3; δ = –0.1 azimuthal angle Ψ = 90°; in moment time t = 0.4 s; steps of computation: Δx = Δz = 4 m, Δt = 0.5 ms 60

Fig. 2.23. Snapshot of spike wave propagation from algorithm (1.23) for parameters: ε = 0.3; δ = –0.1 azimuthal angle Ψ = 120°; in moment time t = 0.4 s; steps of computation: Δx = Δz = 4 m, Δt = 0.5 ms 61

Fig. 2.24. Snapshot of spike wave propagation from algorithm (1.29) for parameters: ε = 0.35; δ = –0.1 azimuthal angle Ψ = 0°; in moment time t = 0.4 s; steps of computation: Δx = Δz = 4 m, Δt = 0.5 ms 62

Fig. 2.25. Snapshot of spike wave propagation from algorithm (1.29) for parameters: ε = 0.35; δ = –0.1 azimuthal angle Ψ = 30°; in moment time t = 0.4 s; steps of computation: Δx = Δz = 4 m, Δt = 0.5 ms 63

Fig. 2.26. Snapshot of spike wave propagation from algorithm (1.29) for parameters: ε = 0.35; δ = –0.1 azimuthal angle Ψ = 45°; in moment time t = 0.4 s; steps of computation: Δx = Δz = 4 m, Δt = 0.5 ms 64

Fig. 2.27. Snapshot of spike wave propagation from algorithm (1.29) for parameters: ε = 0.35; δ = –0.1 azimuthal angle Ψ = 60°; in moment time t = 0.4 s; steps of computation: Δx = Δz = 4 m, Δt = 0.5 ms 65

Fig. 2.28. Snapshot of spike wave propagation from algorithm (1.29) for parameters: ε = 0.35; δ = –0.1 azimuthal angle Ψ = 90°; in moment time t = 0.4 s; steps of computation: Δx = Δz = 4 m, Δt = 0.5 ms 66

Fig. 2.29. Snapshot of spike wave propagation from algorithm (1.29) for parameters: ε = 0.35; δ = –0.1 azimuthal angle Ψ = 120°; in moment time t = 0.4 s; steps of computation: Δx = Δz = 4 m, Δt = 0.5 ms 67

Fig. 2.30. Snapshot of spike wave propagation from algorithm (1.29) for parameters: ε = 0.35; δ = 0.1 azimuthal angle Ψ = 0°; in moment time t = 0.4 s; steps of computation: Δx = Δz = 4 m, Δt = 0.5 ms 68

Fig. 2.31. Snapshot of spike wave propagation from algorithm (1.29) for parameters: ε = 0.35; δ = 0.1 azimuthal angle Ψ = 30°; in moment time t = 0.4 s; steps of computation: Δx = Δz = 4 m, Δt = 0.5 ms 69

Fig. 2.32. Snapshot of spike wave propagation from algorithm (1.29) for parameters: ε = 0.35; δ = 0.1 azimuthal angle Ψ = 45°; in moment time t = 0.4 s; steps of computation: Δx = Δz = 4 m, Δt = 0.5 ms 70

Fig. 2.33. Snapshot of spike wave propagation from algorithm (1.29) for parameters: ε = 0.35; δ = 0.1 azimuthal angle Ψ = 60°; in moment time t = 0.4 s; steps of computation: Δx = Δz = 4 m, Δt = 0.5 ms 71

Fig. 2.34. Snapshot of spike wave propagation from algorithm (1.29) for parameters: ε = 0.35; δ = 0.1 azimuthal angle Ψ = 90°; in moment time t = 0.4 s; steps of computation: Δx = Δz = 4 m, Δt = 0.5 ms 72

Fig. 2.35. Snapshot of spike wave propagation from algorithm (1.28) for parameters: ε = 0.35; δ = 0.1 azimuthal angle Ψ = 0°; in moment time t = 0.4 s; steps of computation: Δx = Δz = 4 m, Δt = 0.5 ms 73

Fig. 2.36. Snapshot of spike wave propagation from algorithm (1.28) for parameters: ε = 0.35; δ = 0.1 azimuthal angle Ψ = 30°; in moment time t = 0.4 s; steps of computation: Δx = Δz = 4 m, Δt = 0.5 ms 74
Fig. 2.37. Snapshot of spike wave propagation from algorithm (1.28) for parameters: ε = 0.35; δ = 0.1 azimuthal angle Ψ = 45°; in moment time t = 0.4 s; steps of computation: Δx = Δz = 4 m, Δt = 0.5 ms 75
Fig. 2.38. Snapshot of spike wave propagation from algorithm (1.28) for parameters: ε = 0.35; δ = 0.1 azimuthal angle Ψ = 60°; in moment time t = 0.4 s; steps of computation: Δx = Δz = 4 m, Δt = 0.5 ms 76
Fig. 2.39. Snapshot of spike wave propagation from algorithm (1.28) for parameters: ε = 0.35; δ = 0.1 azimuthal angle Ψ = 90°; in moment time t = 0.4 s; steps of computation: Δx = Δz = 4 m, Δt = 0.5 ms 77
Fig. 2.40. Snapshot of spike wave propagation from algorithm (1.28) for parameters: ε = 0.35; δ = 0.1 azimuthal angle Ψ = 120°; in moment time t = 0.4 s; steps of computation: Δx = Δz = 4 m, Δt = 0.5 ms 78
Fig. 2.41. Snapshot of spike wave propagation from algorithm (1.28) for parameters: ε = 0.35; δ = –0.1 azimuthal angle Ψ = 0°; in moment time t = 0.4 s; steps of computation: Δx = Δz = 4 m, Δt = 0.5 ms 79
Fig. 2.42. Snapshot of spike wave propagation from algorithm (1.28) for parameters: ε = 0.35; δ = –0.1 azimuthal angle Ψ = 30°; in moment time t = 0.4 s; steps of computation: Δx = Δz = 4 m, Δt = 0.5 ms 80
Fig. 2.43. Snapshot of spike wave propagation from algorithm (1.28) for parameters: ε = 0.35; δ = –0.1 azimuthal angle Ψ = 45°; in moment time t = 0.4 s; steps of computation: Δx = Δz = 4 m, Δt = 0.5 ms 81
Fig. 2.44. Snapshot of spike wave propagation from algorithm (1.28) for parameters: ε = 0.35; δ = –0.1 azimuthal angle Ψ = 60°; in moment time t = 0.4 s; steps of computation: Δx = Δz = 4 m, Δt = 0.5 ms 82
Fig. 2.45. Snapshot of spike wave propagation from algorithm (1.28) for parameters: ε = 0.35; δ = –0.1 azimuthal angle Ψ = 90°; in moment time t = 0.4 s; steps of computation: Δx = Δz = 4 m, Δt = 0.5 ms 83
Fig. 2.46. Snapshot of spike wave propagation from algorithm (1.28) for parameters: ε = 0.35; δ = –0.1 azimuthal angle Ψ = 120°; in moment time t = 0.4 s; steps of computation: Δx = Δz = 4 m, Δt = 0.5 ms 84
Fig. 2.47. Snapshot of spike wave propagation from algorithm (1.23) for parameters: ε = 0.35; δ = 0.1 azimuthal angle Ψ = 0°; in moment time t = 0.4 s; steps of computation: Δx = Δz = 4 m, Δt = 0.5 ms 85
Fig. 2.48. Snapshot of spike wave propagation from algorithm (1.23) for parameters: ε = 0.35; δ = 0.1 azimuthal angle Ψ = 30°; in moment time t = 0.4 s; steps of computation: Δx = Δz = 4 m, Δt = 0.5 ms 86

Fig. 2.49. Snapshot of spike wave propagation from algorithm (1.23) for parameters: ε = 0.35; δ = 0.1 azimuthal angle Ψ = 45°; in moment time *t* = 0.4 s; steps of computation: Δx = Δz = 4 m, Δt = 0.5 ms 87

Fig. 2.50. Snapshot of spike wave propagation from algorithm (1.23) for parameters: ε = 0.35; δ = 0.1 azimuthal angle Ψ = 60°; in moment time *t* = 0.4 s; steps of computation: Δx = Δz = 4 m, Δt = 0.5 ms 88

Fig. 2.51. Snapshot of spike wave propagation from algorithm (1.23) for parameters: ε = 0.35; δ = 0.1 azimuthal angle Ψ = 90°; in moment time *t* = 0.4 s; steps of computation: Δx = Δz = 4 m, Δt = 0.5 ms 89

Fig. 2.52. Snapshot of spike wave propagation from algorithm (1.23) for parameters: ε = 0.35; δ = 0.1 azimuthal angle Ψ = 120°; in moment time *t* = 0.4 s; steps of computation: Δx = Δz = 4 m, Δt = 0.5 ms 90

Fig. 2.53. Snapshot of spike wave propagation from algorithm (1.23) for parameters: ε = 0.35; δ = –0.1 azimuthal angle Ψ = 0°; in moment time *t* = 0.4 s; steps of computation: Δx = Δz = 4 m, Δt = 0.5 ms 91

Fig. 2.54. Snapshot of spike wave propagation from algorithm (1.23) for parameters: ε = 0.35; δ = –0.1 azimuthal angle Ψ = 30°; in moment time *t* = 0.4 s; steps of computation: Δx = Δz = 4 m, Δt = 0.5 ms 92

Fig. 2.55. Snapshot of spike wave propagation from algorithm (1.23) for parameters: ε = 0.35; δ = –0.1 azimuthal angle Ψ = 45°; in moment time *t* = 0.4 s; steps of computation: Δx = Δz = 4 m, Δt = 0.5 ms 93

Fig. 2.56. Snapshot of spike wave propagation from algorithm (1.23) for parameters: ε = 0.35; δ = –0.1 azimuthal angle Ψ = 60°; in moment time *t* = 0.4 s; steps of computation: Δx = Δz = 4 m, Δt = 0.5 ms 94

Fig. 2.57. Snapshot of spike wave propagation from algorithm (1.23) for parameters: ε = 0.35; δ = –0.1 azimuthal angle Ψ = 90°; in moment time *t* = 0.4 s; steps of computation: Δx = Δz = 4 m, Δt = 0.5 ms 95

Fig. 2.58. Snapshot of spike wave propagation from algorithm (1.23) for parameters: ε = 0.35; δ = –0.1 azimuthal angle Ψ = 120°; in moment time *t* = 0.4 s; steps of computation: Δx = Δz = 4 m, Δt = 0.5 ms 96

Fig. 2.59. Comparison of (1.29) and (1.28) for Ψ = 90°; anisotropy parameters: ε = 0.3; δ = 0.1; in moment time *t* = 0.4 s. Version (1.29) in red color full covered by image of version (1.28). Steps of computations: Δx = Δz = 4 m, Δt = 0.5 ms 97

Fig. 2.60. Comparison of the versions (1.29) and (1.28) for Ψ = 60°; anisotropy parameters: ε = 0.3; δ = 0.1; in moment time *t* = 0.4 s. The version (1.29) in red color differ slightly from image (1.28). Steps of computations: Δx = Δz = 4 m, Δt = 0.5 ms 98

Fig. 2.61. Comparison of the versions (1.28) and (1.23) for Ψ = 60°; anisotropy parameters: ε = 0.3; δ = 0.1; in moment time t = 0.4 s. The version (1.28) differ slightly (red color) from image (1.23). Steps of computations: Δx = Δz = 4 m, Δt = 0.5 ms 99

Fig. 2.62. Comparison of the propagation snapshots in time t = 0.4 s for version (1.23) for angle Ψ = 0°, 45° and 90°; anisotropy parameters: ε = 0.3; δ = –0.1 100

Fig. 2.63. Comparison of the propagation snapshots from (1.23) – in black, from (1.28) – in red and from (1.29) – in green; anisotropy parameters: ε = 0.35; δ = –0.1 in moment time t = 0.4 s; azimuthal angle Ψ = 30°. Steps computations: Δx = Δz = 4 m, Δt = 0.5 ms 101

Fig. 2.64. Comparison of the propagation snapshots from (1.23) – in black, from (1.28) – in red and from (1.29) – in green for anisotropy parameters: ε = 0.35; δ = 0.1 in moment time t = 0.4 s; azimuthal angle Ψ = 30°. Steps computations: Δx = Δz = 4 m, Δt = 0.5 ms 102

Fig. 2.65. Comparison of the propagation snapshots from (1.23) – in black, from (1.28) – in red and from (1.29) – in green for anisotropy parameters: ε = 0.35; δ = –0.1 in moment time t = 0.4 s; azimuthal angle Ψ = 60°. Steps computations: Δx = Δz = 4 m; Δt = 0.5 ms 103

Fig. 2.66. Comparison of the propagation snapshots from (1.23) in moment time t = 0.4 s; anisotropy parameters: ε = 0.3; δ = 0.1; for azimuthal angle: Ψ = 0° – in red, Ψ = 15° – in green, Ψ = 30° – in blue, Ψ = 45° – in crimson, Ψ = 60° – in violet, Ψ = 75° – in orange, Ψ = 90° – in black 104

Fig. 2.67. Velocity as a function of the azimuthal angle Ψ in the first quarter of the clockwise polar coordinate system. The ellipsoid character of velocity (Ψ) is seen. In left part of figure we have a series of wavefronts which determine the length of propagation paths for time t = 0.2 s, ε = 0.3; δ = 0.1 105

Fig. 3.1. The geometry of velocity anticline model 115

Fig. 3.2. The zero-offset time section from relations (1.23); anisotropy parameters ε = 0.3; δ = 0.1; azimuthal angle Ψ = 15° 116

Fig. 3.3. The migration from (3.14) for the zero-offset time section from relation (1.23); anisotropy parameters ε = 0.3; δ = 0.1; azimuthal angle Ψ = 15° (Fig. 3.2) 117

Fig. 3.4. The migration from (3.15) for the zero-offset time section from relation (1.23); anisotropy parameters ε = 0.3; δ = 0.1; azimuthal angle Ψ = 15° (Fig. 3.2) 118

Fig. 3.5. The zero-offset time section from relation (1.23); anisotropy parameters ε = 0.3; δ = 0.1; azimuthal angle Ψ = 30° 119

Fig. 3.6. The migration from (3.14) for the zero-offset time section from relation (1.23); anisotropy parameters ε = 0.3; δ = 0.1; azimuthal angle Ψ = 30° (Fig. 3.5) 120
Fig. 3.7. The migration from (3.15) for the zero-offset time section from relation (1.23); anisotropy parameters ε = 0.3; δ = 0.1; azimuthal angle Ψ = 30° (Fig. 3.5) 121
Fig. 3.8. The zero-offset time section from relation (1.23); anisotropy parameters ε = 0.3; δ = 0.1; azimuthal angle Ψ = 45° 122
Fig. 3.9. The migration from (3.14) for the zero-offset time section from relation (1.23); anisotropy parameters ε = 0.3; δ = 0.1; azimuthal angle Ψ = 45° (Fig. 3.8) 123
Fig. 3.10. The migration from (3.15) for the zero-offset time section from relation (1.23); anisotropy parameters ε = 0.3; δ = 0.1; azimuthal angle Ψ = 45° (Fig. 3.8) 124
Fig. 3.11. The zero-offset time section from relation (1.23); anisotropy parameters ε = 0.3; δ = 0.1; azimuthal angle Ψ = 60° 125
Fig. 3.12. The migration from (3.14) for the zero-offset time section from relation (1.23); anisotropy parameters ε = 0.3; δ = 0.1; azimuthal angle Ψ = 60° (Fig. 3.11) 126
Fig. 3.13. The migration from (3.15) for the zero-offset time section from relation (1.23); anisotropy parameters ε = 0.3; δ = 0.1; azimuthal angle Ψ = 60° (Fig. 3.11) 127
Fig. 3.14. The zero-offset time section from relation (1.23); anisotropy parameters ε = 0.3; δ = 0.1; azimuthal angle Ψ = 75° 128
Fig. 3.15. The migration from (3.14) for the zero-offset time section from relation (1.23); anisotropy parameters ε = 0.3; δ = 0.1; azimuthal angle Ψ = 75° (Fig. 3.14) 129
Fig. 3.16. The migration from (3.15) for the zero-offset time section from relation (1.23); anisotropy parameters ε = 0.3; δ = 0.1; azimuthal angle Ψ = 75° (Fig. 3.14) 130
Fig. 3.17. The zero-offset time section from relation (1.23); anisotropy parameters ε = 0.3; δ = 0.1; azimuthal angle Ψ = 90° 131
Fig. 3.18. The migration from (3.14) for the zero-offset time section from relation (1.23); anisotropy parameters ε = 0.3; δ = 0.1; azimuthal angle Ψ = 90° (Fig. 3.17) 132
Fig. 3.19. The migration from (3.15) for the zero-offset time section from relation (1.23); anisotropy parameters ε = 0.3; δ = 0.1; azimuthal angle Ψ = 90° (Fig. 3.17) 133

Fig. 3.20. The zero-offset time section from relation (1.28); anisotropy parameters ε = 0.3; δ = 0.1; azimuthal angle Ψ = 30° 134
Fig. 3.21. The migration from (3.14) for the zero-offset time section from relation (1.28); anisotropy parameters ε = 0.3; δ = 0.1; azimuthal angle Ψ = 30° (Fig. 3.20) 135
Fig. 3.22. The migration from (3.15) for the zero-offset time section from relation (1.28); anisotropy parameters ε = 0.3; δ = 0.1; azimuthal angle Ψ = 30° (Fig. 3.20) 136
Fig. 3.23. The zero-offset time section from relation (1.29); anisotropy parameters ε = 0.3; δ = 0.1; azimuthal angle Ψ = 30° 137
Fig. 3.24. The migration from (3.14) for the zero-offset time section from relation (1.29); anisotropy parameters ε = 0.3; δ = 0.1; azimuthal angle Ψ = 30° (Fig. 3.23) 138
Fig. 3.25. The migration from (3.15) for the zero-offset time section from relation (1.29); anisotropy parameters ε = 0.3; δ = 0.1; azimuthal angle Ψ = 30° (Fig. 3.23) 139
Fig. 3.26. The zero-offset time section from relation (1.28); anisotropy parameters ε = 0.3; δ = 0.1; azimuthal angle Ψ = 60° 140
Fig. 3.27. The migration from (3.14) for the zero-offset time section from relation (1.28); anisotropy parameters ε = 0.3; δ = 0.1; azimuthal angle Ψ = 60° (Fig. 3.26) 141
Fig. 3.28. The migration from (3.15) for the zero-offset time section from relation (1.28); anisotropy parameters ε = 0.3; δ = 0.1; azimuthal angle Ψ = 60° (Fig. 3.26) 142
Fig. 3.29. The zero-offset time section from relation (1.29); anisotropy parameters ε = 0.3; δ = 0.1; azimuthal angle Ψ = 60° 143
Fig. 3.30. The migration from (3.14) for the zero-offset time section from relation (1.29); anisotropy parameters ε = 0.3; δ = 0.1; azimuthal angle Ψ = 60° (Fig. 3.29) 144
Fig. 3.31. The migration from (3.15) for the zero-offset time section from relation (1.29); anisotropy parameters ε = 0.3; δ = 0.1; azimuthal angle Ψ = 60° (Fig. 3.29) 145
Fig. 3.32. The zero-offset time section from relation (1.23); anisotropy parameters ε = 0.5; δ = 0.1; azimuthal angle Ψ = 45° 146
Fig. 3.33. The migration from (3.14) for the zero-offset time section from relation (1.23); anisotropy parameters ε = 0.5; δ = 0.1; azimuthal angle Ψ = 45° (Fig. 3.32) 147
Fig. 3.34. The migration from (3.15) for the zero-offset time section from relation (1.23); anisotropy parameters ε = 0.5; δ = 0.1; azimuthal angle Ψ = 45° (Fig. 3.32) 148

Fig. 3.35. The migration from (3.14) for anisotropy parameters ε = 0.4; δ = 0.2; azimuthal angle Ψ = 45° for the zero-offset time section from relation (1.23) for anisotropy parameters ε = 0.5; δ = 0.1; azimuthal angle Ψ = 45° (Fig. 3.32) 149

Fig. 3.36. The migration from (3.15) for anisotropy parameters ε = 0.4; δ = 0.2; azimuthal angle Ψ = 45° for the zero-offset time section from relation (1.23) for anisotropy parameters ε = 0.5; δ = 0.1; azimuthal angle Ψ = 45° (Fig. 3.32) 150

Fig. 3.37. The migration from (3.14) for anisotropy parameters ε = 0.5; δ = 0.3; azimuthal angle Ψ = 45° for the zero-offset time section from relation (1.23) for anisotropy parameters ε = 0.5; δ = 0.1; azimuthal angle Ψ = 45° (Fig. 3.32) 151

Fig. 3.38. The migration from (3.15) for anisotropy parameters ε = 0.5; δ = 0.3; azimuthal angle Ψ = 45° for the zero-offset time section from relation (1.23) for anisotropy parameters ε = 0.5; δ = 0.1; azimuthal angle Ψ = 45° (Fig. 3.32) 152

Fig. 3.39. The zero-offset time section from relation (1.23); anisotropy parameters ε = 0.5; δ = 0.3; azimuthal angle Ψ = 45° 153

Fig. 3.40. The migration from (3.14) for the zero-offset time section from relation (1.23); anisotropy parameters ε = 0.5; δ = 0.3; azimuthal angle Ψ = 45° (Fig. 3.39) 154

Fig. 3.41. The migration from (3.15) for the zero-offset time section from relation (1.23); anisotropy parameters ε = 0.5; δ = 0.3; azimuthal angle Ψ = 45° (Fig. 3.39) 155

Fig. 3.42. The zero-offset time section from relation (1.23); anisotropy parameters ε = 0.35; δ = –0.2; azimuthal angle Ψ = 30° 156

Fig. 3.43. The migration from (3.14) for the zero-offset time section from relation (1.23); anisotropy parameters ε = 0.35; δ = –0.2; azimuthal angle Ψ = 30° (Fig. 3.42) 157

Fig. 3.44. The zero-offset time section from relation (1.23); anisotropy parameters ε = 0.35; δ = –0.2; azimuthal angle Ψ = 45° 158

Fig. 3.45. The migration from (3.14) for the zero-offset time section from relation (1.23); anisotropy parameters ε = 0.35; δ = –0.2; azimuthal angle Ψ = 45° (Fig. 3.44) 159

Fig. 3.46. The migration from (3.14) for anisotropy parameters ε = 0.35; δ = –0.2; azimuthal angle Ψ = 60° for the zero-offset time section from relation (1.23) for anisotropy parameters ε = 0.35; δ = –0.2; azimuthal angle Ψ = 45° (Fig. 3.44) 160

Fig. 3.47. The zero-offset time section from relation (1.23); anisotropy parameters ε = 0.35; δ = 0.1; azimuthal angle Ψ = 30° 161

Fig. 3.48. The migration from (3.14) for the zero-offset time section from relation (1.23); anisotropy parameters ε = 0.35; δ = 0.1; azimuthal angle Ψ = 30° (Fig. 3.47) 162
Fig. 3.49. The migration from (3.14) for anisotropy parameters ε = 0.35; δ = 0.1; azimuthal angle Ψ = 45° for the zero-offset time section from relation (1.23) for anisotropy parameters ε = 0.35; δ = 0.1; azimuthal angle Ψ = 30° (Fig. 3.47) 163
Fig. 3.50. The zero-offset time section from relation (1.23); anisotropy parameters ε = 0.35; δ = 0.1; azimuthal angle Ψ = 60° 164
Fig. 3.51. The migration from (3.14) for the zero-offset time section from relation (1.23); anisotropy parameters ε = 0.35; δ = 0.1; azimuthal angle Ψ = 60° (Fig. 3.50) 165
Fig. 3.52. The migration from (3.14) for anisotropy parameters ε = 0.35; δ = 0.1; azimuthal angle Ψ = 90° for the zero-offset time section from relation (1.23) for anisotropy parameters ε = 0.35; δ = 0.1; azimuthal angle Ψ = 60° (Fig. 3.50) 166
Fig. 3.53. The zero-offset time section from relation (1.23); anisotropy parameters ε = 0.35; δ = 0.1; azimuthal angle Ψ = 90° 167
Fig. 3.54. The migration from (3.14) for the zero-offset time section from relation (1.23); anisotropy parameters ε = 0.35; δ = 0.1; azimuthal angle Ψ = 90° (Fig. 3.53) 168
Fig. 3.55. The geometry of velocity horst model 169
Fig. 3.56. The zero-offset time section from relation (1.23) for isotropic model 170
Fig. 3.57. The zero-offset migration for the isotropic model (Fig. 3.56) 171
Fig. 3.58. The zero-offset time section for anisotropic VTI model; anisotropy parameters ε = 0.3; δ = 0.1 172
Fig. 3.59. The zero-offset migration for the anisotropic VTI model (Fig. 3.58); anisotropy parameters ε = 0.3; δ = 0.1 173
Fig. 3.60. The zero-offset time section for anisotropic TTI model; anisotropy parameters ε = 0.3; δ = 0.1; dip angle θ = 30° 174
Fig. 3.61. The zero-offset migration for the anisotropic TTI model (Fig. 3.60); anisotropy parameters ε = 0.3; δ = 0.1; dip angle θ = 30° 175
Fig. 3.62. The zero-offset time section for anisotropic TTI model; anisotropy parameters ε = 0.3; δ = 0.1; dip angle θ = 45° 176
Fig. 3.63. The zero-offset migration for the anisotropic TTI model (Fig. 3.62); anisotropy parameters ε = 0.3; δ = 0.1; dip angle θ = 45° 177
Fig. 3.64. The zero-offset time section for anisotropic TTI model; anisotropy parameters ε = 0.3; δ = 0.1; dip angle θ = 60° 178

Fig. 3.65. The zero-offset migration for the anisotropic TTI model (Fig. 3.64); anisotropy parameters ε = 0.3; δ = 0.1; dip angle θ = 60° 179
Fig. 3.66. The zero-offset time section for anisotropic TTI model; anisotropy parameters ε = 0.3; δ = 0.1; dip angle θ = 90° 180
Fig. 3.67. The zero-offset migration for the anisotropic TTI model (Fig. 3.66); anisotropy parameters ε = 0.3; δ = 0.1; dip angle θ = 90° 181
Fig. 3.68. The zero-offset time section for anisotropic HTI model; anisotropy parameters ε = 0.25; δ = 0.1; azimuthal angle Ψ = 0° 182
Fig. 3.69. The zero-offset migration for the anisotropic HTI model (Fig. 3.68); anisotropy parameters ε = 0.25; δ = 0.1; azimuthal angle Ψ = 0° 183
Fig. 3.70. The zero-offset time section for anisotropic HTI model; anisotropy parameters ε = 0.25; δ = 0.1; azimuthal angle Ψ = 30° 184
Fig. 3.71. The zero-offset migration for the anisotropic HTI model (Fig. 3.70); anisotropy parameters ε = 0.25; δ = 0.1; azimuthal angle Ψ = 30° 185
Fig. 3.72. The zero-offset time section for anisotropic HTI model; anisotropy parameters ε = 0.25; δ = 0.1; azimuthal angle Ψ = 60° 186
Fig. 3.73. The zero-offset migration for the anisotropic HTI model (Fig. 3.72); anisotropy parameters ε = 0.25; δ = 0.1; azimuthal angle Ψ = 60° 187
Fig. 3.74. The zero-offset time section for anisotropic HTI model; anisotropy parameters ε = 0.25; δ = 0.1; azimuthal angle Ψ = 90° 188
Fig. 3.75. The zero-offset migration for the anisotropic HTI model (Fig. 3.74); anisotropy parameters ε = 0.25; δ = 0.1; azimuthal angle Ψ = 90° 189
Tab. 1. The comparison of coefficients in relation 1.27 in dependence of Thomsen's parameters 28

Appendix A_1

Tensor components as the function of the tensor C components (for VTI model) and dip angle θ (for $+\theta$) and azimuthal angle Ψ are as follows:

$$d_{11}^{\theta,\Psi} = C_{11}\left[\cos^4\theta\sin^4\Psi + \cos^4\Psi + \frac{1}{2}\cos^2\theta\sin^2(2\Psi)\right] + C_{33}\sin^4\theta\sin^4\Psi +$$
$$+\left(\frac{1}{2}C_{13} + C_{44}\right)\left[\sin^2\theta\sin^2(2\Psi) + \sin^2(2\theta)\sin^4\Psi\right]$$

$$d_{12}^{\theta,\Psi} = d_{21}^{\theta,\Psi} = C_{11}\left\{\cos^2\theta\left[\sin^4\Psi + \cos^4\Psi + \frac{1}{4}\cos^2\theta\sin^2(2\Psi)\right] + \frac{1}{4}\sin^2(2\Psi)\right\} +$$
$$+ C_{13}\left[\frac{1}{8}\sin^2(2\theta)\sin^2(2\Psi) + \sin^2\theta\left(\sin^4\Psi + \cos^4\Psi\right)\right] +$$
$$+\frac{1}{4}C_{33}\sin^4\theta\sin^2(2\Psi) + C_{44}\left[\frac{1}{4}\sin^2(2\theta)\sin^2(2\Psi) - \sin^2\theta\sin^2(2\Psi)\right] -$$
$$- C_{66}\cos^2\theta\left[\sin^2(2\Psi) + 2\left(\sin^4\Psi + \cos^4\Psi\right)\right]$$

$$d_{13}^{\theta,\Psi} = d_{31}^{\theta,\Psi} = C_{11}\left[\frac{1}{4}\sin^2(2\theta)\sin^2\Psi + \sin^2\theta\cos^2\Psi\right] +$$
$$+ C_{13}\left[\sin^4\theta\sin^2\Psi + \cos^4\theta\sin^2\Psi + \cos^2\theta\cos^2\Psi\right] +$$
$$+\left(\frac{1}{4}C_{33} - C_{44}\right)\sin^2(2\theta)\sin^2\Psi - 2C_{66}\sin^2\theta\cos^2\Psi$$

$$d_{14}^{\theta,\Psi} = d_{41}^{\theta,\Psi} = \frac{1}{2}(C_{13} - C_{11})\sin(2\theta)\left[\frac{1}{2}\cos^2\theta\sin\Psi\sin(2\Psi) + \cos^3\Psi\right] +$$
$$+\frac{1}{4}(C_{33} - C_{13})\sin(2\theta)\sin(2\Psi)\sin^2\theta\sin\Psi -$$
$$-\frac{1}{2}C_{44}\sin(2\theta)\sin(2\Psi)\sin\Psi\left[1 - \cos(2\theta)\right] +$$
$$+ C_{66}\sin(2\theta)\left[\frac{1}{2}\sin(2\Psi)\sin\Psi + \cos^3\Psi\right]$$

$$d_{15}^{\theta,\Psi} = d_{51}^{\theta,\Psi} = \frac{1}{2}(C_{11} - C_{13})\sin(2\theta)\sin\Psi\left[\cos^2\theta\sin^2\Psi + \cos^2\Psi\right] +$$
$$+\frac{1}{2}(C_{13} - C_{33})\sin(2\theta)\sin^2\theta\sin^3\Psi -$$
$$-\frac{1}{2}C_{44}\left[\sin(2\theta)\sin(2\Psi)\cos\Psi + \sin(4\theta)\sin^3\Psi\right]$$

$$d_{44}^{\theta,\Psi} = \frac{1}{4}(C_{11} - 2C_{13} + C_{33})\cos^2\Psi\sin^2(2\theta) + C_{44}\left[\cos^2\theta\sin^2\Psi + \cos^2\Psi\cos^2(2\theta)\right] + \\ + C_{66}\sin^2\theta\sin^2\Psi$$

$$d_{45}^{\theta,\Psi} \\ d_{54}^{\theta,\Psi} = -\frac{1}{8}(C_{11} - 2C_{13} + C_{33})\sin(2\Psi)\sin^2(2\theta) + \frac{1}{2}C_{44}\sin(2\Psi)\left[\cos^2\theta - \cos^2(2\theta)\right] + \\ + \frac{1}{2}C_{66}\sin(2\Psi)\sin^2\theta$$

$$d_{46}^{\theta,\Psi} \\ d_{64}^{\theta,\Psi} = \frac{1}{4}(2C_{13} - C_{11} - C_{33})\sin(2\Psi)\sin(2\theta)\cos\Psi\sin^2\theta + \\ + \frac{1}{2}C_{44}\sin(2\theta)\left[\sin\Psi\cos(2\Psi) - \sin(2\Psi)\cos(2\theta)\cos\Psi\right] + \\ + \frac{1}{2}C_{66}\sin(2\theta)\left[\cos\Psi\sin(2\Psi) - \sin\Psi\cos(2\Psi)\right]$$

$$d_{55}^{\theta,\Psi} = \frac{1}{4}(C_{11} - 2C_{13} + C_{33})\sin^2\Psi\sin^2(2\theta) + C_{44}\left[\cos^2\theta\cos^2\Psi + \sin^2\Psi\cos^2(2\theta)\right] + \\ + C_{66}\sin^2\theta\cos^2\Psi$$

$$d_{56}^{\theta,\Psi} \\ d_{65}^{\theta,\Psi} = \frac{1}{4}(C_{11} - 2C_{13} + C_{33})\sin(2\Psi)\sin(2\theta)\sin\Psi\sin^2\theta + \\ + \frac{1}{2}C_{44}\sin(2\theta)\left[\cos\Psi\cos(2\Psi) + \sin(2\Psi)\cos(2\theta)\sin\Psi\right] - \\ - \frac{1}{2}C_{66}\sin(2\theta)\left[\cos\Psi\cos(2\Psi) + \sin\Psi\sin(2\Psi)\right]$$

$$d_{66}^{\theta,\Psi} = \frac{1}{4}(C_{11} - 2C_{13} + C_{33})\sin^2(2\Psi)\sin^4\theta + C_{44}\left[\sin^2\theta\cos^2(2\theta) + \frac{1}{4}\sin^2(2\theta)\sin^2(2\Psi)\right] + \\ + C_{66}\cos^2\theta$$

$$d_{16}^{\theta,\Psi} \\ d_{61}^{\theta,\Psi} = \frac{1}{2}C_{11}\sin(2\Psi)\left[\cos^2\Psi - \cos^2\theta\cos(2\Psi) - \cos^4\theta\sin^2\Psi\right] - \frac{1}{2}C_{33}\sin^4\theta\sin^2\Psi\sin(2\Psi) - \\ - \left(\frac{1}{4}C_{13} + \frac{1}{2}C_{44}\right)\left[\sin(4\Psi)\sin^2\theta + \sin^2(2\theta)\sin(2\Psi)\sin^2\Psi\right]$$

$$d_{22}^{\theta,\Psi} = C_{11}\left[\cos^4\theta\cos^4\Psi + \frac{1}{2}\cos^2\theta\sin^2(2\Psi) + \sin^4\Psi\right] + \frac{1}{2}C_{13}\left[\sin^2(2\theta)\cos^4\Psi + \sin^2\theta\sin^2(2\Psi)\right] + \\ + C_{33}\sin^4\theta\cos^4\Psi + C_{44}\left[\sin^2\theta\sin^2(2\Psi) + \sin^2(2\theta)\cos^4\Psi\right]$$

$$d_{23}^{\theta,\Psi} \\ d_{32}^{\theta,\Psi} = C_{11}\sin^2\theta\left(\cos^2\theta\cos^2\Psi + \sin^2\Psi\right) + C_{13}\left[\cos^2\theta\left(\cos^2\theta\cos^2\Psi + \sin^2\Psi\right) + \sin^4\theta\cos^2\Psi\right] + \\ + C_{33}\cos^2\theta\sin^2\theta\cos^2\Psi - C_{44}\sin^2(2\theta)\cos^2\Psi - 2C_{66}\sin^2\theta\sin^2\Psi$$

$$d_{24}^{\theta,\Psi} = d_{42}^{\theta,\Psi} = \frac{1}{2}(C_{13}-C_{11})\cos\Psi\sin(2\theta)\left(\cos^2\Psi\cos^2\theta+\sin^2\Psi\right)+\frac{1}{2}(C_{33}-C_{13})\cos^3\Psi\sin^2\theta\sin(2\theta)+$$
$$+\frac{1}{2}C_{44}\left[\sin(2\theta)\sin(2\Psi)\sin\Psi+\cos^3\Psi\sin(4\theta)\right]$$

$$d_{25}^{\theta,\Psi} = d_{52}^{\theta,\Psi} = \frac{1}{2}(C_{11}-C_{13})\sin\Psi\sin(2\theta)\left(\cos^2\Psi\cos^2\theta+\sin^2\Psi\right)+$$
$$+\frac{1}{2}(C_{13}-C_{33})\sin\Psi\sin(2\theta)\sin^2\theta\cos^2\Psi+\frac{1}{2}C_{44}\sin(2\Psi)\sin(2\theta)\cos\Psi[1-\cos(2\theta)]-$$
$$-C_{66}\sin(2\theta)\left[\frac{1}{2}\sin(2\Psi)\cos\Psi+\sin^3\Psi\right]$$

$$d_{26}^{\theta,\Psi} = d_{62}^{\theta,\Psi} = \frac{1}{2}C_{11}\sin(2\Psi)\sin^2\theta\left(\cos^2\Psi\cos^2\theta+\sin^2\Psi\right)+$$
$$+\frac{1}{2}C_{13}\sin(2\Psi)\sin^2\theta\left[\cos(2\Psi)-2\cos^2\theta\cos^2\Psi\right]-\frac{1}{2}C_{33}\sin^4\theta\cos^2\Psi\sin(2\Psi)+$$
$$+\frac{1}{2}C_{44}\left[\sin^2\theta\sin(4\Psi)-\sin^2(2\theta)\cos^2\Psi\sin(2\Psi)\right]$$

$$d_{33}^{\theta,\Psi} = C_{11}\sin^4\theta+2C_{13}\sin^2\theta\cos^2\theta+C_{33}\cos^4\theta+C_{44}\sin^2(2\theta)$$

$$d_{34}^{\theta,\Psi} = d_{43}^{\theta,\Psi} = \frac{1}{2}\left(C_{33}\cos^2\theta-C_{11}\sin^2\theta\right)\cos\Psi\sin(2\theta)-\left(\frac{1}{4}C_{13}+\frac{1}{2}C_{44}\right)\cos\Psi\sin(4\theta)$$

$$d_{35}^{\theta,\Psi} = d_{53}^{\theta,\Psi} = \frac{1}{2}\left[(C_{11}-C_{13})\sin^2\theta+(C_{13}-C_{33})\cos^2\theta\right]\sin\Psi\sin(2\theta)+\frac{1}{2}C_{44}\sin\Psi\sin(4\theta)$$

$$d_{36}^{\theta,\Psi} = d_{63}^{\theta,\Psi} = \frac{1}{2}(C_{11}-C_{13})\sin(2\Psi)\sin^4\theta+\frac{1}{2}(C_{13}-C_{33})\sin(2\Psi)\sin^2\theta\cos^2\theta+$$
$$+\frac{1}{2}C_{44}\sin(2\Psi)\sin^2(2\theta)-C_{66}\sin(2\Psi)\sin^2\theta$$

Appendix A_2

$$\det A = \begin{vmatrix} a_{11} & a_{12} & a_{13} \\ a_{21} & a_{22} & a_{23} \\ a_{31} & a_{32} & a_{33} \end{vmatrix} = a_{11}\begin{vmatrix} a_{22} & a_{23} \\ a_{32} & a_{33} \end{vmatrix} - a_{12}\begin{vmatrix} a_{21} & a_{23} \\ a_{31} & a_{33} \end{vmatrix} + a_{13}\begin{vmatrix} a_{21} & a_{22} \\ a_{31} & a_{32} \end{vmatrix} = 0 \tag{A2.1}$$

The results for respective determinants are as follows:

$$\begin{aligned}
a_{11}\left(a_{22}a_{33} - a_{23}^2\right) = {} & k_x^6 d_{11}d_{55}d_{66} + k_y^6 d_{22}d_{44}d_{66} + k_z^6 d_{33}d_{44}d_{55} + \\
& + 2k_x^5 k_y\left[d_{16}d_{55}d_{66} + d_{11}\left(d_{55}d_{66} + d_{26}d_{55}\right)\right] + \\
& + 2k_y^5 k_x\left[d_{66}\left(d_{45}d_{22} + d_{26}d_{44}\right) + d_{16}d_{22}d_{44}\right] + \\
& + k_x^4 k_y^2\left[d_{11}\left(d_{66}d_{44} + d_{22}d_{55} + 4d_{26}d_{45}\right) + 4d_{16}\left(d_{45}d_{66} + d_{26}d_{55}\right) + d_{55}d_{66}^2\right] + \\
& + k_y^4 k_x^2\left[d_{11}d_{22}d_{44} + d_{66}\left(d_{66}d_{44} + d_{22}d_{55} + 4d_{26}d_{45}\right) + 4d_{16}\left(d_{45}d_{22} + d_{26}d_{44}\right)\right] + \\
& + k_z^4 k_x^2\left\{d_{11}d_{33}d_{44} + d_{55}\left[d_{33}d_{66} + d_{45}d_{55} - \left(d_{63} + d_{45}\right)^2\right]\right\} + \\
& + k_x^4 k_z^2\left\{d_{11}\left[d_{33}d_{66} + d_{44}d_{55} - \left(d_{63} + d_{45}\right)^2\right] + d_{55}^2 d_{66}\right\} + \\
& + k_z^4 k_y^2\left\{d_{44}d_{33}d_{66} + d_{55}\left[d_{22}d_{33} + d_{44}^2 - \left(d_{23} + d_{44}\right)^2\right]\right\} + \\
& + k_y^4 k_z^2\left\{d_{66}\left[d_{22}d_{33} + d_{44}^2 - \left(d_{23} + d_{44}\right)^2\right] + d_{55}d_{22}d_{44}\right\} + \\
& + k_x^3 k_y^3\left[\begin{array}{l} 2d_{11}\left(d_{45}d_{22} + d_{26}d_{44}\right) + 2d_{66}\left(d_{45}d_{66} + d_{26}d_{55}\right) + \\ + 2d_{16}\left(d_{66}d_{44} + d_{22}d_{55} + 4d_{26}d_{45}\right) \end{array}\right] + \\
& + k_x^3 k_z^2 k_y\left\{\begin{array}{l} 2d_{11}\left[d_{45}d_{44} + d_{26}d_{33} - \left(d_{63} + d_{45}\right)\left(d_{23} + d_{44}\right)\right] + \\ + 2d_{55}\left(d_{45}d_{66} + d_{26}d_{45}\right) + 2d_{16}\left[d_{33}d_{66} + d_{44}d_{55} - \left(d_{63} + d_{45}\right)^2\right] \end{array}\right\} + \\
& + k_y^3 k_z^2 k_x\left\{\begin{array}{l} 2d_{66}\left[d_{45}d_{44} + d_{26}d_{33} - \left(d_{63} + d_{45}\right)\left(d_{23} + d_{44}\right)\right] + \\ + d_{55}\left(d_{45}d_{22} + d_{26}d_{44}\right) + d_{16}\left[d_{22}d_{33}d_{44}^2 - \left(d_{23} + d_{44}\right)^2\right] \end{array}\right\} + \\
& + k_x^2 k_y^2 k_z^2\left\{\begin{array}{l} d_{55}\left(d_{66}d_{44} + d_{22}d_{55} + 4d_{26}d_{45}\right) + \\ + 4d_{16}\left[d_{45}d_{44} + d_{26}d_{33} - \left(d_{63} + d_{45}\right)\left(d_{23} + d_{44}\right)\right] \end{array}\right\} + \\
& + k_z^4 k_x k_y\left\{2d_{55}\left[d_{45}d_{44} + d_{26}d_{33} - \left(d_{63} + d_{45}\right)\left(d_{23} + d_{44}\right)\right] + 2d_{16}d_{44}d_{33}\right\} \\
& - \omega^6 + \omega^4\left[\begin{array}{l} k_x^2\left(d_{11} + d_{55} + d_{66}\right) + k_y^2\left(d_{22} + d_{44} + d_{66}\right) + \\ + k_z^2\left(d_{33} + d_{44} + d_{55}\right) + 2k_x k_y\left(d_{16} + d_{26} + d_{45}\right) \end{array}\right] - \\
& - \omega^2\left\{\begin{array}{l} \left(k_x^2 d_{11} + k_y^2 d_{66} + k_z^2 d_{55} + 2k_x k_y d_{16}\right)\left[\begin{array}{l} k_x^2\left(d_{55} + d_{66}\right) + k_y^2\left(d_{22} + d_{44}\right) + \\ + k_z^2\left(d_{33} + d_{44}\right) + 2k_x k_y\left(d_{26} + d_{45}\right) \end{array}\right] + \\ + k_x^4 d_{55}d_{66} + k_y^4 d_{22}d_{44} + k_z^4 d_{33}d_{44} + \\ + k_x^2 k_y^2\left(d_{66}d_{44} + d_{22}d_{55} + 4d_{26}d_{45}\right) + \\ + k_x^2 k_z^2\left[d_{33}d_{66} + d_{45}d_{55} - \left(d_{63} + d_{45}\right)^2\right] + k_y^2 k_z^2\left[d_{22}d_{33} + d_{44}^2 - \left(d_{23} + d_{44}\right)^2\right] + \\ + 2k_x^3 k_y\left(d_{45}d_{66} + d_{26}d_{55}\right) + 2k_y^3 k_x\left(d_{45}d_{22} + d_{26}d_{44}\right) + \\ + 2k_z^2 k_x k_y\left[d_{55}d_{44} + d_{26}d_{33} - \left(d_{63} + d_{45}\right)\left(d_{23} + d_{44}\right)\right] \end{array}\right\}
\end{aligned} \tag{A2.2}$$

$$
\begin{aligned}
a_{12}(a_{21}a_{33}-a_{23}a_{31}) &= k_x^6 d_{16}^2 d_{55} + k_y^6 d_{26}^2 d_{44} + k_z^6 d_{54}^2 d_{33} + \\
&+ k_x^5 k_y \left[d_{16}(d_{12}+d_{66}) d_{55} + 2 d_{45} d_{16} \right] + k_y^5 k_x \left\{ d_{26} \left[(d_{12}+d_{66}) d_{44} + 2 d_{45} d_{26} \right] \right\} + \\
&+ k_x^4 k_y^2 \left\{ \begin{matrix} d_{26} d_{16} d_{55} + d_{16} \left[d_{26} d_{55} + d_{16} d_{44} + 2(d_{12}+d_{66}) d_{45} \right] + \\ + (d_{12}+d_{66}) \left[(d_{12}+d_{66}) d_{55} + 2 d_{45} d_{16} \right] \end{matrix} \right\} + \\
&+ k_y^4 k_x^2 \left\{ \begin{matrix} d_{26} \left[d_{26} d_{55} + d_{16} d_{44} + 2(d_{12}+d_{66}) d_{45} \right] + \\ + d_{16} d_{26} d_{44} + (d_{12}+d_{66}) \left[(d_{12}+d_{66}) d_{44} + 2 d_{45} d_{26} \right] \end{matrix} \right\} + \\
&+ k_z^4 k_x^2 \left[d_{16} d_{33} d_{54} + d_{54} (d_{16} d_{33} + d_{54} d_{55}) \right] + \\
&+ k_x^4 k_z^2 \left[d_{16} (d_{16} d_{33} + d_{54} d_{55}) + d_{54} d_{16} d_{55} \right] + \\
&+ k_z^4 k_y^2 \left\{ d_{26} d_{33} d_{54} + d_{54} \left[d_{26} d_{33} + d_{54} d_{44} - (d_{23}+d_{44})(d_{45}+d_{36}) \right] \right\} + \\
&+ k_y^4 k_z^2 \left\{ d_{26} \left[d_{26} d_{33} + d_{54} d_{44} - (d_{23}+d_{44})(d_{45}+d_{36}) \right] + d_{54} d_{26} d_{44} \right\} - \\
&- k_x^4 k_y k_z d_{16} (d_{63}+d_{45})(d_{55}+d_{13}) - k_y^4 k_x k_z d_{26} (d_{63}+d_{45})^2 + \\
&+ k_z^4 k_x k_y \left\{ d_{54} \left[2 d_{45}^2 + (d_{12}+d_{66}) d_{63} - (d_{23}+d_{44})(d_{55}+d_{13}) \right] + (d_{12}+d_{66}) d_{33} d_{54} \right\} - \\
&- k_x^3 k_y^2 k_z d_{16} (d_{63}+d_{45})^2 + \\
&+ k_x^3 k_z^2 k_y \left\{ \begin{matrix} d_{16} \left[2 d_{45}^2 + (d_{12}+d_{66}) d_{33} - (d_{23}+d_{44})(d_{55}+d_{13}) \right] + \\ + d_{54} \left[(d_{12}+d_{66}) d_{55} + 2 d_{45} d_{16} \right] + (d_{12}+d_{66}) (d_{16} d_{33} + d_{54} d_{55}) \end{matrix} \right\} + \\
&+ k_y^3 k_z^2 k_x \left\{ \begin{matrix} d_{54} \left[(d_{12}+d_{66}) d_{44} + 2 d_{45} d_{26} \right] + \\ + (d_{12}+d_{66}) \left[d_{26} d_{33} + d_{54} d_{44} - (d_{23}+d_{44})(d_{45}+d_{36}) \right] + \\ + d_{26} \left[2 d_{45}^2 + (d_{12}+d_{66}) d_{33} - (d_{23}+d_{44})(d_{55}+d_{13}) \right] \end{matrix} \right\} - \\
&- k_y^3 k_x^2 k_z \left[d_{26} (d_{63}+d_{45})(d_{55}+d_{13}) + (d_{12}+d_{66})(d_{63}+d_{45})^2 \right] - \\
&- k_z^3 k_x^2 k_y d_{54} (d_{63}+d_{45})(d_{55}+d_{13}) - k_z^3 k_y^2 k_x d_{54} (d_{63}+d_{45})^2 + \\
&+ k_x^3 k_y^3 \left\{ \begin{matrix} d_{16} \left[(d_{12}+d_{66}) d_{44} + 2 d_{45} d_{26} \right] + d_{26} \left[(d_{12}+d_{66}) d_{55} + 2 d_{45} d_{16} \right] + \\ + (d_{12}+d_{66}) \left[d_{26} d_{55} + d_{16} d_{44} + 2(d_{12}+d_{66}) d_{45} \right] \end{matrix} \right\} + \\
&+ k_z^2 k_y^2 k_x^2 \left\{ \begin{matrix} d_{16} \left[d_{26} d_{33} + d_{54} d_{44} - (d_{23}+d_{44})(d_{45}+d_{36}) \right] + d_{26} (d_{16} d_{33} + d_{54} d_{55}) + \\ + d_{54} \left[d_{26} d_{55} + d_{16} d_{44} + 2(d_{12}+d_{66}) d_{45} \right] - \left[(d_{12}+d_{66})(d_{63}+d_{45})(d_{55}+d_{13}) \right] \end{matrix} \right\} - \\
&- \omega^2 \left[d_{16} k_x^2 + d_{26} k_y^2 + d_{54} k_z^2 + (d_{12}+d_{66}) k_x k_y \right]^2
\end{aligned}
\tag{A2.3}
$$

$$
\begin{aligned}
a_{13}(a_{21}a_{32}-a_{22}a_{31}) = {} & k_x^4k_z^2\{(d_{55}+d_{13})[d_{16}(d_{63}+d_{45})-d_{66}(d_{55}+d_{13})]\}+ \\
& +k_y^4k_z^2\{(d_{45}+d_{36})[d_{26}(d_{23}+d_{44})-d_{22}(d_{45}+d_{36})]\}+ \\
& +k_z^4k_x^2\{(d_{55}+d_{13})[d_{54}(d_{63}+d_{45})-d_{44}(d_{54}+d_{13})]\}+ \\
& +k_z^4k_y^2\{(d_{45}+d_{36})[d_{54}(d_{23}+d_{44})-d_{44}(d_{45}+d_{36})]\}+ \\
& +k_y^3k_z^2k_x\left\{\begin{array}{l}(d_{55}+d_{13})[d_{26}(d_{23}+d_{44})-d_{22}(d_{45}+d_{36})]+\\ +(d_{45}+d_{36})[d_{26}(d_{63}+d_{45})-d_{22}(d_{55}+d_{13})-2d_{26}(d_{45}+d_{36})]\end{array}\right\}+ \\
& +k_x^3k_z^2k_y\{(d_{55}+d_{13})[d_{16}(d_{23}+d_{45})-d_{66}(d_{54}+d_{36})-2d_{26}(d_{55}+d_{13})]\}+ \\
& +k_z^3k_x^2k_y(d_{55}+d_{13})(d_{12}+d_{66})(d_{63}+d_{45})+ \\
& +k_z^3k_y^2k_x[(d_{12}+d_{66})(d_{23}+d_{44})(d_{55}+d_{13})+(d_{45}+d_{36})(d_{12}+d_{66})(d_{63}+d_{45})]+ \\
& +k_x^2k_y^2k_z^2\left\{\begin{array}{l}(d_{55}+d_{13})[d_{26}(d_{63}+d_{45})-d_{22}(d_{55}+d_{13})-2d_{26}(d_{45}+d_{36})]+\\ +(d_{45}+d_{36})[d_{16}(d_{23}+d_{44})-d_{66}(d_{45}+d_{36})-2d_{26}(d_{55}+d_{13})]\end{array}\right\}+ \\
& +k_y^3k_z^3\left\{\begin{array}{l}(d_{55}+d_{13})[d_{54}(d_{23}+d_{44})-d_{44}(d_{45}+d_{36})]+\\ +(d_{45}+d_{36})[d_{54}(d_{63}+d_{45})-d_{44}(d_{55}+d_{13})]\end{array}\right\}+ \\
& +\omega^2\left[(d_{55}+d_{13})k_xk_z+(d_{45}+d_{36})k_yk_z\right]^2
\end{aligned}
\tag{A2.4}
$$

From the relations (A2.1-4) we acquire the expression for the determinant of matrix $\boldsymbol{A}$:

$$
\begin{aligned}
\det A = {} & k_x^6d_{55}(d_{11}d_{66}-d_{16}^2)+k_y^6d_{44}(d_{22}d_{66}-d_{26}^2)+k_z^6d_{33}(d_{44}d_{55}-d_{54}^2)+ \\
& +k_x^5k_y\{2d_{55}[d_{16}d_{66}+d_{11}(d_{66}+d_{26})]-d_{16}[(d_{12}+d_{66})d_{55}+2d_{45}d_{16}]\}+ \\
& +k_y^5k_x\{2[d_{66}(d_{45}d_{22}+d_{26}d_{44})+d_{16}d_{22}d_{44}]-d_{26}[(d_{12}+d_{66})d_{44}+2d_{45}d_{16}]\}+ \\
& +k_x^4k_y^2\left\{\begin{array}{l}d_{11}(d_{66}d_{44}+d_{22}d_{55}+4d_{26}d_{45})+4d_{16}(d_{45}d_{66}+d_{26}d_{55})+\\ +d_{55}d_{66}^2-d_{26}d_{16}d_{55}-d_{16}[d_{26}d_{55}+d_{16}d_{44}+2(d_{12}+d_{66})d_{45}]-\\ -(d_{12}+d_{66})[(d_{12}+d_{66})d_{55}+2d_{45}d_{16}]\end{array}\right\}+ \\
& +k_y^4k_x^2\left\{\begin{array}{l}[d_{11}d_{22}d_{44}+d_{66}(d_{66}d_{44}+d_{22}d_{55}+4d_{26}d_{45})+4d_{16}(d_{45}d_{22}+d_{26}d_{44})]-\\ -d_{26}[d_{26}d_{55}+d_{16}d_{44}+2(d_{12}+d_{66})d_{45}]-\\ -d_{16}d_{26}d_{44}-(d_{12}+d_{66})[(d_{12}+d_{66})d_{44}+2d_{45}d_{26}]\end{array}\right\}+ \\
& +k_z^4k_x^2\left\{\begin{array}{l}d_{11}d_{33}d_{44}+d_{55}[d_{33}d_{66}+d_{45}d_{55}-(d_{63}+d_{45})^2]-d_{54}[d_{55}d_{54}+2d_{16}d_{33}]+\\ +(d_{55}+d_{13})[d_{54}(d_{63}+d_{45})-d_{44}(d_{54}+d_{13})]\end{array}\right\}+ \\
& +k_z^4k_y^2\left\{\begin{array}{l}d_{44}d_{36}d_{66}+d_{55}[d_{22}d_{33}+d_{44}^2-(d_{23}+d_{44})^2]-\\ -d_{54}[2d_{26}d_{33}+d_{54}d_{44}-(d_{23}+d_{44})(d_{45}+d_{36})]+\\ +(d_{45}+d_{36})[d_{54}(d_{23}+d_{44})-d_{44}(d_{45}+d_{36})]\end{array}\right\}+ \\
& +k_x^4k_z^2\left\{\begin{array}{l}d_{11}[d_{33}d_{66}+d_{44}d_{55}-(d_{63}+d_{45})^2]+d_{55}^2d_{66}-d_{16}(d_{16}d_{33}+2d_{54}d_{55})+\\ +(d_{55}+d_{13})[d_{16}(d_{63}+d_{45})-d_{66}(d_{55}+d_{13})]\end{array}\right\}+
\end{aligned}
\tag{A2.5}
$$

$$
\begin{aligned}
&+k_x^3k_z^2k_y\begin{Bmatrix}
2d_{11}\left[d_{45}d_{44}+d_{26}d_{33}-(d_{63}+d_{45})(d_{23}+d_{44})\right]+2d_{55}(d_{45}d_{66}+d_{26}d_{45})+\\
+2d_{16}\left[d_{33}d_{66}+d_{44}d_{55}-(d_{63}+d_{45})^2\right]-\\
-d_{16}\left[2d_{45}^2+(d_{12}+d_{66})d_{33}-(d_{23}+d_{44})(d_{55}+d_{13})\right]-\\
-d_{54}\left[(d_{12}+d_{66})d_{55}+2d_{45}d_{16}\right]-(d_{12}+d_{66})(d_{16}d_{33}+d_{54}d_{55})+\\
+(d_{55}+d_{13})\left[d_{16}(d_{23}+d_{44})-d_{66}(d_{54}+d_{36})-2d_{26}(d_{55}+d_{13})\right]
\end{Bmatrix}-\\
&+k_y^3k_z^2k_x\begin{Bmatrix}
2d_{66}\left[d_{45}d_{44}+d_{26}d_{33}-(d_{63}+d_{45})(d_{23}+d_{44})\right]+\\
+d_{55}(d_{45}d_{22}+d_{26}d_{44})+d_{16}\left[d_{22}d_{33}+d_{44}^2-(d_{23}+d_{44})^2\right]-\\
-d_{54}\left[(d_{12}+d_{66})d_{44}+2d_{45}d_{26}\right]-\\
-(d_{12}+d_{66})\left[d_{26}d_{33}+d_{54}d_{44}-(d_{23}+d_{44})(d_{45}+d_{36})\right]-\\
-d_{26}\left[2d_{45}^2-(d_{12}+d_{66})d_{33}-(d_{23}+d_{44})(d_{55}+d_{13})\right]+\\
+(d_{55}+d_{13})\left[d_{26}(d_{23}+d_{44})-d_{22}(d_{45}+d_{36})\right]+\\
+(d_{45}+d_{36})\left[d_{26}(d_{63}+d_{45})-d_{22}(d_{55}+d_{13})-2d_{26}(d_{45}+d_{36})\right]
\end{Bmatrix}+\\
&+k_x^3k_y^2k_z d_{16}(d_{63}+d_{45})^2+\\
&+k_y^3k_x^2k_z\left[d_{26}(d_{63}+d_{45})(d_{55}+d_{13})+(d_{12}+d_{66})(d_{63}+d_{45})^2\right]+\\
&+k_z^3k_x^2k_y\left[d_{54}(d_{63}+d_{45})(d_{55}+d_{13})+(d_{55}+d_{13})(d_{12}+d_{66})(d_{63}+d_{45})\right]+\\
&+k_z^3k_y^2k_x\begin{bmatrix}
d_{54}(d_{63}+d_{45})^2+(d_{12}+d_{66})(d_{23}+d_{44})(d_{55}+d_{13})+\\
+(d_{45}+d_{36})(d_{12}+d_{66})(d_{63}+d_{45})
\end{bmatrix}+\\
&+k_z^4k_xk_y\begin{Bmatrix}
2d_{55}\left[d_{45}d_{44}+d_{26}d_{33}-(d_{63}+d_{45})(d_{23}+d_{44})\right]+\\
+2d_{16}d_{44}d_{33}-d_{54}\left[2d_{45}^2+(d_{12}+d_{66})d_{63}-(d_{23}+d_{44})(d_{55}+d_{13})\right]-\\
-(d_{12}+d_{66})d_{33}d_{54}+(d_{54}+d_{13})\left[d_{54}(d_{23}+d_{44})-d_{44}(d_{45}+d_{36})\right]+\\
+(d_{45}+d_{36})\left[d_{54}(d_{63}+d_{45})-d_{44}(d_{55}+d_{13})\right]
\end{Bmatrix}+\\
&+k_x^2k_y^2k_z^2\begin{Bmatrix}
d_{55}(d_{66}d_{44}+d_{22}d_{55}+4d_{26}d_{45})+\\
+4d_{16}\left[d_{45}d_{44}+d_{26}d_{33}-(d_{63}+d_{45})(d_{23}+d_{44})\right]-\\
-d_{16}\left[d_{26}d_{33}+d_{54}d_{44}-(d_{23}+d_{44})(d_{45}+d_{36})\right]-d_{26}(d_{16}d_{33}+d_{54}d_{55})-\\
-d_{54}\left[d_{26}d_{55}+d_{16}d_{44}+2(d_{12}+d_{66})d_{45}\right]+\\
+\left[(d_{12}+d_{66})(d_{63}+d_{45})(d_{55}+d_{13})\right]+\\
+(d_{55}+d_{13})\left[d_{26}(d_{63}+d_{45})-d_{22}(d_{55}+d_{13})-2d_{26}(d_{45}+d_{36})\right]+\\
+(d_{45}+d_{36})\left[d_{16}(d_{33}+d_{44})-d_{66}(d_{45}+d_{36})-2d_{26}(d_{55}+d_{13})\right]
\end{Bmatrix}+\\
&+k_x^4k_yk_z d_{16}(d_{63}+d_{45})(d_{55}+d_{13})+k_y^4k_xk_z d_{26}(d_{63}+d_{45})^2+\\
&+k_x^3k_y^3\begin{Bmatrix}
2d_{11}(d_{45}d_{22}+d_{26}d_{44})+2d_{66}(d_{45}d_{66}+d_{26}d_{55})+\\
+2d_{16}(d_{66}d_{44}+d_{22}d_{55}+4d_{26}d_{45})-\\
-d_{16}\left[(d_{12}+d_{66})d_{44}+2d_{45}d_{26}\right]-d_{26}\left[(d_{12}+d_{66})d_{55}+2d_{45}d_{16}\right]-\\
-(d_{12}+d_{66})\left[d_{26}d_{55}+d_{16}d_{44}+2(d_{12}+d_{66})d_{45}\right]
\end{Bmatrix}+
\end{aligned}
$$

$$
\begin{aligned}
&+k_y^3k_z^3\left\{\begin{array}{l}(d_{55}+d_{13})\left[d_{54}(d_{23}+d_{44})-d_{44}(d_{45}+d_{36})\right]+\\+(d_{45}+d_{36})\left[d_{54}(d_{63}+d_{45})-d_{44}(d_{55}+d_{13})\right]\end{array}\right\}+\\
&+k_y^4k_z^2\left\{\begin{array}{l}d_{66}\left[d_{22}d_{33}+d_{44}^2-(d_{23}+d_{44})^2\right]+d_{55}d_{22}d_{44}-\\-d_{26}\left[d_{26}d_{33}+d_{54}d_{44}-(d_{23}+d_{44})(d_{45}+d_{36})\right]-d_{54}d_{26}d_{44}+\\+(d_{45}+d_{36})\left[d_{26}(d_{23}+d_{44})-d_{22}(d_{45}+d_{36})\right]\end{array}\right\}-\\
&-\omega^6+\omega^4\left[\begin{array}{l}k_x^2(d_{11}+d_{55}+d_{66})+k_y^2(d_{22}+d_{44}+d_{66})+\\+k_z^2(d_{33}+d_{44}+d_{55})+2k_xk_y(d_{16}+d_{26}+d_{45})\end{array}\right]-\\
&-\omega^2\left\{\begin{array}{l}\left(k_x^2d_{11}+k_y^2d_{66}+k_z^2d_{55}+2k_xk_yd_{16}\right)\times\\\times\left[k_x^2(d_{55}+d_{66})+k_y^2(d_{22}+d_{44})+k_z^2(d_{33}+d_{44})+2k_xk_y(d_{26}+d_{45})\right]+\\+k_x^4d_{55}d_{66}+k_y^4d_{22}d_{44}+k_z^4d_{33}d_{44}+k_x^2k_y^2(d_{66}d_{44}+d_{22}d_{55}+4d_{26}d_{45})+\\+k_x^2k_z^2\left[d_{33}d_{66}+d_{45}d_{55}-(d_{63}+d_{45})^2\right]+k_y^2k_z^2\left[d_{22}d_{33}+d_{44}^2-(d_{23}+d_{44})^2\right]+\\+2k_x^3k_y(d_{45}d_{66}+d_{26}d_{55})+2k_y^3k_z(d_{45}d_{22}+d_{26}d_{44})+\\+2k_z^2k_xk_y\left[d_{55}d_{44}+d_{26}d_{33}-(d_{63}+d_{45})(d_{23}+d_{44})\right]-\\-\left[k_x^2d_{16}+k_y^2d_{26}+k_z^2d_{54}+k_xk_y(d_{12}+d_{66})\right]^2-\\-\left[k_xk_z(d_{55}+d_{13})+k_yk_z(d_{45}+d_{36})\right]^2\end{array}\right\}
\end{aligned}
$$

Appendix A_3

Coefficients $a_{i,j,k}^{m,n,l}$ are bound to wavenumbers products.

The subscripts mean the coordinates of wavenumbers whereas superscripts power numbers. For ex ample, the coefficient $a_{1,2,3}^{3,2,1}$ is bound to $k_x^3 k_y^2 k_z^1$.

In relation for H(k_x, k_y, k_z, θ, Ψ) we have the following coefficients in form of the combinations of the elasticity tensors components:

$$a_1^6 = d_{55}\left(d_{11}d_{66} - d_{16}^2\right)$$
$$a_2^6 = d_{44}\left(d_{22}d_{66} - d_{26}^2\right)$$
$$a_3^6 = d_{33}\left(d_{44}d_{55} - d_{54}^2\right)$$
$$a_{1,2}^{5,1} = 2d_{55}\left[d_{16}d_{66} + d_{11}\left(d_{66} + d_{26}\right)\right] - d_{16}\left[\left(d_{12} + d_{66}\right)d_{55} + 2d_{45}d_{16}\right]$$
$$a_{2,1}^{5,1} = 2\left[d_{66}\left(d_{45}d_{22} + d_{26}d_{44}\right) + d_{16}d_{22}d_{44}\right] - d_{26}\left[\left(d_{12} + d_{66}\right)d_{44} + 2d_{45}d_{26}\right]$$
$$a_{1,2}^{4,2} = d_{11}\left(d_{66}d_{44} + d_{22}d_{55} + 4d_{26}d_{45}\right) + 4d_{16}\left(d_{45}d_{66} + d_{26}d_{55}\right) + d_{55}d_{66}^2 - d_{26}d_{16}d_{55} -$$
$$- d_{16}\left[d_{26}d_{55} + d_{16}d_{44} + 2\left(d_{12} + d_{66}\right)d_{45}\right] - \left(d_{12} + d_{66}\right)\left[\left(d_{12} + d_{66}\right)d_{55} + 2d_{45}d_{16}\right]$$
$$a_{2,1}^{4,2} = d_{11}d_{22}d_{44} + d_{66}\left(d_{66}d_{44} + d_{22}d_{55} + 4d_{26}d_{45}\right) + 4d_{16}\left[d_{45}d_{22} + d_{26}d_{44}\right] -$$
$$- d_{26}\left[d_{26}d_{55} + d_{16}d_{44} + 2\left(d_{12} + d_{66}\right)d_{45}\right] - d_{16}d_{26}d_{44} + \left(d_{12} + d_{66}\right)\left[\left(d_{12} + d_{66}\right)d_{44} + 2d_{45}d_{26}\right]$$
$$a_{3,1}^{4,2} = d_{11}d_{33}d_{44} + d_{55}\left[d_{33}d_{66} + d_{45}d_{55} - \left(d_{63} + d_{45}\right)^2\right] - d_{54}\left[d_{54}d_{55} + 2d_{16}d_{33}\right] +$$
$$+ \left(d_{55} + d_{13}\right)\left[d_{54}\left(d_{63} + d_{45}\right) - d_{44}\left(d_{54} + d_{13}\right)\right]$$
$$a_{3,2}^{4,2} = d_{44}d_{66}d_{36} + d_{55}\left[d_{22}d_{33} + d_{44}^2 - \left(d_{23} + d_{44}\right)^2\right] - d_{54}\left[2d_{26}d_{33} + d_{54}d_{44} - \left(d_{23} + d_{44}\right)\left(d_{45} + d_{36}\right)\right] +$$
$$+ \left(d_{45} + d_{36}\right)\left[d_{54}\left(d_{23} + d_{44}\right) - d_{44}\left(d_{45} + d_{36}\right)\right]$$

$$a_{1,3}^{4,2} = d_{11}\left[d_{33}d_{66} + d_{45}d_{55} - \left(d_{63} + d_{45}\right)^2\right] + d_{55}^2 d_{66} - d_{16}\left(d_{16}d_{33} + 2d_{54}d_{55}\right) +$$
$$+ \left(d_{55} + d_{13}\right)\left[d_{16}\left(d_{63} + d_{45}\right) - d_{66}\left(d_{55} + d_{13}\right)\right]$$
$$a_{2,3}^{4,2} = d_{66}\left[d_{22}d_{23} + d_{44}^2 - \left(d_{23} + d_{44}\right)^2\right] + d_{55}d_{22}d_{44} - d_{26}\left[d_{26}d_{33} + d_{54}d_{44} - \left(d_{23} + d_{44}\right)\left(d_{45} + d_{36}\right)\right] -$$
$$- d_{54}d_{26}d_{44} + \left(d_{54} + d_{36}\right)\left[d_{26}\left(d_{23} + d_{44}\right) - d_{22}\left(d_{45} + d_{36}\right)\right]$$

$$
\begin{aligned}
a_{1,3,2}^{3,2,1} &= 2d_{11}\left[d_{45}d_{44}+d_{26}d_{33}-(d_{63}+d_{45})(d_{23}+d_{44})\right]+2d_{55}(d_{45}d_{66}+d_{26}d_{54})+\\
&+2d_{16}\left[d_{33}d_{66}+d_{44}d_{45}-(d_{63}+d_{44})^2\right]-d_{16}\left[2d_{45}^2+(d_{12}+d_{66})d_{33}-(d_{23}+d_{44})(d_{55}+d_{13})\right]-\\
&-d_{54}\left[(d_{12}+d_{66})d_{55}+2d_{45}d_{16}\right]-(d_{12}+d_{66})(d_{16}d_{33}+d_{54}d_{55})+\\
&+(d_{55}+d_{13})\left[d_{16}(d_{23}+d_{44})-d_{66}(d_{54}+d_{36})-2d_{26}(d_{55}+d_{13})\right]\\
a_{2,3,1}^{3,2,1} &= 2d_{66}\left[d_{45}d_{44}+d_{26}d_{33}-(d_{63}+d_{45})(d_{23}+d_{44})\right]+d_{55}(d_{45}d_{22}+d_{26}d_{44})+\\
&+d_{16}\left[d_{22}d_{33}+d_{44}^2-(d_{23}+d_{44})^2\right]-d_{54}\left[(d_{12}+d_{66})d_{44}+2d_{45}d_{26}\right]-\\
&-(d_{12}+d_{66})\left[d_{26}d_{33}+d_{54}d_{44}-(d_{23}+d_{44})(d_{45}+d_{36})\right]-\\
&-d_{26}\left[2d_{45}^2-(d_{12}+d_{66})d_{33}-(d_{23}+d_{44})(d_{55}+d_{36})\right]+\\
&+(d_{55}+d_{13})\left[d_{26}(d_{23}+d_{44})-d_{22}(d_{45}+d_{36})\right]+\\
&+(d_{45}+d_{36})\left[d_{26}(d_{63}+d_{45})-d_{22}(d_{55}+d_{13})-2d_{26}(d_{45}+d_{36})\right]\\
a_{1,2,3}^{3,2,1} &= d_{16}(d_{63}+d_{45})^2\\
a_{2,1,3}^{3,2,1} &= (d_{63}+d_{45})(d_{55}+d_{13})d_{26}+(d_{12}+d_{66})(d_{63}+d_{45})^2\\
a_{3,1,2}^{3,2,1} &= d_{54}(d_{63}+d_{45})(d_{55}+d_{13})+(d_{12}+d_{66})(d_{63}+d_{45})(d_{55}+d_{13})\\
a_{3,2,1}^{3,2,1} &= d_{54}(d_{63}+d_{45})^2+(d_{12}+d_{66})(d_{23}+d_{44})(d_{55}+d_{13})+(d_{45}+d_{36})(d_{12}+d_{66})(d_{63}+d_{44})\\
a_{3,1,2}^{4,1,1} &= 2d_{55}\left[d_{45}d_{44}+d_{26}d_{33}-(d_{63}+d_{45})(d_{23}+d_{44})\right]+2d_{16}d_{44}d_{33}-\\
&-d_{54}\left[2d_{54}^2+(d_{12}+d_{66})d_{63}-(d_{23}+d_{44})(d_{55}+d_{13})\right]-(d_{12}+d_{66})d_{33}d_{54}+\\
&+(d_{55}+d_{13})\left[d_{54}(d_{23}+d_{44})-d_{44}(d_{45}+d_{36})\right]+\\
&+(d_{45}+d_{36})\left[d_{54}(d_{63}+d_{45})-d_{44}(d_{45}+d_{13})\right]\\
a_{1,2,3}^{4,1,1} &= d_{16}(d_{63}+d_{45})(d_{55}+d_{16})\\
a_{2,1,3}^{4,1,1} &= d_{26}(d_{63}+d_{45})^2\\
a_{1,2}^{3,3,} &= 2d_{11}(d_{45}d_{22}+d_{26}d_{44})+2d_{66}(d_{45}d_{66}+d_{26}d_{55})+2d_{16}(d_{66}d_{44}+d_{22}d_{55}+4d_{26}d_{45})-\\
&-d_{16}\left[(d_{12}+d_{66})d_{44}+2d_{45}d_{26}\right]-d_{26}\left[(d_{12}+d_{66})d_{55}+2d_{45}d_{16}\right]-\\
&-(d_{12}+d_{66})\left[d_{26}d_{55}+d_{16}d_{44}+2(d_{12}+d_{66})d_{45}\right]\\
a_{2,3}^{3,3} &= (d_{55}+d_{13})\left[d_{54}(d_{23}+d_{44})-d_{44}(d_{45}+d_{36})\right]+(d_{45}+d_{36})\left[d_{54}(d_{63}+d_{45})-d_{44}(d_{55}+d_{13})\right]\\
a_{1,2,3}^{2,2,2} &= d_{55}\left[d_{66}d_{44}+d_{22}d_{55}+4d_{26}d_{45}\right]+4d_{16}\left[d_{45}d_{44}+d_{26}d_{33}-(d_{63}+d_{45})(d_{23}+d_{44})\right]-\\
&-d_{16}\left[d_{26}d_{33}+d_{54}d_{44}-(d_{23}+d_{44})(d_{45}+d_{36})\right]-d_{26}\left[d_{16}d_{33}+d_{54}d_{55}\right]-\\
&-d_{54}\left[d_{26}d_{55}+d_{16}d_{44}+2(d_{12}+d_{66})d_{45}\right]+(d_{12}+d_{66})(d_{63}+d_{45})(d_{55}+d_{13})+\\
&+(d_{55}+d_{13})\left[d_{26}(d_{63}+d_{45})-d_{22}(d_{55}+d_{13})-2d_{26}(d_{45}+d_{36})\right]+\\
&+(d_{45}+d_{36})\left[d_{16}(d_{33}+d_{44})-d_{66}(d_{45}+d_{36})-2d_{26}(d_{55}+d_{13})\right]
\end{aligned}
$$

Appendix A4

After introduction of the Thomsen's parameters ε and δ we derive following relations for respective components [ρ – normalized] of C tensor:

$$\begin{aligned} C_{11} &= V_{P\perp}^2 q = V_{P\perp}^2 (1+2\varepsilon) \\ C_{33} &= V_{P\perp}^2 \\ C_{13} &= \left(1+2\delta\right)^{1/2} C_{33} = V_{P\perp}^2 \left(1+2\delta\right)^{1/2} \end{aligned} \tag{A4.1}$$

where $V_{P\perp}$ is compressional velocity in direction perpendicular to the lamination.

Taking $C_{44} = C_{66} = 0$ and applying approximation $(1 + 2\delta)^{½} \approx 1 + \delta$ we get following relation for (1.15):

$$d_{11} = V_{P\perp}^2 \left[(1+2\varepsilon)\cos^4 \Psi + \sin^4 \Psi + \frac{1}{2}(1+\delta)\sin^2(2\Psi) \right] \tag{A4.2}$$

$$d_{13} = V_{P\perp}^2 \left[(1+2\varepsilon)\cos^2 \Psi + (1+\delta)\sin^2 \Psi \right] \tag{A4.3}$$

$$d_{33} = C_{11} = V_{P\perp}^2 (1+2\varepsilon) \tag{A4.4}$$

$$d_{11} d_{33} - d_{13}^2 = V_{P\perp}^4 \eta_a \sin^4 \Psi \tag{A4.5}$$

where $\eta_a = 2(\varepsilon - \delta)$

$$d_{66} = \frac{1}{2} V_{P\perp}^2 \sin^2(2\Psi)[\varepsilon - \delta] \tag{A4.6}$$

$$d_{63} = \frac{1}{2} V_{P\perp}^2 \sin(2\Psi)[2\varepsilon - \delta] \tag{A4.7}$$

$$d_{66} d_{33} - d_{63}^2 = \frac{1}{2} V_{P\perp}^4 \sin^2(2\Psi) \left\{ (\varepsilon - \delta)(1+2\varepsilon) - \frac{1}{2}[2\varepsilon - \delta]^2 \right\} \tag{A4.8}$$

$$d_{16} = \frac{1}{2} V_{P\perp}^2 \sin\ (2\Psi) \left\{ (2\varepsilon - \delta)\cos^2 \Psi + \delta \sin^2 \Psi \right\} \tag{A4.9}$$

$$d_{11}d_{66} = \frac{1}{2}V_{P\perp}^{4}\sin^{2}(2\Psi)\left[(1+2\varepsilon)\cos^{4}\Psi + \sin^{4}\Psi + \frac{1}{2}(1+\delta)\sin^{2}(2\Psi)\right][\varepsilon-\delta] \tag{A4.10}$$

$$\begin{aligned} d_{11}\left(d_{33}d_{66}-d_{63}^{2}\right) &= \frac{1}{4}V_{P\perp}^{6}\sin^{2}(2\Psi)\left[(1+2\varepsilon)\cos^{4}\Psi + \sin^{4}\Psi + \frac{1}{2}(1+\delta)\ \sin^{2}(2\Psi)\right] \\ &\times \left\{2(1+2\varepsilon)[\varepsilon-\delta]-[2\varepsilon-\delta]^{2}\right\} \end{aligned} \tag{A4.11}$$

$$d_{16}^{2}d_{33} = \frac{1}{4}V_{P\perp}^{6}\sin^{2}(2\Psi)(1+2\varepsilon)\left[(2\varepsilon-\delta)\cos^{2}\Psi + \delta\sin^{2}\Psi\right]^{2} \tag{A4.12}$$

$$d_{13}^{2}d_{66} = \frac{1}{2}V_{P\perp}^{6}\sin^{2}(2\Psi)\left[(1+2\varepsilon)\cos^{2}\Psi + (1+\delta)\ \sin^{2}\Psi\right]^{2}(\varepsilon-\delta) \tag{A4.13}$$

$$d_{13}d_{16}d_{63} = \frac{1}{4}V_{P\perp}^{6}\sin^{3}(2\Psi)\left[(1+2\varepsilon)\cos^{2}\Psi + (1+\delta)\sin^{2}\Psi\right](\varepsilon-\delta)(2\varepsilon-\delta) \tag{A4.14}$$